The Charged Particle Multiplicity at Center of Mass Energies from 900 GeV to 7 TeV measured with the ATLAS Experiment at the Large Hadron Collider

Thesis by

Heather M. Gray

In Partial Fulfillment of the Requirements
for the Degree of
Doctor of Philosophy

California Institute of Technology
Pasadena, California

2011
(Defended November 9, 2010)

© 2011
Heather M. Gray
All Rights Reserved

Kuhlangene isanga nenkohla

Acknowledgements

Over the course of my PhD I was fortunate to work on number of projects with many different people. This makes it impossible to thank each person who contributed to my PhD individually.

Firstly, I'd like to thank my advisor, Emlyn Hughes, for his energy and enthusiasm, for sending me to CERN and allowing me freedom to develop as scientist. Thank you to the other members of the Columbia group.

I had a lot of fun working with all the members of the ATLAS pixel group while commissioning the pixel detector. A special thanks goes to Sara Strandberg with whom I enjoyed building ToothPix, calibrating and commissioning the pixel detector and studying the charge scale in cosmics. Thank you for teaching me how to measure things and how never to give up.

Thank you to all the members, official or not, of the MB1 crew, my companions during the most difficult and exciting part of my PhD. I doubt I'll ever forget the 11pm Saturday meeting. I'd especially like to thank Andi Salzburger, my one-armed companion on many long nights of analysis and who taught me so much about tracking. Thank you for always being there to answer any question no matter the time and your energy which made solving problems so much fun.

I'd like to thank Kevin Einsweiler who seems to know everything there is to know about pixel detectors. Thank you for believing in me and for your patience in answering so many questions on topics ranging from hardware to analysis. Thank you to Beate Heinemann who seems to be a bottomless source of good ideas, enthusiasm and common sense. Working with you taught me many important things about being a physicist.

Most of all, I'd like to thank my friends and family who are increasing dispersed all over the world. Thank you for making me laugh, keeping me sane and always providing a welcoming couch whenever I showed up to visit, and, most importantly for reminding me about the important parts of life apart from work.

Abstract

The first measurements made by the ATLAS experiment at the LHC are presented. The charged particle multiplicity, its dependence on transverse momentum and pseudorapidity, and the relationship between mean transverse momentum and pseudorapidity are measured for events with at least one charged particle in the kinematic range $|\eta| < 2.5$ and $p_T > 500$ MeV. The charged particle multiplicity distributions are measured at the three centre of mass energies at which protons have been collided in the LHC: 900 GeV, 2.36 TeV and 7 TeV. The results are compared to predictions from Monte Carlo models of proton-proton collisions. All models predicted a multiplicity at least 10% lower than was measured. They also failed to predict a sufficient increase in the multiplicity when the centre of mass energy increased from 900 GeV to 7 TeV. Updated models have already been produced using these data, which provide a significantly better description of the properties of proton-proton collisions at LHC energies.

Contents

Appendices

Chapter 1

Introduction

The first collisions from the Large Hadron Collider (LHC) at the European Organization for Nuclear Research (CERN) just outsde Geneva, Switzerland were recorded on the 6^{th} December 2009 at a centre of mass energy of $\sqrt{s} = 900$ GeV. Since that date, the commissioning of the LHC has progressed rapidly: on 13^{th} December 2009 collisions at $\sqrt{s} = 2.36$ TeV made the LHC the highest energy collider in the world and on 30^{th} March 2010, the first collisions at $\sqrt{s} = 7$ TeV were delivered to worldwide media attention. To date, slightly more than 10 $\text{pb}^{-1}$of data have been recorded by ATLAS, and it is expected that a dataset of 100 pb^{-1} - 1 fb^{-1} will have been delivered by the end of 2011. This marks the beginning of an extremely exciting period in particle physics, the LHC era, in which the high energy and intensity of the LHC beams will allow for many stringent tests of the Standard Model of particle physics.

The number of charged particles in an event is one of the most basic observables in hadron-hadron collisions, but it lacks a robust theoretical prescription because most of the particles are produced through interactions involving a small momentum transfer. Such interactions cannot be described by perturbative Quantum Chromodynamics (QCD). Therefore current models are phenomenological and have a large number of parameters which need to be tuned to experimental data. Charged particle multiplicities have been measured using cosmic rays, in fixed target experiments, and at particle colliders in collisions over a wide range of centre of mass energies.

This thesis discusses the measurement of charged particle multiplicity distributions with A Toroidal LHC ApparatuS (ATLAS), one of four large experiments at the LHC, at three different centre of mass energies: $\sqrt{s} = 900$ GeV $\sqrt{s} = 2.36$ TeV and $\sqrt{s} = 7$ TeV. Four different distributions were measured: the charged particle multiplicity, the multiplicity as a function of pseudorapidity, the multiplicity as a function of the transverse momentum, and the average transverse momentum as a function of the multiplicity. These distributions are measured using tracks reconstructed in the ATLAS Inner Detector.

An essential component in measuring charged particle multiplicity distributions is estimating the reconstruction efficiency of charged particles passing through the Inner Detector. The efficiency was estimated using the Monte Carlo simulation of the ATLAS detector; however, detailed studies were made to understand the accuracy of the simulation and to quantify the performance of the track reconstruction algorithms. This estimate of the track reconstruction efficiency and the associated systematic uncertainties are currently used by many other measurements using tracks reconstructed in the Inner Detector.

All the data recorded by ATLAS at $\sqrt{s} = 2.36$ TeV had the silicon strip detector in standby with reduced depletion voltage. This meant that the track reconstruction efficiency was significantly reduced and not described by the simulation. The relative change to the efficiency was measured in data and used to correct the efficiency. This allowed charged particle distributions to be measured at $\sqrt{s} = 2.36$ TeV despite the fact that the detector was not in a fully operational state.

In addition to the measurement of charged particle multiplicities, the calibration, commissioning and performance of the innermost detector of the Inner Detector, the pixel detector, are discussed. A measurement of the charge scale using the cosmic ray data taken prior to the turn-on of the LHC is presented. The charge scale will be shown to be consistent with theoretical predictions within systematic uncertainties.

The charged particle multiplicity per event and unit of pseudorapidity at $\eta = 0$ was measured to be:

- $1.333 \pm 0.003(\text{stat.}) \pm 0.0040(\text{syst.})$ at $\sqrt{s} = 900$ GeV,
- $1.739 \pm 0.019(\text{stat.}) \pm 0.058(\text{syst.})$ at $\sqrt{s} = 2.36$ TeV, and
- $2.409 \pm 0.004(\text{stat.}) \pm 0.061(\text{syst.})$ at $\sqrt{s} = 7$ TeV.

The charged particle multiplicity distributions at $\sqrt{s} = 900$ GeV were the first physics result published by the ATLAS experiment [4]. It will be shown that model predictions of the charged particle multiplicity were low, and, in particular, the increase in the multiplicity from $\sqrt{s} = 900$ GeV to $\sqrt{s} = 7$ TeV was underestimated by all the models studied. These measurements have already provided crucial input to the tuning Monte Carlo generators to describe hadron-hadron collisions at the LHC [126].

Chapter 2

Theory

2.1 The Standard Model of Particle Physics

The Standard Model (SM) of Particle Physics is a framework describing all known elementary particles and their interactions. It incorporates the theories of the electromagnetic, weak and strong forces, but not the theory of gravitation. The SM has withstood extensive tests from many experiments and has accurately predicted a wide range of phenomena. See [31] for a recent review of the SM and a summary of experimental tests.

The building blocks of matter are particles called fermions, which have spin-$\frac{1}{2}$. The fermions can be divided into quarks and leptons and grouped into three generations. Each generation contains a charged and a neutral lepton and an up-type and a down-type quark. All stable matter is made from the first generation because the charged particles in the second and third generations are unstable. Particles in higher generations therefore rapidly decay into the first generation.

The three fundamental forces in the SM are mediated through the exchange of spin-1 bosons with the strength of each force described by a coupling constant. The photon, γ, is the carrier of the electromagnetic interaction; the weak force is carried by the W and Z bosons and eight gluons mediate the strong force. The hypothetical spin-2 graviton would be the mediator of the gravitational force. A problem with the SM is the fact that the symmetry of the electroweak Lagrangian cannot be exact because this would require the weak gauge bosons to be massless. A possible solution is the Higgs mechanism [92, 78, 90], which spontaneously breaks this symmetry by introducing an electroweak doublet of complex scalar fields. Figure 2.1 shows the particles of the Standard Model and the date in which each particle was first discovered. The hypothetical Higgs boson is shown, although it has not been observed.

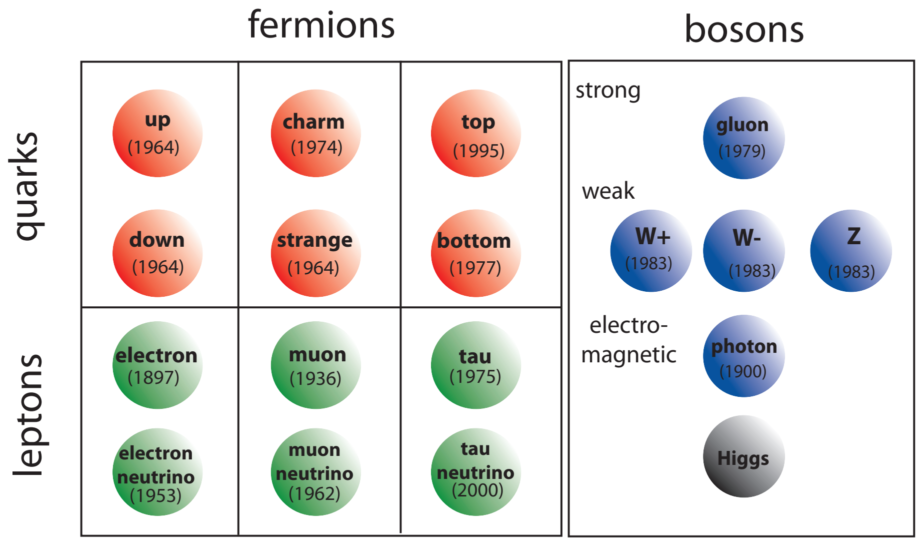

Figure 2.1: The particles of the Standard Model and the year in which they were first observed in an experiment. The quarks are shown in red, the leptons in green and the gauge bosons in grey.

2.1.1 The Strong Interaction

The strong interaction is described by a non-Abelian gauge theory called Quantum Chromodynamics (QCD) [87, 104, 75]. The quantum number of the strong interaction is called colour and occurs in three states typically referred to as red, green and blue. Quarks and gluons are not found as individual particles: rather they are found as bound states containing either two or three quarks, which are called hadrons. All known hadrons are colour singlets: although hadrons consist of coloured quarks, the only possible colour configurations leave the hadron with no residual colour. A meson is a quark-antiquark pair in a colour-anticolour state. Each of the three quarks in a baryon has a different colour. Both of these combinations mean that the hadron is colourless. In addition to the *valence quarks* determining the quantum number of the hadrons, hadrons contain a sea of virtual quarks and gluons, which contribute to the total energy and momentum. The constituents of a hadron are collectively referred to as partons.

The strong interaction between quarks and gluons is derived from the invariance of the Lagrangian under SU(3) rotations in colour space. Local invariance requires the introduction of eight gauge fields into the Lagrangian, which correspond to the eight gluons mediating the strong force. Unlike the photons which mediate Quantum Electrodynamics (QED), the gluons carry colour charge, which means that interactions occur between the gluons. The strength of the strong interaction is described by the strong coupling constant, $\alpha_s = \frac{g_s^2}{4\pi}$, where g_s is the coupling associated with the SU(3) gauge symmetry of the strong force.

The self-interaction of the gluons means that α_s depends on the scale of the interaction. The scale of an interaction is the four momentum transferred between the partons participating in the hard scattering, Q^2. An interaction involving a large transfer of momentum is called *hard* and an interaction involving a small momentum transfer is called *soft*.

At the leading order the strength of the strong coupling is given by:

$$\alpha_s(Q^2) = \frac{12\pi}{(33 - 2n_f)\ln(Q^2/\Lambda^2_{QCD})} \tag{2.1}$$

where n_f is the number of quark flavours and Λ_{QCD} is the QCD renormalisation scale. Equation 2.1 shows that α_s decreases with the inverse logarithm of the interaction strength. Figure 2.2 shows the dependence of α_s on the energy scale. The theoretical predictions for the coupling are compared to experimental results at different energies.

At small distances, or high Q^2, the coupling becomes small and this phenomenon is referred to as *asymptotic freedom* [87, 104]. Therefore, at high Q^2 QCD interactions can be calculated using a perturbative expansion. The accuracy of the calculation improves as more orders of the perturbative expansion are included, however additional diagrams rapidly increase the complexity of the calculation.

At low Q^2, on the other hand, the coupling becomes large, such that soft processes cannot be calculated using a perturbative expansion. The large distance behaviour of the coupling constant leads to a property of the strong interaction known as *confinement*. Confinement means that quarks and gluons are not free, but only appear as hadronic bound states.

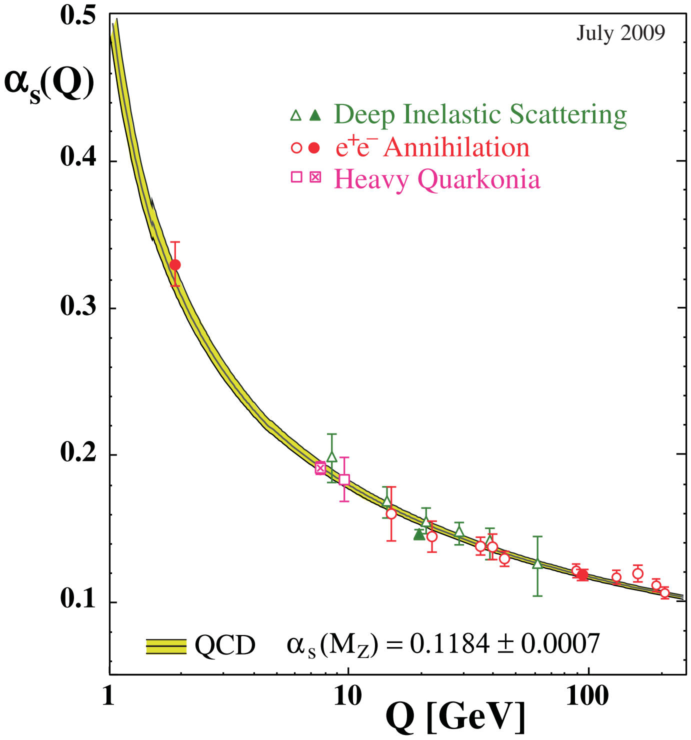

Figure 2.2: Summary of measurements of α_s as a function of the energy scale Q. The curves are QCD predictions for the combined world average value. Full symbols are results based on N3LO QCD, open circles are based on NNLO, open triangles and squares on NLO QCD. The cross-filled square is based on lattice QCD. The filled triangle at $Q = 20$ GeV (from DIS structure functions) is calculated from the original result which includes data in the energy range from Q =2 to 170 GeV. From Ref. [47]

2.2 Hadronic Collisions

Obtaining an appropriate description of the physics of hadron-hadron collisions has been a topic of interest over the past 20 years. Hadronic collisions, some aspects of which are illustrated in Fig. 2.3, are complicated and busy. The incoming hadrons are not elementary particles but composite and their constituent partons are continuously changing. When the two hadrons collide several partons may interact and be scattered in different directions. Either the incoming or outgoing partons may radiate and all outgoing partons hadronise to produce observable particles. Hadronic collisions are extremely complex processes and involve both perturbative and non-perturbative QCD processes.

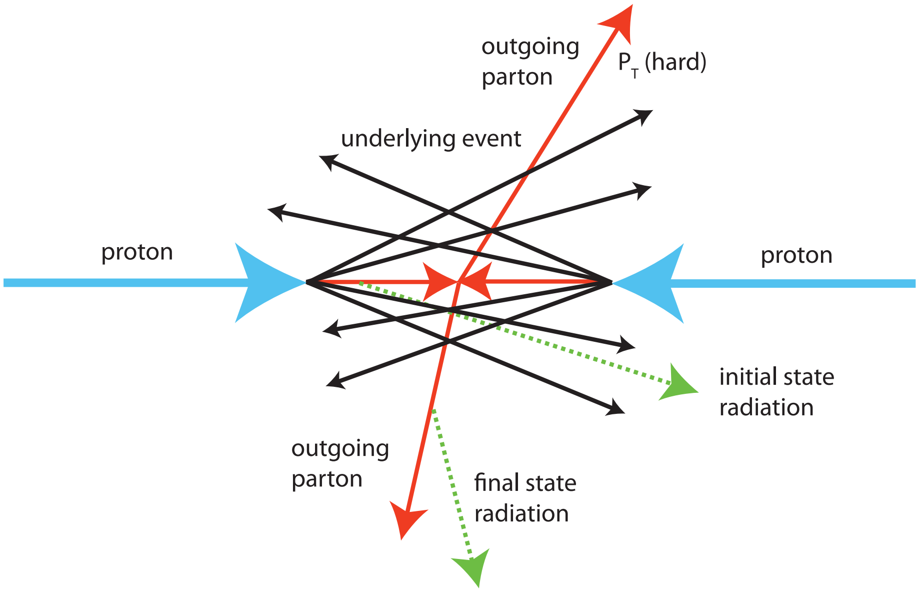

Figure 2.3: Illustration of components of a hard scattering process in a hadron-hadron collision. The incoming protons are shown in blue. The partons undergoing the hard scattering are shown in red. Possible initial and final state radiation is shown using dashed green lines. The particles participating in the underlying event are shown in black.

Fortunately, many of the complicated phenomena are soft, i.e. only involve particles with low momenta. Most physics processes of interest, such as Higgs boson production or supersymmetry, occur through a large momentum transfer. The particles produced through processes in addition to the hard scattering are referred to as being part of the *underlying event*. Therefore, when only the high-p_T particles in an event are studied, the contribution from the soft interactions are typically negligible. In precision studies, such as the measurement of the mass of the top quark, on the other hand, the model used for the underlying event can have a significant impact [136].

A number of components are required to fully describe the properties of hadronic collisions: the matrix elements describing the hard scattering itself, the parton density functions (pdfs) which describe the parton content of the hadrons, the showering of partons before (initial state showers) and after the hard scattering (final state showers), the fragmentation of partons into hadrons and the decays of unstable hadrons. Some components can be studied individually, but there is interference between the different components. For example, particles produced during initial state radiation can interact with the particles produced in the parton shower. Therefore, studying the two processes independently cannot provide a full description.

2.2.1 Hadron-Hadron Scattering and the Factorisation Theorem

The cross-section for the hard scattering of two hadrons can be written as follows:

$$\sigma(P_1, P_2) = \sum_{i,j} \int dx_1 dx_2 f_i(x_1, \mu^2) f_j(x_2, \mu^2) \hat{\sigma}_{ij}(p_1, p_2, \alpha_s(\mu^2), Q^2/\mu^2) \tag{2.2}$$

The four momenta of the two incoming hadrons are P_1 and P_2. Two momenta of the two partons which participate in the hard scattering are $p_1 = x_1 P_1$ and $p_2 = x_2 P_2$. Each parton only has a fraction of the hadron momentum, because each hadron contains many partons. The four momentum transferred between the partons in the hard scattering is Q. The parton distribution functions, $f_i(x, \mu^2)$, depend on the fraction of momentum carried by each parton and the choice of factorisation scale, μ, which will be discussed later. The short distance scattering cross-section for the partons is $\hat{\sigma}_{ij}$. The components of cross-section are illustrated in Fig. 2.4.

Because α_s is small at high energies, the short distance cross-section can be calculated using a perturbation series, i.e. it can be written as:

$$\hat{\sigma} = \alpha_s^k \sum_{m=0}^{n} c^{(m)} \alpha_s^m \tag{2.3}$$

Here, the $c^{(m)}$ are functions of the kinematic variables and the factorisation scale. Different hard processes begin to contribute at different powers of k.

The order at which an observable is calculated refers to how many terms in the perturbative

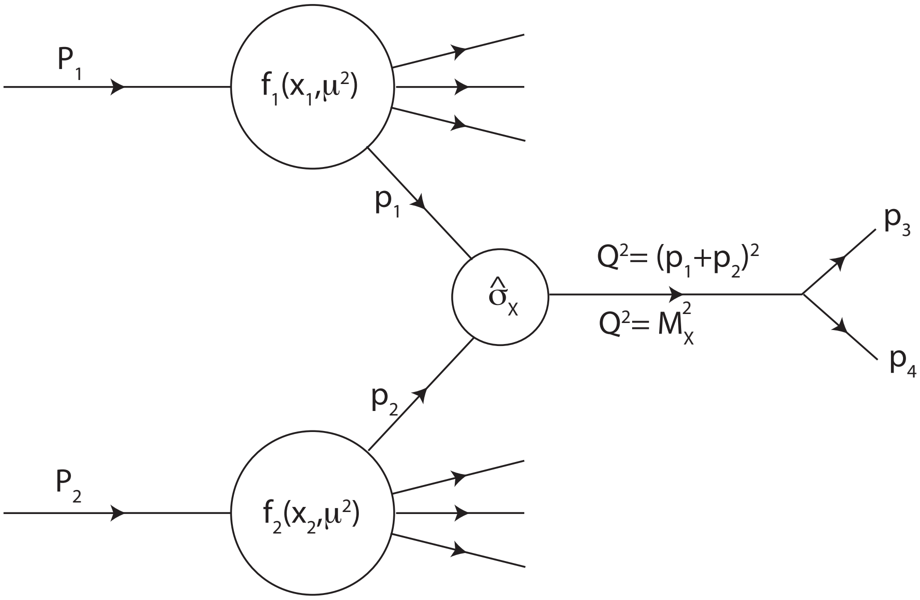

Figure 2.4: The components of the cross-section for the hard scattering of two hadrons with momenta P_1 and P_2. The parton distribution functions, $f_j(x_j, Q^2)$, give the probability to have a parton with a fraction, x_j, of the proton momentum participate in the hard scattering. The cross-section for the parton interaction is $\hat{\sigma_X}$.

expansion were used. At leading order, the short-distance cross-section is the same as the full parton scattering cross-section. At higher orders, the long-distance components of the parton scattering cross-section are removed and described by the parton distribution functions. Essentially, such a factorisation of the calculation is equivalent to regarding those interactions as part of the incoming hadrons. After factorisation, the remaining piece of the cross-section only includes large momentum transfers and can be calculated in perturbation theory. That the cross-section can be factorised into these long and short distance components has been proven to hold at all orders in perturbation theory [63, 64].

The factorisation scale is an arbitrary parameter and can be regarded as the scale which separates the long- and short-distance physics. A parton emitted with transverse momentum less than μ is considered to be part of the hadron structure and absorbed into the parton distribution function. A parton emitted with large transverse momentum is considered to be part of the short distance cross-section. The scale μ is typically chosen to be of the order of the hard scale Q. However, the higher order coefficients in the perturbative expansion vary in such a way that the cross-section at each order is independent of the choice of scale. This property is the basis of the factorisation theorem [72].

2.2.2 The Total Cross-Section and Inelastic Scattering

The total cross-section is a measure of the probability that a pair of protons undergo any interaction. As such, it is the sum of the cross-sections of all possible proton-proton interactions. Interactions can be classified as either elastic or inelastic. In elastic scattering both protons emerge intact and no additional particles are produced. Inelastic scattering occurs when the interaction causes at least one of the incoming protons to be destroyed, i.e., the outgoing particles differ from the incoming particles.

A useful concept when discussing inelastic proton-proton scattering is the pomeron. The concept of a pomeron predates QCD, but, in the context of QCD, it can be regarded as a colourless and flavourless combination of gluons. Pomeranchuck predicted that if the cross-section scales with a power of $\ln s$, the cross-sections of particles and antiparticles become equal at asymptotically large energies [105]. Gribov then introduced the concept of the exchange of a Regge trajectory ensuring such behaviour [86, 12, 132, 41]. The particles on the Regge trajectory are virtual and have the quantum numbers of the vacuum. The pomeron is the sum of all particles on a Regge trajectory.

Measurements of the total cross-section in pp and $p\bar{p}$ scattering as a function of the centre of mass energy are shown in Fig. 2.5. The total cross-section is fit by $\sigma_{tot}^{pp} = 21.75s^{0.0808} + 56.1s^{-0.4525}$ where s is the square of the centre of mass energy of the collision [70]. The first term accounts for the contribution from pomeron exchange and the second reggeon exchange.

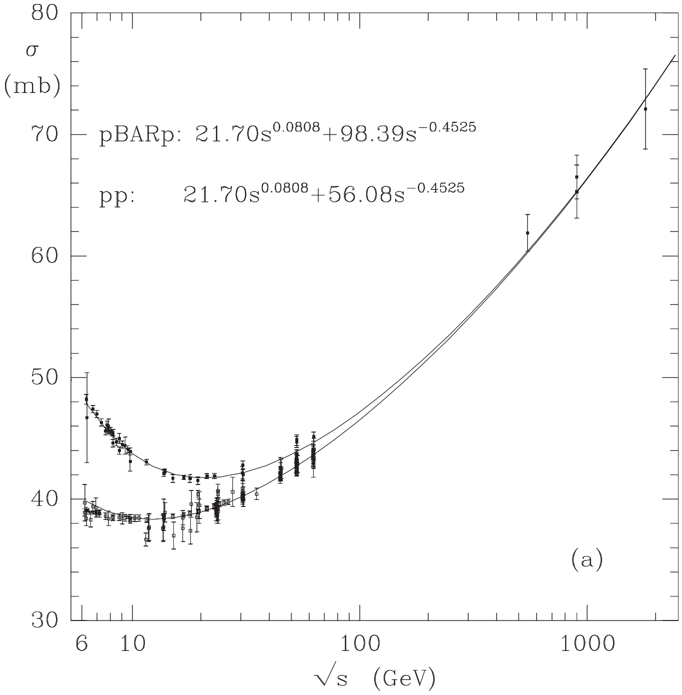

Figure 2.5: Measurements of the total cross-section in pp and $p\bar{b}$ scattering as a function of the centre of mass energy. The curves show the results of a two component fit, in which the first term describes pomeron exchange and the second describes Reggion exchange [70]

Three important types of inelastic interactions are illustrated in Fig. 2.6. Inelastic interactions in which colour charge is exchanged are referred to as non-diffractive (ND) interactions. In single diffraction (SD) a single pomeron is exchanged between the two protons and one of the incoming protons forms a diffractive system. In double diffraction (DD) a single pomeron is also exchanged, but both of the protons form diffractive systems. The exchange of two pomerons is referred to as central diffraction (CD). The non-diffractive interactions are the inelastic process with the largest cross-section.

Non-, single- and double- diffractive events have different multiplicities and topologies. The

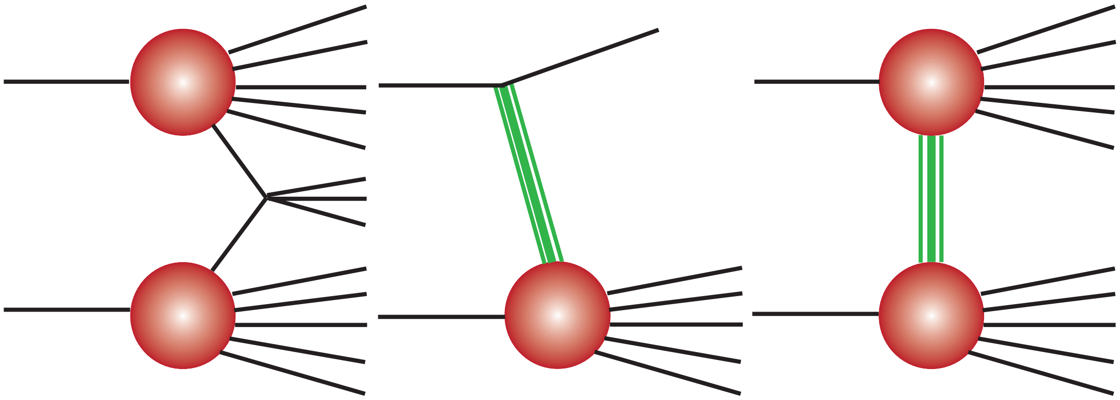

(a) Non-diffractive (b) Single-diffractive (c) Double-diffractive

Figure 2.6: Three different categories of inelastic proton-proton collisions. Non-diffractive interactions occur when colour charge is exchanged between the two protons. In single (double)-diffraction a pomeron is exchanged between the two protons and one (two) of the protons forms a diffractive system, which dissociates.

exchange of colour charge in non-diffractive events results in a large number of particles being produced at central rapidity. However, the multiplicity falls sharply at forward rapidity. In a single-diffractive event, the proton which breaks up produces particles at high rapidity. The other incoming particle is essentially undisturbed and has the rapidity of the beam. In a double-diffractive event particles are produced symmetrically at positive and negative forward rapidity, with fewer particles produced in the central region. Both non-diffractive and double-diffractive interactions are symmetric about $\eta = 0$.

2.3 Monte Carlo Descriptions of Hadronic Collisions

Event generators are used to simulate particles produced in collisions. They combine rigorous theoretical calculations such as perturbative QCD with phenomenological approaches. The properties of the phenomenological models are controlled by a large number of free parameters. Event generators are typically referred to as Monte Carlo generators because random number generators are used to generate distributions that are correct on average.

To simulate high-energy proton-protons collisions, interactions involving a large momentum transfer are calculated using perturbative QCD, while soft processes use different phenomenological approaches. Obtaining an accurate simulation of the soft component is particularly important, because the typical LHC collision includes multiple proton-proton interactions, most of which had a small transfer of momentum.

2.3.1 PYTHIA

PYTHIA [110] is one of the most widely used event generators and combines perturbative QCD with phenomenologically motivated models. Soft proton-proton interactions are described in PYTHIA using a leading order QCD $2 \rightarrow 2$ matrix element augmented by initial and final state showers and multiple parton interactions. Multiple parton interactions are those involving partons in the proton other than the partons which undergo the hard scattering.

The transition between pQCD and phenomenological models is governed by a tunable scale parameter called p_T^{min}, the momentum transfer in the hard interaction. This regulates the divergence of the $2 \rightarrow 2$ parton-parton perturbative cross-section at low momenta. The same parameter also determines the number of additional parton-parton interactions that occur in a single proton-proton collision. Fixing the amount of multiple parton scattering allows the hard $2 \rightarrow 2$ scattering to be extended down to $p_T^{hard} = 0$ without divergence. Finally, effects such as interactions with beam remnants or colour reconnection, which allow partons produced in a shower to interact according to their colour charge, are applied. PYTHIA has many tunable free parameters, a number of which have a significant influence on the generated distributions.

The tunes discussed in Section 2.5 were produced using PYTHIA 6.4. The most recent version is PYTHIA 8[111], which includes an improved model of diffraction and allows for colour reconnection between final state radiation and multiple parton interactions, but this version has only recently begun to be used by experimental collaborations.

PYTHIA contains a number of different models to describe parton showers. These differ in the order in which the partons in the event are allowed to shower. Two common ways in which the partons can be ordered are by virtuality or transverse momentum. The p_T-ordered shower allows the hardest interactions to occur first. Most of the tunes use the mostly recently implemented model of multiple parton interactions [113, 112]. This model allows multiple parton interactions to be interleaved with the parton showers, such that interplay between the two is correctly modelled. The total cross-section in PYTHIA is parameterised by the fit discussed in Section 2.2.2.

2.3.2 PHOJET

PHOJET [76, 77] uses the Dual Parton Model (DPM) [57, 58, 59, 62, 81, 39, 94, 95, 40, 61] to simulate a smooth transition between hard and soft scales. The DPM uses non-perturbative topological expansions of QCD to describe soft interactions.

Inelastic events are described using cut pomerons corresponding to the exchange of a soft gluon, which results in colour string being drawn between the beam remnants. The uncut pomerons provide virtual corrections preserving unitarity. As the pomerons can be both hard and soft, PHOJET provides a smooth transition between the soft and hard scales. Hard interactions are calculated using pQCD and hadronisation uses the routines from PYTHIA.

In contrast to PYTHIA, PHOJET includes the central diffractive component in the simulation. The simulation of parton fragmentation in PHOJET use the routines from PYTHIA. PHOJET is a more traditional model of soft QCD interactions, but it is no longer being actively developed.

2.3.3 Cross-sections for Minimum Bias Processes

Table 2.1 lists the cross-sections predicted by PYTHIA 6.4 and PHOJET for the different processes at the three centre of mass energies discussed here. PHOJET predicts a total cross-section that is 5-10% higher than the prediction by PYTHIA. At all centre of mass energies the cross-section of the non-diffractive component is the largest, followed by the single and double diffractive components. The fraction of diffractive events differs between the two generators by 20-30%. The central diffractive component is not simulated by PYTHIA, however PHOJET predicts that its cross-section is a factor of three smaller than the double diffractive component.

2.4 Experimental Studies of Soft Hadronic Interactions

Two complementary experimental techniques are used to study the properties of soft hadronic interactions. Soft hadronic interactions can either be studied directly by measuring inclusive charged particle multiplicity distributions, called minimum bias physics, or indirectly, by attempting to separate the hard and soft components in a single event, called underlying event studies. Both techniques provide complimentary views of soft interactions [114] and either or both can be used to tune the parameters of the phenomenological models.

Process Type	900 GeV [mb]	2.36 TeV [mb]	7 TeV [mb]
PYTHIA			
Non-diffractive (ND)	34.4	40.2	48.5
Single diffractive (SD)	11.7	12.7	13.7
Double diffractive (DD)	6.4	7.7	9.3
Total Inelastic	52.5	60.6	71.5
PHOJET			
Non-diffractive (ND)	39.9	50.3	61.5
Single diffractive (SD)	10.5	10.6	10.7
Double diffractive (DD)	3.5	3.9	3.9
Central diffractive (CD)	1.1	1.2	1.3
Total Inelastic	55.0	66.0	77.4

Table 2.1: Cross-sections for the three components of the minimum bias sample at $\sqrt{s} = 900$ GeV, 2.36 TeV and 7 TeV as predicted by PYTHIA 6 and PHOJET.

Minimum bias physics studies the multiplicity of charged particles using an inclusive trigger. Because the hard scattering rate is much lower than the soft scattering rate, such inclusive studies measure the properties of the soft interactions. In underlying event measurements, on the other hand, properties of particles in regions transverse to a high-p_T jet are studied. The idea of such measurements is to identify and remove the particles produced by the hard scattering such that the remaining components of the event, which are soft, can be studied.

2.4.1 The Underlying Event

In studies of the underlying event, the direction of the leading calorimeter jet is used to isolate regions in $\eta - \phi$ phase that are insensitive to the hard scattering. Figure 2.7 shows how four regions in ϕ can be defined with respect to the direction of the leading jet. The *toward* region contains particles correlated with the jet in ϕ, while the *away* region contains particles anti-correlated with the jet in ϕ. In dijet events, the away region would typically contain a second jet. The *transverse* region is perpendicular to the plane of the hard scattering and is therefore very sensitive to activity in the event in addition to the hard scattering. This separation assumes that there is no interplay between the hard and the soft interactions.

Two types of underlying event measurements have been made. In the leading jet analysis [16], the multiplicity in the transverse region is studied as a function of the p_T of the leading jet. In the MIN-MAX analysis [14], the two transverse cones are sorted according to their charged particle multiplicity into a minimum and a maximum cone. The multiplicity is then measured in the maximum and minimum cones. Recent measurements of the underlying event by ATLAS can be found in [129].

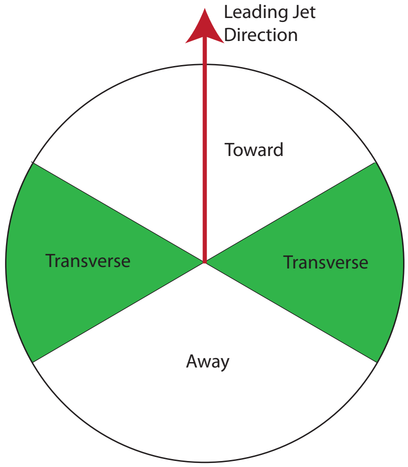

Figure 2.7: The definition of the regions used in measurements of the underlying event.

2.4.2 Minimum Bias

The name *minimum bias* refers to the trigger used to select events used to study charged particle multiplicity distribution. The trigger is designed to be as inclusive as possible to not introduce a bias towards events containing high p_T particles or containing many particles. The charged particle multiplicity of these events are used to study the properties of soft interactions. The typically measured distributions are the number of charged particles per event, n_{ch}, the number of charged particles as a function of the pseudorapidity, $dN_{ch}/d\eta$, and the transverse momentum, dN_{ch}/dp_T. More recently the average momentum as a function of the number of charged particles has been measured because this has been shown to be useful in constraining the colour reconnection parameters in PYTHIA(see Section 2.5.1).

The charged particle pseudorapidity density, $dN_{ch}/d\eta$, is strongly correlated with the rate of parton-parton scattering. It is sensitive to the fraction of the energy of the collision that is converted into soft particles, which are produced at central pseudorapidity. As the collision energy increases, the rate of multiple parton interactions per collision rises, which increases the density at central pseudorapidity. Particle production becomes more central at higher collision energies.

The charged particle multiplicity and distributions are typically one of the first measurements made by a collider experiment, because little luminosity is required due to the large production cross-section. As one of the largest uncertainties in the phenomenological models is the extrapolation of the multiplicity as a function of energy, the more energies at which the data is collected, the more accurate the tuning. In practice, however, generators are typically tuned at the centre of mass energy of the collider before further physics measurements are made.

Many previous minimum bias studies have been so-called non single diffractive (NSD) measurements. The typical minimum bias trigger requires activity on both sides of the detector, which removes a large fraction of single diffractive events. The data are then corrected using Monte Carlo simulation to remove any further contribution from the single diffractive components. The resulting distributions are called non single diffractive. There are two problems with such measurements. Most importantly, the correction to remove the single diffractive component needs to be made using a specific Monte Carlo model. Therefore the final measured distributions depend to some extent on the model used to make the correction, which makes comparisons to other models more challenging. In addition, the measured distributions include very few diffractive events, which is one reason that models of diffraction are poorly constrained. Therefore the results discussed in Section 10 were selected using a single arm trigger and no correction was made to remove the single diffractive components. These distributions are referred to as inclusive inelastic distributions and are designed to facilitate comparisons to Monte Carlo models.

Figure 2.8 shows charged particle multiplicity distributions predicted by Pythia with the MC09 tune and Phojet. The contributions from each of the diffractive components are shown separately. The two generators predict similar pseudorapidity distributions. Phojet predicts larger contribution from the diffractive components at high multiplicity and large transverse momentum. Phojet predicts that the most probable number of charged particles in a non-diffractive event is two, while Pythia predicts that it is one.

2.4.3 Previous Minimum Bias Measurements

Many previous experiments have measured charged particle multiplicity distributions at different centre of mass energies. Most frequently the multiplicity distribution or the multiplicity as a func-

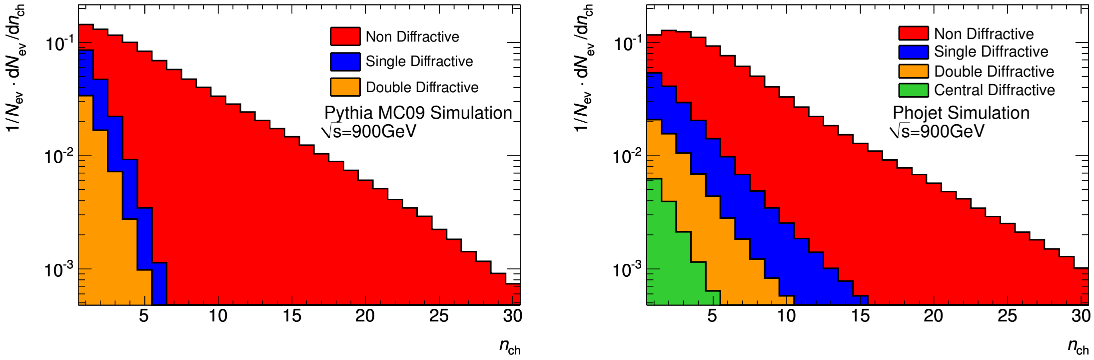

(a) Multiplicity Pythia

(b) Multiplicity Phojet

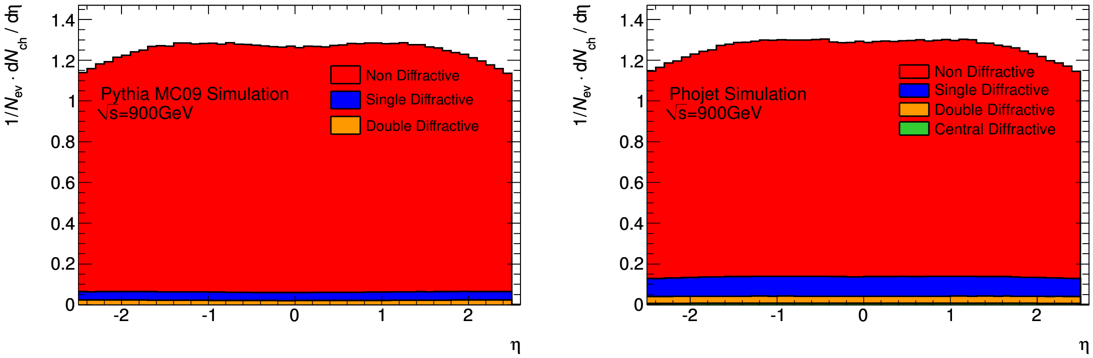

(c) Pseudorapidity Pythia

(d) Pseudorapidity Phojet

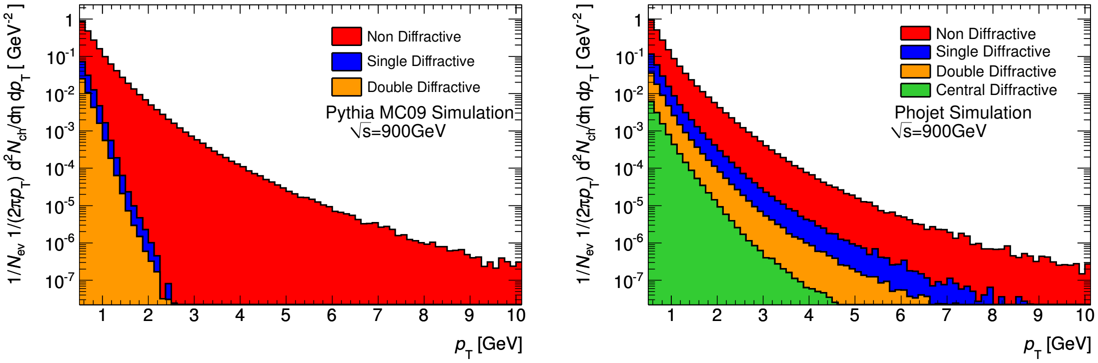

(e) Transverse Momentum Pythia

(f) Transverse Momentum Phojet

Figure 2.8: The charged particle multiplicity (top), multiplicity vs η (middle) and multiplicity vs p_T (bottom) in non- (red), single- (blue) and double- (orange) diffractive events at $\sqrt{s} = 900$ GeV predicted by the ATLAS MC09 tune of Pythia (left) and by Phojet (right). For Phojet the contribution from the central diffractive component is shown in green. Pythia does not simulate the central diffractive component.

tion of pseudorapidity was measured. The measurements are either inelastic (INEL) or non-single diffractive (NSD). Recent collider experiments include the Split Field Detector (SFM) [55] and the Streamer Chamber Detector [130] at the Intersecting Storage Ring (ISR); the Underground Area 1 (UA1) [20, 38], Underground Area 5 (UA5) [29, 26, 33, 28, 24, 25, 27, 34, 35] and the P238 experiment [91] at the Super Proton Synchrotron (SPS); and E735 [22, 100] and the Collider Detector at Fermilab (CDF) [8, 10, 11, 13] at the Tevatron. Table 2.2 summarises these measurements and indicates the centre of mass energies, the measurement type, and the measured distributions.

Experiment	Centre of Mass Energy [GeV]	Measurement Type	n_{ch}	$dN_{ch}/d\eta$
SFM	30.4, 44.5, 52.6, 62.2	NSD, INEL	X	
Streamer Chamber Detector	23.6, 30.8, 45.2, 53.2, 62.8	INEL	X	X
UA1	200, 500, 900	NSD	X	
	540	NSD		X
UA5	53	NSD	X	
	200, 546, 900	NSD	X	X
	53, 546	INEL	X	X
	200, 900	INEL	X	
	540	INEL		X
CDF	630	NSD		X
	1800	NSD	X	X
E735	300, 500, 1000, 1800	NSD	X	

Table 2.2: Summary of previous experimental measurements of charged particle multiplicity distributions.

It is interesting to compare multiplicity distributions as a function of the centre of mass energy. If the dependence on the centre of mass energy could be predicted, it would be no longer necessary to tune phenomenological models at each collider energy. However, this is far from the case at present as it would necessitate more sophisticated models of soft hadronic interactions. Figure 2.9 shows the pseudorapidity density for energies ranging from $\sqrt{s} = 23.6$ GeV (ISR) to $\sqrt{s} = 1.8$ TeV (Tevatron). Both the multiplicity at central pseudorapidity and the rate at which the multiplicity decreases with increasing pseudorapidity increase with the centre of mass energy.

Another way to study the dependence of the multiplicity on the centre of mass energy of the collision is to compare the average number of charged particles at central pseudorapidity. The average multiplicity at $|\eta| = 0$ as a function of the centre of mass energy is shown in Fig. 2.10 as measured by the different experiments. Inelastic measurements are shown by filled markers; NSD

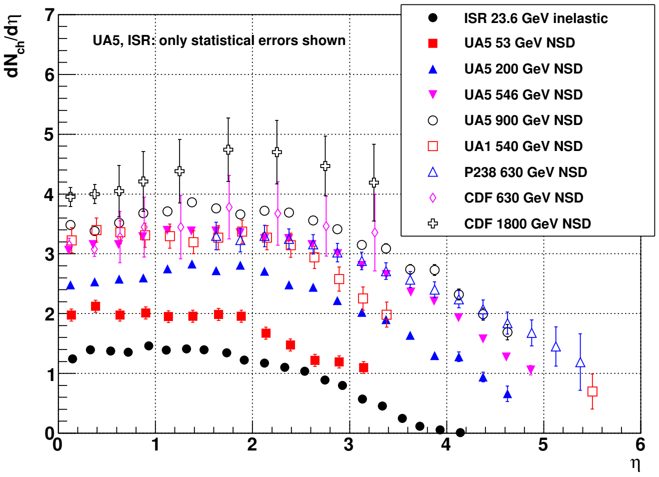

Figure 2.9: The charged particle multiplicity as a function of the pseudorapidity for different centre of mass energies [88].

measurements by open markers. The pseudorapidity density, $\frac{dN_{ch}}{d\eta}|_{\eta=0}$, increases monotonically with $\sqrt{s}$. The average multiplicity in NSD measurements is higher than in INEL measurements because removing the single diffractive component removes many low multiplicity events thereby resulting in a higher average multiplicity.

The two curves show the results of fits with simple scaling functions. The black curve uses the form $a + b \ln s$, which describes the data below $\sqrt{s} \approx 1$ TeV. This is a scaling predicted by Feynman who argued that at asymptotically large energies, the mean number of particles should increase logarithmically with $\sqrt{s}$ [80], i.e., $\langle N \rangle \propto \ln \sqrt{s}$. For energies above 1 TeV, the multiplicity increases more rapidly than predicted by Feynman scaling. A fit with an additional term proportional to the square of the logarithm is shown, which improves the agreement at higher energies, but worsens the description at low p_T.

2.5 Tuning Monte Carlo Generators

One of the most important applications of measurements of soft hadronic collisions is the tuning of Monte Carlo generators. This is because most generators use phenomenological models to describe soft hadronic interactions, which have many free parameters. These parameters need to be tuned

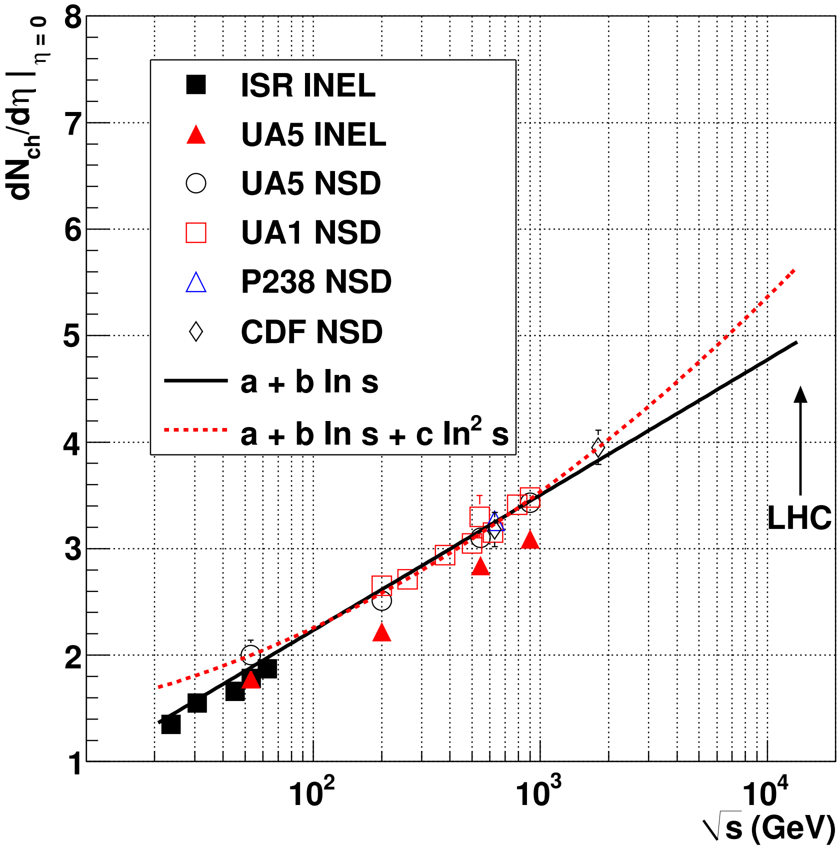

Figure 2.10: The average charged particle multiplicity density at $\eta = 0$ as a function of centre of mass energy. The increase in the multiplicity with $\sqrt{s}$ is compared to two simple fit functions [88].

based on experimental measurements. In particular, there are large uncertainties on extrapolating the parameters from one centre of mass energy to another. Recent tuning efforts have focussed on PYTHIA, which will be discussed more in the next section.

2.5.1 Parameters for Tuning

The basic components of PYTHIA that require tuning are the descriptions of:

- Final state radiation and hadronisation,
- Initial state radiation and primordial k_T,
- Underlying event, beam remnants, colour reconnection, and
- Energy scaling.

The tuned parameters also depend on the parton distribution function used. The parameters describing final state radiation are tuned separately by making the assumption that partons hadronise in the same way in hadron-hadron collisions as in electron-positron collisions. Therefore the tunes discussed here use the parameters describing final state radiation and hadronisation tuned using LEP data by the Professor collaboration [56]. The cut-off scale[1], for initial state radiation, PARP(62), and the cut-off scale for momentum smearing for primordial k_T, PARP(93), are tuned using the Drell-Yan p_T spectrum. Neither have a significant impact on the multiplicity or underlying event distributions, therefore they will not be discussed further here.

Two important sets of parameters that require tuning are those describing multiple parton interactions (MPI) and colour reconnection. Multiple interactions in PYTHIA are modelled as $2 \to 2$ scattering processes in addition to the hard interaction. Because they occur at low x and low Q^2, they are sensitive to the modelling of the parton density functions in these regions.

The most important parameter for MPI is PARP(82), which is the cut-off parameter of the multiple parton interaction model. It can be regarded as the energy below which the individual partons are no longer resolved, such that only coherent scattering of the complete proton is possible. The variation of the cut-off parameter with the centre of mass energy depends on an additional parameter, PARP(90).

---

[1] A cut-off scale is a scale above or below which the process is not modelled.

Two additional parameters that describe MPI are the parameters that control the degree of overlap between the particles in the two protons. These control how often the two protons undergo a central, hard scattering or a less central, soft scattering and is modelled using a double Gaussian probability density function. The fraction of matter in the inner proton core is determined by PARP(83) and in the outer proton core by PARP(84).

Colour reconnection describes colour interference between partons and is controlled by two parameters: PARP (78), used to control the probability that a string does not participate in colour annealing and PARP (77), used to suppress the colour annealing of fast moving strings.

2.5.2 Tuning Strategies

Parameters are tuned by making comparisons between predicted and measured distributions. What varies between tunings are the selection of experimental results used in the tuning and the strategy used to vary the parameters to determine the optimal values. Tunings have typically been made either manually, in which parameter variations are determined by eye, or by brute force, in which the parameter space is scanned by generating events on an n-dimensional grid. Neither of these techniques is well-suited to tuning a large set of parameters.

More recently, a set of automated tools to perform tuning and comparisons between data and simulation have been developed. RIVET [134] provides a library of experimental analyses and tools to calculate physical observables from an event record of a Monte Carlo generator. The PROFESSOR [56] tool parametrises the generator response in each observable bin. A goodness of fit function is then defined and minimised to obtain the optimal parameter values. Weights can be assigned to different observables to force certain features to be described. These tools were used to produce the ATLAS MC09c tunes.

2.5.3 Recent Tunes

The charged particle multiplicity distributions measured by ATLAS will be compared to the predictions from six different tunes to Monte Carlo models in Section 10. Salient aspects of the different tunes will now be discussed.

The Perugia tunes [115] were produced by tuning PYTHIA 6.4 to minimum bias measurements from UA5 and CDF. No underlying event measurements were used in the tuning. It uses the p_T-

ordered parton showering algorithms and the most recent MPI model from Pythia. There are a number of different Perugia tunes, which emphasise different aspects of the data or vary the parton distribution function. The default tune, Perugia0, which uses the CTEQ5L pdf, will be used here. The DW tune [21] was produced by tuning Pythia to CDF measurements of the underlying event and Drell-Yan data. No minimum bias measurements were used in the tuning. The DW tune uses the virtuality ordered parton showering from Pythia. The DW tune was based on a previous tune, Tune A, obtained from fits to the CDF I minimum bias and underlying event measurements, but also included the Z boson p_T, and the dijet $d\phi$ measurement from D0. In total, 15 different parameters were tuned. The Perugia0 tune successfully describes properties of the underlying event, while the DW tune successfully describes properties of minimum bias measurements. This confirms that the two measurements provide complementary views of the same underlying process.

The ATLAS collaboration has produced a number of tunes using Pythia. The tunes are derived from both underlying event and minimum bias measurements from CDF (from both Run 1 and Run 2 of the Tevatron) and dijet angular correlations from D0. In total, 16 different parameters were tuned, but many of the parameters were found to only have a small impact on charged particle multiplicity distributions. In the Monte Carlo 2009 tuning (MC09) [119] produced in 2009 prior to LHC data, PARP(82) and PARP(90) had the largest impact on the multiplicity distributions.

The CDF measurement of the dependence of $\langle p_T \rangle$ on N_{ch} [8] was released shortly after the MC09 tuning was completed. This distribution is particularly sensitive to the parameters used to describe the colour reconnection. Therefore an additional tune, MC09c [119], was produced using this distribution, which reduced the tuned value of PARP(78). Apart from $\langle p_T \rangle$ vs. n_{ch} the predictions from MC09c are very similar to those of MC09.

Once the measurements of charged particle multiplicity distributions at 900 GeV and 7 TeV discussed in Section 10 had been made, a new tune, ATLAS Minimum Tune 1 (AMBT1) was produced. The AMBT1 tune includes a new parameter, PARP(77), which suppresses colour reconnection in fast moving strings to improve the description of the $\langle p_T \rangle$ vs n_{ch} distribution.

Chapter 3

Overview of the Charged Particle Multiplicity Measurement

3.1 Measured Distributions

This thesis discusses the measurement of the following four charged particle multiplicity distributions:

$$
\begin{gathered}
\frac{1}{N_{\mathrm{ev}}} \cdot \frac{\mathrm{d}N_{\mathrm{ch}}}{\mathrm{d}\eta} \\
\frac{1}{N_{\mathrm{ev}}} \cdot \frac{1}{2\pi p_{\mathrm{T}}} \cdot \frac{\mathrm{d}^2 N_{\mathrm{ch}}}{\mathrm{d}\eta \mathrm{d}p_{\mathrm{T}}} \\
\frac{1}{N_{\mathrm{ev}}} \cdot \frac{\mathrm{d}N_{\mathrm{ev}}}{\mathrm{d}n_{\mathrm{ch}}} \\
\langle p_{\mathrm{T}} \rangle \ \mathrm{v}s.\ n_{\mathrm{ch}}
\end{gathered}
$$

where

- N_{ev} is the number of events containing at least one charged primary particle with $|\eta| < 2.5$ and $p_T > 500$ MeV,
- N_{ch} is the total number of charged particles in all events,
- n_{ch} is the number of charged particles in an event and
- $\langle p_{\mathrm{T}} \rangle$ is the average transverse momentum in an event

Primary charged particles were defined as charged particles with a mean lifetime of greater than 3×10^{-9} s directly produced in a pp interaction or from the subsequent decay of particles with a shorter lifetime. The precise value of the cut on the particle lifetime is an arbitrary choice, but the purpose is to select particles that do not decay before they have passed through the Inner Detector.

3.2 Track Selection

Tracks were reconstructed using the inside-out track reconstruction algorithms using information from all three sub-detectors of the Inner Detector. The performance of the track reconstruction algorithms is discussed in Section 6. Three different categories of tracks were used in the analysis. The tracks used to measure charged particle distributions are referred to as *selected tracks*. A selected track was reconstructed by the inside-out track reconstruction algorithm and satisfies

- $p_T > 500$ MeV,
- $|\eta| < 2.5$,
- at least one hit in the pixel detector,
- at least six hits in the SCT,
- transverse impact parameter with respect to the primary vertex, $|d_0^{PV}| < 1.5$ mm, and
- longitudinal impact parameter with respect to the primary vertex, $|z_0^{PV}| \sin \theta^{PV} < 1.5$ mm

The parametrisation used by the ATLAS experiment to describe the trajectory of a charged particle is discussed in Section 6.1. The requirements for a selected track is common to the three analyses except the SCT hit cut, which is not used in the $\sqrt{s} = 2.36$ TeV analysis (see Section 8.5). The multiplicity of selected track in an event will be denoted as n_{sel}.

3.3 Event Selection

Events were selected by requiring:

- One or more counters of the MBTS trigger to be above threshold on either side: this is referred to as the single MBTS trigger,

- a primary vertex reconstructed from at least three tracks ($\sqrt{s} = 900$ GeV) or two tracks when the beam spot is used in the vertex reconstruction ($\sqrt{s} = 2.36$ TeV and $\sqrt{s} = 7$ TeV) and
- at least one selected track.

The higher probability of multiple interactions at $\sqrt{s} = 7$ TeV required the introduction of a veto to reject events containing pile up.

3.4 Correction Strategy

To measure the charged particle multiplicity, the raw track spectra were corrected for the detector response. The three major components of the correction were the trigger, vertex and track reconstruction efficiency. In addition, non-primary tracks were removed. Non-primary tracks include secondary tracks from particles produced by the decay of primaries and fake tracks which do not correspond to the trajectory of a single charged particle.

Ideally all correction factors would have been measured in data. However, measuring the track reconstruction efficiency in data is challenging due to the lack of an ideal reference for the primary particles, and requires a large dataset. Therefore, the track reconstruction efficiency, secondaries and fakes were calculated using a Monte Carlo simulation. The efficiency was calculated for events containing a reconstructed primary vertex. This permits the application of cuts to reject tracks from particles that do not originate from the primary interaction. These requirements are particularly important due to the assumption that the efficiency from simulation can be applied to data, because extremely poorly reconstructed tracks and the non-collision beam background were removed.

The trigger and vertex reconstruction efficiency, in contrast, were measured in data, but were found to have a strong dependence on the number of tracks in the event. Correcting for this dependence on the track multiplicity necessitated introducing the following complexity to the corrections procedure.

As the trigger and vertex efficiency were measured in data, they are parametrised as a function of the number of reconstructed tracks. However, the track reconstruction efficiency corrects the distributions of reconstructed tracks to distributions of primary charged particles. Therefore, the trigger and vertex corrections need to be applied before the track reconstruction efficiency. In addition, because of the impact parameter cuts used to define selected tracks, selected tracks are only defined in events which contain a primary vertex. Therefore an additional track collection was used, the *pre-selected tracks*, which are tracks passing all cuts except for the constraints with respect to the primary vertex. Instead, pre-selected tracks are required to have the transverse impact parameter calculated with respect to the beam spot, $d_0^{BS} < 4$ mm. The multiplicity of pre-selected tracks is denoted by $n_{\mathrm{Sel}}^{\mathrm{BS}}$. The trigger and vertex efficiency are therefore measured as a function of the number of pre-selected tracks in data without requiring the event to contain a primary vertex. The trigger and vertex corrections are applied to the events before the correction for the track reconstruction efficiency is applied.

A third collection of tracks is used as input to the primary vertex reconstruction algorithm. These *vertex tracks* are reconstructed by any of the Inner Detector track reconstruction algorithms, which have $p_T > 150$ MeV and $d_0^{BS} < 4$ mm.

In summary, there are three different classes of tracks used in the analysis:

- Selected tracks used to measure the multiplicity distributions
- Pre-selected tracks used to measure the trigger and vertex efficiency
- Vertex tracks used to reconstruct the primary vertex

3.5 Datasets

The data used was recorded at the three centre of mass energies at which collisions have been delivered by the LHC: 900 GeV [4], 2.36 TeV [120] and 7 TeV [121]. The same basic analysis strategy is used at each centre of mass energy. However, there were small differences and, in particular, the analysis at $\sqrt{s} = 2.36$ TeV required additional corrections. This is because the collisions at $\sqrt{s} = 2.36$ TeV occurred when the conditions of the beam from the LHC had not been declared to be stable. This meant that the SCT was in standby with a reduced sensor bias voltage to ensure detector safely. The detection efficiency of the SCT was therefore significantly lower than in general and this lowered efficiency was not described by the simulation. Therefore a correction to the track reconstruction efficiency was derived from data (see Section 8.5). The datasets and simulation samples used for each of the three analyses are described in Appendix C.

3.6 Efficiencies

3.6.1 Trigger Efficiency

Events were triggered using the single MBTS trigger, which required at least one MBTS scintillator to be above threshold. Section 7.1 discusses how the efficiency of the single MBTS trigger, $\epsilon_{trig}(n_{\mathrm{Sel}}^{\mathrm{BS}})$, was measured in data using a control trigger stream. The trigger efficiency is parametrised in terms of the number of pre-selected tracks on which it depends weakly. No dependence on the track transverse momentum or the pseudorapidity was observed.

3.6.2 Vertex Reconstruction Efficiency

The vertex reconstruction efficiency, $\epsilon_{vtx}(n_{\mathrm{Sel}}^{\mathrm{BS}})$ was measured in data as function of the number of pre-selected tracks as discussed in Section 7.2. In events containing a single selected track, the efficiency depends on the pseudorapidity of the selected track. Therefore a correction for the vertex reconstruction efficiency as a function of the η is applied for events containing a single pre-selected track.

3.6.3 Tracking Efficiency

The efficiency to reconstruct a charged primary particle, $\epsilon_{trk}(p_T, \eta)$, was estimated using the Monte Carlo simulation. The efficiency is parametrised as a function of p_T and η . A correction was applied to the simulation to reproduce the longitudinal beam spot size in data. Extensive comparisons between data and simulation were performed to establish that the simulation describes the data to a high level of accuracy. These studies were used to estimate the systematic uncertainty on the track reconstruction efficiency. For the analysis at $\sqrt{s} = 2.36$ TeV, a data-driven correction is applied to the efficiency to account for the SCT being in standby. See Section 8 for discussion of the tracking efficiency and systematic uncertainties.

3.6.4 Secondaries

Despite the requirements on the impact parameters and the number of pixel hits, a small number of secondary particles produced in the decays of primary particles are included in the analysis. The number of secondaries as a function of p_T is estimated from the simulation. The estimation of a normalisation factor to account for possible differences between data and simulation obtained by comparing the number of tracks with large transverse impact parameter (Section 8.6).

3.7 Correction Procedure to Primary Particle Distributions

The procedure used to correct the measured distributions for the detector response is discussed in Section 9. The corrections are applied using weights, which were applied on either the event or track level.

Events lost due to the trigger and vertex requirements were corrected for using a weight, w_{ev}, applied to each event:

$$w_{\mathrm{ev}}(n_{\mathrm{Sel}}^{\mathrm{BS}}) = \frac{1}{\epsilon_{\mathrm{trig}}(n_{\mathrm{Sel}}^{\mathrm{BS}})} \cdot \frac{1}{\epsilon_{\mathrm{vtx}}(n_{\mathrm{Sel}}^{\mathrm{BS}})},$$

where $\epsilon_{\mathrm{trig}}(n_{\mathrm{Sel}}^{\mathrm{BS}})$ and $\epsilon_{\mathrm{vtx}}(n_{\mathrm{Sel}}^{\mathrm{BS}})$ are the trigger and vertex reconstruction efficiencies.

The p_T and η distributions of selected tracks were corrected by using a weight applied to each track:

$$w_{\mathrm{trk}}(p_{\mathrm{T}}, \eta) = \frac{1}{\epsilon_{\mathrm{trk}}(p_{\mathrm{T}}, \eta)} \cdot (1 - f_{\mathrm{sec}}(p_{\mathrm{T}})) \cdot (1 - f_{\mathrm{ps}}(p_{\mathrm{T}}, \eta)),$$

where ϵ_{trk} is the track reconstruction efficiency and $f_{\mathrm{sec}}(p_{\mathrm{T}})$ is the fraction of secondaries. The fraction of fakes was shown to be negligible. Due to the p_T and η resolution a certain fraction of the selected tracks are produced by particles outside the kinematic phase space. This was corrected for using a factor from simulation, $f_{\mathrm{ps}}(p_{\mathrm{T}}, \eta)$. Migrations between bins were found to depend only on the track momentum resolution and were corrected for using a resolution function obtained from simulation.

For the two distributions expressed as a function of n_{ch}, a track-level correction was applied by using Bayesian unfolding [67] to correct the number of selected tracks to the number of charged particles. A matrix, $M_{\mathrm{ch,Sel}}$, which expresses the probability that a particular multiplicity of selected tracks n_{Sel} is due to n_{ch} particles, was populated from the simulation and applied to obtain the n_{ch} distribution from the data. The n_{ch} distribution obtained was then used to repopulate the matrix, and the number of selected tracks was corrected for a second time. This procedure was repeated until it converged.

The unfolding matrix did not correct for events lost because no tracks were reconstructed in such events. To correct for these missing events, a correction factor, $f_W = 1/(1-(1-\langle\epsilon_{trk}\rangle)^{n_{\mathrm{ch}}})$ was applied to the n_{ch} distribution. The average track reconstruction efficiency integrated over p_T and η is denoted by $\langle\epsilon_{trk}\rangle$. This correction is based on the assumption that events which contained k charged particle, have a probability, $(1-\langle\epsilon_{trk}\rangle)^k$, of containing zero reconstructed tracks. This assumes that the track reconstruction efficiency is independent of the charged particle multiplicity, which is the case for low multiplicity events.

To calculate the $\langle p_{\mathrm{T}}\rangle$ versus n_{ch} distribution, each event was weighted by $w_{\mathrm{ev}}(n_{\mathrm{Sel}}^{\mathrm{BS}})$. For each n_{Sel} the reconstructed average p_{T} was converted to the average p_{T} of the primary charged particles. The matrix $M_{\mathrm{ch,Sel}}$ was then applied as described above.

The charged particle multiplicity as a function of pseudorapidity and transverse momentum was measured at $\sqrt{s}$ = 900 GeV, $\sqrt{s}$ = 2.36 TeV and $\sqrt{s}$ = 7 TeV. However, the lack of a simulation sample describing the efficiency of the SCT in standby made estimating the contents of the $M_{\mathrm{ch,Sel}}$ needed to unfold the n_{ch} distribution difficult. Therefore, at $\sqrt{s}$ = 2.36 TeV the charged particle multiplicity and $\langle p_{\mathrm{T}}\rangle$ vs n_{ch} were not measured.

Chapter 4

The ATLAS Experiment at the Large Hadron Collider

4.1 The Large Hadron Collider

The Large Hadron Collider (LHC) [99, 79] located just outside Geneva beneath the French-Swiss border, is the world's newest and most powerful tool for research in particle physics. It is designed to collide protons at a centre of mass energy of 14 TeV once it has been fully commissioned. Commissioning began in September 2008 and the highest energy collisions to date have been at a centre of mass energy of 7 TeV[1].

The LHC is installed in a circular tunnel, 26.7 km in circumference, which was constructed for the Large Electron Positron (LEP) collider. The tunnel is at a depth ranging from 45 to 100 m and is inclined at approximately 1.4% to the vertical. In total there are eight straight sections and eight arcs, which allow for a maximum of eight collision points[2]. Figure 4.1 is a schematic diagram of the LHC with each of the eight collision points labelled.

Experiments which study the particles produced in the LHC collisions are located at four of these eight points. Two large general purpose detectors designed to search for physics processes beyond the Standard Model, A LHC ApparatuS (ATLAS) and the Compact Muon Solenoid Experiment (CMS) [15] are located at Point 1 and Point 5, respectively. Two smaller specialised experiments, A

---

[1] The results discussed in Section 10 use data recorded at the three different centre of mass energies at which protons have been collided in the LHC: 900 GeV, 2.36 TeV and 7 TeV.

[2] The straight sections are longer than needed for a hadron collider like the LHC, because the tunnel was designed for LEP. As LEP was an electron-positron collider, the straight sections were needed to contain radio-frequency cavities to compensate for the energy lost through synchrotron radiation.

Large Ion Collider Experiment (ALICE) [9], which will study the properties of lead-lead collisions, and the Large Hadron Collider Beauty Experiment (LHCb) [30], an experiment designed to study physics using bottom quarks, are located at Point 2 and Point 8, respectively. Two of the remaining points contain equipment used for beam cleaning (Points 3 and 7); Point 4 contains radio-frequency cavities; and Point 6 is the location of the beam dump.

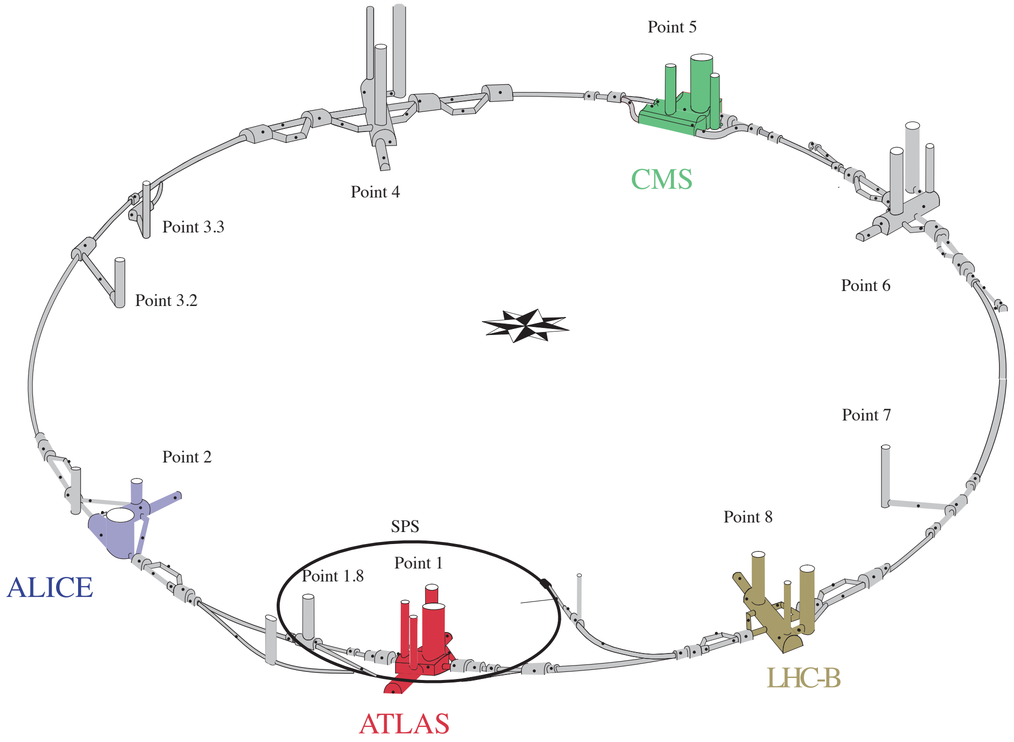

Figure 4.1: Schematic diagram of the Large Hadron Collider (LHC) [79]. The eight possible proton crossing points are labelled as Points 1-8. The buildings for the four large LHC experiments: ATLAS (Point 1), ALICE (Point 2), CMS (Point 5) and LHCb (Point 8) are coloured.

Each of the two beams, which travel in opposite directions around the ring, contain protons. Therefore the two beams need independent magnet systems, because the particles in the beams have the same charge[3]. The 3.7 m diameter of curved sections of the tunnel is not large enough to contain two completely separate rings, therefore a twin-bore magnet system was designed in which

---

[3] This is in contrast to the Tevatron collider at Fermilab, which collides protons with antiprotons. As the particles have opposite charge and move in the opposite direction, both beams require a magnetic field with the same orientation. A different choice was made for the LHC to avoid the technical challenges in producing and storing antiprotons.

the two rings share the same cold mass [52].

To maximise the discovery potential for new physics, particle physics experiments need accelerators that produce collisions at the highest possible rate at the highest possible energy.

The number of events of a signal process is determined by:

$$N_{event} = L\sigma_{event} \tag{4.1}$$

where L is the luminosity of the accelerator, in number of particles per unit area per unit time, and σ_{event} is the cross-section, or interaction probability, of the process in question. Therefore the study of rare processes with low cross-sections requires the highest possible luminosity. The luminosity depends on parameters of the beam and can be written as:

$$L = \frac{N_b^2 n_b f_{rev} \gamma_r}{4\pi\sigma_x\sigma_y} F \tag{4.2}$$

where

- N_b is the number of particles per bunch
- n_b is the number of bunches per beam
- f_{rev} is the frequency at which the beams circulate the ring
- σ_x, σ_y represent the width of the beam in the transverse direction where the shape is assumed to be approximated by a Gaussian distribution
- γ_r is the relativistic gamma-factor

The LHC has been designed for a luminosity of 10^{34} cm^{2}s. Safely commissioning the LHC requires slowly increasing the collision energy and the luminosity. At present the highest instantaneous luminosity is 5.1×10^{30} cm^{2}s, which is five orders of magnitude larger than that delivered for the first collisions at 7 TeV in March 2010. The luminosity was increased by increasing the number of particles per bunch by an order of magnitude, the number of bunches per beam, and the transverse width of the beam at the interaction points[4]. The luminosity was increased in a number of steps to slowly increase the total energy stored in the magnets.

---

[4] The so-called β^* function describes one component of the width of the beam, due to the focusing magnets in the tunnel. The other component is the emittance, which is determined by the temperature of the protons in the beam. The square root of their product gives a 1σ measure of the beam width.

The cross-sections of many physics processes increase with the beam energy. The energy at which particles in the beam collide is determined by

$$B\rho = \frac{p}{e} \tag{4.3}$$

where B is the field of the dipole magnets used to bend the proton beam around the ring, ρ is the bending radius, p is the proton momentum and e is the proton charge. For a fixed accelerator size, the maximum energy is limited by the maximum field of the dipoles. An energy of 7 TeV per proton in the LHC requires a high magnetic field in the dipoles of 8.33 T. Such an extreme magnetic field was obtained by using superconducting dipole magnets, which operate at a temperature of 1.9 K. It takes approximately six weeks for the dipoles to be cooled from room temperature to their operating temperature. In addition to the 1232 dipole magnets, 392 quadrupole magnets are used to focus the beams.

The first proton-proton beam was injected in the LHC on the 10 September 2008. Unfortunately, just over a week later on 19 September, during powering tests of the main dipole circuit of Sector 3-4 of the LHC, a fault occurred in the electrical bus connection between a dipole and a quadrupole magnet. A number of magnets underwent mechanical damage and a significant amount of helium was released into the tunnel. A total of 53 magnets were removed from the tunnel to be either cleaned or repaired. This incident [60] led to a delay in the LHC operation of more than a year while the magnets were repaired and a system was developed to detect abnormal electrical resistance in bus bars and the interconnections between magnets.

The first proton-proton collisions were produced by the LHC on 23 November 2009 at $\sqrt{s} =$ 900 GeV. However, the stable beam flag[5] was not declared, therefore many of the sensitive detectors, such as the silicon detectors, were off, resulting in lower quality data. The first collisions with the stable beam flag were recorded on 30 November 2009 and over the next 10 days, approximately 12 μb^{-1} of data at $\sqrt{s} = 900$ GeV was recorded. The LHC became the highest energy collider in the world on 8 December 2009, when protons were collided at $\sqrt{s} = 2.36$ TeV for the first time. Collisions at $\sqrt{s} = 2.36$ TeV were recorded by ATLAS on 13 and 15 December, but again without the stable beam flag having been declared. The first collisions at $\sqrt{s} = 7$ TeV were recorded on 30

---

[5] The stable beam flag is one of the operating states of the LHC. It is declared once the beam is fully under control and no further adjustments are required. Once the stable beam flag has been declared, the more sensitive detectors are switched on.

March 2010 with all detectors fully operational. Figure 4.2 shows the luminosity delivered by the LHC and recorded by ATLAS in the first 3 months of LHC operation at 7 TeV. The insets show displays of the first events of different types recorded by ATLAS. The increase in luminosity during the first few months of LHC operation has been dramatic and ATLAS has achieved an extremely high data-taking efficiency.

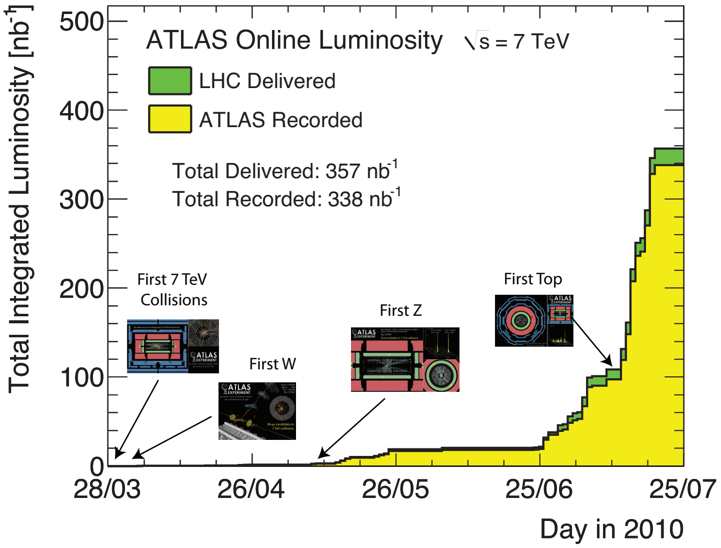

Figure 4.2: The integrated luminosity recorded by ATLAS in the first 3 months of LHC operation at 7 TeV The insets show selected first candidate events of different types recorded by ATLAS. The arrows indicate the date on which the event was recorded [122].

4.2 ATLAS: A Toroidal Tracking LHC ApparatuS

ATLAS is the largest of the four LHC experiments and has been designed to measure a wide range of physics processes. Fast, radiation hard-electronics and sensor elements and high detector granularity are used to cope with the high particle flux from the LHC. ATLAS has full azimuthal coverage and a large acceptance in pseudorapidity. The coordinate system used by ATLAS is discussed in Appendix A.1.

The ATLAS detector is shown in Fig 4.3. The detector is 44 m long and 25 m high, cylindrical in shape and symmetric about z with respect to the interaction point. ATLAS contains a number

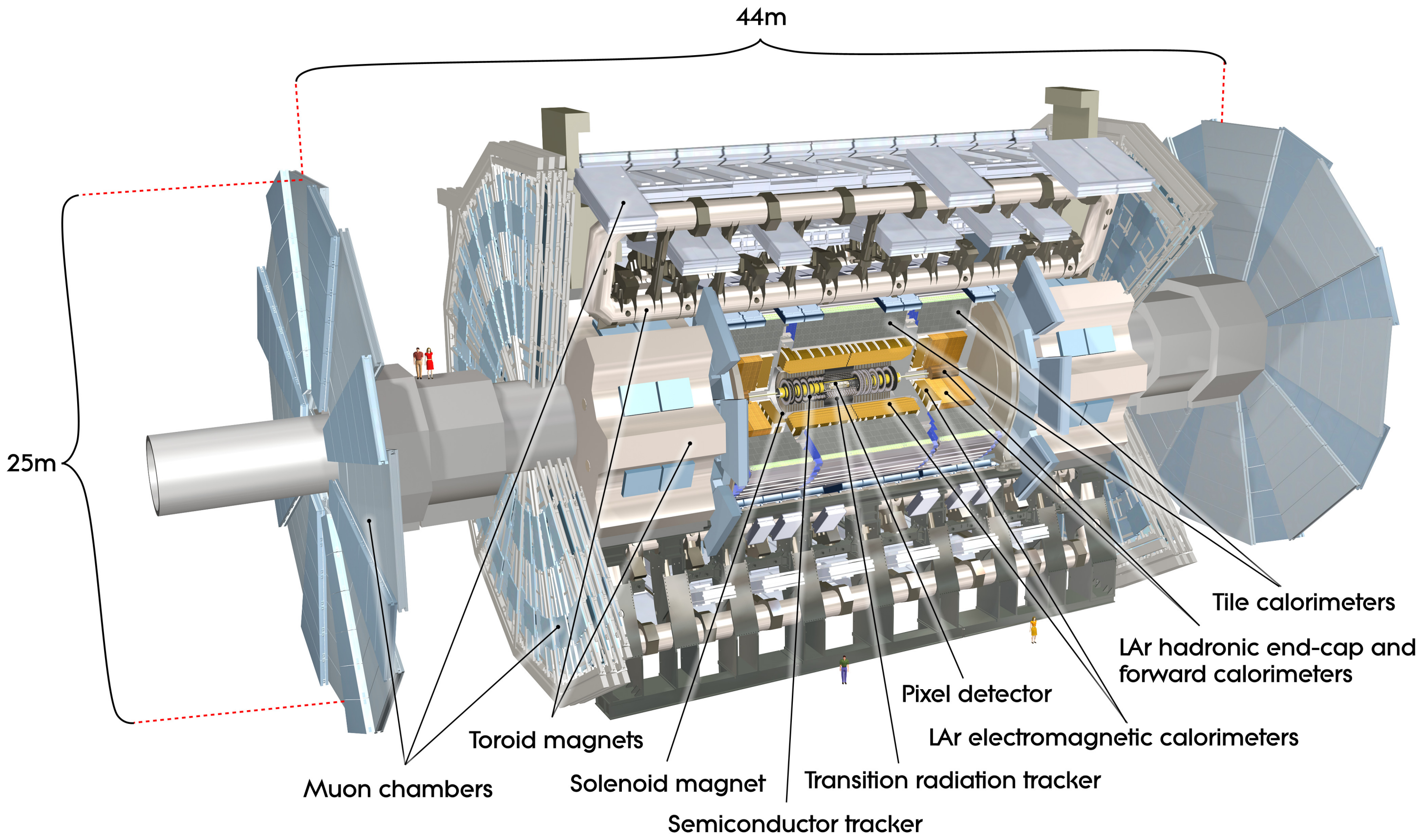

Figure 4.3: The components of the ATLAS detector. The location of the individual sub-detectors are located [2].

Detector Component	η coverage		Required resolution
	Measurement	Trigger	
Tracking	± 2.5		$\sigma_{p_T}/p_T = 0.05\% p_T \oplus 1\%$
EM Calorimetry	± 3.2	± 2.5	$\sigma_E/E = 10\%/\sqrt{E} \oplus 0.7\%$
Hadronic Calorimetry			
Barrel and End-cap	± 3.2	± 3.2	$\sigma_E/E = 50\%/\sqrt{E} \oplus 3\%$
Forward	$3.1 < \|\eta\| < 4.9$	$3.1 < \|\eta\| < 4.9$	$\sigma_E/E = 100\%/\sqrt{E} \oplus 10\%$
Muon Spectrometer	± 2.7	± 2.4	$\sigma_{p_T}/p_T = 10\%$ at $p_T = 1$ TeV

Table 4.1: The pseudorapidity coverage and approximate resolution of the different components of the ATLAS detector [2].

of different sub-detectors providing complimentary measurements in the following four major subsystems:

- The Inner Detector (ID) to measure the trajectories of electrically charged particles
- The calorimeter to measure the energies of charged and neutral particles
- The muon spectrometer to measure the trajectories of muons
- The magnet system to bend charged particles to allow their momentum to be measured

Table 4.1 summarises the coverage in pseudorapidity and the resolution of the different components of ATLAS. The resolution has a constant term, which ultimately limits the possible resolution, and a term which varies with either the transverse momentum or the energy. The number of readout channels per sub-detector falls by approximately an order of magnitude in each step away from the interaction point. All sub-systems are capable of triggering events except for the Inner Detector. Different technologies are used for trigger and precision components to achieve both a high trigger rate and as precise measurements as possible.

4.2.1 The Magnet System

ATLAS features a striking hybrid system of four large superconducting magnets. The magnet system is 22 m in diameter and 26 m long and has a total stored energy of 1.6 GJ. A central solenoid provides a 2 T axial magnetic field for the Inner Detector and a barrel toroid and two end-cap toroids provides a toroidal magnetic field of 0.5 T in the barrel and 1 T in the end-caps.

The solenoid is a single-layer coil made of a Niobium-Titanium superconductor and is operated at 4.5 K with a current of 7.7 kA. The barrel and end-cap toroids are made from a Nb/Ti/Cu conductor wound into pancake-shaped coils. The toroids operate at a temperature of 4.6 K with a current of 20.5 kA.

The finite number of coils in the toroids mean that the field is not perfectly toroidal but follows a regular eight fold pattern (Fig. 4.4 (a)). The largest variations in the field strength are in the region between the barrel and the end-cap (Fig. 4.4 (b)). Accurate knowledge of the magnetic field is vital for precise track measurements, therefore the muon spectrometer is equipped with approximately 1730 Hall cards to measure the magnetic field to an accuracy of 0.3%.

The design of the ATLAS magnet system is significantly different to the single 4 T solenoid used by CMS. The choice of design for the magnet system, once made, was the driving force behind the further choices in the detector design.

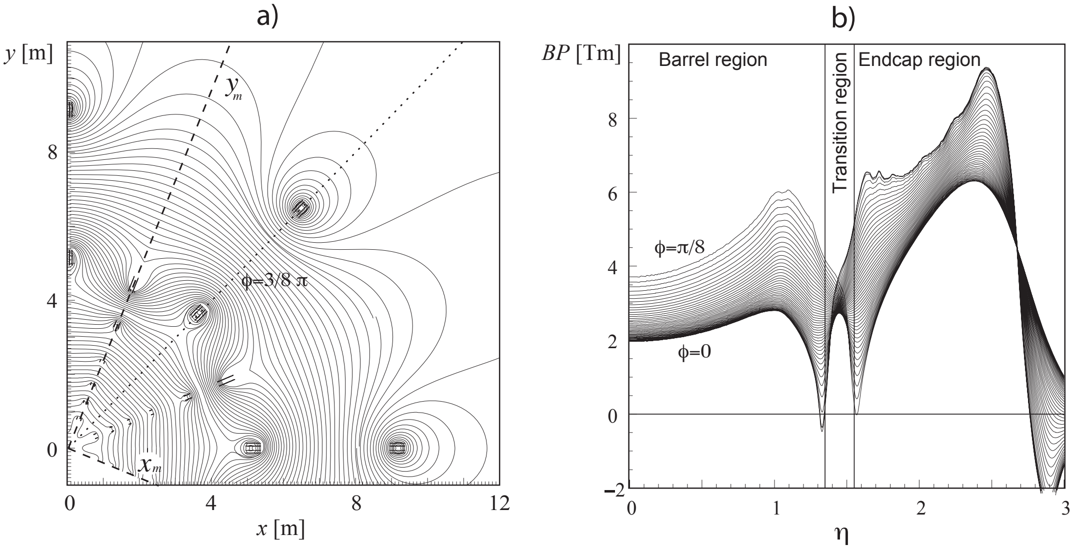

Figure 4.4: The magnetic field of the muon spectrometer. a) The magnetic field strength in the transverse plane illustrating a quarter of the eightfold symmetry. b) The magnetic field as a function of the pseudorapidity. The highly inhomogeneous region between $1.4 < |\eta| < 1.6$ is the transition region between the barrel and the end-cap toroids.

4.2.2 The Inner Detector

The ATLAS Inner Detector (ID) [117, 118] comprises three sub-detectors, which use complementary technologies to obtain optimal track reconstruction and vertex identification in the high-multiplicity

LHC environment. Figure 4.5 shows the three sub-detectors of the Inner Detector: the silicon pixel detector [19, 3] (pixel), the silicon microstrip detector (SCT) and the Transition Radiation Tracker (TRT). As the solenoid deflects particles in the transverse plane, each sub-detector has the highest precision in this plane to obtain the best possible momentum measurement. The tracks used to study the charged particle multiplicities discussed in Section 10 were reconstructed using all three sub-detectors of the ID.

4.2.2.1 The Pixel Detector

The silicon pixel detector is the innermost tracking detector of the ATLAS experiment. In order to provide at least three measurement points per track for $|\eta| < 2.5$, it has three barrel layers and six disk layers. The three barrel layers are located at a radii of 5.05 cm, 8.85 cm and 12.25 cm and the three disks in each end-cap are located at $|z| = 49.5$ cm, 58.0 cm and 65.0 cm.

Each of the 1744 modules contains more than 46080 pixels, most of which are $50{\times}400$ μm in size. This yields an intrinsic measurement accuracy of 10 μm (R-ϕ) $\times$ 115 μm (z) in the barrel. The pixel detector measures the charge deposited by a particle passing through a pixel, which is used to discriminate against noise and to further improve the resolution. In total, there are approximately 80 million read-out channels in the pixel detector. See Section 5 for a more detailed description of silicon detectors and the pixel detector.

4.2.2.2 The Semi-Conductor Tracker

The Semi-Conductor Tracker (SCT) surrounds the pixel detector. Silicon strips were used instead of pixels because the particle density decreases with the radial distance from the interaction point. This means that it has significantly fewer read-out channels than the pixel detector. The SCT has 4088 modules in four barrel layers and nine disks in each end-cap. An SCT module consists of two sensors glued back-to-back with a stereo angle of 40 mrad. The stereo angle allows a measurement to be made along the length of the strip. The intrinsic accuracy in the barrel is 17 μm in the $R-\phi$ direction and 580 μm in the z-direction. The disks have the same measurement accuracy in $R-\phi$ and 580 μm in the R. In contrast to the pixel detector, the read-out of the SCT is binary and provides no information about the amount of deposited charge. There are approximately 6.3 million read-out channels in the SCT.

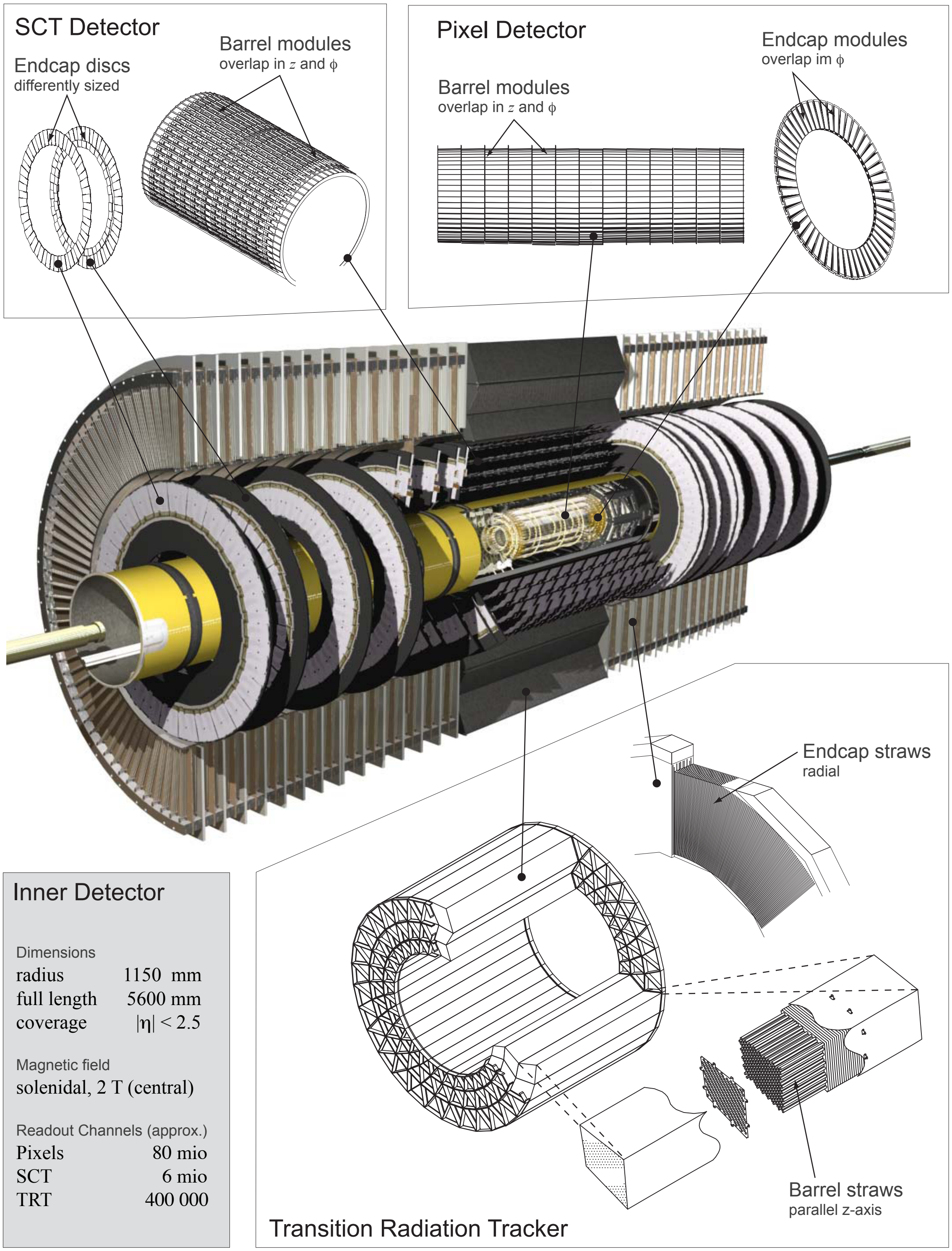

Figure 4.5: The components of the ATLAS Inner Detector. The insets show details of the components of the three sub-detectors: the pixel detector, the SCT and the TRT[108].

4.2.2.3 The Transition Radiation Tracker

The Transition Radiation Tracker (TRT) surrounds the SCT. It provides a large number of measurements, typically 30 per track, using straw tubes with a diameter of 4 mm. The straw tubes have an tungsten anode at the centre and are filled with a $Xe/CO_2/O_2$ gas mixture. When a charged particle passes through a straw, the gas is ionised and the charge drifts to the anode. The time that it takes the charge to reach the wire is used to measure the distance that the particle passed from the wire.

The straws in the TRT barrel are 144 cm long and lie parallel to the beam axis, whereas in the end-cap they are 37 cm long and arranged radially in wheels. This means that the TRT only provides information in the barrel in the $R-\phi$ direction with an accuracy of 130 μm. Therefore to reconstruct the full trajectory the silicon detectors are needed in conjunction with the TRT. The straws are interleaved with fibres and foils so that an electron passing through produces photons through transition radiation. The photons are absorbed by the gas, producing a large amount of charge. The TRT read-out has two thresholds: a low one to measure ionisation and a high one to identify these photons, which allow electrons to be identified using the TRT. In total, there are 176 modules in the TRT containing 351,000 read-out channels.

4.2.3 The Calorimeters

The calorimeter system (Fig. 4.6) consists of an electromagnetic and a hadronic calorimeter covering $|\eta| < 4.9$. It comprises a wide range of technologies, adapted to the varying physics requirements and the radiation environment. The fine granularity of the electromagnetic calorimeter allows for precise measurements of electrons and photons within $|\eta| < 2.5$. The coarser granularity of the hadronic and forward calorimeters is sufficient for the physics requirements of jet and $\not{E}_T$ measurements.

4.2.3.1 The Electromagnetic Calorimeter

The electromagnetic calorimeter is segmented into a barrel ($|\eta| < 1.475$) and two end-caps ($1.375 < |\eta| < 3.2$) within separate cryostats. The barrel electromagnetic calorimeter and the solenoid share a single cryostat to minimise the amount of material in front of the calorimeter. The barrel is split in half at $z = 0$ by a 4 mm-wide gap. The end-caps are split into inner ($2.5 < |\eta| < 3.2$) and outer ($1.375 < |\eta| < 2.5$) wheels.

The electromagnetic calorimeter is a lead and liquid argon sampling calorimeter with accordion-shaped lead absorber plates and kapton electrodes. The accordion geometry provides gapless ϕ coverage and allows for fast signal extraction. The thickness of the lead plates varies with η to optimise the energy resolution. The calorimeter is segmented in the central region ($|\eta| < 2.5$) into three layers for the identification of the secondary maxima of electromagnetic showers to distinguish between neutral pions and electrons. The inner endcap wheel has two layers. A presampler detector is used to correct for the energy lost by electrons and photons before the calorimeter in the range $|\eta| < 1.8$.

The electromagnetic calorimeter has a total thickness of approximately 22 radiation lengths[6] (X_0) in the barrel and 24 X_0 in the end-caps. This is sufficient to contain electromagnetic showers and limit the punch-through of particles from jets into the muon system.

4.2.3.2 The Hadronic Calorimeters

The hadronic calorimeter system consists of the tile calorimeter, the hadronic end-cap calorimeter (HEC) and the forward calorimeter (FCAL). The tile calorimeter has a barrel, $|\eta| < 1.0$, and two extended barrels, $0.8 < |\eta| < 1.7$. The two wheels of the HEC cover $1.7 < |\eta| < 3.2$ and the FCAL $3.1 < |\eta| < 4.9$. The pseudorapidity acceptance of the HEC overlaps slightly with the FCAL to reduce the drop in material density in the transition region between the detectors.

The tile calorimeter is a sampling calorimeter with steel absorbers interleaved with scintillating tiles. It is segmented azimuthally into 64 modules and three layers in depth. The total thickness of the tile calorimeter is 9.7 X_0 at $\eta = 0$. Both the HEC and the FCAL use liquid argon as the active scintillating medium, however the absorbers differ because the radiation environment varies rapidly with η. The HCAL and the first FCAL module have copper absorbers, while the remaining two FCAL modules have tungsten absorbers. Each wheel of the HEC was assembled from 32 identical wedge-shaped modules with each module having two layers. The FCAL is the most forward of the calorimeters and contains only three modules. It is approximately 10 X_0 thick.

---

[6] A radiation length of a material is the mean distance over which the energy of an electron is reduced by a factor of $1/e$ through bremsstrahlung and 7/9 of the mean free path for pair production by a high-energy photon.

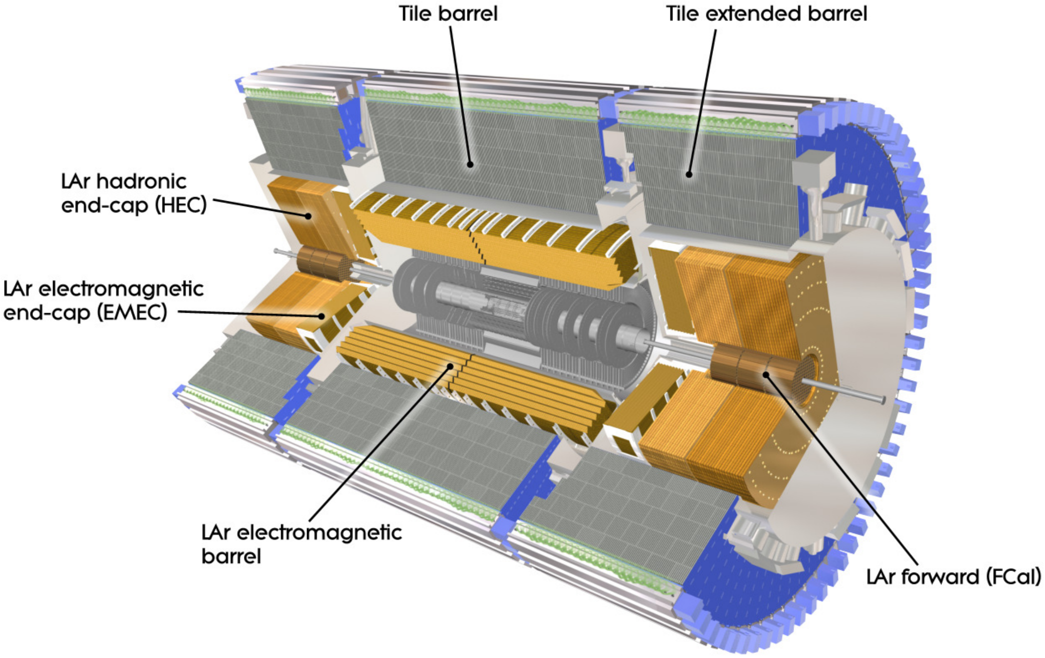

Figure 4.6: The electromagnetic and hadronic (tile, HEC and FCAL) components of the ATLAS calorimetry [2].

4.2.4 The Muon System

The muon spectrometer (Fig. 4.7) surrounds the calorimeters and is the outermost component of the ATLAS detector. It is a high precision tracking detector designed to detect and measure the momentum of charged particles exiting the calorimeters in the pseudorapidity range of $|\eta| < 2.7$. Trigger coverage is provided for $|\eta| < 2.4$. The spectrometer follows an eight-fold azimuthal symmetry due to the structure of the toroidal magnet system, and is designed to achieve a standalone transverse momentum measurement of better than 10% for muons with $p_T = 1$ TeV. Muon momenta from 3 GeV to ∼3 TeV can be measured using the muon spectrometer alone. The momentum measurements can be extended to lower p_T in conjunction with information from the Inner Detector.

The momentum is measured using the magnetic deflection of muons by the large superconducting air-core toroid magnets. The magnet configuration (see Section 4.2.1) is designed to provide a field orthogonal to the muon trajectories. The three layers of chambers in the barrel are arranged concentrically around the beam axis, while the three planes of chambers in the end-caps are perpendicular to the axis of the beam. The muon spectrometer uses four different technologies: two for the precision measurements and two for the trigger.

The Monitored Drift Tubes (MDTs) provide precision tracking for $|\eta| < 2.7$. An MDT is a gas-filled aluminium tube with a diameter of 30 mm with a tungsten wire at the centre. A single tube has a radial resolution of 80 μm, but no longitudinal measurement. An MDT chamber consists of between three and eight layers of drift tubes such that an average resolution of 35 μm per chamber is obtained. In the forward regions, $2.0 < |\eta| < 2.7$, the innermost MDT layer was replaced by Cathode Strip Chambers (CSCs) because they have finer granularity and a 7 ns timing resolution for the higher track density. The CSCs are multiwire proportional chambers with the cathode planes segmented into strips in orthogonal directions. The CSC chamber resolution is 40 μm in the plane in which the tracks are bent by the magnetic field and 5 mm in the plane in the transverse direction. Both the MDTs and the CSCs use an $\mathrm{Ar/CO_2}$ gas mixture.

The muon trigger chambers provide a momentum-dependent muon trigger, allow for bunch crossings to be identified and provide a measurement of the position coordinate along the tubes of the MDTs. Resistive Plate Chambers (RPCs) are used in the barrel for $|\eta| < 1.05$ and Thin Gap Chambers (TGCs) in the end-cap for $1.05 < |\eta| < 2.4$. The RPCs consist of two pairs of Bakelite plates filled with a gas mixture of 97% tetrafluorethane ($\mathrm{C_2H_2F_2}$) and 3% isobutane ($\mathrm{C_4H_{10}}$). The RPCs provide a spatial resolution of 10 mm and a timing resolution of 1.5 ns. The TGCs are similar to multi-wire proportional chambers, but with an anode pitch larger than the distance between the cathode and the anode. Both the RPCs and TGCs are read-out using two orthogonal sets of strips: one set parallel to the MDT wires and one set orthogonal. The TGCs are used in the end-cap because they can handle high rates with better resolution than the RPCs. The gas mixture used in the TGCs is carbon dioxide (CO_2) and n-pentane (n-C_5H_{12}). The TGC spatial resolution is 2-6 mm and the timing resolution is 4 ns. The RPCs were used instead of TGCs in the barrel because they were less expensive and are sufficient to trigger on the lower muon flux.

In total, there are 339k MDT, 30.7k CSC, 359k RPC and 318k TGC chambers in the muon system.

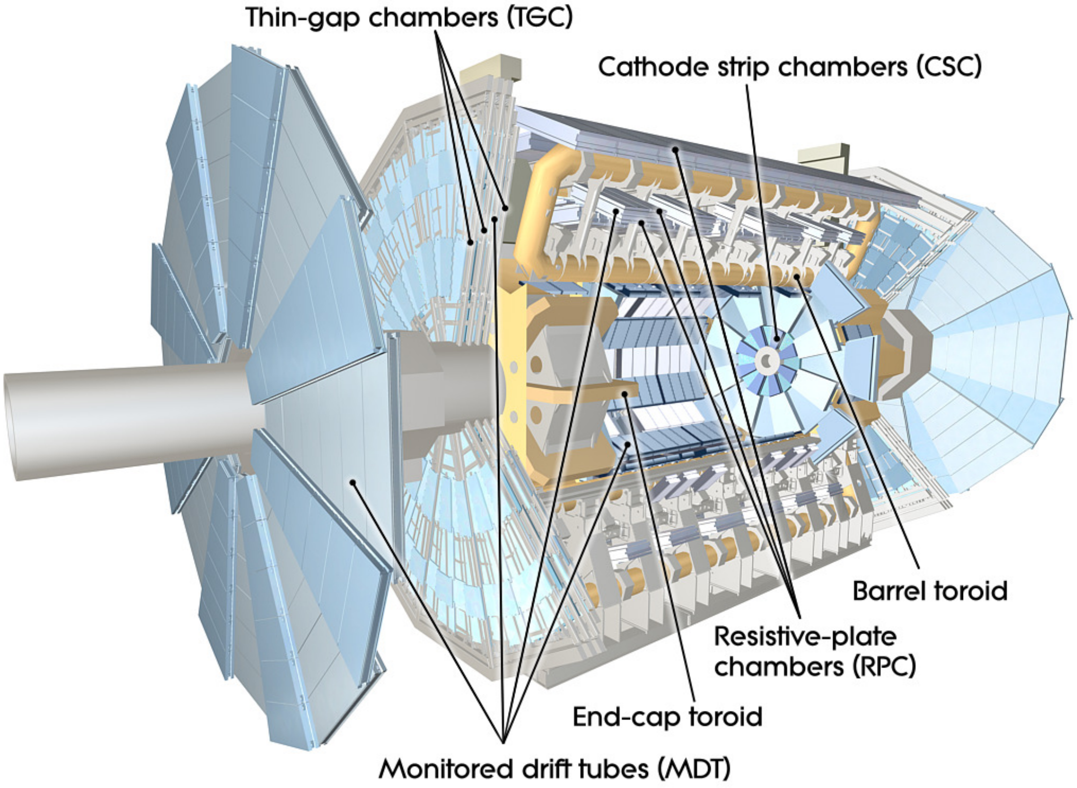

Figure 4.7: The components of the Muon Spectrometer and toroidal magnet system [2].

4.2.5 Forward Detectors

The three specialised small detector systems located in the forward region are shown in Fig. 4.8. Two of these systems are used for luminosity measurements. LUminosity measurement using Cerenkov Integrating Detector (LUCID) lies at $z = \pm 17$ m. LUCID is used to determine the relative luminosity by measuring inelastic scattering in the forward region. It is primarily used to monitor the luminosity and beam conditions. Absolute Luminosity for ATLAS (ALFA), at $z = \pm 240$ m, obtains the absolute total luminosity by measuring the elastic-scattering amplitude at small angles. ALFA consists of scintillating fibre trackers located inside Roman pots. The luminosity detectors were calibrated using Van Der Meer scans[131]. The current uncertainty on the luminosity is 11% with the uncertainty dominated by the knowledge of the beam currents. The Zero-Degree Calorimeter (ZDC) is located at $z = \pm 140$ m and will be used to determine the centrality of heavy-ion collisions by tagging very forward neutrons. The ZDC modules consist of alternating layers of quartz rods and tungsten plates and have a pseudorapidity acceptance of $|\eta| > 8.2$ for neutral particles.

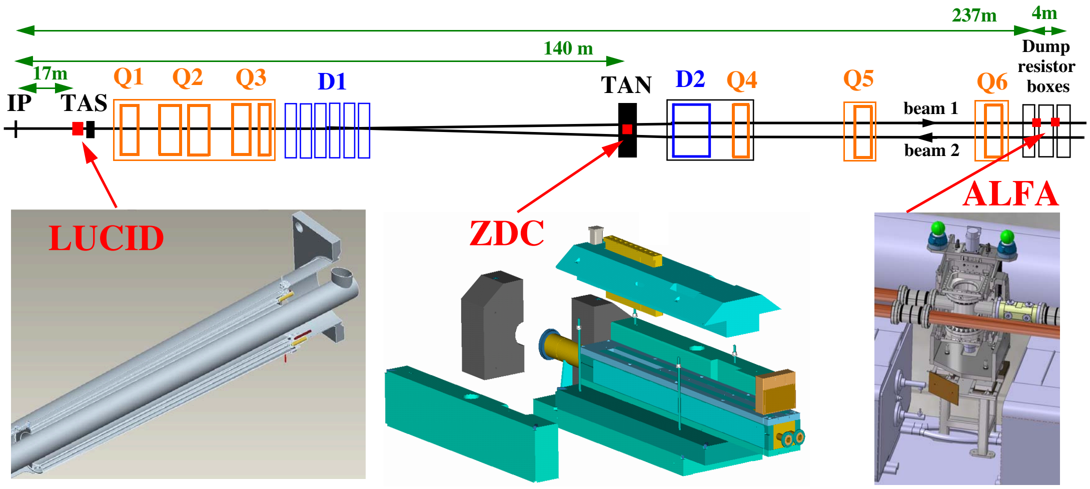

Figure 4.8: Pictures of the three forward detectors and their location along the beam-line. The distance from the ATLAS interaction point is labelled. [2].

4.2.6 The Trigger and Data-Acquisition System

The ATLAS trigger system will be used to select events containing interesting physics from the nominal bunch crossing rate of 40 MHz[7]. Three levels of event selection are used to reduce the rate to a few hundred Hz, the maximum rate at which events can be written to disk. The levels are referred to as Level-1 (L1), Level-2 (L2) and the Event Filter (EF). The triggers at each subsequent level refine the decisions from the previous level by applying more sophisticated criteria.

The L1 trigger is designed to reduce the rate to 75 kHz[8]. Only a limited amount of information from a subset of the detector is used in order to allow the decision of whether the event should be accepted to be made within 2.5 μs. Events containing high transverse momentum muons are identified using information from the muon spectrometers, while events containing high transverse momentum electrons, photons or jets, or large amounts of missing energy are identified using information from the calorimeters using a reduced granularity. The Minimum Bias Trigger Scintillators (see Section 4.2.6.1) are used to identify pp collisions containing minimal activity. The Central Trigger Processor (CTP) processes the output from all triggers.

One or more regions containing interesting features in each event, Regions-of-Interest (RoIs), are defined while the L1 decision is calculated. The L2 triggers then use all available detector information within the RoIs. The triggers at L2 are designed to reduce the trigger rate to approximately 2.5 kHz. In the final stage of event selection, the event filter uses offline analysis algorithms to reduce the event rate to 200 Hz.

Sub-detector specific Read-Out Drivers (RODs) collate data from several front-end (FE) data streams. Once an event has been accepted by the L1 trigger, the data are transferred from the FE to the RODs. The data from the RODs are temporarily stored by the Read-Out System while the data associated to a RoI is accessed by the L2 trigger. Those events selected by the L2 trigger are transferred to the event-building system and the EF for final trigger selection. Those events selected by the event filter are move to permanent storage at the CERN computer centre. The events undergo a two-step reconstruction procedure: an initial reconstruction allows the data to be used for detector calibration, the results of which are used as input for the second pass of reconstruction. At this point the data are distributed on the GRID to be used in physics analyses.

The rate of the individual triggers at each level is adjusted using a factor referred to as a pre-scale

---

[7] The collision rate from the LHC is significantly lower at present because the largest number of filled bunches to date has been 13 of the 2880 possible bunches.

[8] The current rate at which L1 is operated is typically 10-20 kHz.

and the set of enabled triggers and their pre-scales is referred to as a trigger menu. Changing the menu and pre-scales allows bandwidth to be used optimally while the luminosity and background conditions are changing. The data analysed here were obtained during the first few days of LHC operation. At this time, the collision rate was extremely low such that only the L1 trigger was enabled and a very limited trigger menu was used. With the increasing luminosity, the HLT was first enabled in pass-through mode, which recorded the trigger decision for each event without actually rejecting any events. Once the HLT had been commissioned, the full trigger chain was enabled, however the trigger menus will continue to evolve with increasing luminosity.

4.2.6.1 The Minimum Bias Trigger Scintillators

Section 10 studies events collected using the Minimum Bias Trigger Scintillators (MBTS). The MBTS are segmented scintillator paddles located close to the beam-pipe, which trigger on the energy deposited by charged particles traversing the scintillator. This means that events triggered by the MBTS are not biased towards events containing high energy interactions. The MBTS detector consists of 32 scintillator paddles, each of which is 2 cm thick. The paddles are arranged into 2 disks and installed on the inner face of the cryostats of the end-cap calorimeters at $z = \pm 356$ cm. Each disk has an inner and outer ring covering $2.82 < |\eta| < 3.84$ and $2.09 < |\eta| < 2.82$ respectively. The light emitted by each scintillator is transmitted through a wavelength-shifting optical fibre to a photomultiplier tube (PMT). A hit in the MBTS is defined by a signal in a single panel above an adjustable discriminator threshold.

The Beam Pick-Up based Timing System (BPTX) [101] detectors are electrostatic pick-up detectors, which are located at ±175 m on either side of ATLAS. The BPTX are used both to monitor the transverse beam position and as part of the L1 trigger to identify when a bunch of protons passes through ATLAS. The inelastic proton-proton collisions studied in this thesis were identified by a coincidence between the MBTS and the BPTX as discussed in Section 7.1.

4.3 Summary

The ATLAS experiment is the largest of the four experiments that has just begun recording data from collisions produced by the LHC. Since detector installation was completed in 2008, it has been commissioned using first cosmic-ray [128, 5] and, more recently, collision data [6]. Figure 4.10 (a)

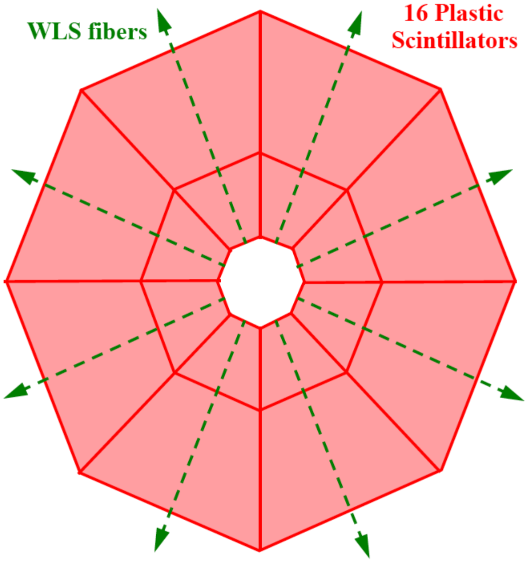

Figure 4.9: Illustration of the configuration of the 16 scintillators in each of the two MBTS disks.

shows the very first LHC collision event recorded by ATLAS and Fig. 4.10 (b) one of the first events recorded by ATLAS for collisions at centre of mass energy of 7 TeV. More than 97% of the read-out channels of each sub-detector are operational.

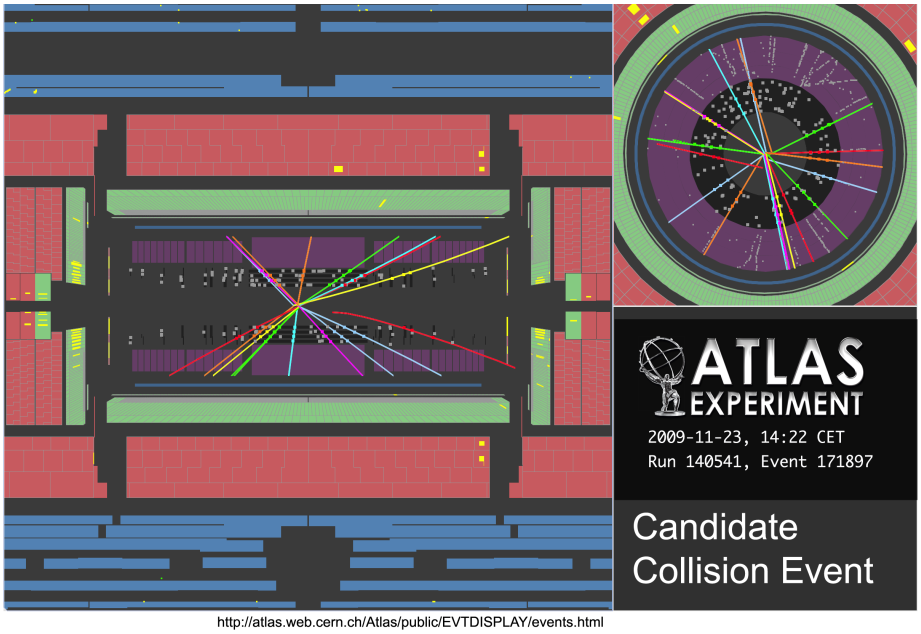

(a) $\sqrt{s} = 900$ GeV

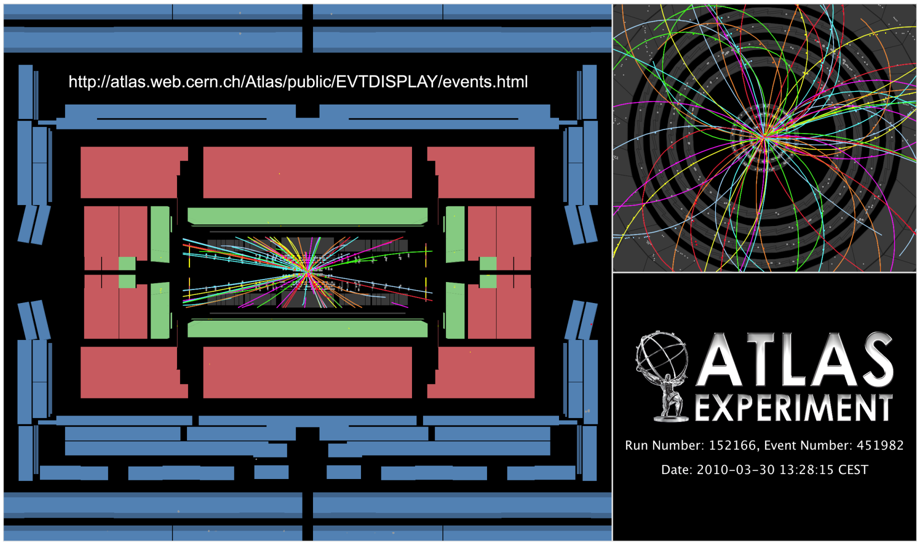

(b) $\sqrt{s} = 7$ TeV

Figure 4.10: a) The first LHC collision event recorded by ATLAS on 23 November 2009. The tracks for the charged particles are straight because the magnetic field of the solenoid was off. b) One of the first collision events at 7 TeV recorded with the full ATLAS detector on from 30 March 2010. Both events are examples of inelastic proton-proton collisions.

Chapter 5

The ATLAS Pixel Detector

5.1 Silicon Detectors

Silicon detectors measure the passage of charged particles to extremely high spatial precision. They are therefore typically situated close to the interaction point where the particle density is highest. The closer the first layer of silicon to the interaction point, the better the track parameter resolution, but the higher the radiation dose. Therefore the optimal detector placement involves balancing the performance with the detector lifetime.

Silicon can be either positively or negatively doped by introducing impurities into the silicon lattice. Positively doped silicon (p-type) is typically produced by introducing boron atoms. As boron has three valence electrons in comparison to silicon's four, boron borrows an electron from the lattice to fill its valence bonds. The result is a missing negative charge, which is called a *hole.* Negatively doped silicon (n-type) is typically produced by introducing phosphorus atoms, which have five valence electrons. In this case, an electron is released which can migrate through the lattice.

A pn junction, illustrated in Fig. 5.1, is created from a piece of p-doped and a piece of n-doped silicon. Free holes and electrons, which drift due to thermal diffusion, can pass through the junction. This creates an excess of negative charge on the p-side and an excess of positive charge on the n-side. As the excess charge increases, an electrical potential builds up. Once this potential exceeds the energy needed for electrons and holes to cross the barrier, the flow of charge stops. The region near the junction is depleted of mobile charge carriers and is called the *depletion region.*

An external voltage applied across a pn junction is called a *bias voltage.* The bias voltage is

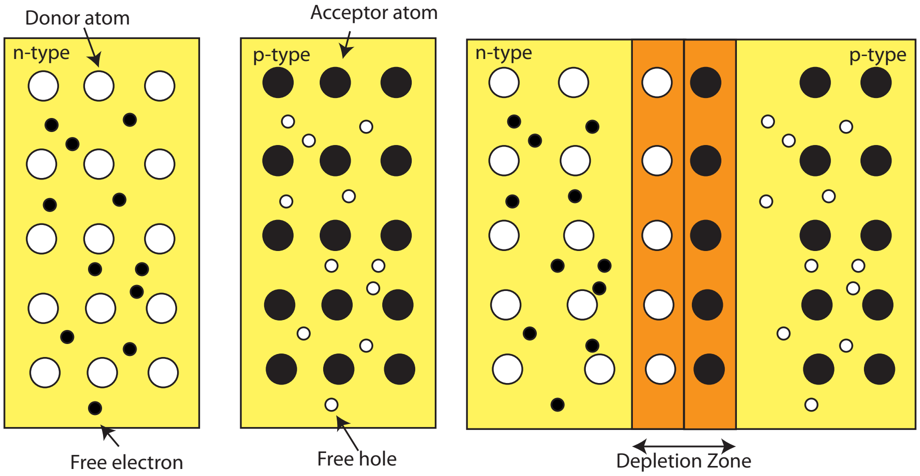

Figure 5.1: Illustration of pn junction

normally large enough that the depletion zone extends across the whole sensor so that there are no free charge carriers. The voltage can be applied either with or against the flow of charge. A forward bias, which has the positive supply on the p-side and negative supply on the n-side, yields a large flow of charge. A reverse bias extends the depletion zone such that the charge flow with a reverse bias is very small and called the *leakage current*. Silicon detectors typically use sensors made from reverse biased pn junctions.

An ionising particle, such as a charged pion or a muon, propagating through a silicon detector ionises the silicon atoms and produces pairs of electrons and holes along its trajectory. The number of electron-hole pairs produced is proportional to the energy lost by the particle. The externally applied electric field makes the electrons and holes move in opposite directions and pulls them to the sensor surface. The charge drifts to the surface and produces a pulse of current through induction, which is detected using charge sensitive electronics. The integral of the pulse is proportional to the amount of charge deposited by the ionising particle.

5.1.1 Energy Loss of Charged Particles in Matter

Charged particles traversing matter lose energy through interactions [31]. These occur via different processes including inelastic scattering from atomic electrons, elastic scattering from nuclei, emission of Cherenkov radiation, nuclear interactions and bremsstrahlung.

The amount of energy lost by a particle passing through matter depends on the particle type and energy. At the energies typical of particle physics experiments, electrons and positrons typically lose most of their energy through bremsstrahlung, while for heavier particles it occurs mostly through inelastic collisions. The Bethe-Bloch equation describes the mean rate of energy loss of moderately relativistic charged heavy particles with the precision of a few percent:

$$-\left\langle \frac{dE}{dz} \right\rangle = Kz^2 \frac{Z}{A} \frac{1}{\beta^2} \left[\frac{1}{2} \ln \frac{2m_e c^2 \beta^2 \gamma^2 T_m ax}{I^2} - \beta^2 - \frac{\delta(\beta\gamma)}{2} \right] \tag{5.1}$$

It accounts for energy lost through inelastic, elastic and Cherenkov processes but the accuracy can be improved by including corrections for the density and shell effects. Figure 5.2 shows the average energy lost by muons as a function of their momentum. It is large for very low momentum particles but falls rapidly with increasing momentum before reaching a minimum. A particle with this minimum energy is typically referred to as a minimum ionising particle (MIP). For larger momenta, the energy loss rises slowly, flattens out and then rises steeply due to radiative energy losses. This region is referred to as the relativistic rise.

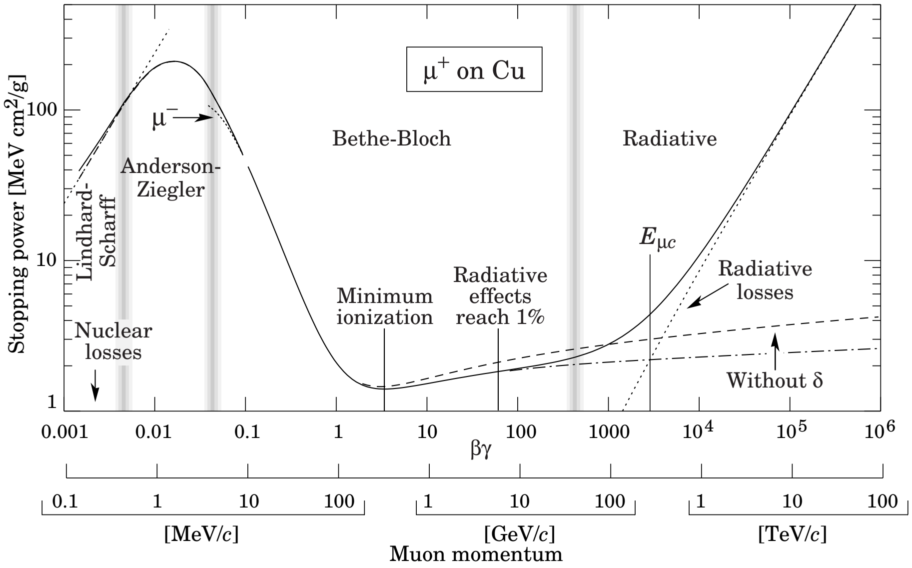

Figure 5.2: The average energy lost by muons in copper as a function of $\beta\gamma = p/Mc$ from [31]

5.2 The ATLAS Pixel Detector

The Pixel Detector is the innermost tracking detector of ATLAS. It uses silicon technology and contains more than 80 million channels, which provide excellent spatial resolution to meet the requirements for track reconstruction at the LHC design luminosity of $\mathcal{L} = 10^{34}$ cm^{-2}s^{-1}. It plays a critical role in the identification and reconstruction of secondary vertices from the decays of b-quarks. Moreover, the spatial resolution allows for the primary interaction vertex to be reconstructed in an environment with approximately 20 interactions per bunch crossing at the design luminosity.

The pixel tracking system consists of the active components of the pixel detector, the internal services, the mechanical support structures, the pixel support tube and the external services. The active detector components are assembled into a barrel and two end-caps. The pixel support tube contains the pixel detector and the internal services. The external services are connected to the internal services at the end of the pixel support tube.

The three layers of the barrel are constructed from mechanical structures referred to as staves with 13 modules mounted on each stave. The innermost layer, (L0), consists of 22 staves, the second layer (L1) consists of 38 staves and the third layer (L2) consists of 52 staves. The corresponding mechanical structures in the end-cap are the sectors. Each disk is assembled from eight sectors with each sector consisting of six modules. There are three disks in each end-cap. In total, the pixel detector contains 1744 modules corresponding to an active area of 1.7 m^2.

5.2.1 The Pixel Detector Module

The basic components of the pixel detector are the modules. Figure 5.3 illustrates the components of a pixel module: a silicon sensor, front-end electronics and the flex-hybrids containing control circuits.

A module consists of 47232 pixels on a 250 μm thick slightly n-bulk silicon sensor. Regions of high positive (p$^+$) and negative (n$^+$) charge are implanted on each side of the sensor. The charge is collected on the side of the n$^+$ implants, which allows the sensor to be operated for a longer period after irradiation. During initial operation, the depletion zone grows with increasing bias voltage from the p-side towards the n-side. The sensor needs to be fully depleted, because the region around the pixels is only depleted once the sensor is fully depleted. Irradiation causes type inversion, in which the bulk changes from n-type to p-type, and the depletion zone grows with increasing bias voltage from the n-side to the p-side. In this case the sensor can be used if it is not fully depleted, because the depletion zone extends from the pixels.

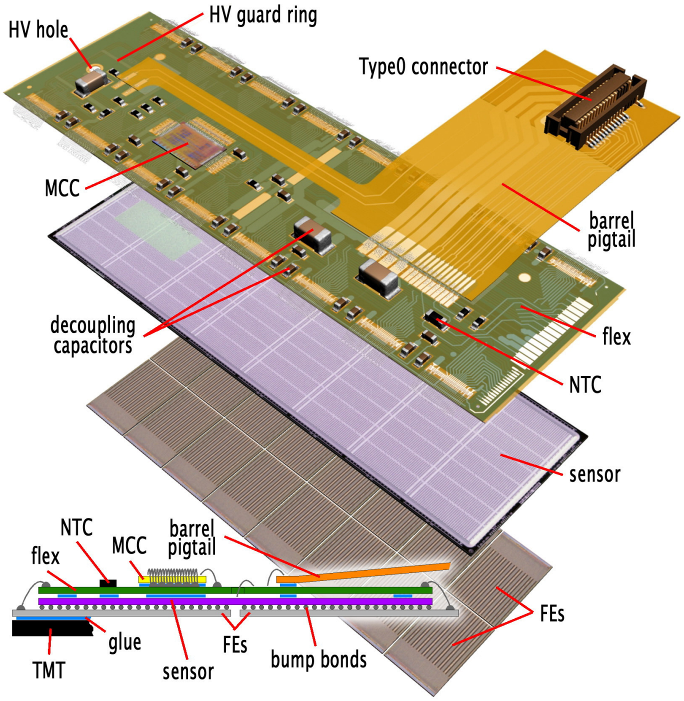

Figure 5.3: The three basic components of a pixel detector module: a flex hybrid containing control circuits (top), a silicon sensor (middle) and the front-end (FE) electronics (bottom). [69]

Each pixel is bump-bonded to one of the sixteen front-end (FE) chips per module. The chip contains 2880 pixel cells arranged in an 18 × 160 matrix. The components of single cell in the FE chip are shown in Fig. 5.4. Each cell consists of an analogue and a digital block. In the analogue block, the sensor charge is amplified and compared to a programmable threshold. In the digital block, the pixel hit address and timestamp of the leading and trailing edge are transferred to buffers located in the peripheral regions of the chip and stored for 3.2 μs. If a trigger signal with the same timestamp is received within that time the hits are read-out, otherwise they are discarded.

Most pixels are 50 x 400 μm in size. To ensure sensitivity in the regions between chip boundaries, 11% of the pixels have a size of 50 μm $\times$600 μm and are referred to as *long* pixels. A different strategy is used to cover the chip boundary in the short pixel direction, because such an increase in

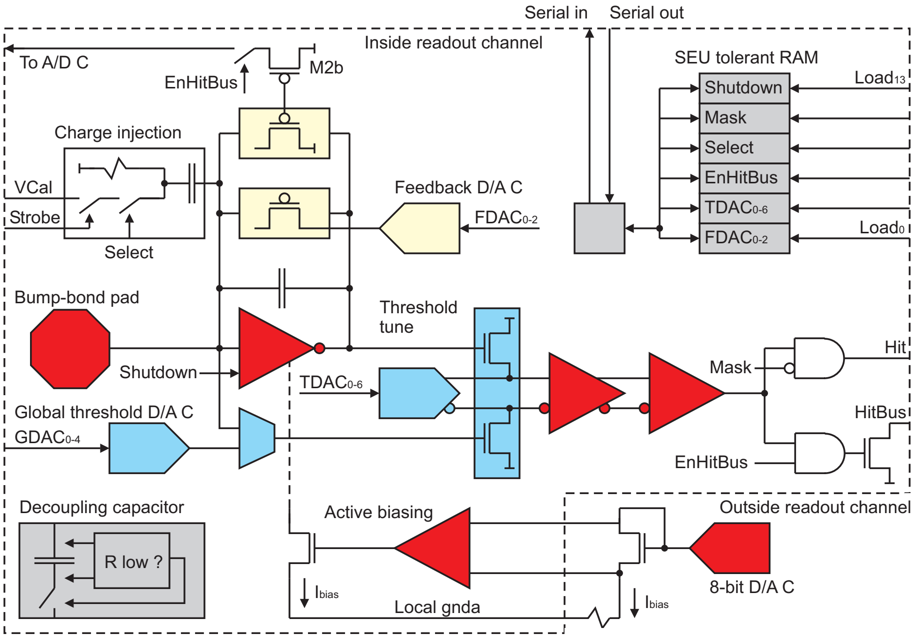

Figure 5.4: The components of a pixel FE chip [3]

size would degrade the measurement precision. Instead, multiple pixels are read-out by the same read-out channel. The 8 pixels lying in the boundary region are connected to one of the neighbouring pixels as illustrated in Fig. 5.5. These pixels are referred to as *ganged* pixels. The connections are only made to every second pixel to allow ambiguities to be resolved in the clustering algorithms. The pixels between the ganged pixels are referred to as *inter-ganged* pixels. Combinations of the two categories are possible for pixels, which lie close to the chip corners. In total there are five different types of pixels: normal (93.7%), long (10.6%), ganged (2.2%), inter-ganged (1.6%), long-ganged (0.3%) and long inter-ganged (0.2%). This connection strategy is the reason that the number of read-out channels (46080) differs from the number of pixels (47232) in a module.

The charge sensitive preamplifier contains a feedback circuit in which the constant discharge current saturates at high signal amplitudes. This means that the return to baseline of the pulse is close to linear, such that the width of the discriminator pulse output is proportional to the input charge. The width of the discriminator output, the so-called Time-Over-Threshold (ToT) is therefore used to measure the amplitude of the signal. The ToT is measured by counting in units of the 40 MHz MCC clock. As this frequency is the same as the LHC bunch crossing frequency,

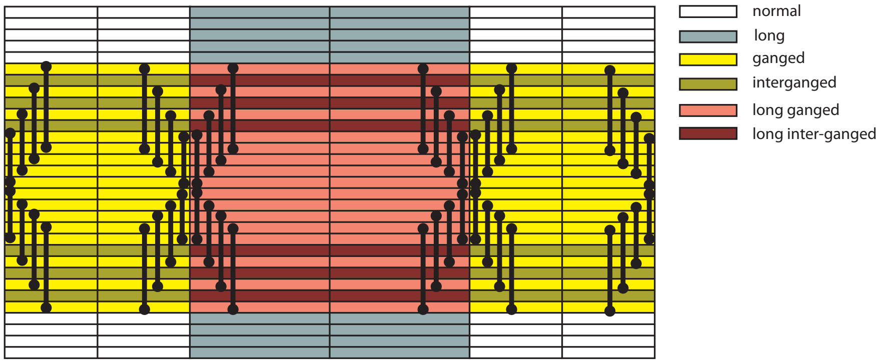

Figure 5.5: The six different classes of pixel. The normal pixels (white) are 50 × 400 μm in size. The long pixels (blue) are 600 μm long. The ganged pixel (yellow) are two pixels which share a read-out channel. The inter-ganged pixels (dark yellow) are normal pixels between ganged pixels. The combinations of the two are the long ganged pixels (red) and the long inter-ganged pixels (dark) red. The connections between the ganged pixels are indicated.

the units typically used are called bunch crossings (BC).

Each pixel cell in the FE chip contains a 14-bit control register, which is used to tune several parameters for each pixel. The group of bits used to control a specific parameter is called a Digital-to-Analog-Converter (DAC). The most commonly used are the 3-bit FDAC, which are use to trim the feedback current to tune the ToT response and the 7-bit TDAC, which are used to trim the threshold. In addition, there are global DACs, which are used to tune the scale of the feedback current (IFDAC) and threshold (GDAC) for all pixels on a single FE chip.

Signal and power are routed to the module through a 100 μm thick flexible printed circuit, which is called a flex-hybrid. The module controller chip (MCC) is situated on the flex-hybrid. The barrel modules are connected to the electrical services via microcables on an additional foil called a pigtail. The micro-cables for the end-cap modules are attached without the pigtail connection. The presence or absence of this pigtail is the only difference between modules in the barrel versus the end-cap.

The MCC controls the modules. During module configuration it writes values to the global FE chip registers and parameters for each pixel cell. The MCC distributes the L1 triggers, and the reset, calibration and timing signals to the FE chips. Finally, the MCC reads out and builds events. To achieve this, the data received from the FE are deserialised and buffered into First In, First

Out electronic control circuits (FIFOs) by the Receiver. The Event Builder then extracts the data from the FIFOs and builds the event. The completed event is then transmitted upstream to the Read-Out Driver (ROD).

5.2.2 Electronics for Read-Out, Timing and Control

The major components of the off-detector read-out and control system are the optoboards, the Back of Crate (BOC) cards, the Read Out Drivers (RODs) and the Read Out Systems (ROSs). The optoboards and Back of Crate cards make the optical link system. The communication between the BOC and the optoboards occurs via optical fibres. The optoboards are not located on the detector but within the pixel package at the Patch Panel 0 (PP0)[1] region. The RODs are specific to each sub-detector, while the same ROSs are used by all sub-systems. The pixel ROD is a 9U-VME module and is located in a ROD crate. Each crate contains 16 RODs, a Trigger, Timing and Control Interface Module (TIM), and a single board computer (SBC). The software on the SBC controls the components in the ROD crate.

The read-out system transfers the data from the module to the offline processing. Figure 5.6 illustrates the components of the read-out architecture. The flow of data is from left to right: from the modules, through the optical link system to the off-detector electronics.

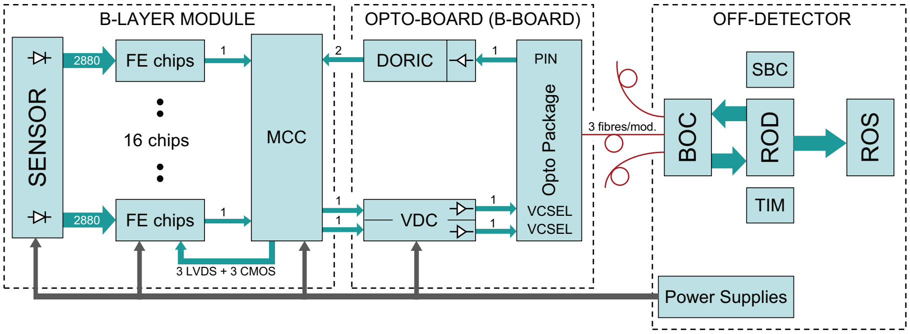

Figure 5.6: The components of the readout system of the pixel detector [116]

The signals from the modules to the optoboards are transmitted through low voltage differential signaling (LVDS) electrical connections. The signals are received by a Vertical-cavity surface-emitting laser (VCSEL) Driver Chip (VDC) located on the optoboard. The signals are then trans-

---

[1] The locations at which cable connections are made are called Patch Panels. Patch Panels are numbered in ascending order from the detector towards the services.

mitted by Vertical-Cavity Surface-Emitting Laser (VCSEL). The optical signals are converted back to electrical signals by the receiver (RX) plug-in on the BOC. The electrical signals are transmitted by the BOC to the RODs. Data is routed directly from the RODs upstream in the data acquisition chain to the ROSs using custom optical links (S-Links).

The rate at which the module needs to be read out depends on the luminosity, the L1 trigger rate and the distance from the module to the interaction point. To ensure no data loss occurs once the LHC has reached design luminosity, the different layers of the pixel detector are read out at different rates. The modules of L0 are read out at 160 MHz and therefore use two up-links to double the bandwidth. The L1-modules and the disks are read-out at 80 MHz, while the L2-modules are read-out at 40 MHz.

The down-link transmits clock, commands and configuration data to the modules. The electrical data from the ROD or TIM are converted by the BOC into optical signals and sent to the optoboard by the transmitter (TX) plug-in. The down-link between the BOC and optoboard uses bi-phase mark encoding, which allows the 40 Mb/s control stream to be sent on the same channel as the 40 MHz clock. The signals are received by the PiN diode array on the optoboard and then decoded by the Digital Optical Receiver (DORIC) on the optoboard to recover both the data stream and the clock signal. The DORIC then transmits the signals to the module.

5.2.2.1 The Pixel Detector Read-Out Driver

A schematic view of the ROD is shown in Fig. 5.7. The primary purpose of the ROD is to configure modules, propagate trigger signals and format data. In addition, it is used to calibrate and monitor the detector. The electronics components are either Field Programmable Gate Arrays (FPGAs) or Digital Signal Processors (DSPs). There are two components that control the ROD. The Controller FPGA controls the real-time data-flow functions, such as the transmission of commands to the FE chips, the trigger generation during calibration and the transmission of triggers from the TIM. The Master DSP communicates with the VME host and coordinates the configuration, calibration and data-taking of the ROD.

Figure 5.7 also shows the passage of data through the ROD. Data from the BOC enters the ROD via the formatters. In the formatters, the data are split into parallel streams. If a Level 1 accept is received, the data are transmitted from the formatters to the Event Builder (EB). The EB builds an event fragment and checks the Level 1 trigger identifier and the bunching crossing identifier and records any discrepancies with those expected from the trigger chain. Once a full event is ready in the EFB, which includes the header, body and trailer, it is transmitted to the router. The router transmits the event in 32-bit words to the S-Link at 40 MHz. If the S-Link receives data at a faster rate than it can be transferred to the ROS, back pressure is applied to the ROD data path. As the different FIFOs fill up, the back pressure reaches earlier parts of the chain, until the data transmission from the formatters stops. The router also traps data, which is passed to the DSPs for error monitoring. The slave DSPs are primarily used for calibration of the pixel detector, in which the various possible configurations of the FE chips are scanned to obtain optimal detector performance. The software developed to control the DSPs is described in [50].

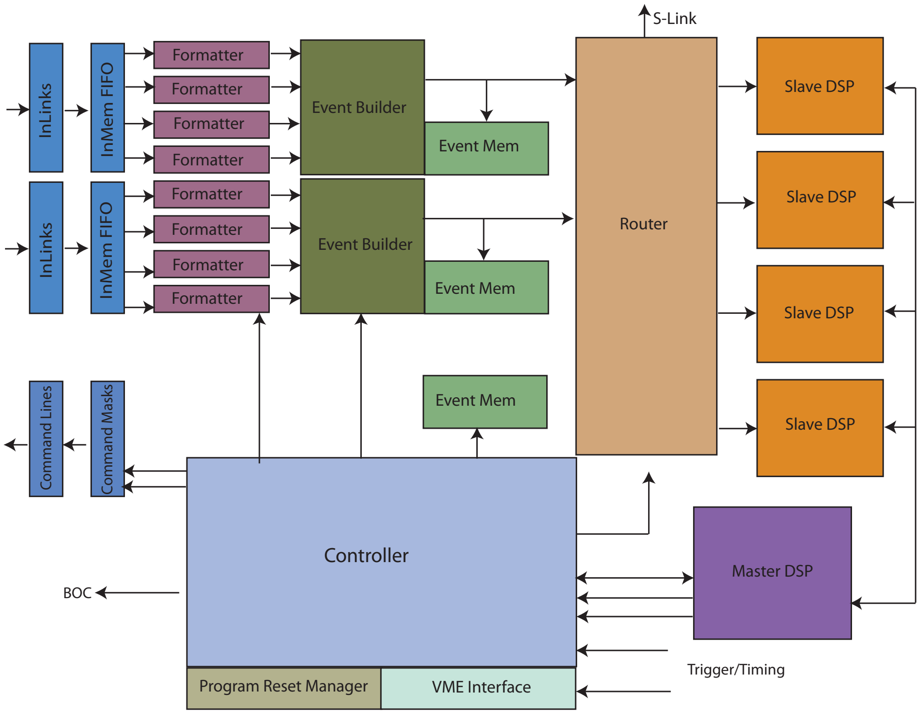

Figure 5.7: The components of the Read Out Drivers (RODs) of the pixel detector. The flow of data is from left to right and is indicated by arrows.

5.2.3 Services

The services used to power and monitor the pixel detector are referred to as the Detector Control System (DCS). The DCS components are summarised in Fig. 5.8. The digital (V_{DD}) and analog

(V_{DDA}) supplies for the FE chips are supplied by a low voltage power supply made by WIENER. The power from the Wiener is split by the low voltage Patch Panel 4 (LV PP4) and transmitted to the regulator stations. The regulator stations are installed as close as possible to the detector (approximately 10 m) to minimise the voltage drop over the long distance between the detector and the power supplies. In addition the regulator stations protect the electronics against transient voltage spikes. A typical pixel module receives 2.1 V of digital voltage and 1.7 V of analog voltage.

The bias voltage of 150-600 V[2] for the sensors, V_{DET}, is provided by the high voltage power supply, which uses commercial modules from Iseg. The high voltage is distributed by a corresponding patch panel, HV PP4.

The power to the optoboards is provided by the SC-Olink, which provides a 6 V low-voltage supply for the VDC and DORIC chips, V_{VDC}, and a 10 V bias voltage for the PiN diode.

The temperature and humidity of the environment are monitored by the Building Block Monitoring (BBM). The temperatures of the modules, optoboards and the regulator stations are monitored by the Building Block and Interlock Monitoring (BBIM). The output of the BBIM, all components of the power supply system and the BOC are connected to the Interlock System, which is a hardware based system designed to ensure detector safety. For example, if the module temperatures are too high, the power supplies are automatically switched off.

5.3 Calibration of the Pixel Detector

The pixel detector has a number of configurable settings, which must be tuned to ensure optimal detector performance. First, error-free optical communication needs to be established with all modules. Then, the parameters on the front-end chip must be tuned to achieve a uniform response throughout the detector to the deposited charge. Finally, the timing must be adjusted to be consistent with the other ATLAS detector systems.

The calibration of the 80 million channels of the pixel detector is a challenging task both in terms of time to collect the data and the volume of data that must be analysed. A distributed system has been implemented to perform the calibration. In addition, much of the analysis is performed by the DSP processors to reduce the volume of data downloaded from the RODs to disk.

---

[2] A voltage of 150 V is sufficient to fully deplete pixel detector sensors before irradiation. Once the sensors begin to be damaged by radiation the bias voltage will be increased up to a maximum of 600 V.

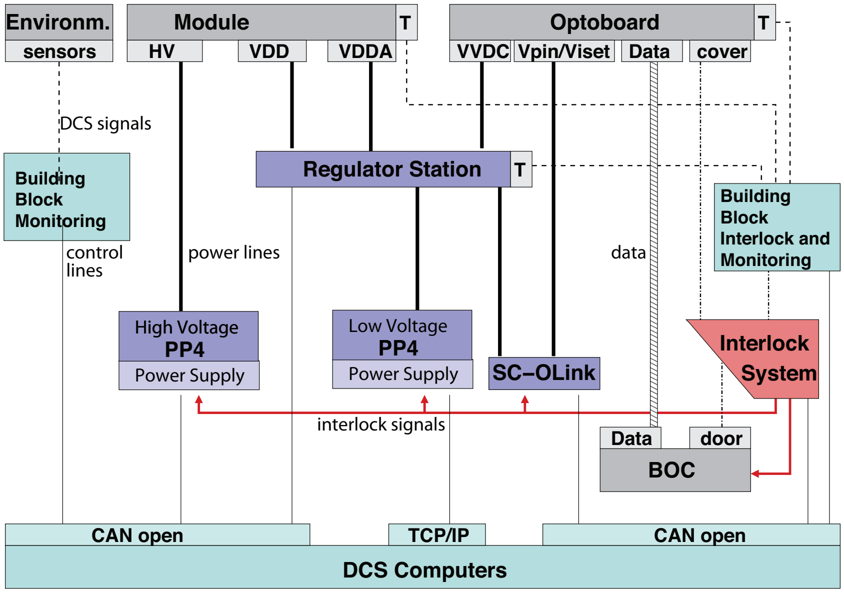

Figure 5.8: The components of the Detector Control System used to power the detector and to monitor conditions to ensure detector safety [3].

The full pixel detector was calibrated for the first time at the end of 2008. The results from this tuning period are discussed here.

5.3.1 Optical Tuning

There are three stages to the tuning of the optical parameters [71]: verify that information can be sent to the modules, verify that information can be received from the modules, and, finally, tune the parameters to obtain optimal information transmission. The transmission of information to the modules is verified by sending light from the Tx-plugin on the BOC through the fibre and measuring the increase in current on the optoboard PIN diode. The transmission of data from the modules is verified by setting the modules to transmit a 20 MHz clock pattern through the up-link fibres to the BOC. The receipt of the signal is measured by the PIN-diode on the Rx-plugin on the BOC.

There are two parameters that need to be tuned to get data from the modules: the signal threshold and the delay. These are obtained by scanning through a set of possible values to find a setting in which the transmission of the 20 MHz clock pattern is error-free. This is checked by verifying that the received data contains an equal number of zeros and ones. A third parameter that is tuned is the voltage applied to the VCSEL, which is tuned to obtain stable signal transmission. Certain channels for which the VCSEL on the detector do not reach full power immediately after being switched on require a second round of tuning. These modules are set to transmit a known pseudo-random pattern of data, in which the correct value of each bit is checked by the BOC. This provides a more stringent test of any possible problems the optical transmission and allows the optical parameters of these modules to be tuned.

The successful tuning of the optical parameters is verified by injecting a pulse into each read-out channel beyond the discriminator and checking whether the signal is received by the BOC. This validates both the optical tuning and the functionality of the digital components of the FE chip. The analog circuitry is tested similarly by injecting a charge well above the discriminator threshold into each read-out channel before the preamplifier. If the hit is received by the BOC, this verifies that the analog circuitry of the FE chip is functional.

5.3.2 Threshold Tuning

A pixel is only read out if the signal is larger than an adjustable threshold. This limits the amount of noise data transferred from the modules. The charge that this threshold corresponds to for a specific pixel is measured using a *threshold* scan. At each step in a threshold scan, a certain amount of charge is injected a fixed number of times and the number of hits received by the BOC are counted. A full threshold scan is made by scanning with different values of injected charge. Figure 5.9 shows how the fraction of recorded hits increases as a function of the injected charge for a typical scan. The threshold is defined as the charge at which the hit efficiency is 50%. A noise-free chip would produce a step-like threshold function. Therefore the width of the turn-on curve is regarded as a measure of the noise of the pixel. This width is calculated from the difference in charge between an injection efficiency of 16.5% and 83.5%.

The threshold of each individual pixel is tuned [44] to ensure a uniform response to a fixed amount of charge across the detector. The tuning algorithm injects the charge corresponding to the desired threshold and varies the parameters on the FE chip until the fraction of reconstructed hits is 50%. The values of the threshold and noise after the 2008 tuning period are shown in Fig. 5.10. As expected, the threshold in Fig. 5.10 (a) has been tuned to the same value independently of the

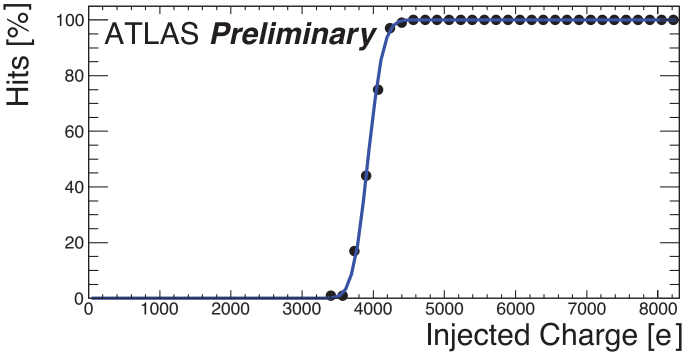

Figure 5.9: Example of the fraction of expected hits obtained from a single pixel as a function of the injected charged [44]. The fit is a Gaussian error function.

pixel type. However, the noise in Fig. 5.10 (b) varies between the pixel types. The long pixels have a larger capacitive load, which translates into increased noise. The ganged pixels, in which two pixels are connected to a single FE chip, have twice the noise for the same reason. The interganged pixels have the same properties as the normal pixels.

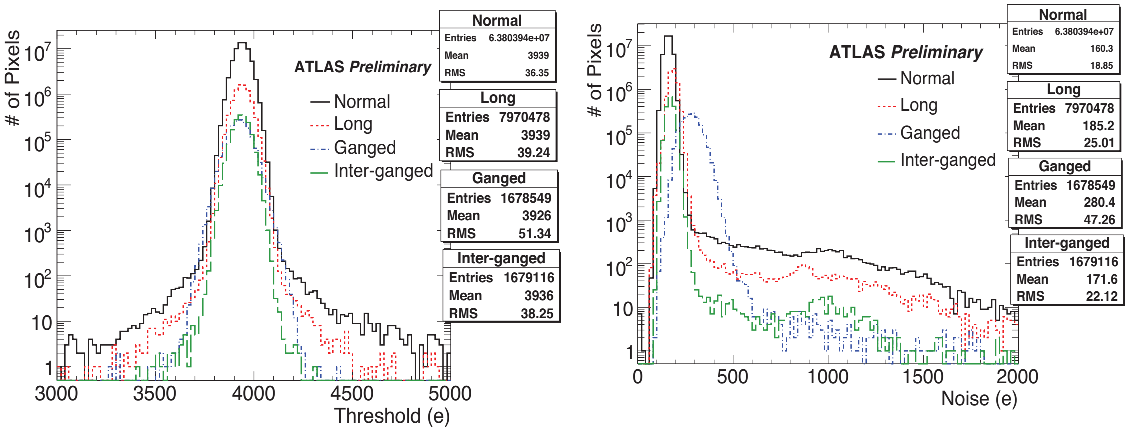

(a) Threshold

(b) Noise

Figure 5.10: The threshold and noise distributions for 94% of the detector after the November 2008 tuning [44]. The values are shown for the normal (black), long (dashed, red), ganged (dot-dashed, blue) and inter-ganged (green) pixels separately.

The threshold was initially tuned to 4000 electrons. The studies discussed in Section 5.4 motivated the reduction of this threshold to 3.5 and 3 ke in subsequent tunings. This was to remove the bias in the measured charge for particles with large incidence angle to the sensor surface.

5.3.3 Tuning and Calibration of the Time-Over-Threshold Signal

The time at which the leading and falling edges of the signal cross the threshold are recorded for each hit. The difference in time in units of 40 MHz between the falling and leading edge is referred to as the time-over-threshold (ToT). The programmable current in the feedback loop of the preamplifier ensures that the ToT increases almost linearly with the deposited charge. The bunch crossing in which the hit is registered is determined by the time stamp of the leading edge.

Every hit that is read out contains this ToT information. The parameters which control the ToT circuitry are tuned [83] for each pixel to ensure that a charge of 20 ke corresponds to a ToT of 30 BC. The dispersion of the ToT across pixels in a front-end chip is approximately 0.7 bunch crossings. Figure 5.11 shows the distribution of the ToT threshold using the tuning produced during the module production to that after the 2008 tuning. After the November 2008 tuning, the mean ToT values is 29.8 BC and the dispersion over the pixels is 0.70 BC [83]. The small bias in the mean value is not fully understood but caused by differences to the ToT measured while tuning and in a subsequent ToT scan.

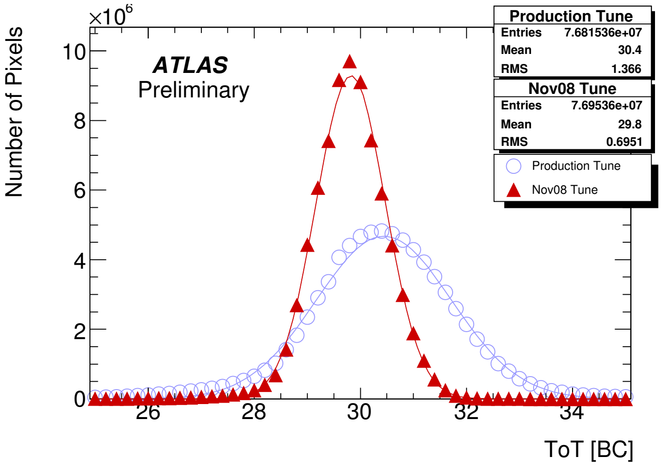

Figure 5.11: The time-over-threshold (ToT) distribution for pixels with an injected charge of 20 000 electrons with the tuning performed during module production (open) and after the 2008 tuning (closed) [83].

The ToT tuning procedure adjusts the response of the FE to a 20 ke charge, however the response at higher and lower charge also needs to be uniform. Therefore, a calibration curve of the ToT dependence as a function of the charge is derived for each FE chip. Figure 5.12(a) shows the ToT as a function of charge for a single FE chip. This calibration curve is used offline to convert from the measured ToT signal in data back to the value of the charge. Figure 5.12(b) compares the charge predicted by the ToT calibration function from the measured ToT to the actual injected charge as a function of the injected charge. The charge residual is small at low charge values, which indicates a reliable ToT calibration function, but becomes large at high values of the charge.

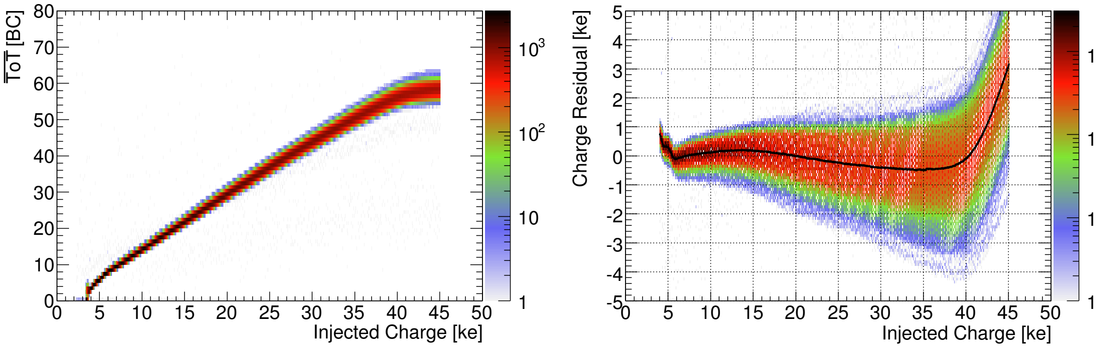

(a) ToT vs charge

(b) Charge residual vs charge [83].

Figure 5.12: a) The ToT as a function of the injected charge. b) The difference between the charge predicted by the ToT calibration function and the injected charge as a function of the injected charge.

5.4 Verifying the Charge Scale of the Pixel Detector with Cosmic Ray Data

5.4.1 Overview

During calibration it is implicitly assumed that exactly 20 ke of charge is injected into the charge circuitry. An ionising particle, such as a muon, passing through a sensor deposits an amount of charge that can be predicted from the distance of depleted silicon traversed. A measurement of the most probable value of the deposited charge can be used to verify the charge scale and thus be used to calibrate the charge injection circuitry. A similar measurement was performed on a few hundred modules during production by irradiating the modules with a ^{241}Am source [73]. The measured charge was 4% lower than the theoretically predicted charge of 16.2 ke for a pixel detector sensor.

This section discusses a measurement of the charge scale of the pixel detector using cosmic-ray muons. As the amount of deposited charge depends on the distance of silicon traversed, the data is fit in bins of propagation distance to extract the most probable value (MPV) and the full width at half maximum (FWHM) of the charge as discussed in Section 5.4.4. The MPV obtained from these fit is then fit as a function of the track propagation distance using the expected theoretical dependence. The method has a single free parameter, a scale factor, C, which allows the charge scale to float. The method is applied both to data and to the GEANT4 [17] simulation and, in each case, with and without the 2 T field of the solenoidal magnet turned on. Further details of this measurement are found in [68], including an alternative method also used to extract the charge scale.

The data were taken during combined ATLAS (September-October 2008) and Inner Detector (November 2008) cosmic data-taking. Data were taken both with and without the presence of the 2 T solenoid field in the Inner Detector. The term field on/off will be used to refer to datasets collected with the solenoidal magnetic field on/off.

5.4.2 Theoretical Models of Energy Loss in Silicon

The mechanism of energy loss in silicon was discussed in Section 5.1. The pixel detector measures the number of electron-hole pairs produced by a particle passing through the sensor. The number of electron-hole pairs is referred to as the ionisation, J, and is related to the total energy lost by the particle, Δ, by a factor W, which is the average energy to produce an electron-hole pair:

$$\Delta = WJ \tag{5.2}$$

The value of W depends on the material temperature, particle type and particle energy. For silicon, W has been measured to be 3.67 ± 0.02 eV [102], 3.6310 ± 0.0025 eV [107] and 3.66 ± 0.03 eV [109]. These measurements were made at room temperature using either electrons or photons with energies up to 1.5 MeV. A review [93] finds W to be 3.68 ± 0.02 eV with no significant variation for energies ranging from a few keV to 1 MeV. No measurements have been made for particles with energies at the scale expected in high-energy physics experiments.

The energy lost by a particle traversing a silicon detector depends on the particle type and momentum according to the Bethe-Bloch formula. The probability density function of the energy loss is known as a straggling function. Straggling functions for different propagation distances in silicon have been calculated with various techniques including convolution methods and simulations. Recent results were obtained by Bichsel using a convolution method [48]. This method calculates the straggling function for an extremely short propagation distance, and then convolutes this straggling function with itself to obtain the result for twice the propagation distance. This is repeated to obtain straggling functions for sensor thickness.

As the energy loss distribution is highly skewed, the mean is poorly defined and sensitive to experimental cut-offs at high energy. Therefore the most probable value (MPV) is used instead. The increase of the MPV with the propagation distance has been parametrised as follows by Bichsel [48]:

$$\mathrm{MPV}(\Delta) \quad = \quad l(190 + 16.3 \ln l) \qquad [110 < l < 1000\ \mu\mathrm{m}] \tag{5.3}$$

where MPV(Δ) is the most probable value of the energy loss in eV, and l is the distance of silicon traversed by the particle in microns. The parametrisation is valid for particles with $p > 50$ GeV. The energy loss in the GEANT4 simulation reproduces the energy loss to within 1.2% of the parametrisation. The parametrisations agree with the experimental results from which they were obtained [48] to within 2%, therefore they are used to fit the MPV of the charge distribution as a function of the track propagation distance. This 2% is estimated as the systematic uncertainty on the theoretical parametrisation.

Because the charge gives the ionisation, J, rather than the energy loss, Δ, the parametrisations must be scaled with the energy W using Eq. 5.2 when used to fit the charge. For the data, $W = 3.68$ eV [93] is used. The simulation used an older value, $W = 3.62$ eV, but this is corrected for in both methods. A 2% systematic uncertainty on W accounts for variations with momentum and temperature [48]. An additional 0.5% uncertainty accounts for the spread in the measured values of W.

A track traversing an ATLAS pixel sensor at normal incidence is expected to have an ionisation MPV of 19.0 ke and FWHM of 7.1 ke. The measured FWHM is expected to be broader due to effects including detector noise, threshold and the non-uniformity of the ToT response across a front-end chip.

5.4.3 Analysis Procedure

The charge measurement is performed using pixel clusters. Pixel clusters are groups of hits from neighbouring pixels. The charge is the sum of charge of each pixel in the cluster. Only clusters in the barrel, containing no ganged pixels, are studied. In addition, clusters with a pixel in either the row or column adjacent to the module edge are discarded, as well as clusters containing more than one pixel in the long pixel direction. Clusters are required to be associated with a reconstructed track, and hence termed *clusters on track*, to remove any clusters from noise. Tracks are required to have at least two hits in the Pixel Detector barrel and a significant number of hits in the remaining inner detectors: $5 \cdot \text{SCT Barrel Hits} + \text{TRT Barrel Hits} >= 30$ [84].

The track propagation distance in the sensor is related geometrically to the track incidence angle: $l = t/\cos\alpha$, where t is the sensor thickness. During module production, the average sensor tile thickness was measured to be 253.7±0.7 μm [85]. However, ∼3.6 μm of this thickness is inactive because it consists of inactive metallisation layers and depositions of silicon-oxide and silicon-nitride on the sensor surface. Therefore the average active thickness is 250.1 μm. The simulation used a constant sensor thickness of 250 μm.

The *total* track incidence angle, α, is defined relative to the normal vector to the module surface. It is calculated from the two component track angles as $\tan\alpha = \sqrt{\tan^2\theta + \tan^2\phi}$. The angle θ is directed in the long pixel direction and ϕ in the short pixel direction. For barrel modules, θ is the angle in the z-direction and ϕ circles around the barrel. Figure 5.13 clarifies the relationship between the three incidence angles.

As α increases, the total amount of deposited charge increases. Using Eq. 5.3 a 15% increase in the MPV of the deposited charge is expected (from 19.0 ke to 21.8 ke), when α increases from 0 to 0.5 radians. This variation must be taken into account in finding the MPV. Fits are made in bins of the track propagation distance. The fits are also performed separately on clusters containing either one, two or three pixels in the ϕ direction.

At large α, despite the large cluster charge, the charge per pixel is small because the cluster size is also large. If the charge per pixel is near threshold, the cluster can split and be reconstructed as multiple clusters. This effect, which occurs at large α, biases the charge to low values. Therefore clusters are vetoed if an additional cluster is reconstructed within the same module. As cosmic-ray

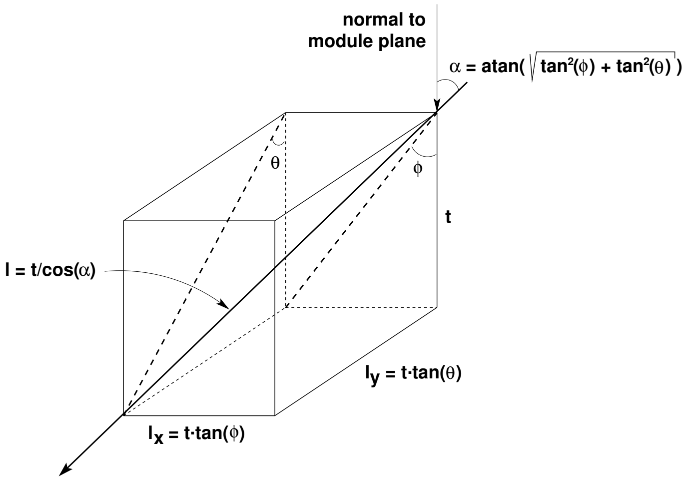

Figure 5.13: Calculation of the total track incidence angle, α, from the component track incidence angles. The angles are shown with the module orientated horizontally and the normal to the module surface vertical. The label l_x is the track propagation distance in the short pixel direction and l_y is the propagation in the long pixel direction[68].

events typically contain a single track and a noise rate of 10^{-10} hits/bunch crossing/pixel [1], the number of clusters lost due to an additional track or a noise hit in the same module is negligible [36].

When the magnetic field is on, the electrons produced in the module by a traversing particle drift at an angle known as the Lorentz angle (see [43]). For the barrel modules, the drift is in the positive ϕ direction. For track angles $\gtrsim 0.1$ rad, the cluster size is smaller for the magnetic field on than off. For angles $\lesssim 0.1$ rad, the opposite is true, i.e. the cluster size is larger for field on than off. See [36] for further discussion on cluster properties with and without the magnetic field.

The particle momentum can only be measured for the field on data. Ideally, only tracks with $p > 50$ GeV would be used to match the particle momenta used in the theoretical calculation, but as the cosmic ray spectrum decreases rapidly with momentum, this would retain insufficient statistics for the measurement. Therefore a cut of $p > 5$ GeV is implemented to limit the bias from low momentum tracks. This results in a measured energy loss corresponding closely to that of a muon with $p = 5$ GeV because the number of tracks decreases rapidly with momentum. The field off measurement is expected to be slightly biased to low values, because no cut on momentum can be applied.

Table 5.1 summarises the number of tracks and clusters used in the analysis [84]. A good cluster

Table 5.1: The number of tracks and clusters of cosmic-ray data and cosmic-ray simulation samples.

	Data		Simulation	
Field	Off	On	Off	On
Tracks	131338	126017	178070	184646
Clusters	1234663	1302766	2112396	2111490
Clusters On Track	586853	576687	817280	816519
Good Clusters	443026	437027	661509	657044

is defined as a cluster passing all cuts used for the charge scale measurement.

5.4.4 Fitting to Extract the Most Probable Value

The Most Probable Value (MPV) is obtained by fitting the charge distribution. A convolution of a Landau and a Gaussian [82] is used, because a Landau distribution alone does not describe the straggling functions of energy loss in silicon detectors. The Gaussian component also absorbs various experimental effects such as detector noise and the fact that the ToT calibration function is only calculated per front-end chip. The convolution function is obtained from the following integral:

$$f(Q) = N \int_{Q-5\sigma_G}^{Q+5\sigma_G} L(x, \mathrm{MPV}_L, \sigma_L) G(x, Q, \sigma_G) dx \tag{5.4}$$

where

- Q: Deposited Charge
- L: Landau function
- G: Gaussian function
- x: Integration variable used to perform the convolution integral

There are four parameters to the fit:

- MPV_L: Most Probable Value of the Landau distribution
- σ_L: Width of the Landau distribution
- σ_G: Width of the Gaussian distribution
- N: Normalisation constant

The width of the Landau and Gaussian are partially correlated. Figure 5.14 shows two examples of fits to the data. Because the Landau function is not symmetric, the MPV of the convolution is not equal to the MPV of the Landau distribution. Depending on the Gaussian width, the MPV of the convolution is typically ~700-800 electrons larger. The term MPV will only refer to the MPV of the convoluted function. Pseudoexperiments were used in order to determine the error on the MPV from the errors on the individual fit parameters. Correlations between the different fit parameters were accounted for. The fits were only performed on histograms containing at least 500 entries to ensure stability.

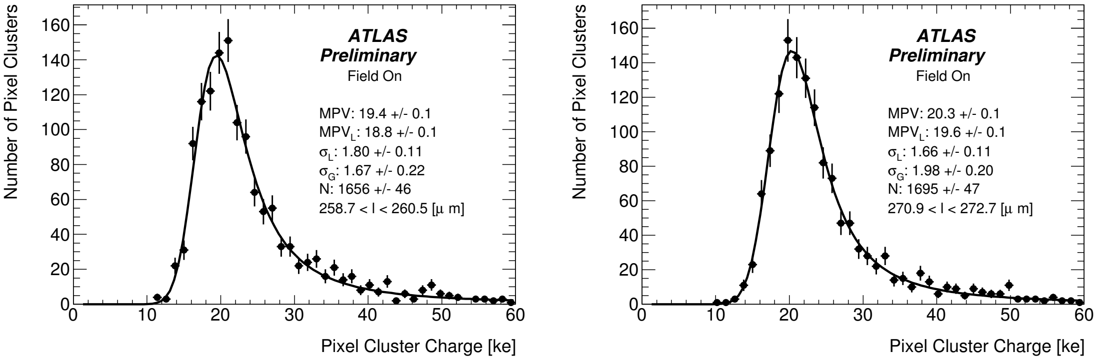

Figure 5.14: Examples of the charge distributions fit with a convolution of a Landau and a Gaussian for 2-pixel clusters at two different ranges of track propagation distance: $258.7 < l < 0.260.5$ μm (left) and $270.9 < l < 272.7$ μm (right) for field on.

5.4.5 Determination of the Absolute Charge Scale

If the charge deposited in a pixel is below the 4 ke threshold, it is not read out. This can, however, significantly bias the charge measurement. However, by selecting clusters in a limited angular range, the biased clusters can be removed.

The angular range over which the 2-pixel clusters are unbiased was determined to be $-0.04 < \alpha < 0.44$ rad for field on and $0 < \alpha < 0.24$ rad for field off [36]. The angular ranges are different for field on and off due to modifications to the cluster size caused by the Lorentz drift in the magnetic field. Figures 5.15(a) and 5.15(b), which show the number of reconstructed clusters of different size as a function of the track incidence angle, provide support for these ranges. This is because, to first order, if, at a particular track incidence angle, only 1- or 2-pixel clusters are reconstructed, but no 3-pixel clusters, the 2-pixel clusters are expected to be free from bias. For simplicity only positive α was used. These angular ranges correspond to the following variation in track propagation distance: 250 μm $< l <$ 276.3 μm and 250.1 μm $< l <$ 257.3 μm for field on and off.

The unbiased clusters are fit with the expected theoretical dependence using a free parameter, C, to allow the charge scale to float: $\mathrm{MPV}(l) = (C/W)l(190 + 16.3 \ln l)$.

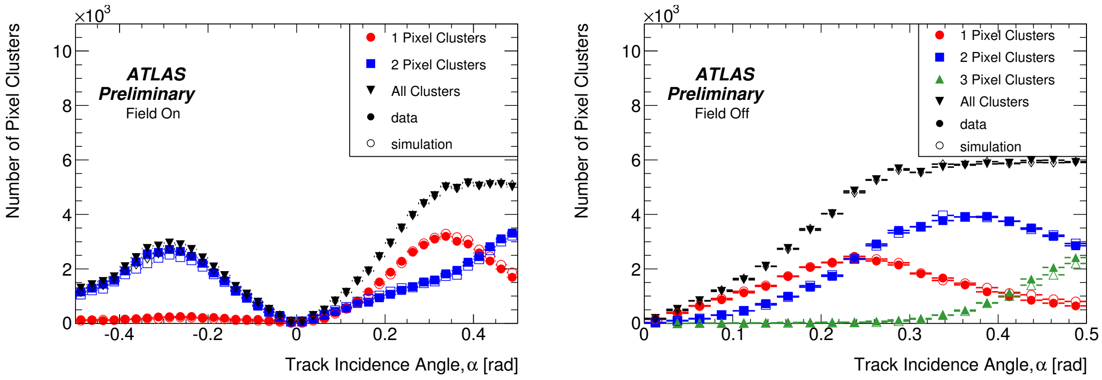

(a) Field On

(b) Field Off

Figure 5.15: The number of reconstructed clusters as a function of the track incidence angle for data (closed points) and simulation (open points).

Figures 5.16(a) and 5.16(b) show the MPV as a function of the distance traversed for field on and off. The open circles show the results for the simulation and the closed circles for the data. The values obtained for C are shown in Table 5.2. That $C_{\text{simulation}} \approx 1$ means that the measured charge is the same as the simulated charge and confirms that the bias from the threshold has been controlled in these angular ranges. However, $C_{\text{data}} < 1$ for both field on and off. $C_{\text{data\_BOff}} = 0.957$ is lower than $C_{\text{data\_BOn}} = 0.986$. This difference is not fully accounted for by the fact that no momentum cut is applied, which is only expected to bias $C_{\text{data\_BOff}}$ by approximately -0.5% (see Section 5.4.6).

5.4.6 Sources of Systematic Uncertainty

Uncertainties on the measurement of the charge scale are caused by a number of effects. These include uncertainties on the theoretical expressions, the energy to produce an electron-hole pair (W),

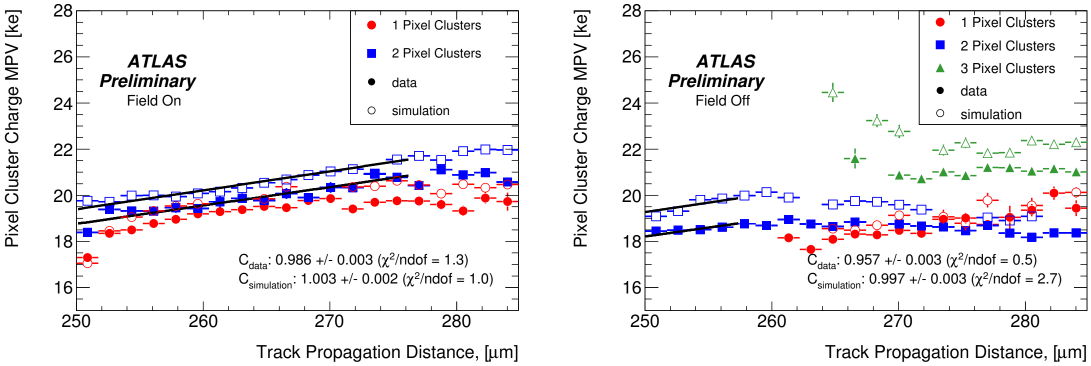

(a) Field On (b) Field Off

Figure 5.16: The MPV of the deposited charge for 1-, 2- and 3-pixel clusters as a function of the track propagation distance in silicon together with the fit to the 2-pixel clusters to obtain C for tracks at normal incidence for simulation (open points) and data (closed points).

Table 5.2: The Charge Scale obtained for Cosmic-Ray Data and Simulation.

Field	Data		Simulation	
	C_{data}	χ^2/ndof	$C_{\text{simulation}}$	χ^2/ndof
On	0.986 ± 0.003	1.3	1.003 ± 0.002	1.0
Off	0.957 ± 0.003	0.5	0.997 ± 0.003	2.7

the particle momentum, sensor thickness and the range of propagation distance used to determine the charge scale.

The dominant systematic uncertainties are the 2% uncertainty on the theoretical parametrisation and the 2.1% uncertainty on W. The uncertainty on W has two components: 0.5% for the variation between values determined by different experiments and 2% for uncertainties on the extrapolation to higher particle momenta. As the average sensor thickness has an uncertainty of 0.6 μm [85], it introduces a negligible systematic uncertainty of 0.2%.

The amount of charge deposited depends on the momentum of the particle [32]. The charge scale is not measured in bins of momentum and angle due to low statistics. Therefore, a momentum cut of 5 GeV is applied to limit the bias from the momentum dependence, and a 1% uncertainty is assigned to account for any remaining momentum bias. This uncertainty was obtained from Table 5.3, which lists the results in three momentum bins. A variation of ~1% on C is observed between the different momentum bins. As no momentum measurement is available for the field off data, the difference between C with no momentum cut and one with $p > 5$ GeV (0.5%) is assigned as an additional systematic uncertainty for the field off data. As the track momentum spectrum differs between simulation and data, the simulation was reweighted to reproduce the data. This results in a 0.2% variation in the charge scale.

Table 5.3: The scale factor for the MPV for different momentum ranges. Results are shown for both the data and simulation for field on only.

Cut	Data		Simulation	
	C_{data}	χ^2/ndof	$C_{\text{simulation}}$	χ^2/ndof
No Cut	0.981 ± 0.002	1.4	1.000 ± 0.002	0.9
$p > 5$	0.986 ± 0.003	1.3	1.003 ± 0.002	1.0
$5 < p < 10$	0.976 ± 0.005	1.1	0.991 ± 0.004	1.4
$10 < p < 20$	0.988 ± 0.004	1.5	1.004 ± 0.004	1.5
$20 < p < 50$	0.987 ± 0.005	0.5	1.008 ± 0.004	1.2

Finally, systematic uncertainties on the overall charge scale were assigned. The uncertainty due to the angular range used in the fit was estimated by excluding points at the edge of the fit range. The variation was found to be 0.2% (0.5%) for field on (off). The bias due to possible charge lost in a second pixel in the long pixel direction was found to be at the sub-percent level.

Table 5.4 summarises the different systematic uncertainties, which are added together in quadrature. The total systematic uncertainty is $3 - 4\%$. The charge scale for field on data is measured to be 0.99 ± 0.03, which is consistent with unity within uncertainties. The error is dominated by systematic uncertainties. The charge scale is measured to be 3% lower for data taken with the magnetic field off than with the magnetic field on.

Table 5.4: Systematic uncertainties for the measurement of the charge scale.

Systematic uncertainty	Field On	Field Off
Theoretical	2%	
W	2.1%	
Sensor Thickness	0.2%	
p-Dependence	1%	1.1 %
Range	0.2 %	0.5 %
Total	3.1%	3.1%

Chapter 6

Track Reconstruction and Performance of the ATLAS Inner Detector

6.1 Track Parametrisation and Reconstruction

The reconstruction of the trajectories of charged particles, or tracks, is a fundamental component of event reconstruction in high-energy physics experiments. Track reconstruction algorithms have two stages: the process of finding track candidates, the *pattern recognition*, and the estimation of the parameters to describe the particle trajectory, the *track fitting*. Both require a detailed and accurate description of the detector and a parametrisation to describe the charged particle trajectories.

A charged particle traversing through the detector deposits energy through ionisation in sensitive detector elements, which are read out by the electronics to form *hits*. The aim of the pattern recognition is to identify the collection of hits corresponding to a single particle. Hits from other charged particles or detector noise, called *fake hits*, need to be avoided because they decrease the measurement accuracy. The hit collection is processed by the track fitting algorithms to estimate the parameters that describe the trajectory of the particle. Fake hits can be eliminated or flagged during the track fitting if they contribute disproportionately to the fit quality, typically the χ^2. Expected hits on tracks, which are not found, are referred to as *holes*[1].

---

[1] Holes are estimated by following the track trajectory and comparing the hits on a track with the modules that the track passes through. Inactive modules or channels such as edge areas on the silicon sensors are not counted as holes.

The quality of a track reconstruction algorithm can be judged by two criteria: what fraction of tracks are reconstructed, the *track reconstruction efficiency*, and how well the track parameters represent those of the charged particle, the *track parameter resolution*. The two criteria are not fully independent because, for example, hits misassociated during the pattern recognition process will decrease the quality of the measurement of the track parameters.

The track reconstruction algorithms used by ATLAS are collectively referred to as New Tracking or NEWT [65]. NEWT includes a number of configurable algorithms, which are run sequentially to reconstruct tracks as efficiently as possible. The primary sequence is known as the *inside-out* sequence, which reconstructs tracks from the centre of the detector outwards.

The different stages of the pattern recognition of the inside-out track reconstruction sequence are illustrated in Fig. 6.1. The inside-out sequence of NEWT begins with seed finding from groups of three space points[2] in the silicon layers. The seeds are then used to build roads to find hits while moving towards the outer edge of the silicon detector. Hits can be attached to multiple track candidates. The ambiguity solver rejects poor track candidates until the hits are only attached to the most promising track candidates. The silicon track candidate is fit and an extension to the TRT is probed. Finally, a track fit is performed to provide the final estimate of the track parameters.

A charged particle in a uniform magnetic field follows an approximately helical trajectory[3], which can be parametrised by a set of five parameters with two of the parameters using a non-trivial sign convention. The following parameters (see Fig. 6.2) in the helical representation are used:

$$\tau = (d_0, z_0, \phi_0, \cot\theta, q/p_T) \tag{6.1}$$

where

- The transverse impact parameter, d_0, is the distance of closest approach of the trajectory to the reference point in the $x - y$ plane.

- The longitudinal impact parameter, z_0, is the z coordinate of the track at the point of closest approach.

- The angle, ϕ_0, is the azimuthal angle between the track and the tangent at the point of closest

---

[2] Space points are built from a single pixel hit or two SCT hits as discussed in Section 6.2.1

[3] The assumption of a perfect helical track model ignores effects from multiple scattering and energy loss, which depend on the particle's energy and the amount of material the particle has traversed. These effects are taken into account in the track fit and the propagation of the track parameters.

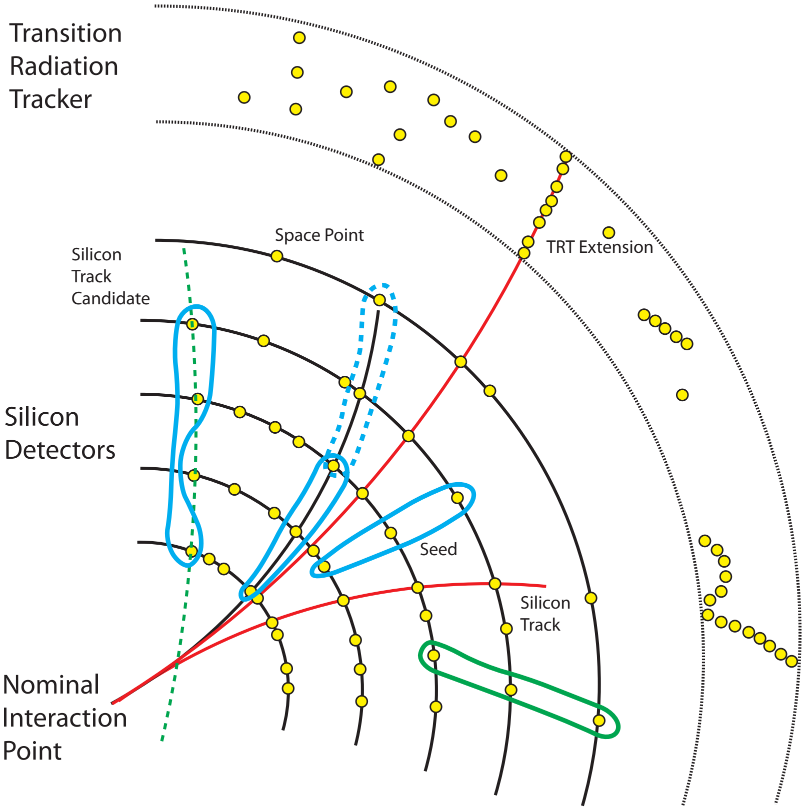

Figure 6.1: Illustration of the stages of the track pattern recognition in a simplified model of the Inner Detector. The space points are shown in yellow. The seeds reconstructed from combinations of space points are indicated in blue. The dashed blue seed illustrates a case where two seeds correspond to the trajectory of the same charged particle. The green seed is rejected by the requirement that the seed be consistent with a particle from the nominal interaction point. The track candidates are shown with lines. The green dashed track candidate is rejected because it is inconsistent with the nominal interaction point. The red track candidate is a fully reconstructed silicon track with no TRT extension. A track reconstructed using information from all three subdetectors is shown in black.

approach.

- The polar angle, θ is the angle the track makes in the $r - z$ plane. It can be transformed into the pseudorapidity with $\eta = -\ln\tan\theta/2$.
- The curvature, q/p, is the inverse of the momentum with the sign determined by the charge of the particle.

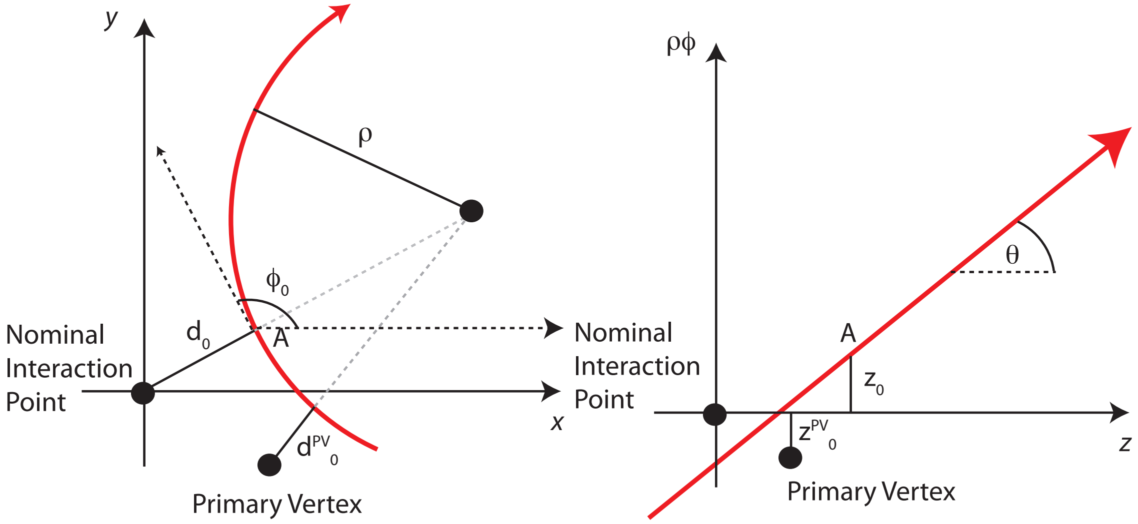

(a) Transverse Projection

(b) Longitudinal Projection

Figure 6.2: The five track parameters projected into the transverse (a) and longitudinal (b) plane.

The sign of the transverse impact parameter is determined by the following convention from [18]:

$$\operatorname{sign}(d_0) = \operatorname{sign}((\vec{p} \times \hat{z}) \cdot \vec{d}) \tag{6.2}$$

where $\vec{d}$ is a vector from the reference point to the point of closest approach, $\hat{z}$ is unit vector in the direction of the positive z-axis and $\vec{p}$ is the momentum estimate.

The impact parameters can be calculated with respect to any appropriate reference point. Three commonly used references points are the nominal interaction point, $(0, 0, 0)$, in the ATLAS coordinate system (d_0, z_0), the reconstructed primary vertex (d_0^{PV},z_0^{PV}) or the beam spot (d_0^{BS}, z_0^{BS}). The beam spot is calculated by averaging the reconstructed primary vertex over a short data-taking period.

The resolution of a track parameter is defined as the difference between the parameter of the reconstructed track and the true primary particle. Excellent momentum and vertex resolution are needed for many physics measurement. The resolution of both primary and secondary vertices is determined by the resolution of the impact parameters. The transverse impact parameter distribution is often used in track selection because it provides a powerful handle to separate primaries from secondary particles.

The detector description refers to the accuracy with which the simulation describes the location and properties of each element of the detector. The two most important ingredients are the alignment, the level to which the location of each element is known, and accuracy with which the simulation describes the material in the detector. Other important aspects of the detector description are the location of inactive detector elements and the location of the interaction, which determines from where the tracks originate (see Appendix B.2 and B.3).

Many studies based on Monte Carlo (MC) simulation have been used to optimise the different components of the track reconstruction sequence. The performance of the track reconstruction algorithms in data has previously been validated using test beam [66] and cosmic-ray commissioning runs [128]. This chapter discusses selected aspects of the performance of the NEWT reconstruction algorithms in data and simulation. The performance of the stages of the pattern recognition algorithms from seed finding to the track extension into the TRT is discussed in Section 6.2 (also in [123]). Section 6.3 compares the final track parameters in data and simulation (also in [125]). Finally, Section 6.4 discusses a technique used to study the material budget of the ID.

For all studies, the simulation samples were corrected to reproduce the detector and beam conditions present during data taking as closely as possible. The most significant corrections included

- reweighting or filtering the events to reproduce the longitudinal beamspot position measured during data taking, see Appendix B.2
- removal of hits from inactive silicon modules in the digitisation step, see Appendix B.3

Sections 6.3 and 6.4 use data from collisions at a centre of mass energy of $\sqrt{s} = 900$ GeV, while Section 6.2 uses data from $\sqrt{s} = 7$ TeV. However, the centre of mass energy of the collision is not particularly important because the focus is on track-level comparison between data and simulation. It is only the multiplicity and transverse momentum distributions that are significantly changed by the centre of mass energy. A sufficiently dense collision environment does affect the pattern recognition efficiency. However, the increase in the track density between $\sqrt{s} = 900$ GeV and $\sqrt{s} = 7$ TeV is not large enough for this to be a significant effect at the initial luminosities after the startup of the LHC.

6.2 Track Reconstruction Algorithms

This section studies the performance of the pattern recognition by comparing distributions between data and simulation at each step in track recognition. It discusses the properties of the seeds, the discrimination between track candidates within the ambiguity solver and the efficiency with which tracks are extended into the TRT.

6.2.1 Track Seeding in the Silicon Detector

The first step in track reconstruction is the creation of three-dimensional space points from the silicon hits. Pixel clusters provide local two-dimensional positions on a module surface at a known radius and therefore transform directly into space points. On the contrary, SCT clusters do not transform directly into space points because a single strip provides a precise measurement in only one direction. Instead, space points are formed by combining the information from pairs of clusters from a SCT module.

Track seeds are built from these space points. Seeds are groups of three space points with each space point in a unique layer of the silicon detector. The number of space points required to form a seed is configurable; the default of three maximises the number of possible combinations and provides sufficient information for a momentum estimate. A minimum distance between space points in a seed is required to exclude seeds containing multiple space points in the same detector layer.

Crude requirements are imposed on the seeds within the pattern recognition to limit the combinations and to optimise the execution speed. These cuts include requirements on the impact parameter and the transverse momentum. Figure 6.3(a) compares the number of seeds reconstructed in each event in data and simulation. The seed multiplicity does not agree, nor was it expected to because only the non-diffractive simulation sample was used and the underlying particle multiplicities differ [4]. The noise level in the pixel detector was significantly overestimated in the simulation samples, which can be expected to result in additional seeds. A track seed is a collection of space points and does not provide a parameterisation of track parameters. Therefore a crude estimate of the perigee parameters was made by assuming a perfect helical track model in a constant magnetic field (see Appendix B.1).

In addition to the multiplicity, the p_T spectrum (Fig. 6.3(b)) differs between data and simulation resulting in apparent differences in the properties of other track parameters. To correct for this, the p_T distribution of the seeds in the simulation was reweighted to the p_T spectrum of the seeds in data.

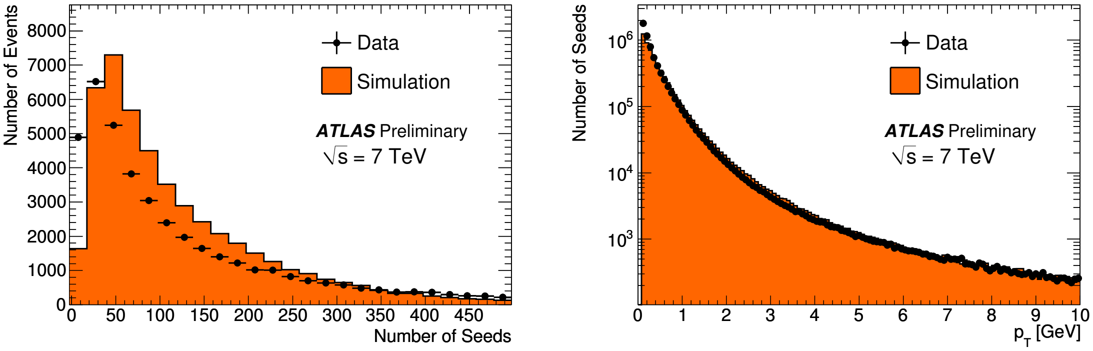

(a) Seed Multiplicity

(b) p_T spectrum

Figure 6.3: Number of track seeds per event in data and simulation (a), normalised to the same number of events. Transverse momentum distribution of all track seeds in data and simulation before reweighting (b), normalised to the same number of seeds.

The seed impact parameter distributions cannot be calculated with respect to the primary vertex because, at this stage of the pattern recognition tracks have not yet been formed, which means that primary vertex reconstruction have not yet been executed. Therefore the beam spot was used as the reference point for the trajectory representation. Figure 6.4 compares the seed transverse impact parameter distribution as a function of the azimuthal angle in data, when the parameters are expressed with respect to either the nominal interaction point or the beam spot. The sinusoidal dependence of d_0 with respect to ϕ is due to the displacement of the beam spot from the origin in the $x - y$ plane (Fig. 6.4 (a)). The overlap regions between the modules on the 22 carbon fibre staves of the innermost layer of the pixel detector are visible in Fig. 6.4 (b) demonstrating the good d_0 resolution of the seeds.

6.2.1.1 Properties of Seeds in Data and Simulation

A seed consists of groups of three space points in the silicon detector. The properties of the seed depend on the location of the individual space points from which the seed has been reconstructed.

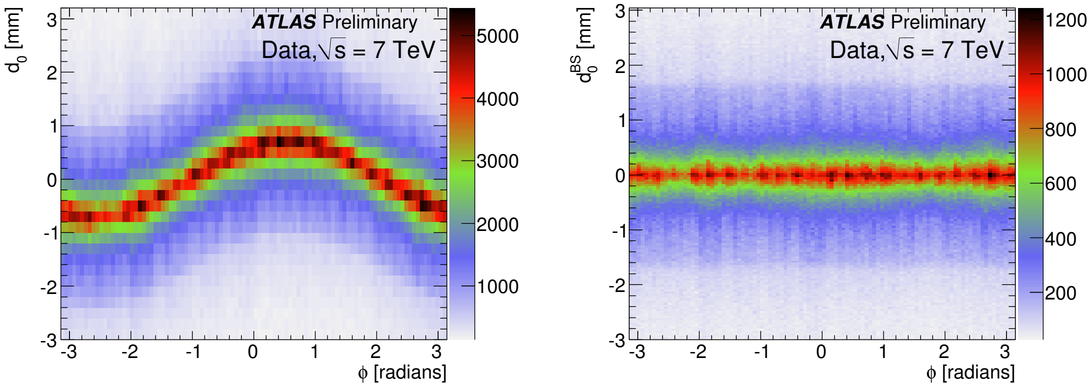

(a) With respect to the Nominal Interaction Point

(b) With respect to the Beam Spot

Figure 6.4: The transverse impact parameter of the seeds as a function of the azimuthal angle in data.

Figure 6.5 compares the position of each space point contributing to a track seed in data (points) and simulation (histogram). Figure 6.5(a) compares the total distance of all space points throughout the detector from the origin, while Fig. 6.5(b) compares the radial distribution for the seeds in the barrel. Data and simulation are observed to be in good agreement for both distributions. The layers of the pixel detector and the SCT are clearly visible in the radial distribution.

Figure 6.6 compares the transverse and longitudinal impact parameters with respect to the beam spot of the seeds in simulation and data. As expected, the width of the transverse impact parameter distribution is smaller than that of the longitudinal impact parameter due to the narrower beam spot width in the transverse plane. The discontinuity in the d_0 distribution, well described by the simulation, is caused by cuts applied in the seed-finding algorithm that depend on the transverse momentum. A discrepancy is observed in the tails of the d_0 distribution.

The angular distributions of seeds in simulation after reweighting the p_T spectrum is compared to data in Fig. 6.7. The increase in the number of seeds for $\eta > 2$ in Fig. 6.7 (a) is due to the number of possible combinations of hits due to the number of layers in the end cap. The small excess of seeds at central pseudorapidity is due to the contribution from looping particles (see Section 6.2.2). The shape of the distribution of the azimuthal angle is dominated by the location of disabled modules in the pixel detector, which is correctly described in the simulation as shown in Fig. 6.7 (b).

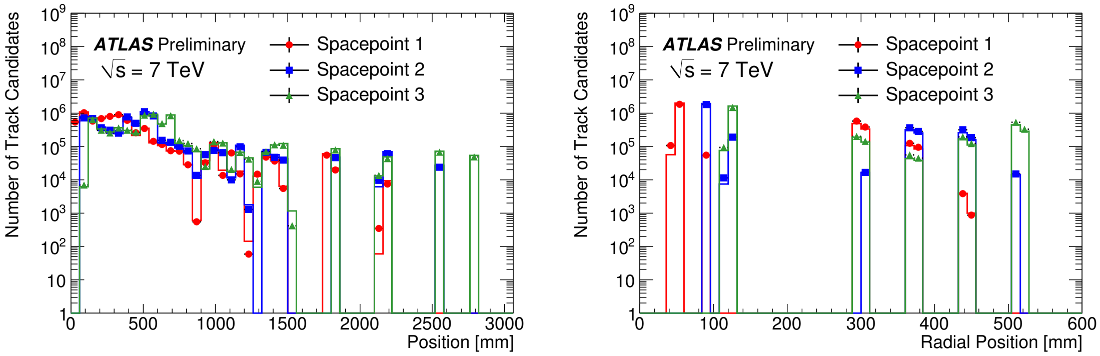

(a) Full Detector

(b) Barrel

Figure 6.5: Distance of each of the three space points in all seeds from the origin for the full detector (a) and the radial distribution of each of the three space points in track seeds in the barrel region (b). The space points in data are shown using markers and the simulation using a histogram. The p_T spectrum of the simulation has been reweighted to agree with the measured p_T distribution for data. The distributions are normalised to the same number of seeds.

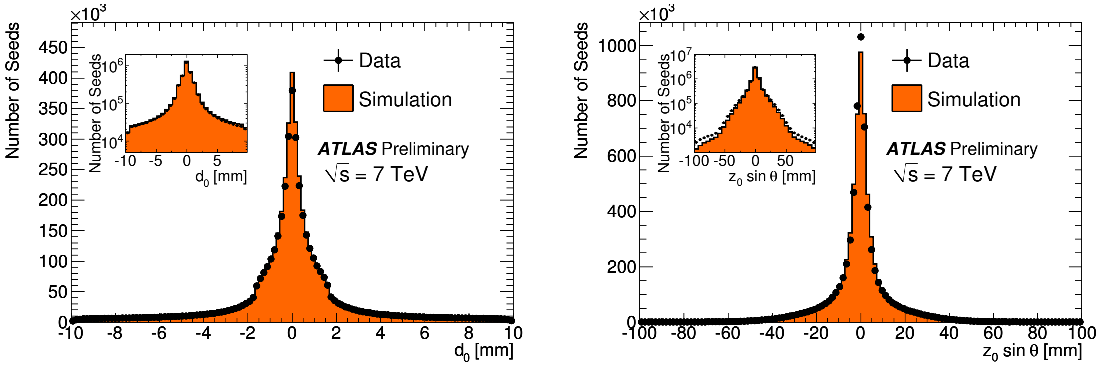

(a) Transverse Impact Parameter

(b) Longitudinal Impact Parameter

Figure 6.6: The impact parameter distributions of the seeds in data and simulation. The p_T spectrum of the simulation has been reweighted to agree with that for data. The distributions are normalised to the same number of seeds.

6.2.1.2 Seed Survival

A window search is applied in the seed propagation direction to build a track candidate. Any hits within the road window are collected and track candidates are built using a combinatorial Kalman

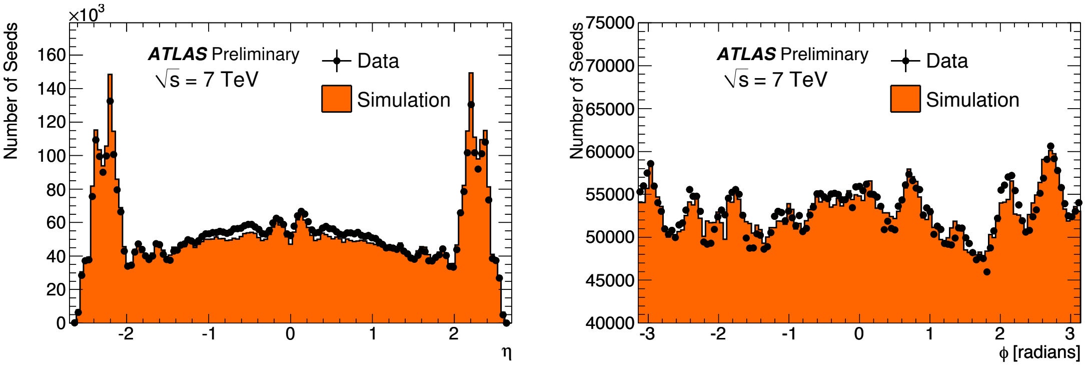

(a) Pseudorapidity

(b) Azimuthal Angle

Figure 6.7: The pseudorapidity and azimuthal angle distributions of the seeds in data and simulation. The p_T spectrum of the simulation has been reweighted to agree with that in the data. The distributions are normalised to the same number of seeds.

filter [106]. Seeds can fail to become track candidates for different reasons. If all clusters in a seed have already been associated with a track candidate or if the road search fails to find sufficient hits to meet the track candidate hit requirements, the seed is discarded.

Each seed can become at most a single track candidate. This will be referred to as *survival* of the seed. Seed survival is only possible if the track candidate found through a window search meets certain configurable quality requirements. Seeds for which all clusters have already been used to build a track candidate are rejected. The rate of seed survival as a function of the pseudorapidity (a) and p_T (b) is shown in Fig. 6.8. Approximately 35% of the seeds in the data and 38% of the seeds in the simulation become track candidates. One possible reason for the discrepancy in the survival rate could be differences in the noise between data and simulation. A significantly higher noise rate would result in more seeds, but these should be rejected by the ambiguity solver. The purpose of a staged pattern recognition chain is to achieve a dynamic system, where the survival rate is convoluted with the multiplicity of seeds per track candidate. Figure 6.9 shows the η distribution of surviving seeds in both data and simulation. The discrepancies shown in the pseudorapidity distribution of all seeds in Fig. 6.7(a) has almost entirely disappeared.

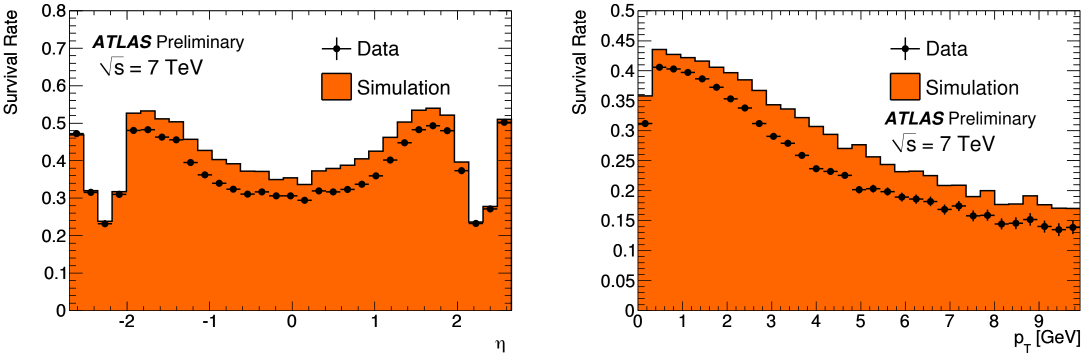

(a) Pseudorapidity (b) Transverse Momentum

Figure 6.8: The fraction of seeds which become track candidates as a function of η and p_T . The seed p_T spectrum of the simulation has been reweighted to agree with that in the data.

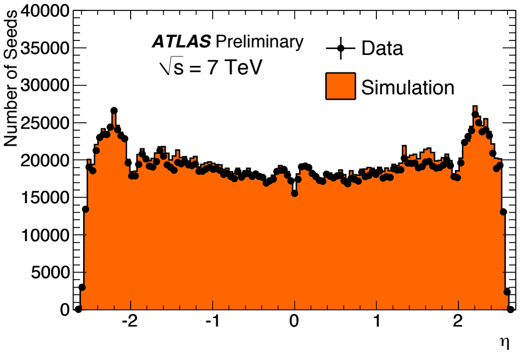

Figure 6.9: The pseudorapidity distribution of the surviving seeds. The distributions are normalised to the same number of surviving seeds.

6.2.1.3 Seed Resolution

The seed finding algorithms were modified to access truth level information from the detector simulation. Therefore, the generated particle that deposited charge in the cluster associated to the space point could be identified. This allows a seed to be associated to a generated particle. More than one particle can contribute to a single cluster and hence to a space point. All such particles were identified and the leading particle was defined as the one that contributed to the maximum number of clusters in a seed. Figure 6.10 shows the track parameter resolutions of track seeds that were matched to generated particles in comparison to the final track resolutions. The resolutions depend on the particle composition and momentum spectrum. The momentum and d_0 resolutions of track seeds are approximately a factor of three worse than the final tracks. In addition, a clear bias in the mean of the momentum estimate is observed for track seeds. This is due to the fact that energy loss corrections have not been applied to track seeds. The azimuthal resolution of track seeds is the parameter closest to the final track resolution. The estimation of the pseudorapidity is poor because it is crudely estimated from the average η of the three space points.

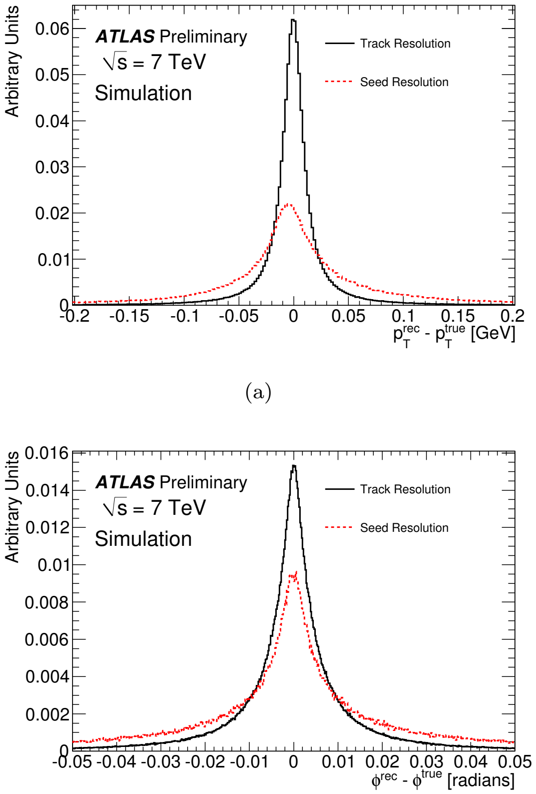

(a)

(b)

(c)

(d)

Figure 6.10: The resolution of the seed parameters in comparison to the final track resolutions in simulation. The distributions are normalised to unit area.

6.2.2 Ambiguity Solving of Track Candidates

The concept of ambiguity solving in track reconstruction was first introduced in the era of the LEP experiments [135]. It incorporates a staged pattern recognition approach: a very loose track candidate search, which allows for a huge number of combinatorial track candidates is followed by a stringent ambiguity processor that compares and rates the individual tracks by assigning a relative track score to each track. The track candidates entering the ambiguity solver contain a small fraction of candidates which are purely combinatorial collections of hits. The track candidates compete against each other for the highest score and for the hits that are shared between them.

The track scoring follows a robust approach based on simple measures of the track quality. Hits assigned to a track increase the track score according to the weight fraction for the different sub-detectors, while holes penalise the track by reducing its score. The weight fractions respect the intrinsic resolutions and potential hit multiplicities in the different sub-detectors. Finally, the χ^2 contribution from the track fit is taken into account in the final track score. Track candidates can be merged within the ambiguity solving to favour complete track segments over incomplete track segments or purely random hit combinations.

The distribution of the track score for accepted and rejected candidates is compared in Fig. 6.11 for data and simulation. The peaks in the distribution reflect the scores assigned to tracks containing different numbers of hits. The distribution of the accepted and rejected tracks is generally well-modelled by the simulation, however the dips in the simulation of the rejected candidates are slightly more pronounced. Figure 6.12 shows the dependence of the track score on p_T in data and simulation. The bands are due to the fact that the score contains a factor depending on the logarithm of the transverse momentum. Therefore, if two track candidates have been reconstructed with comparable hit content, the track with the higher transverse momentum is favoured by the ambiguity solver.

There are two stages at which tracks can be rejected in the ambiguity solver:

- **initial stage:** tracks are excluded before track scoring in the ambiguity solver when certain minimal criteria are not met. These include a predefined minimal momentum cut or simple hit requirements. For example, tracks with holes in both the pixel detector and the SCT are rejected. Tracks rejected by the ambiguity solver at this stage are assigned a score of zero.
- **scoring stage:** tracks do not pass the ambiguity solving stage when they are too low in the

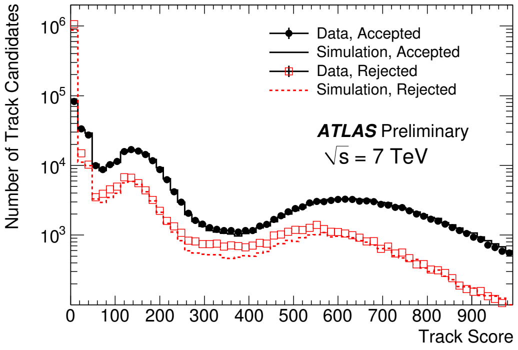

Figure 6.11: Track score in the ambiguity solver for accepted and rejected tracks. The distributions are normalised to the same number of track candidates.

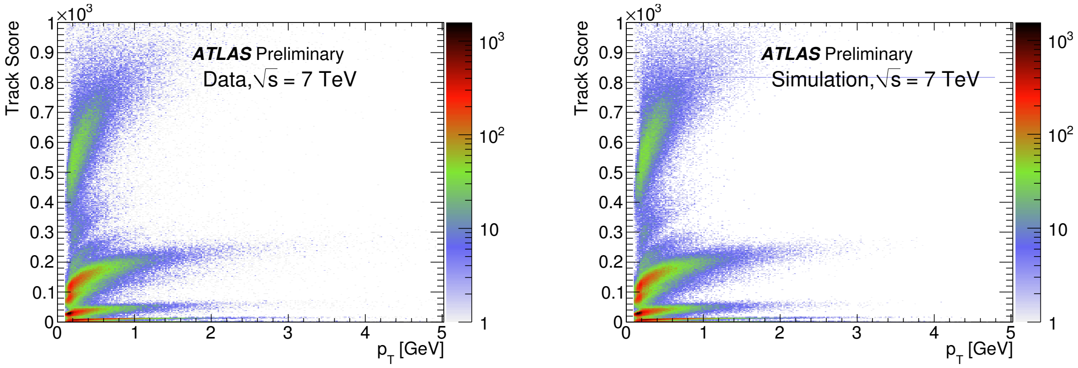

(a) Data

(b) Simulation

Figure 6.12: The track candidate score used in the ambiguity solving as a function of the transverse momentum.

relative track scoring hierarchy or are merged with other track candidates.

In rare cases a failed track fit may also result in a rejection of the track candidate. Figure 6.13 shows the number of track candidates as a function of η at different stages of the ambiguity processing for tracks with $p_T > 100$ MeV and $p_T > 500$ MeV. The distribution are normalised such that the numbers of accepted track candidates are equal in data and MC. The shape of each distribution agrees reasonably well between data and simulation, but the fraction of track candidates rejected because they obtained a score of zero is significantly higher in data than simulation, for tracks with

$100 < p_T < 500$ MeV. For tracks with $p_T > 500$ MeV, the level of agreement between simulation and data improves noticeably.

A distinctive feature of the distributions in Fig. 6.13 (a) is the peak at central pseudorapidity, which is most pronounced for track candidates rejected in the initial stage. This topology is present in both data and simulation and only occurs for tracks with lower transverse momentum. This has been identified to be due to particles with momentum low enough such that they loop around the silicon detector multiple times before exiting, in the following referred to as *loopers*. Track segments from loopers with central pseudorapidity values are more likely to survive the initial cuts in the pattern recognition. In particular, a requirement of a maximal longitudinal impact parameter z_0 suppresses loopers at forward pseudorapidity. Figure 6.14 shows the number of track candidates which correspond to the same primary particle as a function of η (a) and p_T (b) in simulation. At central values of η there are significantly more duplicate track candidates, in the same region where the peak is observed. Most of the duplicates have low values of transverse momentum.

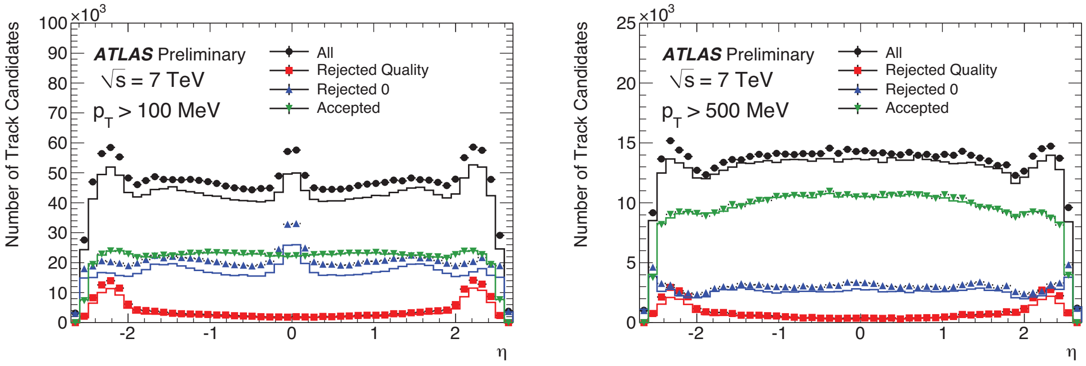

(a) $p_T > 100$ MeV

(b) $p_T > 500$ MeV

Figure 6.13: Number of track candidates as a function of η entering the ambiguity solver (black), rejected because they are assigned a track score of zero (blue), rejected because of quality cuts (red) and accepted as resolved tracks (green) in the different stages inside the ambiguity solver in data and simulation. The number of track candidates in data are shown as markers and the simulation as histograms. The p_T distribution of the accepted track candidates in the simulation have been reweighted and normalised to the accepted track candidates in the data.

Figure 6.15 (a) shows that the transverse momentum spectrum of track candidates accepted by the ambiguity solver is significantly harder in simulation than in data. The number of candidates per

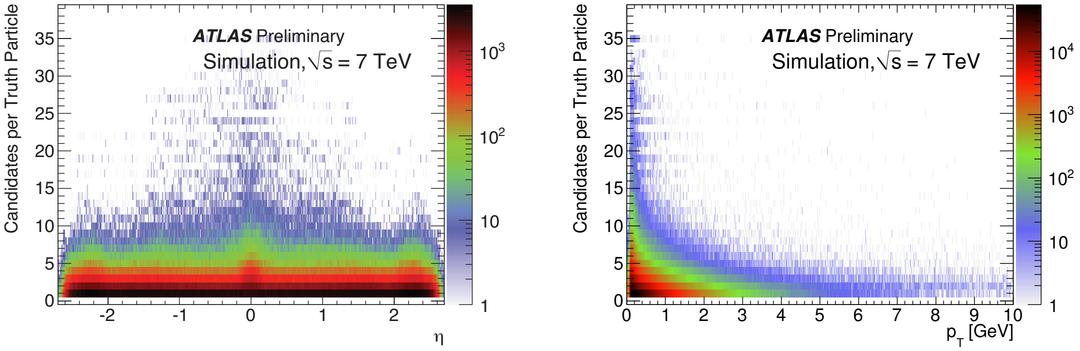

(a)

(b)

Figure 6.14: The number of duplicate track candidates for a single primary particle in simulation as a function of η (a) and p_T (b)

event for simulation and data is compared in Fig. 6.15 (b). The multiplicity is significantly lower in data than in simulation, which reflects the differences in the multiplicity of the underlying samples. The η and ϕ distribution of the accepted candidates, after the p_T spectrum has been reweighted to agree between data and simulation, are compared in Fig. 6.16. After reweighting, the simulation describes the η distribution of the track candidates extremely well. The small discrepancies in the number of track candidates as a function of ϕ (Fig. 6.16 (b)) are due to differences in the lateral beam spot position and non-operational elements of the detector.

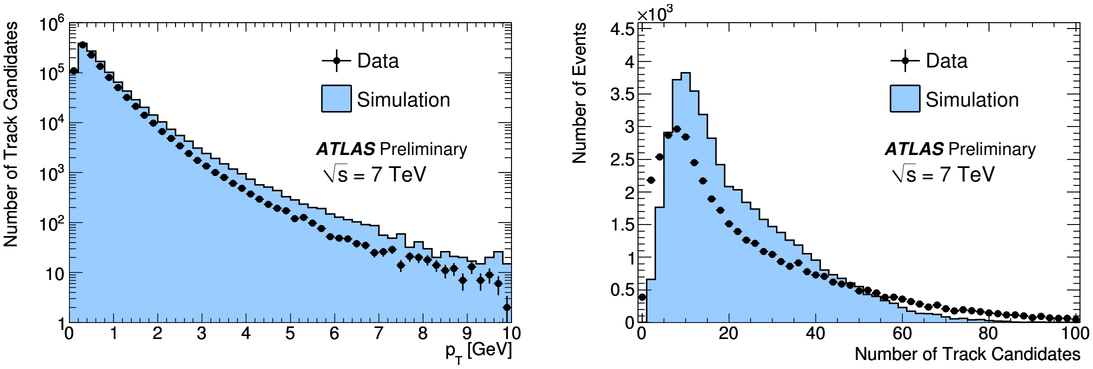

(a)

(b)

Figure 6.15: The transverse momentum distribution of the track candidates accepted by the ambiguity solver (a), normalised to the number of accepted track candidates. The number of track candidates per event accepted by the ambiguity solver algorithm (b). The p_T spectrum for simulated data has been reweighted to the data and the distribution was normalised to the same number of events.

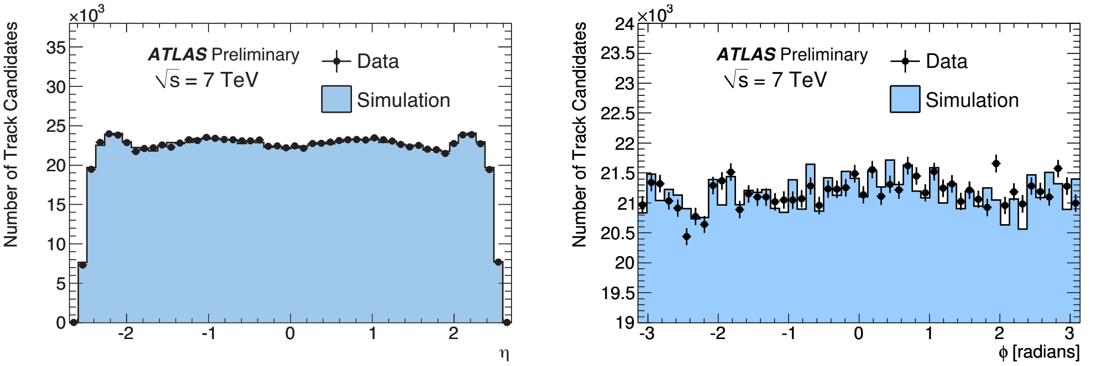

(a)

(b)

Figure 6.16: The number of tracks accepted by the ambiguity solver as a function of η and ϕ. The simulation has been reweighted to the p_T spectrum of the data and normalised by the number of tracks.

6.2.3 Track Extension into the TRT

The final step in the pattern recognition is to probe the TRT for a possible extension. TRT hits are found by following the propagation direction of the track reconstructed using information from the silicon detectors. The TRT extension is performed in two steps to find all possible extensions, which are then resolved by an ambiguity processor. A TRT segment is required to have at least 15 hits to be considered a successful extension.

Figure 6.17 compares the TRT efficiency obtained in data and simulation. As the TRT detector only provides coverage within $|\eta| < 2.2$, the efficiency drops significantly for $|\eta| > 2.1$. The extension efficiency is also reduced around $\eta \approx 0$ where the glass connectors between the TRT barrel drift tubes are located. However, both these characteristics are well reproduced by the simulation.

The track parameters estimated before and after the extension into the TRT are compared in Fig. 6.18. The extension of a track into the TRT improves the transverse momentum estimate significantly due to the increase to the length of the track. However, the impact parameters do not change significantly, because the distance of these additional measurement points from the reference point, mean that they contribute little to the impact parameter resolution.

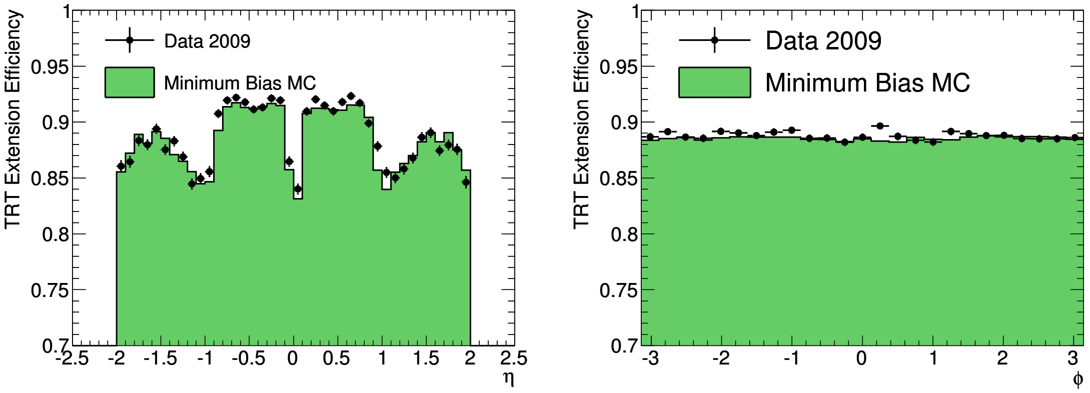

(a) η (b) ϕ

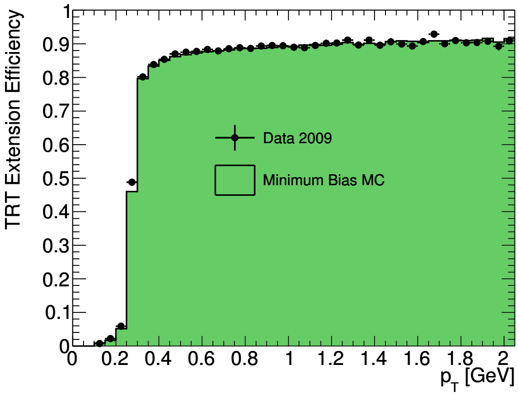

(c) p_T

Figure 6.17: The efficiency to attach a TRT segment to a silicon track as a function of the parameters of the track reconstruction in the silicon detectors in data (points) and simulation (histogram).

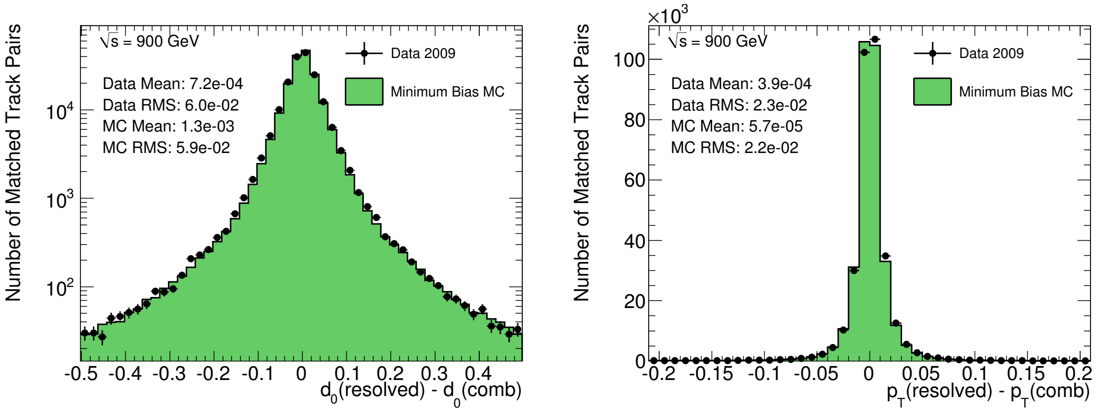

(a) η

(b) p_T

Figure 6.18: The difference in track parameters between tracks before and after the extension into the TRT in data (points) and simulation (histogram).

6.3 Performance of the Track Reconstruction Algorithms

The performance of the complete track reconstruction algorithms was studied by comparing the distributions of the final track parameters between data and simulation at $\sqrt{s} = 900$ GeV. The z-vertex distribution of the simulation was corrected to match the data.

6.3.1 Module and Hit Assignment Efficiencies

The number of assigned hits per track is a simple quantity to measure, however it is particularly sensitive to many details of how well the simulation describes the data. The efficiency for an individual silicon module to produce a hit when a charged particle passes through the sensor is close to 100%, however simulating the number of hits accurately relies on the description of inactive detector elements as discussed in Section B.3. The number of hits also depends on the level of accuracy of the description of the material in the simulation and the size and position of the beam spot.

Figure 6.19 shows the total number of Pixel and SCT hits per track for all inside-out tracks, while Fig. 6.20 illustrates the complementary distribution, the number of holes per track. The number of holes is an even more sensitive measure of the simulation quality. These are crucial ingredients of the pattern recognition and used to resolve ambiguities and favour high quality tracks over incomplete tracks. The description of the total number of holes is the same between data and simulation to the 10% level for the SCT and to the 20% level for the pixel detector.

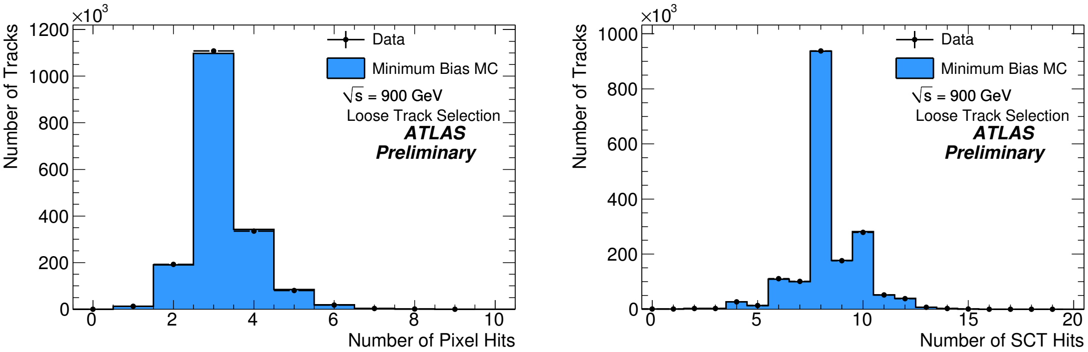

Figure 6.19: Number of Pixel and SCT hits on track for all inside-out tracks.

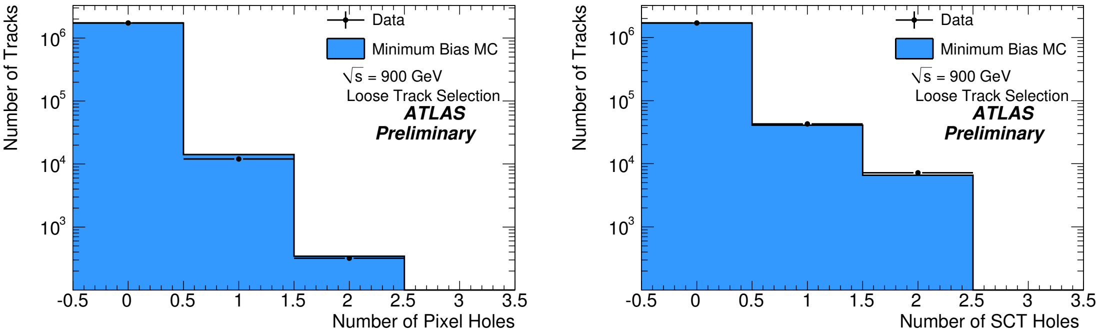

Figure 6.20: Number of Pixel and SCT holes on track for all inside-out tracks.

The degree of agreement between data and simulation in the total number of hits per track is excellent. Figure 6.21 and Fig. 6.22 shows the number of pixel and SCT hits per track as a function of pseudorapidity, η, and azimuthal angle, ϕ, at the primary vertex. The structure of the disks in the SCT end cap are reproduced by the simulation. The level of agreement also indicates that inactive modules are accounted for correctly in the reconstruction of the data and simulation. The remaining discrepancies are thought to arise from differences in the transverse position of the beam spot between simulation and data.

6.3.2 Impact Parameter Distributions

Figure 6.23 shows the d_0 distribution in linear and logarithmic scale. Here, no requirement on the impact parameters applied apart from the requirements within the pattern reconstruction. There is good agreement between simulation and data, in particular in the tail of the distribution. Remaining differences in the core distribution are thought to be due to remaining module misalignments in the data.

The longitudinal impact parameter z_0 is shown in Fig. 6.24. Similar to the transverse impact parameter, there is excellent agreement between data and simulation in the tails of the distribution, but discrepancies in the core. The longitudinal impact parameter is a less powerful variable to separate tracks from primary and secondary particles, but will become a very important measure for distinguishing between tracks from different pile-up vertices during future high luminosity conditions.

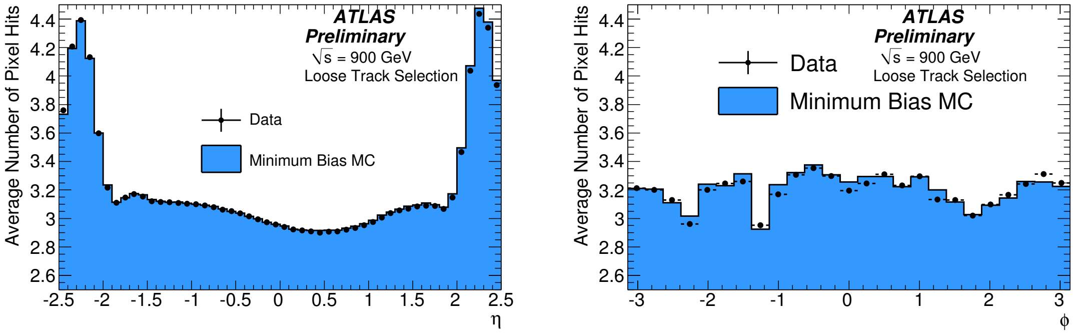

(a) As a function of η

(b) As a function of ϕ

Figure 6.21: Average number of pixel hits per selected track as a function of pseudorapidity and azimuthal angle of the track, respectively. The distributions are shown for both simulation and data. The structure is mainly influenced by the inactive pixel modules that have also been masked in the digitisation process of the simulation samples to reproduce the run conditions.

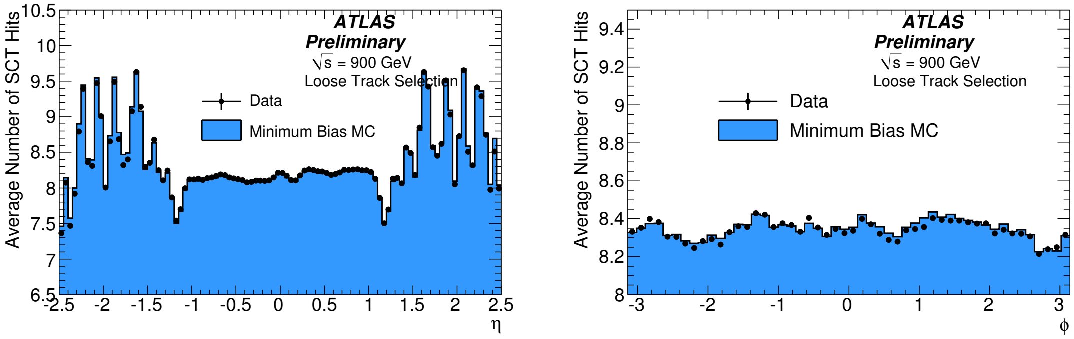

(a) As a function of η

(b) As a function of ϕ

Figure 6.22: Average number of SCT hits per selected track as a function of the pseudorapidity and azimuthal angle of the track, respectively.

The impact parameter resolution depends on the pseudorapidity of the particle. This is due to the strong η dependence of the amount of material inside the tracking detector and due to the increasing extrapolation distance from the first measurement to the primary vertex. Figure 6.25 shows the width of the transverse and longitudinal impact parameter distributions as a function

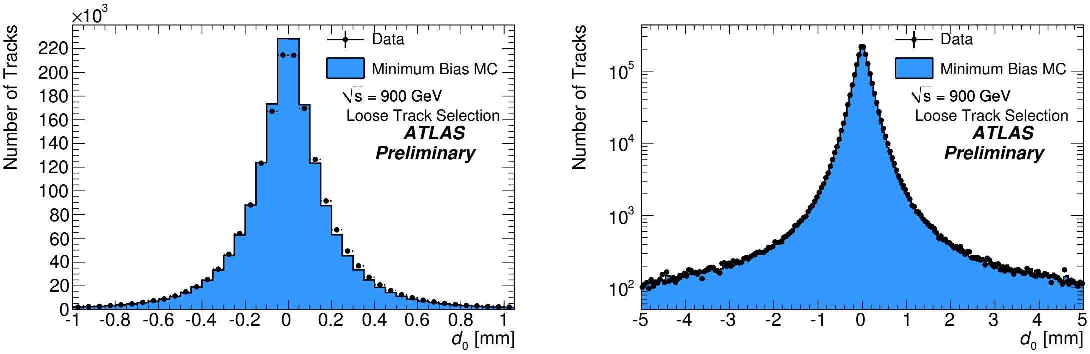

(a) linear scale (b) logarithmic scale

Figure 6.23: Transverse impact parameter distributions d_0 in Monte Carlo and data. The impact parameter is defined with respect to the reconstructed vertex.

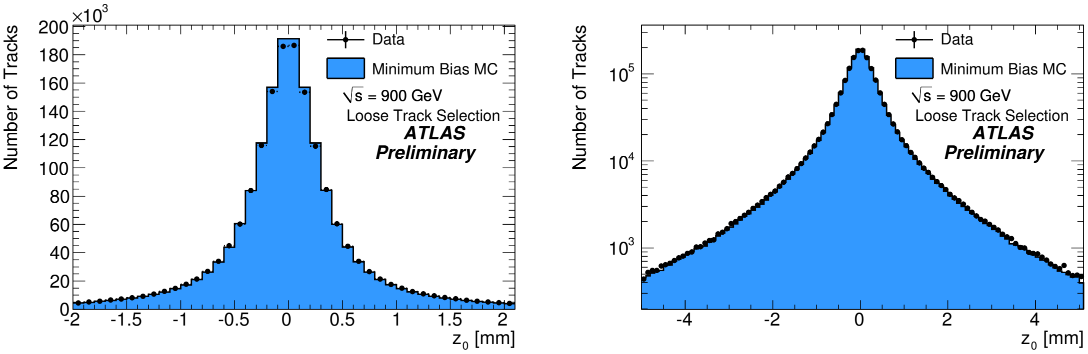

(a) linear scale (b) logarithmic scale

Figure 6.24: Longitudinal impact parameter distributions z_0 in Monte Carlo and data. The impact parameter is defined with respect to the reconstructed vertex.

of η for data and simulation. The width was calculated from the entries within 3σ of the mean for each impact parameter. Good agreement between data and simulation can again be observed, except for $-2.5 < \eta < -2.4$, where the width is larger in simulation than in data.

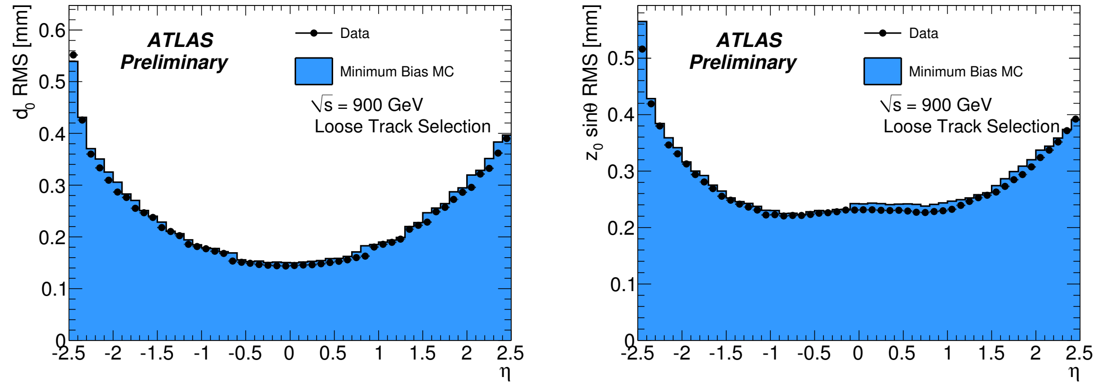

(a) d_0 RMS (b) $z_0 \cdot \sin\theta$ RMS

Figure 6.25: The RMS of the impact parameter distributions vs. η in Monte Carlo and data.

6.4 Using Tracks to Study the Material Budget of the Inner Detector

Silicon detectors provide extremely accurate measurements of the trajectories of charged particles. However, they typically contain many nuclear interaction lengths of material. This material is not only in the silicon sensors themselves, but also in areas such as the cooling system and the support structures. Almost every charged particle that passes through the silicon detector without undergoing a nuclear interaction is reconstructed and the probability of a nuclear interaction depends on the number of nuclear interaction lengths of material that the particle passes through. This means that the degree to which the reconstruction efficiency of a charged particle is known is determined by how well the material of the silicon detector is understood.

Many techniques can be used to obtain constraints on the amount of material in the Inner Detector. The most precise results will be obtained by studying the rate of conversions at each location in the detector. However, this technique requires significantly more data than was recorded at $\sqrt{s}$ = 900 GeV. Another technique studies the mass of the K_S as a function of its production position and the angle at which each of the two pions propagate [49]. This technique requires a smaller amount of data; however, the interpretation of the results in terms of the material budget is challenging. Finally, studies of the length of reconstructed tracks have been used to understand how well the material is modelled by the simulation. This study is discussed here and, in particular, how it was used to obtain constraints on the amount of material between the pixel detector and the SCT.

Figure 6.26 shows the estimated amount of material in radiation lengths in the components of the silicon detector as a function of the pseudorapidity. The material varies strongly with the pseudorapidity with the minimum in the central barrel for $|\eta| < 0.8$ and the largest amount of material around $|\eta| = 1.8$. The material in the services for the detector is shown in pink and this makes a significant contribution to the total material budget. Most of these services are located between the pixel detector and the SCT. In addition, the composition is less well known than other components of the detector. For these reasons, estimating how well this material is described by the simulation is particularly important. The technique described here studies the rate at which tracks reconstructed in the pixel detector, *pixel tracklets*, are extended into the SCT. A successful *SCT extension* occurs when a pixel tracklet is matched to a combined track. Therefore the SCT extension efficiency is calculated as follows:

$$\epsilon_{\text{SCT Ext}} = \frac{N_{pix}^{match}}{N_{pix}} \tag{6.3}$$

where N_{pix} is the number of pixel tracks and N_{pix}^{match} is the number of pixel tracks matched to a combined track.

The combined tracks are reconstructed using the inside-out algorithm with the standard settings. The pixel tracklets are also reconstructed with the inside-out algorithm, but with requirements on the number of hits and holes designed for tracks reconstructed in the pixel detector only. Track selection criteria are applied to the pixel tracklets only. The conclusions do not change, however, if quality cuts are placed on the combined tracks.

6.4.1 The SCT Extension Efficiency in Data and Simulation

The level to which the simulation describes the material between the pixel detector and the SCT can be estimated by the degree to which the SCT efficiency agrees between data and simulation.

The efficiency is measured using a specific criteria to make an association between pixel tracklets and combined tracks. Two different criteria were used. The first required a certain number of hits to be common to the pixel tracklet and the combined track. The second matched the pixel tracklet

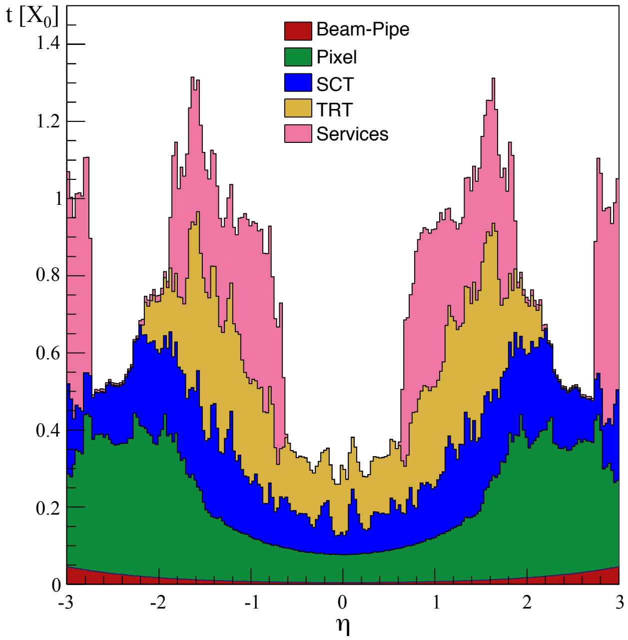

Figure 6.26: Simulation of the material in the different components of the Inner Detector in radiation lengths (X_0) using information from the construction of the detectors.

to the closest combined track in a cone of radius, $\Delta R = \sqrt{\Delta\eta^2 + \Delta\phi^2}$. The number of common hits and the maximum separation distance between the tracks required for a successful match was varied. It was found the numerical value of the efficiency varied with the different requirements, however the level of agreement between data and simulation was unchanged. Therefore, the matching criteria used required a single common hit, to obtain the highest possible efficiency and to avoid bias to the track parameters from the matching.

Figure 6.27 compares the SCT extension efficiency in data and simulation as a function of the track parameters of the pixel tracklets. In many regions the agreement between the two is excellent. The most notable discrepancy, however, is that at high values of pseudorapidity the efficiency is significantly lower in the data than in the simulation. This occurs in two regions: around $|\eta| = 2$ and more dramatically for $2.2 < |\eta| < 2.5$ and is in marked contrast to the excellent agreement in the central barrel region. These localised inefficiencies mean that the overall efficiency in data is lower than in simulation when shown as a function of other track parameters.

Other features that are not fully reproduced by the simulation include inefficiencies at specific values of ϕ (Fig. 6.27(b)) and the slope of the efficiency in the region in which it varies significantly (Fig. 6.27(c)). The latter could provide evidence that the momentum resolution of either the pixel tracklets or the combined tracks is worse in data than in simulation. The lower efficiency in data for tracks, which contain a larger number of pixel hits (Fig. 6.27(d)), is closely related to the discrepancies at high η. Tracks reconstructed with these pseudorapidity values pass through more layers of the pixel detector, because they pass through part of the barrel and the end caps. This means that pixel tracklets, which contain larger number of pixel hits are essentially only found in the forward region.

The track parameters of each pair of matched tracks can be compared to evaluate the effectiveness of the match and the relative quality of the two track collections. The variable shown in Fig. 6.28 is the difference between the track parameter value for the combined track and the pixel tracklet. Most features of these distributions are well-described by the simulation and, in particular, the longitudinal track parameter $\Delta\eta$. The mean and width of each distribution in data and simulation is indicated, which highlights that some of the distributions such as $\Delta\phi$ distribution do not have a central value of zero. This indicates a bias in these track parameters for at least one of the track collections. Despite these small but interesting features noted, these distributions show that the matching procedure is matching tracks with very similar track parameters and that the track parameter resolution is modelled to a reasonable level by the simulation.

6.4.2 Sensitivity of the SCT Extension Efficiency to Material

The sensitivity of the SCT extension efficiency to additional material was calibrated using simulation samples. Two samples were produced in which the density of the material in the support structures in the pixel detector and the SCT had been artificially increased such that the total material in radiation lengths was increased by 10% or 20% respectively.

As the technical implementation of these samples involved changing the numerical value of the density of the material used to simulate the support structures, both corresponded to a significantly larger increase in material when measured in nuclear interaction lengths. Such samples are clearly unphysical, therefore these samples can only be used to obtain constraints on the material in terms of radiation lengths or nuclear interaction lengths, but never both at the same time. The amount of material in nuclear interaction lengths in these simulation samples is shown in Fig. 6.29 for both

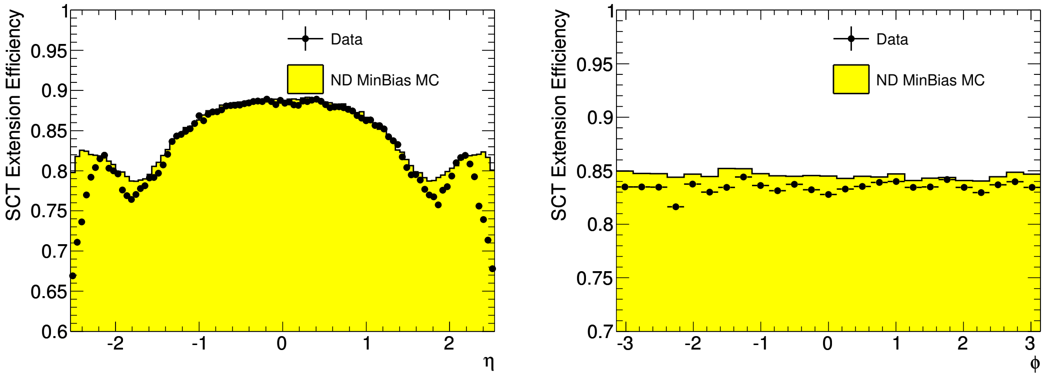

(a) η

(b) ϕ

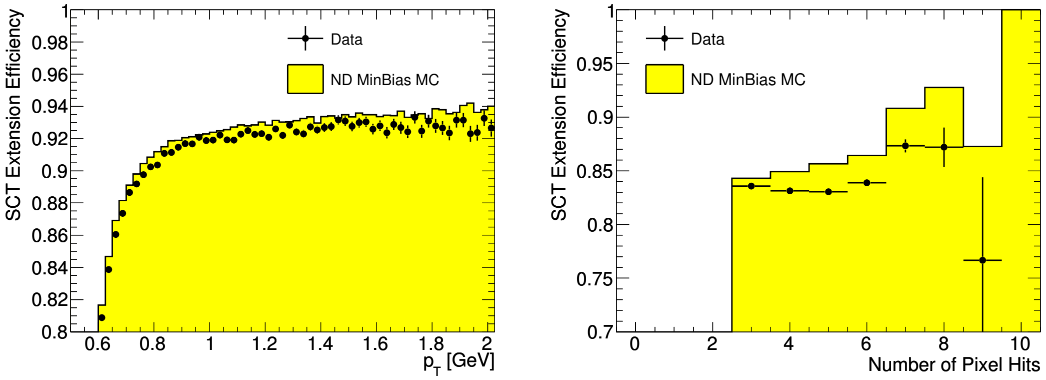

(c) p_T

(d) $N_{PixelHits}$

Figure 6.27: The SCT extension efficiency in data (markers) and simulation (filled yellow histogram) as a function of selected track parameters of the pixel tracklets.

the pixel volume and the SCT volume. This illustrates that the so-called 10% sample, actually corresponds more closely to a relative increase of 20% in the material in nuclear interaction lengths.

The SCT extension efficiency as a function of pseudorapidity obtained from the three samples with different amounts of material is compared in Fig. 6.30. The efficiency decreases uniformly with each uniform increase in material. However, despite the large increase in the material in nuclear interaction lengths: $\sim 40\%$ for the 20% sample, the efficiency has only decreased by approximately 2%. This is because these samples do not include additional material between silicon detectors, which would have decreased the SCT extension efficiency more significantly. The observed drop

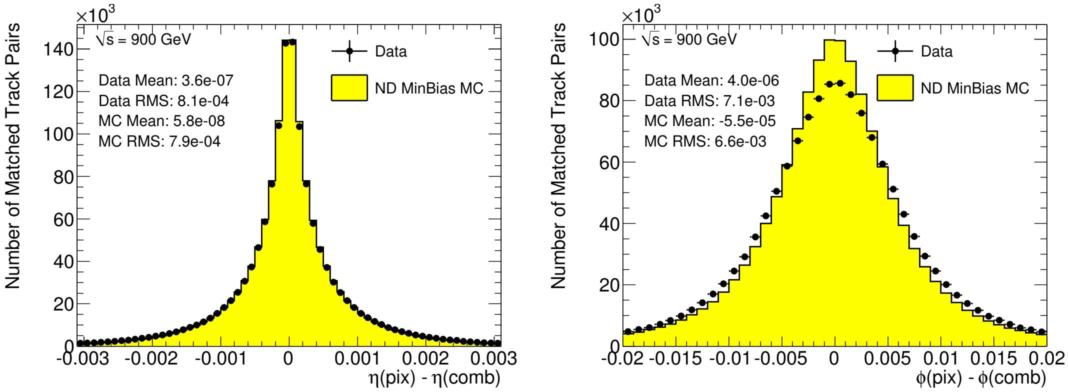

(a) η

(b) ϕ

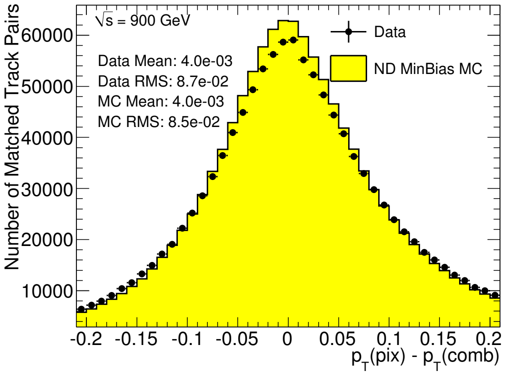

(c) p_T

Figure 6.28: The difference in track parameters between the pixel tracklet and the combined track for pairs of matched tracks. The data is shown with markers and the simulation by the filled yellow histogram.

in efficiency is due to the change in the number of tracks which undergo interactions in the first two layers of the SCT. These tracks have not yet passed through enough layers of silicon to obtain sufficient hits to meet the requirements for becoming a combined track.

6.4.3 SCT Extension Efficiency and the Pixel Detector Services

It turned out that the material description of the Service Quarter Panels (SQPs) was not fully described in the simulation in use at the start of the LHC. In particular, there was a significant

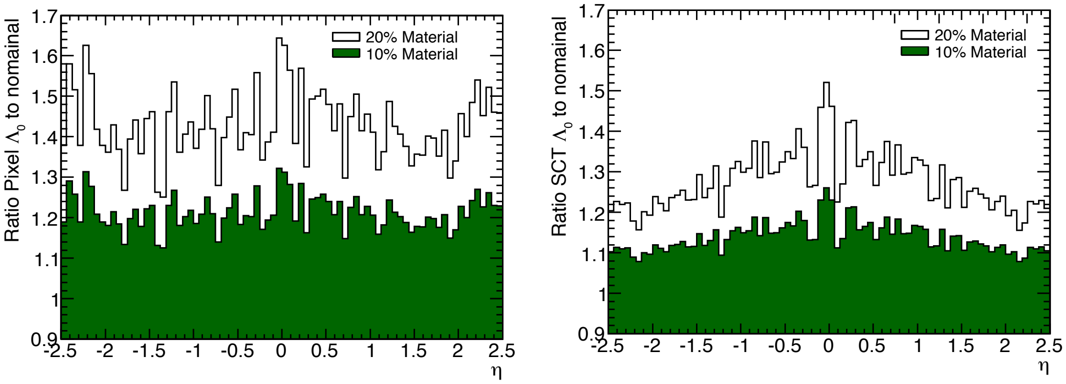

Figure 6.29: The ratio of the material in nuclear interactions lengths in the samples with 10% (open) and 20% (closed) extra material to the nominal simulation for the pixel detector (left) and the SCT (right)

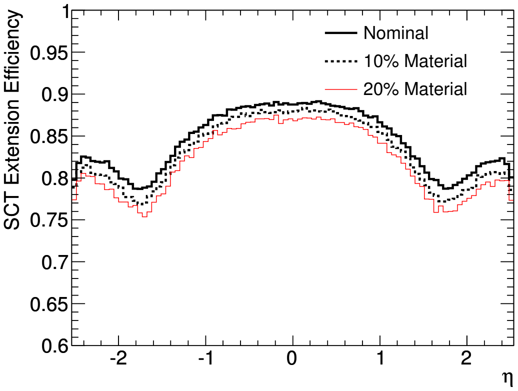

Figure 6.30: Comparison of the SCT extension efficiency for the simulation samples containing the nominal amount of material to the additional 10% and 20% samples

amount of material missing in the so-called Patch Panel 0 (PP0) region, at the end of the pixel detector. This missing material was identified shortly after the first data had been delivered by the LHC.

Figure 6.31(a) shows the octagonal structures which were added to the simulation to crudely model the material in this region. These structures are located just behind the pixel end caps. The illuminated cone shows all possible trajectories for a particle with $\eta = 2.12$. Particles with higher pseudorapidity pass through this additional material. A photograph of the PP0 region is shown in Fig. 6.31(b), which illustrates the complexity of modelling all components of this material. The amount of material in radiation lengths as a function of the pseudorapidity is compared to the previous version used in simulation in Fig. 6.32(a). The increase in the material for $|\eta| > 2.3$ is large and rises to almost a 50% increase by $\eta = 2.5$.

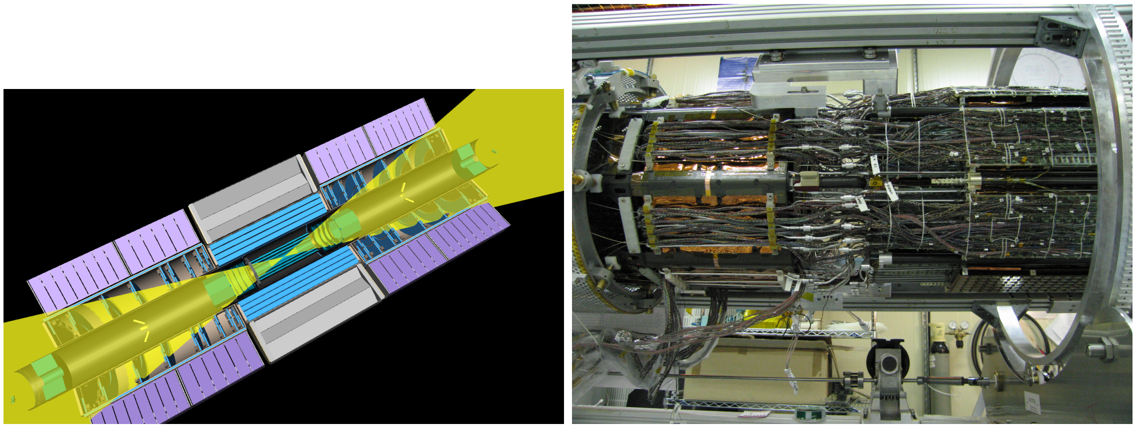

(a)

(b)

Figure 6.31: (a) The octagonal structures added to the simulation to model the material in the PP0 region from the VP1 detector geometry display. The cone shows that tracks with $\eta > 1.12$ would pass through this material (b) A photograph of the PP0 region before the detector was inserted into ATLAS

The SCT extension efficiency in data is compared to the simulation sample produced with (GE0-08-05) and without the material (GEO-08-02) in the PP0 region in Fig. 6.32(b). The SCT extension efficiency decreases by almost 10% for $|\eta| > 2.2$ and the agreement with the data is dramatically improved. Nonetheless, there are remaining discrepancies in the SCT extension efficiency around $\eta = 2$ and for $\eta > 2.3$, which may indicate that this geometry could be refined further in the future.

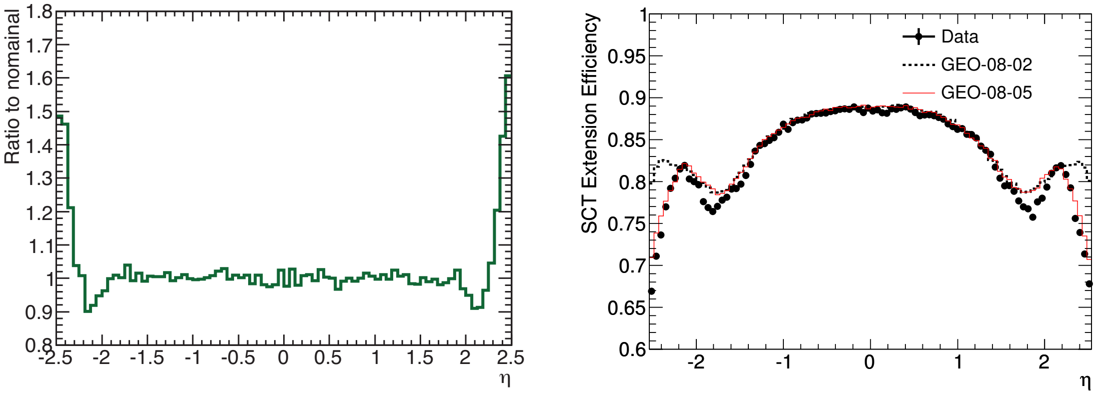

(a) (b)

Figure 6.32: The ratio of the material in radiation lengths in the detector geometry containing the PP0 description to the nominal geometry as a function of the pseudorapidity (a). Comparison of the SCT Extension Efficiency from data to the simulation samples produced either with (GE0-08-05) or without (GEO-08-02) the material in PP0 region (b).

Chapter 7

Event Selection Efficiency and Backgrounds

This section discusses the estimation of the event selection efficiency. It covers the trigger efficiency, vertex reconstruction efficiency and an estimate of the contamination from sources other than proton-proton collisions.

7.1 Trigger Efficiency

Most previous charged particle multiplicity measurements have been made using data selected with a double-arm coincidence trigger. Because this requirement removes a large fraction of diffractive events, the distributions are typically further corrected to completely remove the single diffractive component (the different types of inelastic interactions were introduced in Section 2.2.2.) The measurement presented here, however, uses a single arm trigger to select events and applies no correction to remove the single diffractive component. It is the specially designed minimum bias trigger that makes the measurement of these inclusive charged particle spectra possible.

Events were selected using a trigger combining information from the MBTS scintillators and the BPTX (see Section 4.2.6.1). The BPTX was used to ensure that only events triggered at the time when two bunches of protons were passing through the ATLAS interaction point were selected[1]. If one or more counters of the MBTS scintillators were above threshold, the trigger will be referred to as the single MBTS trigger. The double hit MBTS trigger requires at least two scintillators to be

---

[1] This is referred to as a trigger corresponding to filled, colliding bunches.

above threshold, while the double-sided MBTS trigger requires a hit in each side of the MBTS. Each trigger in ATLAS is identified within the software by a unique string. The strings for the three MBTS triggers are: MBTS_1 for the single MBTS trigger, MBTS_2 for the double-hit MBTS trigger and MBTS_1_1 for the double-sided MBTS trigger.

The efficiency of the single MBTS trigger for events passing the offline selection was measured in data. The efficiency needs to be measured in data, because the MBTS trigger scintillators were very poorly modelled in the simulation used at $\sqrt{s} = 900$ GeV and $\sqrt{s} = 2.36$ TeV [2]. An ad-hoc simulation of the trigger was developed and used to assess systematic uncertainties [45]. The ad hoc simulation scaled down the simulated energy in a scintillator. If any scintillator had a hit above threshold after this correction, the single MBTS trigger was assumed to have fired. Figure 7.1 compares the trigger efficiency in data to the default simulation and the ad hoc simulation with different scale factors. The ad hoc simulation with a scale factor of 90 reproduces the efficiency measured in data, while the default simulation overestimates the efficiency.

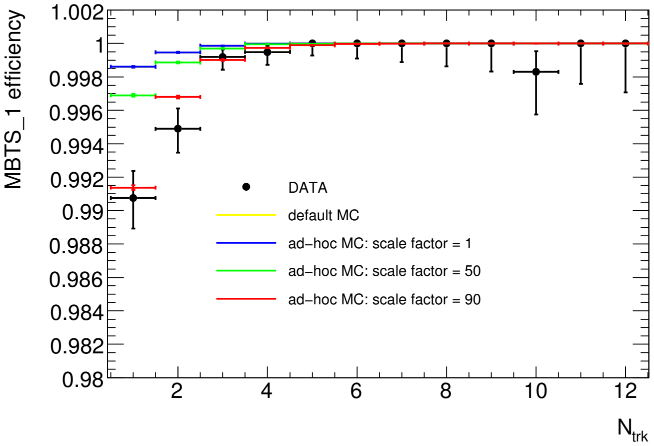

Figure 7.1: The single MBTS efficiency in data at $\sqrt{s} = 900$ GeV compared to the default trigger simulation and the ad hoc simulation with different scale factors [45].

Ideally, the trigger efficiency would be measured using events satisfying the offline event selection criteria selected by the BPTX triggers. As the only requirement made within the BPTX trigger is the presence of colliding beams, the efficiency would be fully unbiased. However, the BPTX

---

[2] Incorrect values for the calibration constants were used such that the energy deposited in each counter was significantly overestimated

triggers were pre-scaled during data-taking such that only 10^{-3} of the events passing the trigger were recorded. Additionally, the probability of an inelastic collision is only $\sim 0.01\%$, therefore only 406 events meeting the offline selection criteria were selected by the BPTX at 900 GeV. Therefore, the control trigger stream used to measure the trigger efficiency was the Minimum Bias space point trigger. The space point trigger selected events containing at least seven (four) pixel and SCT space points at $\sqrt{s} = 900$ GeV ($\sqrt{s} = 7$ TeV). The algorithm runs as part of the Level 2 trigger on events randomly selected from the filled, colliding bunches at Level 1.

The efficiency of each MBTS trigger is defined as the fraction of events accepted by the space point trigger and passing offline event selection which pass the MBTS trigger. In total 19037 events at $\sqrt{s} = 900$ GeV [45] and 12498 at $\sqrt{s} = 7$ TeV [98] meeting both space point trigger and offline requirements were used to measure the trigger efficiency. Figure 7.2 shows the efficiency of the three MBTS triggers as a function of the number of pre-selected tracks at $\sqrt{s} = 900$ GeV. The efficiency in data is compared to the results from the ad hoc simulation. The efficiency is lower in events with few tracks but increases with the track multiplicity and becomes fully efficient for events containing many tracks. As expected, the single MBTS trigger is the most efficient because it applies a subset of the requirements for the other two triggers.

Any correlation between the space point trigger and the single MBTS trigger biases the efficiency measurement. The correlation was investigated in simulation by comparing the difference in the trigger efficiency in events with and without the space point trigger. No change in the efficiency was observed for events with at least two pre-selected tracks, but the efficiency for $n_{\mathrm{Sel}}^{\mathrm{BS}} = 1$ was 0.15% lower without the space point trigger. This value was applied as a correction factor to the measured trigger efficiency. The systematic uncertainty on the correction was estimated to be 0.11% by varying the scale factor used to produce the ad hoc simulation. Other systematic uncertainties on the trigger efficiency are 0.1% due to statistical uncertainties and 0.1% due to the differences between selection requirements of pre-selected and selected tracks.

The trigger efficiency and estimated systematic uncertainties are shown in Fig. 7.3 for data taken at $\sqrt{s} = 900$ GeV and $\sqrt{s} = 7$ TeV. The trigger efficiency is higher at $\sqrt{s} = 7$ TeV due to improvements to the configuration of the MBTS scintillators [124]. The high voltage was increased and the trigger thresholds adjusted, resulting in a higher trigger efficiency. As sufficient data to measure the trigger efficiency was not recorded at $\sqrt{s} = 2.36$ TeV, the trigger efficiency from $\sqrt{s} = 900$ GeV was used. The high efficiency and small systematic uncertainty of the single MBTS

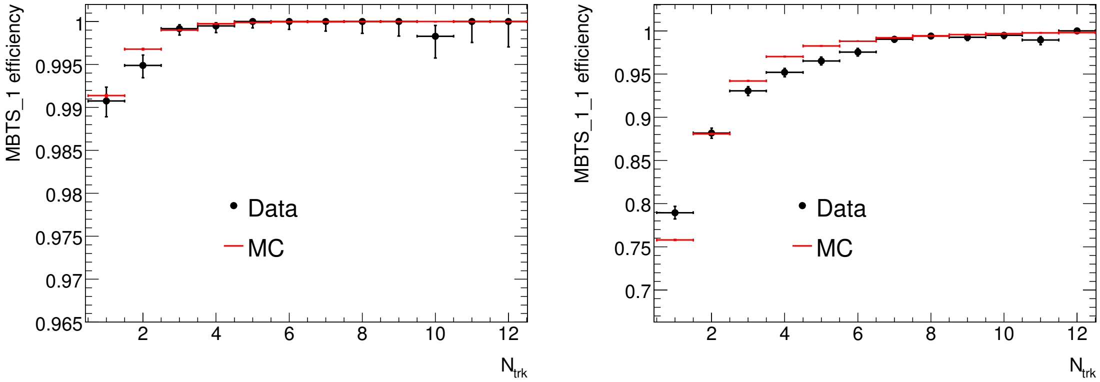

(a) single MBTS trigger

(b) double-sided MBTS trigger

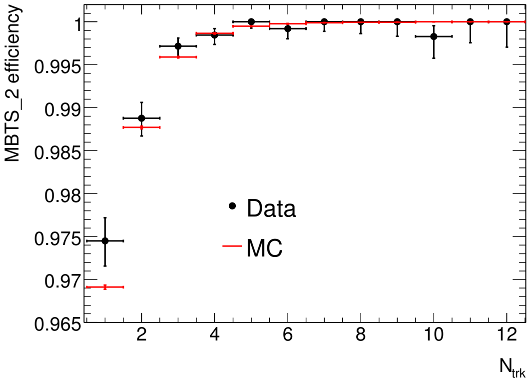

(c) double hit MBTS trigger

Figure 7.2: The efficiency of the MBTS triggers as a function of the number of pre-selected tracks in data and simulation at $\sqrt{s} = 900$ GeV [45].

trigger result in a negligible contribution to the final systematic uncertainties on the charged particle multiplicity distributions.

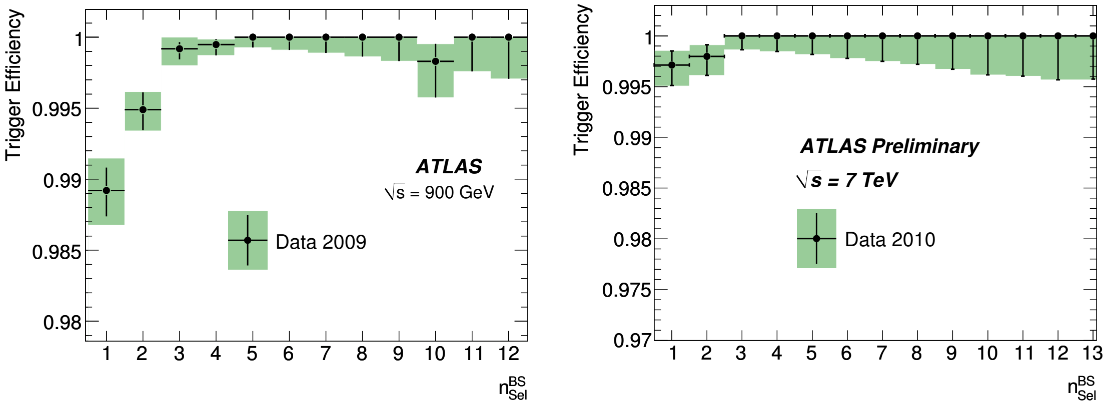

(a) $\sqrt{s} = 900$ GeV [4]

(b) $\sqrt{s} = 7$ TeV [121]

Figure 7.3: The efficiency of the single MBTS trigger as a function of the number of pre-selected tracks. The vertical bars represent the statistical uncertainty, while the shaded areas represent the statistical and systematic uncertainties added in quadrature.

7.2 Vertex Reconstruction Efficiency

Events were required to contain a reconstructed primary vertex to remove backgrounds due to beam interactions and to improve the impact parameter resolution for improved rejection of secondary particles. The number of reconstructed primary vertices per event was used to identify and veto events containing multiple proton-proton interactions, also referred to as pile-up.

7.2.1 Vertex Reconstruction

Vertex reconstruction algorithms aim to compute the location of the primary proton-proton interaction from the reconstructed tracks. As in track reconstruction, primary vertex reconstruction can be regarded as consisting of two stages: the *vertex finding* algorithm, which identifies tracks that can be associated with a vertex candidate and the *vertex fitting* algorithm, which determines the vertex position.

7.2.1.1 Vertex Reconstruction at $\sqrt{s} = 900$ GeV

The algorithm used to reconstruct primary vertices at $\sqrt{s} = 900$ GeV is known as the *Billoir* [51] *Full Vertex Fitter*. It performs an iterative χ^2 minimisation while forcing the impact parameters of the tracks to be at the primary vertex on each iteration [103]. As the number of events containing multiple pp interactions was expected to be negligible at $\sqrt{s} = 900$ GeV, the algorithm was configured to reconstruct at most a single primary vertex in each event.

The tracks used by the vertex reconstruction algorithm fulfill a looser set of requirements than the selected tracks used in the analysis. Vertex tracks included tracks reconstructed by any of the track reconstruction algorithms[3], which met the following requirements:

- transverse momentum: $p_T > 150$ MeV,
- transverse impact parameter: $|d_0^{BS}| < 4$ mm,
- error on the transverse impact parameter: $\sigma_{d_0} < 0.9$ mm,
- error on the longitudinal impact parameter: $\sigma_{z_0} < 10$ mm,
- at least 1 pixel hit, 4 SCT hits and at least 6 silicon[4] hits

The cuts on the vertex tracks were deliberately chosen to be looser than the selected tracks to ensure that events with few selected tracks were not rejected by the vertex reconstruction algorithm. The most significant difference was the inclusion of tracks with lower transverse momentum.

A single primary vertex candidate in each event was reconstructed from all tracks satisfying these criteria. As this vertex candidate can contain tracks from secondary vertices or poorly reconstructed tracks, an iterative procedure was applied to identify and remove those tracks. The track with the largest χ^2 contribution to the vertex fit was removed and a new vertex candidate was created. The procedure was repeated until all tracks contributing to the vertex have a χ^2 contribution smaller than a fixed cut or until there are only two tracks left in the vertex. The value used for the cut on χ^2 was 15. This iterative strategy was found to be more robust against the contribution from fake tracks than the previous strategy that removed all tracks with large χ^2 contributions in a single step [103].

---

[3] In particular, this included tracks reconstructed by the low-p_T algorithm, which reconstructed tracks with $p_T >$ 150 MeV and with only five silicon hits.

[4] The number of silicon hits is the sum of the hits in the pixel detector and the SCT.

The position of the beam spot was determined [23] using an unbinned maximum likelihood fit to the vertices in a short collision period of approximately 10 minutes[5]. The beam spot was only calculated for those periods in which at least 100 vertices were reconstructed. The beam spot is determined during the initial online processing of the data and used subsequently during offline reconstruction. The beam spot is used to select the tracks used in the vertex fit but it can also be applied as a constraint in the vertex fit. Using the beam spot as a constraint improves the vertex resolution in the transverse dimension by approximately a factor of two for vertices containing few tracks. For vertices containing many tracks, the beam spot constraint has no effect. In certain cases, though, using the beam spot constraint was found to bias the position of these low multiplicity vertices. For this reason the beam spot constraint was not used in the analysis at $\sqrt{s} = 900$ GeV.

The vertices used in the $\sqrt{s} = 900$ GeV analysis were required to contain at least three tracks. This was because the quality of vertices containing only two tracks was found to be too low. In simulation, these two-track vertices were found to have a low correlation with the true vertex position and to include a significant fraction of fake vertices.

7.2.1.2 Vertex Reconstruction at $\sqrt{s} = 2.36$ TeV and $\sqrt{s} = 7$ TeV

The probability of additional proton-proton interactions increases with the centre of mass energy of the collisions and the luminosity. Therefore for the analyses at $\sqrt{s} = 2.36$ TeV and $\sqrt{s} = 7$ TeV, the ATLAS implementation of the Billoir Full Vertex Fitter was replaced by an adaptive vertex finding algorithm [133] capable of reconstructing multiple primary vertices in an event.

A slightly looser set of requirements were applied to select the vertex tracks at $\sqrt{s} = 2.36$ TeV and $\sqrt{s} = 7$ TeV. The following cuts were looser than at $\sqrt{s} = 900$ GeV:

- transverse impact parameter: $|d_0^{BS}| < 4$ mm,
- error on the transverse impact parameter: $\sigma_{d_0} < 5$ mm, and
- at least 0 pixel hits, 4 SCT hits and 6 silicon hits

A vertex seed was obtained by locating the maximum number of tracks as a function of z. The adaptive vertex fitting algorithm performs a χ^2 fit using the seed and the tracks near the seed. Instead of rejecting tracks with a large χ^2 value, weights were applied to reduce their contribution

---

[5] More precisely, the fit was performed for vertices from five luminosity blocks. A luminosity block is a unit of recorded data that has a typical duration of 2 minutes.

to the fit. The value of weight was determined by estimating the probability that the track belongs to the vertex. The fit was iterated to determine the final track weights. Further details of the adaptive vertex finding algorithms can be found in [133].

Any track more than 7 standard deviations from the vertex was used to seed a new vertex. The fitting and seeding procedure was repeated until no unassociated tracks remained or no additional vertices could be found. The value of 7 standard deviations was tuned to minimise the number of events containing split vertices: events in which a single interaction was reconstructed as multiple vertices. In contrast to the algorithm used at $\sqrt{s} = 900$ GeV, the beam spot position was used as a constraint in the vertex fit, because it significantly improved the transverse position resolution. In the longitudinal direction, the beam spot constraint did not improve the vertex resolution, however it removed outliers. After reconstruction, vertices were ordered in decreasing size of the sum of the square of the transverse momenta of the fitted tracks so that the first vertex corresponds to the interaction involving the largest momentum transfer.

In contrast to the analysis at $\sqrt{s} = 900$ GeV, the vertices reconstructed by the adaptive vertex finding algorithm were not required to contain at least three tracks, because the quality of vertices containing two tracks was found to be sufficient.

7.2.1.3 Contamination from Multiple Primary Interactions

As the probability of multiple primary interactions at $\sqrt{s} = 900$ GeV was estimated to be negligible, the vertex reconstruction algorithm was configured to reconstruct at most a single vertex per event. However, in the data analysed at $\sqrt{s} = 7$ TeV in which the peak instantaneous luminosity was 1.1×10^{27} cm^{-2}s^{-1}, the rate of such additional interactions was estimated to be $\sim 10^{-3}$. Such a low total rate means that additional interactions occurred in only a small fraction of the total events. Nonetheless, it could bias certain measured distributions such as the tails of the n_{ch} distribution. Therefore, the properties of events containing multiple reconstructed vertices were studied and cuts were developed to reject events containing pile-up [121, 42].

Figure 7.4 shows the correlation between the number of tracks per vertex between the first and second vertex in events with at least two reconstructed vertices. The vertices are numbered by decreasing size of the quadratic sum of the transverse momentum of tracks in the vertex. Because the simulation contains a single proton-proton interaction only, the rate at which two vertex events are reconstructed was used to estimate the rate of split vertices. Figure 7.4(b) shows that these fake vertices typically contain few tracks.

In data that contains pile-up (Fig. 7.4(a)]) there are significantly more events containing a second vertex with a significant number of tracks. Therefore the pile-up veto rejected events containing at least two reconstructed vertices if the second vertex contained at least four tracks. The second vertex was required to contain at least four tracks to limit the number of split vertices rejected. This cut removed 487 events or $\sim 0.1\%$ of the $\sqrt{s} = 7$ TeV sample [121, 42].

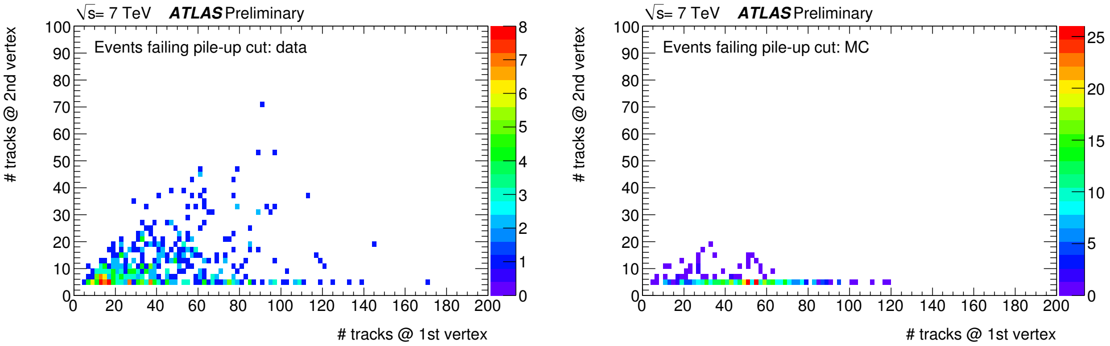

(a) Data

(b) Simulation

Figure 7.4: The correlation between the number of tracks in the first or second reconstructed vertex for events containing at least two vertices at $\sqrt{s} = 7$ TeV [121]. The Monte Carlo samples simulated a single *pp* interactions only, i.e., no pile-up

7.2.2 Vertex Reconstruction Efficiency

The vertex reconstruction efficiency is the number of events containing a reconstructed vertex divided by the number of events passing the trigger selection. The efficiency was measured as a function of the number of pre-selected tracks in data. Figure 7.5 compares the vertex efficiency in data to simulation. The efficiency for each of the components of the minimum bias simulation is shown separately, as well as the efficiency when the three samples are weighted according to their cross sections. The vertex efficiency increases with the number of pre-selected tracks to become fully efficient for events containing at least three pre-selected tracks. The efficiency to reconstruct a three-track vertex is not zero in events with two pre-selected tracks because the cuts on the vertex tracks are looser than on the pre-selected tracks. The efficiency differs between the simulation samples due to differences in the kinematic distributions. The efficiency is well-modelled by the mixed simulation sample except for events containing no pre-selected tracks. However events containing no pre-selected tracks are not used in the analysis.

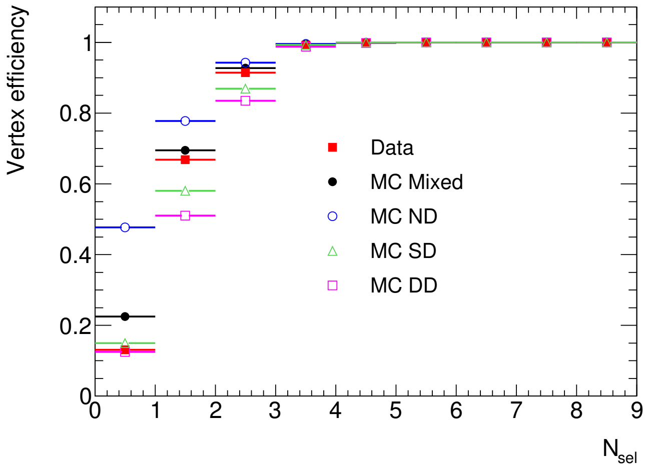

Figure 7.5: The vertex reconstruction efficiency as a function of the number of pre-selected tracks in data and simulation at $\sqrt{s}$ = 900 GeV [23]. The mixed simulation sample consists of the non-diffractive, single and double diffractive samples weighted according to their predicted cross-sections.

The vertex reconstruction efficiency as a function of p_T and η in data is shown in Fig. 7.6. The efficiency is shown separately for events containing different numbers of pre-selected tracks. For events with at least two pre-selected tracks, no significant dependence on p_T or η is observed. In events containing a single pre-selected track, on the other hand, the efficiency decreases from 70% at central pseudorapidity to 60% at forward pseudorapidity. Therefore, the vertex efficiency was parametrised as a function of the number of pre-selected tracks for $n_{\mathrm{Sel}}^{\mathrm{BS}} >= 2$ and as a function of the pseudorapidity for $n_{\mathrm{Sel}}^{\mathrm{BS}} = 1$. The η-dependent correction for $n_{\mathrm{Sel}}^{\mathrm{BS}} = 1$ was not applied at $\sqrt{s}$ = 2.36 TeV because there was not enough data to allow it to be measured with adequate precision.

7.2.3 Systematic Uncertainties

The vertex efficiency can vary with time due to changes to the beam or detector conditions. The systematic uncertainty was estimated by studying the change to the vertex efficiency between data taken at different times. A significant variation was only observed for events containing few tracks.

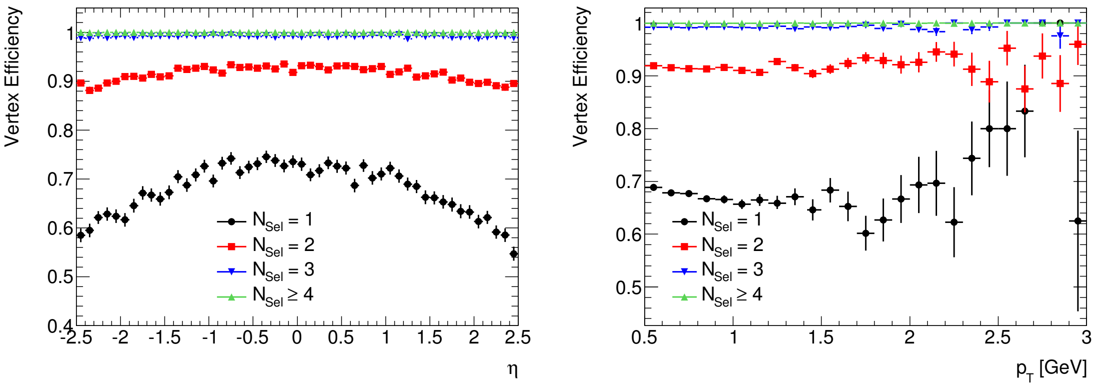

(a) Pseudorapidity

(b) Transverse Momentum

Figure 7.6: The vertex reconstruction efficiency as a function η and p_T for events with different numbers of pre-selected tracks at $\sqrt{s} = 900$ GeV [23].

Multiplicity	$n_{\mathrm{Sel}}^{\mathrm{BS}} = 1$	$n_{\mathrm{Sel}}^{\mathrm{BS}} = 2$	$n_{\mathrm{Sel}}^{\mathrm{BS}} = 3$
Run Variation	1%	0.5%	0.1%
Beam Background	0.32%	$< 0.1\%$	$< 0.1\%$
Total	1%	0.5%	0.1%

Table 7.1: The systematic uncertainties on the vertex reconstruction efficiency at $\sqrt{s} = 900$ GeV as a function of the pre-selected track multiplicity.

Section 7.3 shows that the total number of events from beam background was small. The systematic uncertainty on the vertex reconstruction efficiency was estimated by studying the number of events in unpaired bunches containing a reconstructed vertex. It was found to be at the sub-percent level for $n_{\mathrm{Sel}}^{\mathrm{BS}} = 1$ and negligible for events containing more tracks.

The systematic uncertainty on the efficiency due to the rate of split vertices was studied in simulation and found to be negligible. It was estimated that the pile-up cut removed $\sim 0.03\%$ of events containing a single interaction, while $\sim 0.02\%$ of events were either reconstructed as a single vertex or not removed by the cut. The rate of these events varied with the number of pre-selected tracks, however it was estimated to be less than 1% for any number of pre-selected tracks.

The systematic uncertainties estimated as a function of the number of pre-selected tracks are shown in Table 7.1.

7.2.4 Summary

The measured values of the vertex reconstruction efficiency for each centre of mass energy are shown in Fig. 7.7. For events containing $\gtrsim 3-4$ pre-selected tracks, the vertex reconstruction algorithm is fully efficient. The increase in the efficiency between 900 GeV and 7 TeV for events containing few tracks is due to changes in the vertex reconstruction algorithm and the decrease in the requirement of the number of tracks per vertex coming from the beam spot constraint. The efficiency at $\sqrt{s} = 2.36$ TeV is lower because of the lower SCT efficiency, which reduced the track and hence the vertex reconstruction efficiency. The systematic uncertainties on the vertex reconstruction efficiency are small and make a negligible contribution to the uncertainties for the final distributions.

7.3 Non-collision Backgrounds

Two possible sources of backgrounds from sources other than proton-proton collisions, cosmic rays and beam background, were studied [89], and both were found to be negligible.

The fraction of cosmic background events was estimated using:

$$r_{\text{cosmic total}} = N_{\text{bunch}} t_{\text{readout}} N_{\text{MBTS}} r_{\text{cosmic}} \tag{7.1}$$

where

- N_{bunch} is the number of proton bunches colliding at ATLAS
- t_{readout} is the MBTS read-out window (8×25 ns)
- N_{MBTS} is the number of MBTS scintillators (32)
- r_{cosmic} is the cosmic rate of a single MBTS scintillator (1 Hz)

For a typical dataset recorded at $\sqrt{s} = 900$ GeV, run 142383, in which there were 8 pairs of colliding bunches, this results in an estimated cosmic rate of 6×10^{-5} Hz. As the mean rate of single MBTS triggers recorded during this run was 31 Hz, the fraction of cosmic background events is estimated to be below 10^{-6} [46].

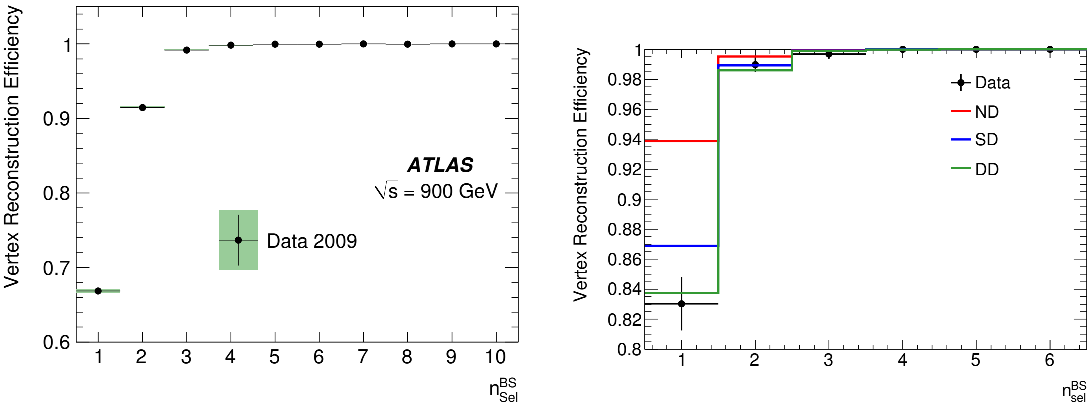

(a) $\sqrt{s} = 900$ GeV [4]

(b) $\sqrt{s} = 2.36$ TeV

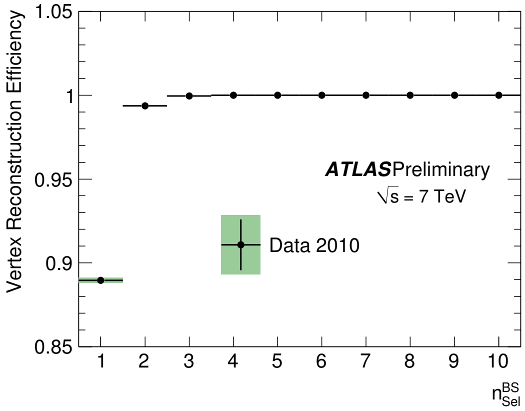

(c) $\sqrt{s} = 7$ TeV [121]

Figure 7.7: The vertex reconstruction efficiency as a number of pre-selected tracks for data at the three centre of mass energies. The bars indicate the size of the statistical uncertainty and the green bands the sum of the statistical and systematic uncertainties added in quadrature.

Beam-induced background can arise from collisions of protons with the collimators or with other particles inside vacuum in the beam pipe. The rate of this background was estimated by studying the events from the unpaired proton bunch crossings. Unpaired bunch crossings are those in which only one of the two beams contained a proton bunch. The difference in time between the signals received from each side of the MBTS scintillators was used to study the contribution from the beam background [89].

Figure 7.8 shows the difference in time between the two sides of the MBTS in paired bunches (unfilled histogram) and unpaired bunches (red filled histogram). The timing difference for collisions peaks at zero because they occur at the centre of ATLAS, i.e., it takes the particles the same amount of time to reach the scintillators on each side. However, the timing difference for events in which only one of the beams contained a bunch of protons peaks at 21 ns, which is the time it takes from particles to propagate from the scintillators on one side to those on the other side.

The distribution is shown for all events and for events after all selection cuts. Only 12 of the events from the unpaired bunches survived all the selection cuts, which leads to an estimated beam background of approximately 10^{-5}. The systematic uncertainty on this estimate was assessed to be at least an order of magnitude by comparing the number of events in the paired and unpaired bunches before event selection. Even with such a large uncertainty, the beam background is still negligible. A similar study concluded that the beam background as $\sqrt{s} = 7$ TeV was similarly negligible [121].

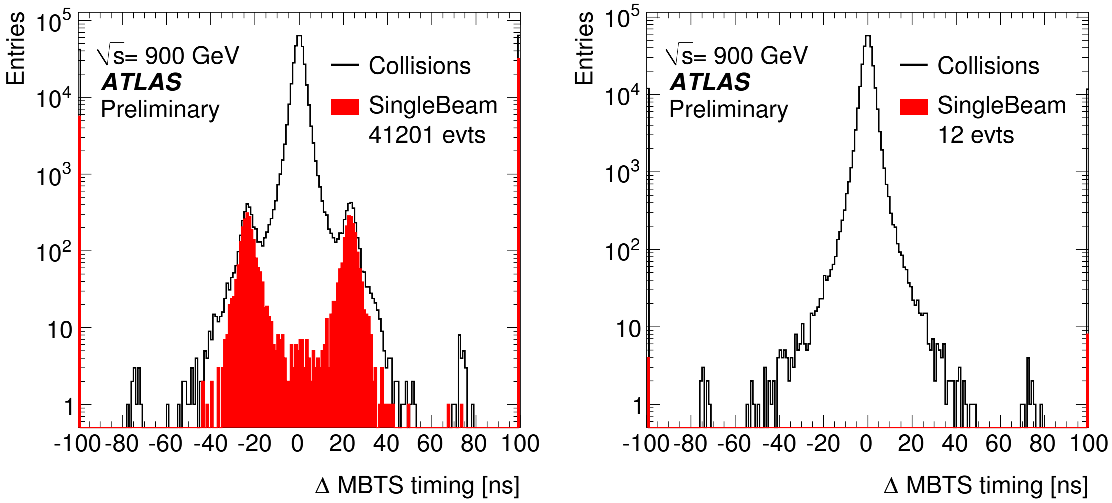

Figure 7.8: The difference in the timing between the two sides of the MBTS scintillators for all events (a) and after all selection cuts (b) at $\sqrt{s} = 900$ GeV [89]

Chapter 8

Track Reconstruction Efficiency

The track reconstruction efficiency is defined as the fraction of charged particles passing through the detector that are reconstructed as tracks. The efficiency depends on properties of the particles such as p_T and η and was calculated as follows:

$$\epsilon_{bin}(p_T, \eta) = \frac{N_{\rm gen}^{\rm matched}(p_T, \eta)}{N_{{\rm gen}(p_T, \eta)}} \tag{8.1}$$

where $N_{{\rm gen}(p_T, \eta)}$ is the number of generated charged particles and $N_{\rm gen}^{\rm matched}(p_T, \eta)$ is the number of generated charged particles which were matched to a reconstructed track. In low density environments where tracks are not close enough such that double track resolution[1] plays a role, the efficiency depends on the track properties such as p_T and η, but not on the centre of mass energy of the collisions. Therefore, this section will focus on the study of the track reconstruction efficiency derived from simulation and its systematic uncertainty at $\sqrt{s}$ = 900 GeV. Most results can be applied directly at higher centre of mass energies.

The track reconstruction efficiency is calculated using simulated Monte Carlo events, which means that the dominant systematic uncertainty is due to the level of agreement between data and simulation. The efficiency depends on the definition of a primary particle, the algorithms and cuts used to reconstruct tracks, and the criteria used to associate generated particles with reconstructed tracks.

A number of factors can result in a particle passing through the detector not being reconstructed. Clearly, particles outside the detector acceptance cannot be reconstructed so distributions are only

---

[1] The double track resolution is the distance by which tracks must be separated to be reconstructed.

measured for charged particles within the acceptance of the tracking detectors: $|\eta| < 2.5$. Particles that pass through gaps in the detector acceptance or through inactive detector elements cannot be reconstructed. This means that the efficiency depends on how accurately the detector geometry and inactive detector elements are included in the simulation. Particles have a certain probability of undergoing a hadronic interaction with the detector material and being destroyed. If this interaction occurs before the particle has produced enough hits to meet the reconstruction requirements, the track will not be reconstructed.

Figure 8.1(a) shows the rate of hadronic interactions within the Inner Detector as a function of the pseudorapidity. The interaction rate increases with η due to the increase in the detector material in the forward regions. The interaction rate is large, i.e., between 10 and 20% of all hadrons undergo nuclear interactions, therefore it is the leading source of inefficiency in track reconstruction.

The track reconstruction efficiency as a function of the radius at which the generated particle undergoes an interaction is shown in Fig. 8.1(b). The efficiency is close to a step function: almost every particle which reaches a radius of $\sim$500 mm without interacting is reconstructed. In order to meet the requirement of 6 SCT hits, a particle needs to have passed through at least 3 layers of the SCT. The efficiency does not quite reach 100% for such particles due to tight track selection cuts. As the efficiency depends strongly on the rate of hadronic interactions, any inaccuracies in the material budget have a large impact on the uncertainty for the track reconstruction efficiency. As this is the leading systematic uncertainty for the charged particle multiplicities, detailed studies of the uncertainty on the material budget were performed and are discussed in Sections 6.4 and 8.7.1.

8.1 Primaries, Secondaries and Fakes

Primary charged particles are defined as charged particles with a mean lifetime greater than 3×10^{-9} s directly produced in a *pp* interaction, or charged particles produced from the decay of particles with a shorter lifetime. The precise value of the cut on the particle lifetime is an arbitrary choice, but it is used to select particles that do not decay before reaching the detector following the convention from Ref. [54]. More than 90% of the primary particles are charged pions, but also $e^{\pm}$, $\mu^{\pm}$, $K^{\pm}$, $p^{\pm}$, $\Sigma^{\pm}$, $\Xi^{\pm}$ and $\Omega^{\pm}$ are included. The latter three particle types typically reach the pixel detector, but are almost never reconstructed.

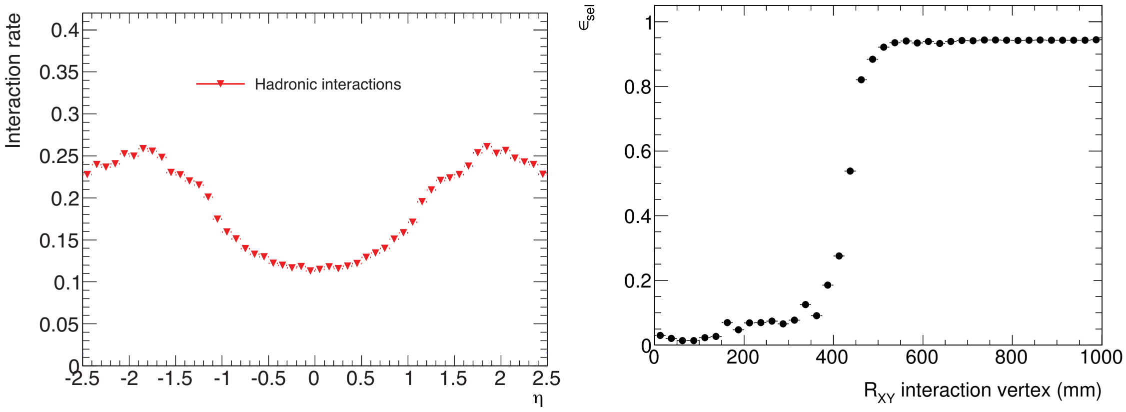

(a)

(b)

Figure 8.1: The rate of interactions within the ID as a function of the pseudorapidity (a) and the track reconstruction efficiency for particles with $p_T > 500$ MeV as a function of radius at which the first interaction occurs, R_{XY}, (b) at $\sqrt{s} = 900$ GeV [37].

Any charged particle which is not a primary is called a *secondary.* Secondary particles are produced from primaries by a number of mechanisms: strange hadron decays, decays of pions and kaons in flight, photon conversions and hadronic interactions with the detector material.

Reconstructed tracks which are not associated with either primaries or secondaries are termed *fakes*. Fakes include tracks reconstructed from detector noise or from combining hits produced by different particles. The fraction of tracks considered to be fake depends on the technique used to associate reconstructed tracks to generated particles.

8.2 Truth Matching Techniques

A matching criterium relating reconstructed tracks to primary particles needs to be defined to determine if a generated particle has been successfully reconstructed. Three different truth matching techniques were studied.

Hit matching associates particles and tracks based on the number of hits per track that correspond to a generated particle. The average number of hits per track and the improvement to the track parameter resolution from each hit vary significantly between the three sub-detectors. Therefore, the fraction of matched hits was calculated using the following formula with weights applied to the hits from each sub-detector:

$$r_{hit} = \frac{10 \cdot N_{pix}^{gen} + 5 \cdot N_{SCT}^{gen} + N_{TRT}^{gen}}{10 \cdot N_{pix}^{rec} + 5 \cdot N_{SCT}^{rec} + N_{TRT}^{rec}} \tag{8.2}$$

where

- N_{det}^{rec} is the number of reconstructed hits per track
- N_{det}^{gen} is the number of reconstructed hits which correspond to the generated particle

The precise values of the weights are arbitrary. The silicon hits have larger weights than the TRT hits because there are, on average, many more TRT hits per track. The pixel hits are weighted twice as much as the SCT hits because the number of pixel hits are more than a factor of two fewer than the number of SCT hits per track. In addition, the precision and distance from the interaction point of each hit determine how much each hit contributes to the track parameter resolution. A larger value of r_{hit} means that a larger fraction of the hits of the reconstructed track were produced by the generated particle. A hit match was considered to be successful when r_{hit} is greater than 0.55. If a track has two possible matches, the match with the highest value of r_{hit} is selected.

Cone matching associates a generated particle to the closest reconstructed track in an angular cone around the generated particle. The radius of the cone was calculated from:

$$\Delta R = \sqrt{\Delta\phi^2 + \Delta\eta^2} \tag{8.3}$$

where Δx is the difference between the generated and reconstructed track parameter, x. A cone match is successful if a reconstructed track is found within a ΔR value of 0.5.

Figure 8.2 shows the distributions of r_{hit} and ΔR. The red triangles show the distributions after the alternate matching criteria has been applied: i.e. Fig. 8.2(a) shows the r_{hit} distribution for tracks with a successful cone match and Fig. 8.2(b) the ΔR distribution for tracks with a successful cone match.

In general, both methods make the same matches. The hit matching has very few matches below 50% not equal to zero. The distribution of ΔR has two components: a peak near zero for the correct matches and a flat tail due to combinatorial matches. Cutting the distribution at 0.05 accepts almost all tracks within the peak, but very few from the tail.

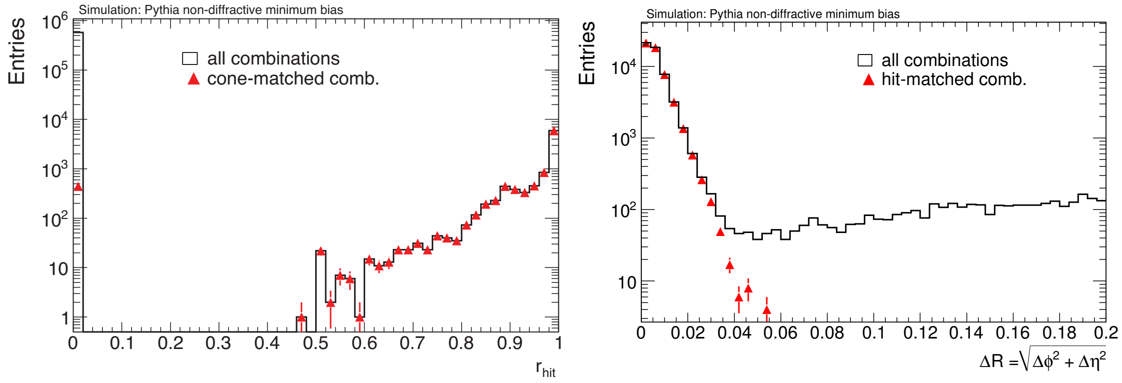

(a) Hit-based Matching

(b) Cone-based Matching

Figure 8.2: Distribution of the weighted fraction of matched hits (a) and the angular separation between generated and reconstructed particles (b). All possible matches are shown in black, while the red filled triangles show the hit fraction (angular distance) for matches satisfying $\Delta R < 0.05$ ($r_{hit} > 0.55$) [37].

The efficiency can also be calculated without a matching criterium. As such, the *inclusive efficiency* is calculated by dividing the number of reconstructed tracks by the number of generated tracks:

$$\epsilon_{bin}(p_T, \eta) = \frac{N_{\text{rec}}(p_T^{rec}, \eta^{rec})}{N_{\text{gen}(p_T^{gen}, \eta^{gen})}} \tag{8.4}$$

The inclusive efficiency is a slightly different quantity from the efficiency using hit or cone matching because it depends on the track parameter resolution in addition to the track reconstruction efficiency. This is because the reconstructed tracks must be binned in terms of the reconstructed track parameters.

The track reconstruction efficiency for each of the three truth matching methods is shown in Fig. 8.3. The inclusive matching efficiency is approximately 2% higher because it includes tracks from secondary particles (see Section 8.6 for an estimate of the rate of secondaries). Since the two methods obtain very similar estimates for the efficiency, cone matching was chosen because it is conceptually simpler. The difference in the efficiency between hit and cone matching, 0.4%, is used as an estimate of the systematic uncertainty due to the choice of the truth matching method.

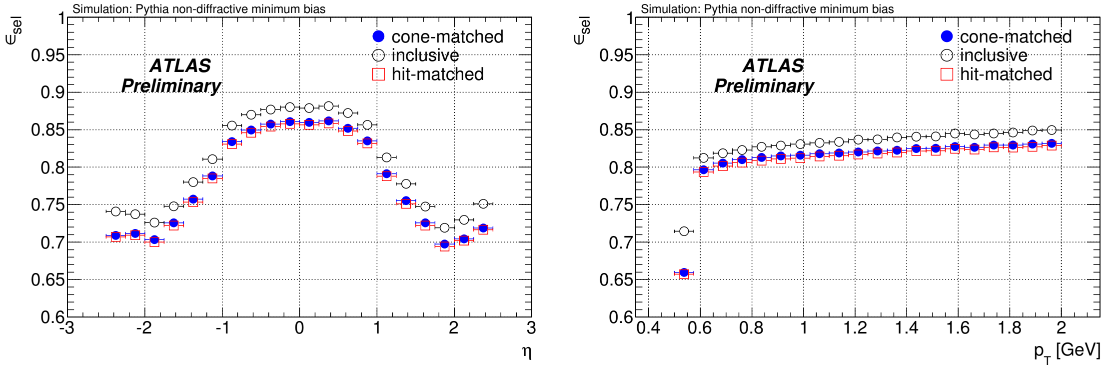

(a) As a function the pseudorapidity

(b) As a function of the transverse Momentum

Figure 8.3: Comparison of the track reconstruction efficiency obtained using the three different matching techniques at $\sqrt{s} = 900$ GeV [37].

8.3 Track Reconstruction Algorithms

Tracks are reconstructed by the ATLAS software [65] using a number of individual algorithms which are run sequentially on the hit collection. The final track collection is the combination of the tracks reconstructed by each algorithm. The two basic types of algorithm are called inside-out and back-tracking. The inside-out algorithm reconstructs tracks starting from the pixel detector and adding hits while moving radially outwards. The back-tracking algorithm reconstructs tracks starting from the TRT and adding hits while moving towards the centre of the detector. The inside-out algorithm is more efficient at reconstructing primary particles, while the back-tracking algorithm has a higher efficiency for secondaries. Each algorithm can be run multiple times with a different configuration to ensure that particles with different properties are reconstructed as efficiently at possible.

Tracks were reconstructed for the $\sqrt{s} = 900$ GeV analysis in three stages: the inside-out algorithm with $p_T > 500$ MeV, back-tracking with $p_T > 500$ MeV and a second pass of the inside-out algorithm with $p_T > 100$ MeV and lower track quality requirements. The order in which the algorithms run is significant because hits that have already been associated to a track are not considered by the subsequent algorithm. This means that high quality tracks are reconstructed first and, once their corresponding hits have been removed, a looser configuration can be used to reconstruct lower quality tracks without an overwhelming fake rate. Figure 8.4(a) shows the efficiency of the inside-out and low-p_T algorithms as a function of p_T.

The studies performed in the context of the analysis at $\sqrt{s} = 900$ GeV motivated several improvements to the track reconstruction algorithms. These improvements were used for the subsequent analyses at $\sqrt{s} = 2.36$ TeV and $\sqrt{s} = 7$ TeV. The momentum cut on the initial inside-out algorithm was lowered to 100 MeV and to 300 MeV for the back-tracking. Two passes of the inside-out sequence were added to reconstruct tracks with low transverse momentum: the first reconstructs tracks with $p_T > 100$ MeV using hits in either of the silicon detectors, called Low-p_T, and the second reconstructs tracks with $p_T > 50$ MeV using pixel detector information only, called Very Low-p_T.

A number of other improvements were made to allow primary tracks to be reconstructed efficiently down to 50 MeV, which are discussed in [7]. Here the most significant change is the reduction of the p_T cut on the primary inside-out sequence. This allows for the 5% systematic uncertainty for $500 < p_T < 600$ MeV discussed Section 8.7.2 to be reduced to 1% for the $\sqrt{s} = 2.36$ TeV and $\sqrt{s} = 7$ TeV analyses. Figure 8.4(b) compares the number of primary tracks reconstructed by the different algorithms at $\sqrt{s} = 7$ TeV.

Section 6.1 contains a detailed validation of the performance of the inside-out track reconstruction algorithm in data and simulation.

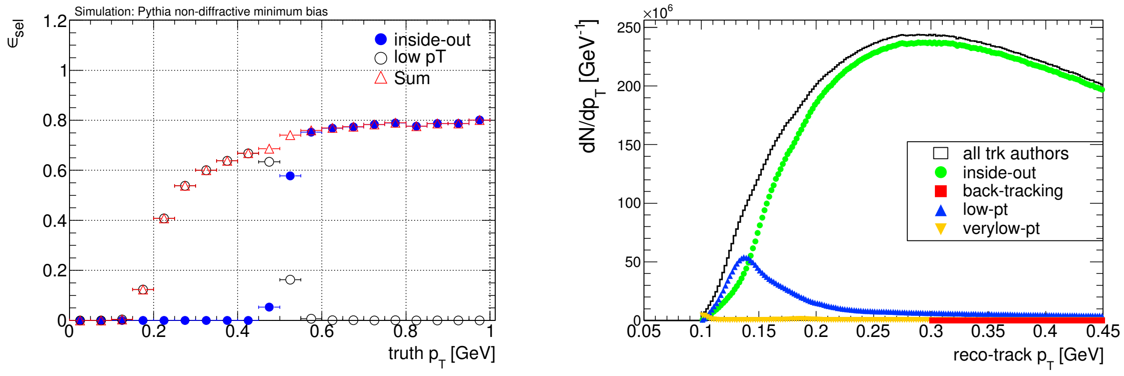

(a) $\sqrt{s} = 900$ GeV [37]

(b) $\sqrt{s} = 7$ TeV [7]

Figure 8.4: The track reconstruction efficiency as a function of p_T for the inside-out algorithms used at $\sqrt{s} = 900$ GeV (a). The number of reconstructed primary tracks as a function of p_T for the track reconstruction algorithms used at $\sqrt{s} = 7$ TeV (b)

8.4 Track Selection Cuts

The cuts used to define selected tracks were introduced in Section 3. These cuts were designed to select only well-reconstructed primary tracks for which the tracking efficiency could be accurately estimated. The cuts on the impact parameters, $|d_0^{PV}| < 1.5$ mm and $|z_0^{PV} \sin\theta| < 1.5$ mm reject a significant fraction of tracks from secondary particles. The largest discriminatory power is provided by using impact parameters expressed at the primary vertex, therefore the track reconstruction efficiency was only measured for events containing a primary vertex. The cuts on the number of pixel and SCT hits were optimised to minimise inefficiencies due to inactive detector elements while controlling the rate of fake and mismeasured tracks. No requirement was placed on the number of TRT hits. Section 6.3 compares the properties of the distributions used for track selection between data and simulation.

Figure 8.5 shows the fraction of reconstructed tracks after each track selection cut is applied sequentially as a function of track η. The efficiency of the pixel and SCT hit cuts is well-described by the simulation, however the efficiency of the impact parameter cuts are a few % higher in simulation than data. This does not necessarily mean that the primary track reconstruction efficiency differs between data and simulation, because the cumulative efficiency is calculated with respect to all reconstructed tracks.

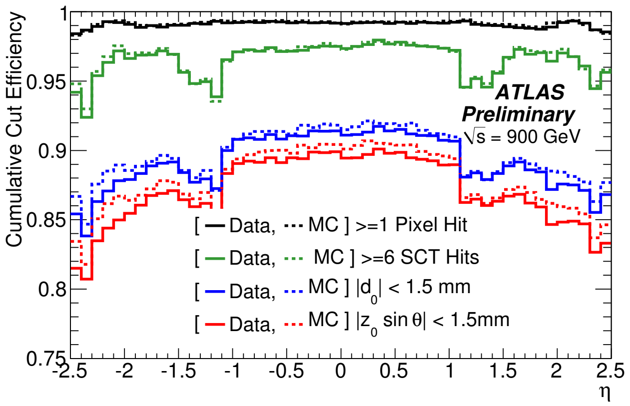

Figure 8.5: The cumulative efficiency of each track selection cut with respect to all reconstructed tracks in data and simulation as a function of η at $\sqrt{s} = 900$ GeV. The efficiency in data is the solid histogram and the efficiency in simulation is the dashed histogram.

The systematic uncertainties due to the track selection cuts were assessed using the $N-1$ cut technique. This compares the efficiency of each track selection cut in data and simulation by calculating the ratio of the number of tracks after all cuts to the number of tracks with all cuts but the cut in question, i.e.:

$$\epsilon_{cut}^{N-1} = \frac{N_{trk}^{\text{N cuts}}}{N_{trk}^{\text{N}-1\text{ cuts}}} \tag{8.5}$$

For example, the $N-1$ efficiency of the pixel hit cut is number of tracks passing the d_0, z_0, pixel and SCT hit cuts to the number of tracks passing the d_0, z_0 and SCT hit cut. As no truth information is used, the efficiency can be measured in data as well as in simulation.

Figure 8.6 compares the $N-1$ efficiency obtained in data and simulation. The $N-1$ efficiency is shown for the cut used to define the selected tracks, from which the systematic uncertainty was estimated, and for a tighter cut, which accentuates any possible differences between data and simulation. Because the tails of the d_0 distribution were used to estimate the fraction secondaries, a slightly different definition was used to avoid double counting it as a systematic uncertainty. Instead of removing the d_0 cut completely to define the $N-1$ efficiency, the cut value was varied by ± 0.5 mm.

Figure 8.6(a) shows that requiring a single hit in the pixel detector rejects very few tracks, whereas a requirement of two pixel hits would result in an efficiency varying as a function of η. This variation is the result of the location of inactive pixel modules. For this reason and because the $N-1$ efficiency for two pixel hits is not fully described by the simulation, only a single pixel hit was required.

The $N-1$ efficiency of requiring six hits in the SCT varies strongly as a function of η (Fig. 8.6(b)) due to the varying number of SCT layers that a particle passes through. The shape is well described by the simulation except for small differences at large value of the pseudorapidity.

For the impact parameter cuts, the $N-1$ efficiency decreases with increasing η as the impact parameter resolution worsens. Small differences in the efficiency between data and simulation are visible at the edge of the detector acceptance. The efficiency is not symmetric in η because collisions occurred more often at negative than positive z.

The difference in the $N-1$ efficiency of each cut between data and simulation is shown in Fig. 8.7. This difference was used for the systematic uncertainty due to the Monte Carlo modelling of each selection cut. As the correlations between the different cuts were not studied, the uncertainties

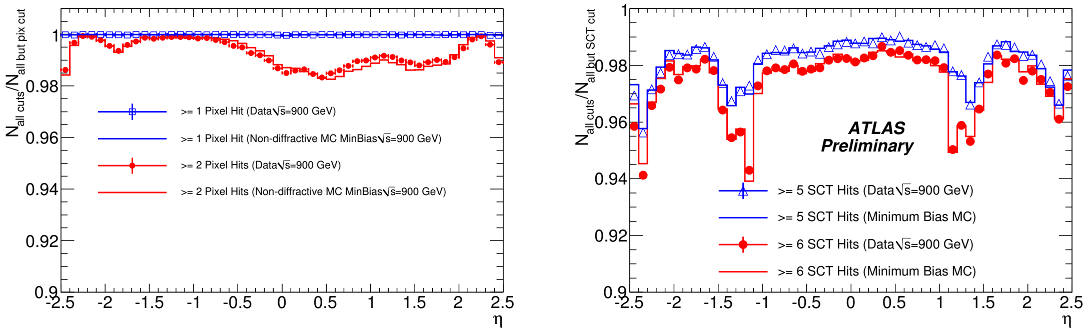

(a) Pixel Hits

(b) SCT Hits

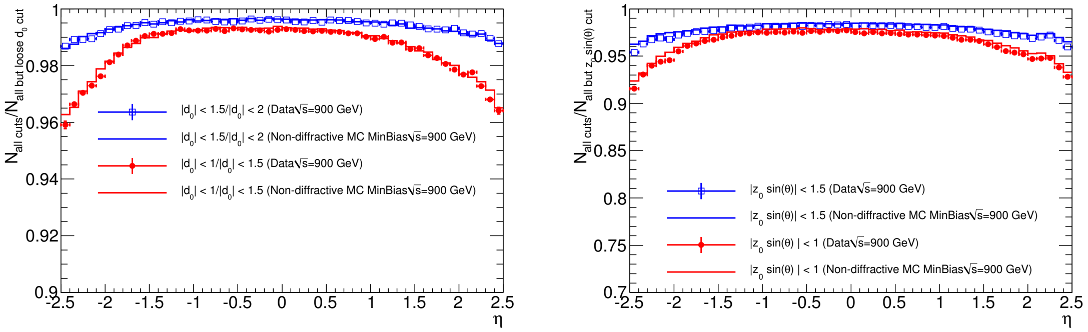

(c) Transverse Impact Parameter

(d) Longitudinal Impact Parameter

Figure 8.6: The $N-1$ efficiency of the four track selection cuts in data (solid histogram) and simulation (dashed histogram) at $\sqrt{s} = 900$ GeV.

were conservatively assumed to be fully correlated. Therefore the total systematic uncertainty due to selection cuts shown in Fig. 8.7(b) was calculated from the linear sum of the absolute value of the difference for each cut. Generally, the total systematic uncertainty is less than 1%.

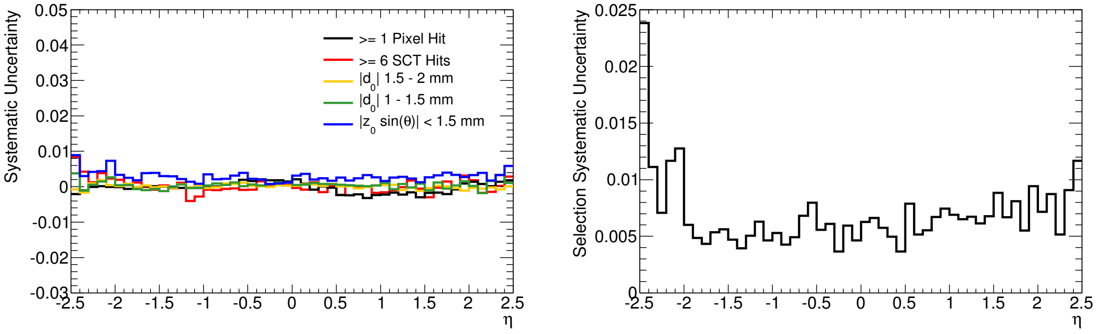

(a) Individual Cuts

(b) Total

Figure 8.7: The difference between the $N-1$ efficiency for each track selection cut in data and simulation (a) and the total estimated systematic uncertainty due to the selection cuts from the linear of the individual uncertainties (b) at $\sqrt{s} = 900$ GeV

8.5 Tracking Efficiency with the SCT in Standby

In the data recorded at $\sqrt{s} = 2.36$ TeV, stable beam conditions were never declared. As a consequence, the SCT was in standby with the sensor bias voltage reduced from 150 V to 20 V. The voltage was lowered to prevent high currents being produced with a large particle flux through the sensor. A bias voltage of 20 V led to lower hit efficiencies and increased noise. This is because 20 V is not sufficient to fully deplete the sensor volume. This mode will be referred to as *standby* mode and the configuration with the SCT fully depleted at 150 V as *nominal* mode. Figure 8.8 shows how the distribution of the number of tracks as a function of η is significantly altered when the SCT is operated in standby mode. This reflects the fact that the track reconstruction efficiency is not only lower when the SCT is in standby, but also varies significantly as a function of η . This is because, when the SCT is not fully depleted, the hit efficiency varies with the amount of silicon traversed, which in turn depends on the incidence angle that the track makes with the surface of the module.

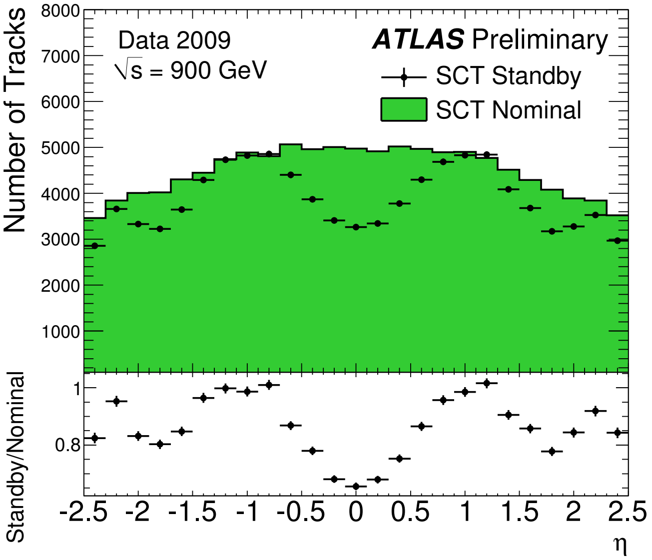

Figure 8.8: The number of reconstructed tracks in data at $\sqrt{s} = 900$ GeV as a function of η with the SCT in nominal and standby at $\sqrt{s} = 900$ GeV. The distributions are normalised to the number of events passing the trigger requirement.

Therefore, the following data-driven correction to the primary track reconstruction efficiency was estimated and applied:

$$\epsilon(x) \quad = \epsilon_{\mathrm{MC}}(x) \cdot \epsilon_{\mathrm{corr}}(\eta) \tag{8.6}$$

The correction is derived using a dataset taken at $\sqrt{s} = 900$ GeV in which a portion of a run was recorded with the SCT in standby. The correction factor, ϵ_{corr}, is the ratio of the number of reconstructed tracks with the SCT in standby ($N_{\mathrm{tr}}^{\mathrm{sb}}$) to the number of reconstructed tracks with the SCT at nominal ($N_{\mathrm{tr}}^{\mathrm{nom}}$):

$$\epsilon_{\mathrm{corr}}(\eta) = \frac{N_{\mathrm{tr}}^{\mathrm{sb}}(\eta)}{N_{\mathrm{tr}}^{\mathrm{nom}}(\eta)} \tag{8.7}$$

Figure 8.9(a) shows the correction factor as a function of η. As ϵ_{corr} was found to have no strong dependence on p_T, the correction was only made as a function of η to minimise its statistical uncertainty. The small potential dependency on the particle momentum due to slightly different ionisation was not significant in comparison to the statistical limitation of the dataset. At low

p_T, tracks bend more in the transverse plane such that they have a longer path length in silicon. The change to the efficiency was calculated and found to be negligible. Although kaons are more heavily ionising than pions at low p_T, the fraction of kaons is small, such that even if kaons were reconstructed with twice the efficiency, the change to the average efficiency would be at the sub-percent level.

The track reconstruction efficiency at $\sqrt{s} = 2.36$ TeV before and after correction is shown in Fig. 8.9(b). The uncertainties on the correction factor shown are statistical, and the size of this variation (2 %) is used to estimate the systematic uncertainty due to the correction. In addition, the number of tracks as a function of η was compared between the data taken with the SCT in standby at $\sqrt{s} = 900$ GeV and $\sqrt{s} = 2.36$ TeV. Although sensitive to the shape of the underlying particle multiplicity distribution, the bin-by-bin variation in the multiplicity was taken as an estimate of the size of the systematic uncertainty on this correction by assuming that it was independent of the centre of mass energy. The relative fraction varies as a function of η from 1 to 5%. An additional systematic uncertainty on the correction factor was estimated from the average deviation, which is 3%.

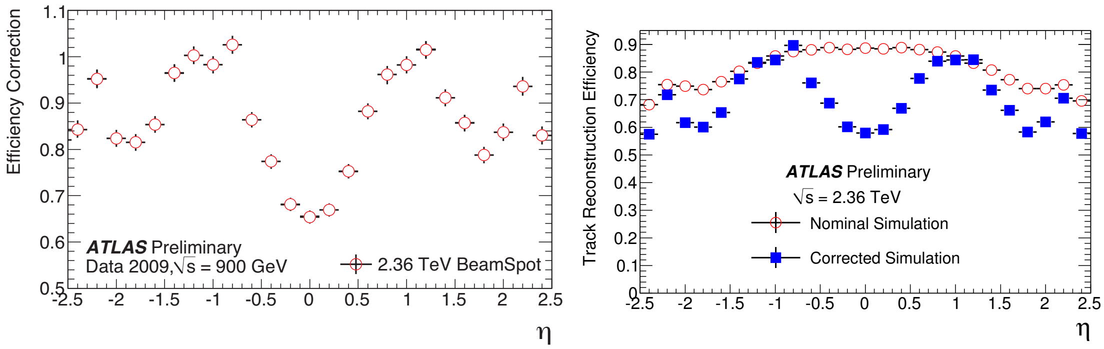

(a)

(b)

Figure 8.9: The correction applied to the track reconstruction efficiency at $\sqrt{s} = 2.36$ TeV to account for the SCT being in standby (a) and the track reconstruction efficiency at $\sqrt{s} = 2.36$ TeV with (corrected) and without (nominal) the correction (b).

8.6 Measurement of the Secondary Rate

Secondary particles typically have larger impact parameters than primary particles because they are produced away from the location of the primary interaction. Cuts were applied to the impact parameters to minimise the fraction of secondaries accepted. In addition, the tails of the transverse impact parameter distribution were used to determine the rate of secondaries in data with respect to the simulation.

Figure 8.10 (a) shows the d_0 distribution in data and simulation. The distribution of secondaries from the simulation, in green, shows how the fraction of secondaries increases with d_0. The ratio of d_0 between data and simulation is shown in Fig. 8.10 (b). The small differences in the shape of the core of the distribution are due to differences in the p_T spectrum between data and simulation. For larger values of d_0 the ratio is flat. A fit to the primary and secondary templates in the range of $2 < d_0 < 10$ mm yielded a scaling factor of 1.00 ± 0.02 in the rate between data and simulation. The uncertainty is purely statistical. This means that the rate of secondaries in data is the same as that predicted by simulation.

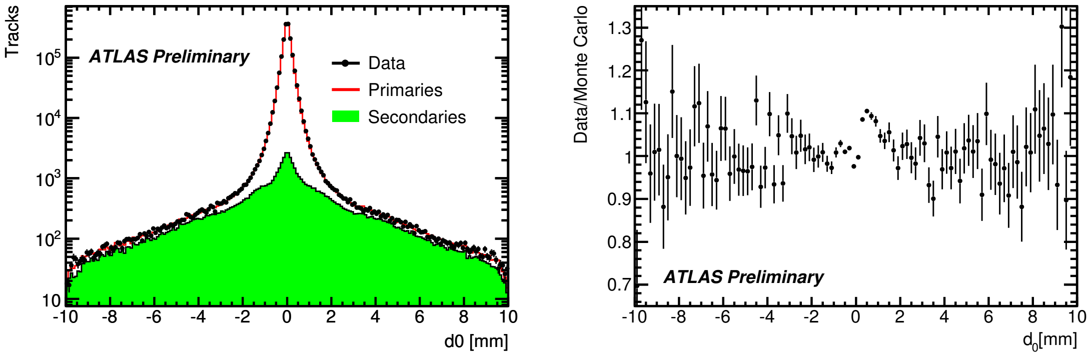

(a)

(b)

Figure 8.10: a) Comparison of the d_0 distribution in data (points) and simulation (histogram). The secondary template is shown in green. b) Ratio of d_0 in data to simulation [97].

The systematic uncertainties on the secondary rate were estimated by varying aspects of the fit procedure. The scale factor varied by 3% if the fit was made to the fraction of secondaries while fixing the fraction of primaries and by 2% when the total number of tracks in data was fixed. The scale factor varied by 1% when the fit range was varied by 0.03 mm and by 3% when the fraction of secondaries from decays or hadronic interactions was varied. From these various contributions, the total systematic uncertainty on secondary rate was estimated to be 5%.

As most secondaries are produced in hadronic interactions in the detector material, the rate of secondaries varies as a function of the pseudorapidity (see Fig. 8.11(a)). The fraction of secondaries as a function of p_T is shown in Fig. 8.11(b) at $\sqrt{s} = 900$ GeV and $\sqrt{s} = 2.36$ TeV. The rate of secondaries increases with the centre of mass energy because the average secondary p_T spectrum increases with the p_T spectrum of the parent primaries. The secondary rate was corrected as a function of p_T and η with the distributions estimated in simulation, but using the normalisation factor derived from data.

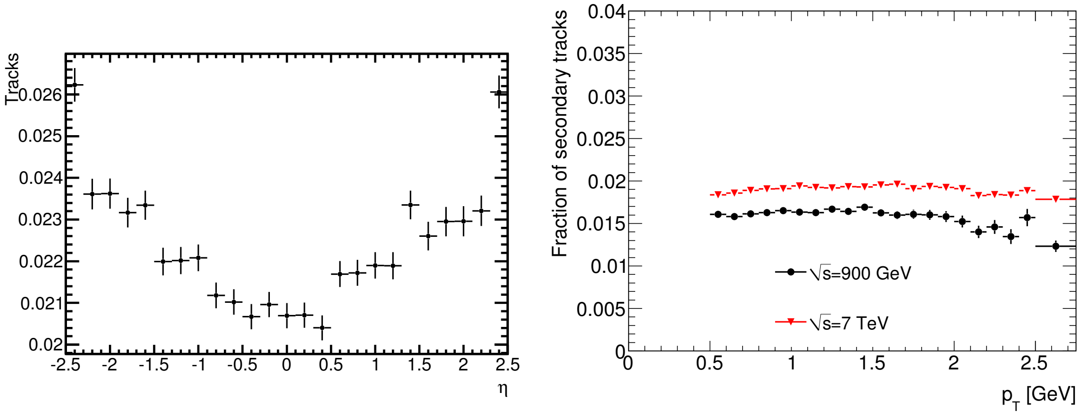

(a) As a function the pseudorapidity[97]

(b) As a function of the transverse momentum[42]

Figure 8.11: The fraction of secondary tracks as a function of η and p_T .

The rate of secondaries was measured using the same strategy at $\sqrt{s} = 7$ TeV, but the lack of an appropriate simulation sample at $\sqrt{s} = 2.36$ TeV meant that the method could not be applied. However, as it was well described in simulation at both $\sqrt{s} = 900$ GeV and $\sqrt{s} = 7$ TeV, it is assumed that it was also well-described at $\sqrt{s} = 2.36$ TeV. Figure 8.12 compares the d_0 distribution in data at $\sqrt{s} = 900$ GeV between when the SCT was at nominal or in standby. There is no change to the core of the distribution, but the tails are ∼20% lower. This is not evidence of a lower secondary rate, but the low SCT hit efficiency means that the requirements on the number of silicon hits per track disfavours less well-reconstructed tracks that would populate the tails of the distributions. If the distributions are compared for tracks with the same number of hits, the tails of the distribution agree well. Therefore, no systematic uncertainty on the rate of secondaries was assigned due to the change in the tails of the d_0 distribution with the SCT in standby mode.

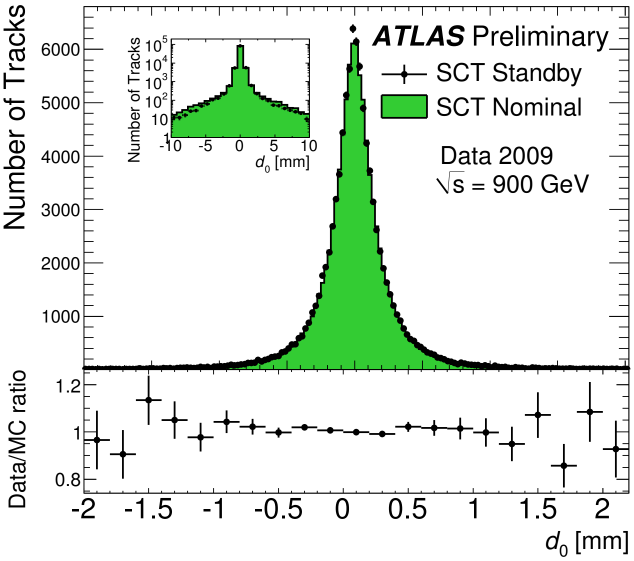

Figure 8.12: The transverse impact parameter distribution with the SCT at nominal or in standby at $\sqrt{s}$ = 900 GeV. The inset shows the ratio of the d_0 distribution with the SCT in standby to nominal.

The final estimate of the rate of secondaries in the selected track sample was $2.20 \pm 0.05(\text{stat.}) \pm 0.11(\text{syst.})\%$ at $\sqrt{s} = 900$ GeV, and $2.25 \pm 0.02(\text{stat.}) \pm 0.11(\text{syst.})\%$ at $\sqrt{s} = 7$ TeV. The rate of fake tracks was estimated to be below 10^{-3} at all centre of mass energies in simulation and was therefore neglected.

8.7 Further Systematic Uncertainties on the Efficiency

8.7.1 Material

The leading cause of track reconstruction inefficiency is hadronic interactions, the rate of which is proportional to the amount of material in the Inner Detector. Therefore, the uncertainty on the material budget translates directly into an uncertainty on the track reconstruction efficiency. The ultimate constraints on the material in the Inner Detector are expected to be determined using photon conversions. However, an accurate study of photon conversions requires an ample quantity of data, significantly more than was recorded at $\sqrt{s} = 900$ GeV. A number of alternative techniques were pursued to estimate the level of agreement between data and simulation.

Simulation samples in which the total material budget in the Inner Detector had been increased by 10% or 20% (see Section 6.4.2) were used to determine the sensitivity of each technique to the material. Figure 8.13 shows the ratio of the track reconstruction efficiency for each sample with respect to the nominal simulation. The decrease in the efficiency compared to the nominal simulation is large: approximately 3% for the sample with 10% additional material. The efficiency decreases more at low transverse momenta because such tracks have a higher probability of undergoing multiple scattering. The change to the efficiency varies with η and is inversely proportional to the distribution of the detector material.

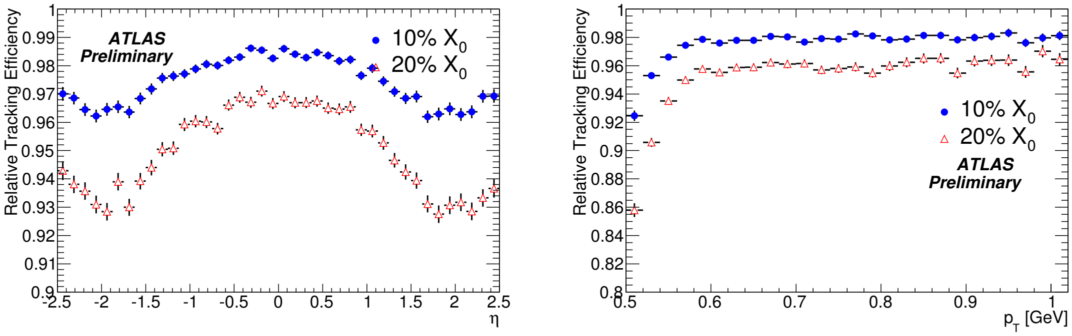

(a) As a function the pseudorapidity

(b) As a function of the transverse Momentum

Figure 8.13: The ratio of the track reconstruction efficiency in the simulation samples with additional material to the efficiency in the nominal simulation at $\sqrt{s} = 900$ GeV.

Two categories of methods were used to assess the sensitivity to additional material. The first is sensitive to the amount of material in radiation lengths and the second to the amount of material in nuclear interaction lengths. Together they provide complementary views of the material of the detector.

A technique sensitive to the number of radiation lengths in the detector is the mass of the K_s^0 meson [49]. The K_s^0 decays into two charged pions, which interact while traversing the detector material. Inaccuracies in the detector material cause the correction to track momenta due to energy lost through ionisation to be incorrect, which biases the reconstructed K_s^0 mass. The width of the

K_s^0 is sensitive to multiple scattering. The mean and width of the K_s^0 mass are a function of the radius at which the K_s^0 are shown in Fig. 8.14(a) for data and simulation. The results in data lie between the results predicted by the nominal simulation and simulation with 10% additional material [49].

The length of tracks in the SCT is sensitive to the amount of material in nuclear interaction lengths. More nuclear interaction lengths result in a larger number of short tracks. This was studied in two different ways: by comparing the $N-1$ efficiency of the SCT hit requirement between data and the simulation samples with additional material, and by comparing the rate of tracks containing different patterns of hits and holes in the SCT (see [37]). Figure 8.14(a) shows the $N-1$ efficiency of requiring 6 SCT hits in data, the nominal simulation and the additional material samples. The data is consistent with the nominal simulation sample for all η except at the edge of the detector acceptance. The systematic uncertainty due to the material budget in these regions has already been discussed in the context of the SCT extension efficiency in Section 6.4. Otherwise both methods estimated the uncertainty on the material budget to be smaller than 10%.

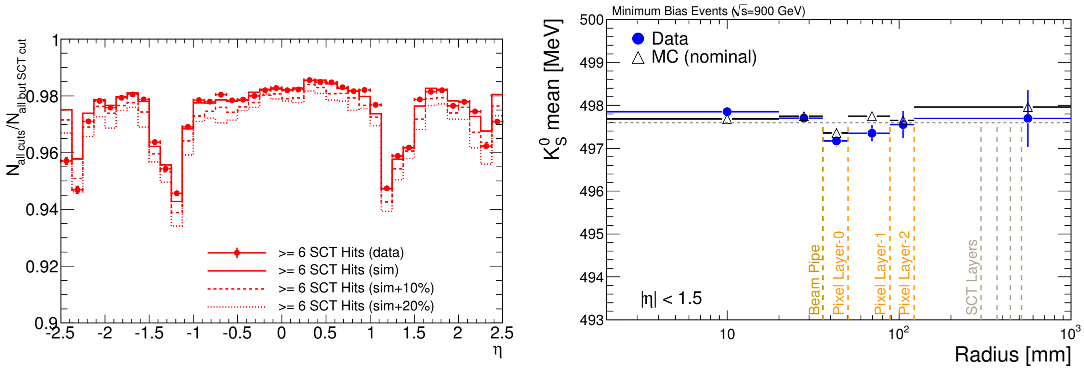

(a) Track Length

(b) K_s^0 Mass [37]

Figure 8.14: a) The $N-1$ efficiency of the SCT hit cut in data compared to the nominal simulation and the simulation with additional material b) and the mean of the K_s^0 mass as a function of the decay radius in data and simulation at $\sqrt{s} = 900$ GeV.

The systematic uncertainty due to the GEANT4 [17] model of hadronisation was studied by comparing simulations produced using two different hadronisation models. No statistically significant difference in the number of reconstructed tracks was observed when comparing the default model used in ATLAS, QGSP (Quark Gluon String Precompound) [17] to the FTFP (Fritiof Precompound) [17] model.

All the studies discussed here and further studies in [37] provided strong evidence that the description of the material budget in simulation was better than 10%. The largest decrease to the track reconstruction efficiency as a function of η between the nominal and 10% extra material simulation was found to be 3% (see Fig. 8.13(a)). This was therefore applied conservatively as a global systematic uncertainty on the efficiency for all η.

8.7.2 Uncertainties at Low-p_T

The track reconstruction efficiency for particles with momenta just above the p_T cut depends on the p_T resolution. In addition, at $\sqrt{s} = 900$ GeV, the track reconstruction algorithms applied the same p_T cut at each stage of the pattern recognition. This means that the efficiency in this region depends not only on the final p_T resolution, but also the p_T resolution at each stage of the pattern recognition. Most importantly this depends on how well each resolution is modelled by the simulation. To estimate how different the resolution could be between data and simulation, the ratio of the number tracks in successive p_T bins in shown in Fig. 8.15. The ratio was used instead of the raw p_T spectrum to minimise differences between data and simulation in the shape of the p_T spectrum. Data and simulation differ by approximately 5% for $500 < p_T < 600$ MeV. An uncertainty of 5% in this region corresponds to an uncertainty of approximately 15-20% on the track resolution.

The size of the systematic uncertainty at low p_T motivated the changes to the track reconstruction configuration discussed in Section 8.3. As the internal cut was lowered to 100 MeV for the analyses at $\sqrt{s} = 2.36$ TeV and $\sqrt{s} = 7$ TeV, the efficiency no longer depends on the track resolution at the internal stages of the pattern recognition. Nonetheless, it does depend on the final track resolution. Varying this resolution by 10% changed the efficiency by 1%, which was taken as the systematic uncertainty. The change to the efficiency when varying the resolution did not depend strongly on the shape of the p_T spectrum.

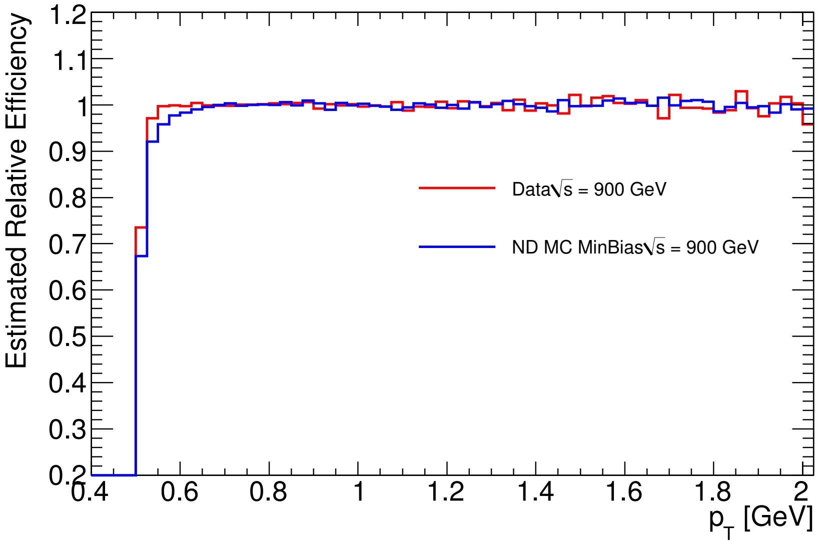

Figure 8.15: The bin-to-bin ratio of the transverse momentum spectrum in data (red) and simulation (blue) at $\sqrt{s} = 900$ GeV. The value for each bin is the ratio of the number of the tracks in that bin to the number of tracks in the next bin.

8.7.3 Alignment

Large inaccuracies in the positions of detector elements, or misalignments, can reduce the track reconstruction efficiency. Smaller misalignments can increase the track parameter resolution such that reconstructed tracks do not pass the track selection cuts. In either case the track reconstruction efficiency is reduced. The analysis at $\sqrt{s} = 900$ GeV used a set of detector alignment constants that were produced using the cosmic ray data. Because cosmic rays typically pass through ATLAS vertically, the number of cosmic tracks passing through the end cap were small, resulting in large uncertainties on the positions of the detector elements in the end-cap.

The size of the uncertainty on the efficiency due to alignment was estimated using two techniques. Simulation samples were produced in which the positions of the detector elements were distorted. Two samples were produced: the first smeared the positions by the expected residual misalignment after one day of collision data; the second by the expected misalignment after 100 days of collision data. All samples used the same input dataset. The number of selected tracks varied by less than 1% between the nominal and the day one misalignment samples, except in the end-caps where the difference was up to 2%. The variation between the nominal and the day 100 sample was at the sub-percent level.

The alignment constants were continually being updated as data at $\sqrt{s} = 900$ GeV was recorded. Each iteration improved the accuracy of the estimate of the detector positions. The same data was reconstructed using two subsequent alignment sets and the number of selected tracks was compared. The change to the number of tracks was less than 1% with slightly larger changes observed in the end caps.

Using these two studies, the uncertainty on the track reconstruction efficiency due to misalignment was estimated to be at most 1%.

8.7.4 Particle Composition

The track reconstruction efficiency depends on the type of the charged particle. This means that the total efficiency is sensitive to the fraction of different particle types, which depends on the accuracy of the production cross-sections in simulation. The track reconstruction efficiency was calculated when the fraction of pions, kaons and protons was varied by ±10% and the fraction of electrons and muons by a factor of 3. As the overwhelming fraction of particles are charged pions, the total efficiency varied by only 0.2%. Therefore the systematic uncertainty due to the particle composition was taken as 0.2%.

8.7.5 Mismeasured Tracks at High-p_T

The track momentum resolution improves with increasing transverse momentum because the scattering cross-section decreases with momentum. However, the charged particle p_T spectrum falls very rapidly, such that at high p_T the distribution becomes sensitive to small non-Gaussian tails in the momentum resolution. These tails are produced by tracks from low-p_T particles for which the momentum estimate is poor. Most of such tracks are produced by pions, which scatter between the pixel detector and the SCT such that the track segment in the pixel detector and the SCT have significantly different momenta. The fraction of these mismeasured tracks in the selected tracks is strongly suppressed by the 6 SCT hit cut requirement because it removes shorter tracks.

The fraction of mismeasured tracks increases with increasing transverse momentum. However, the momentum range studied in the $\sqrt{s} = 900$ GeV and $\sqrt{s} = 2.36$ TeV analyses is small enough

Systematic Uncertainty	Systematic
Truth Primary Definition	±0.4%
Track Selection	±2.5% ($2.4 < \|\eta\| > 2.5$) ±1% ($2 < \|\eta\| < 2.3$) ±0.5% (otherwise)
Standby Correction	5*%
Material	±3%**
Alignment	±1%
SCT Extension	±6% ($2.2 < \|\eta\| < 2.5$) ±4% ($1.6 < \|\eta\| < 2.2$)
Low p_T	±5%***, ±1% ($0.5 < p_T < 0.6$ GeV)
Particle Composition	±0.2%
Total at $\sqrt{s} = 900$ GeV	8.3% ($2.4 < \|\eta\| < 2.5$; $p_T > 0.6$ GeV) 3.9 % ($\eta = 0$; $p_T > 0.6$ GeV) 6.8 % ($\eta = 0$; $0.5 < p_T < 0.6$ GeV)
Total at $\sqrt{s} = 2.36$ TeV	6 % ($\eta = 0$; $p_T > 0.6$ GeV)
Total at $\sqrt{s} = 7$ TeV	4.6 % ($\eta = 0$; $0.5 < p_T < 0.6$ GeV)

Table 8.1: Summary of the systematic uncertainties on the tracking efficiency. All systematic uncertainties are quoted relative to the tracking efficiency, except for the uncertainty on the material (**) which is absolute. ***Denotes an uncertainty applied at $\sqrt{s} = 900$ GeV only. *Denotes an uncertainty applied at $\sqrt{s} = 2.36$ TeV only.

so that few of these tracks are accepted. The $\sqrt{s} = 7$ TeV analysis, on the other hand, covers a larger range in transverse momentum. As these mismeasured tracks occur most often at high-η, the fraction was estimated by studying the shape of the η distribution in bins of p_T to determine at what p_T it changes. The fraction of these mismeasured tracks was estimated to be smaller than the statistical uncertainty in each transverse momentum bin. See [7] for further discussion of cuts used to estimate and suppress the rate of such tracks.

8.8 Summary

The systematic uncertainties on the track reconstruction efficiency are summarised in Table 8.1. As the track reconstruction efficiency does not depend on the centre of mass energy, the systematic uncertainties are for the most part identical for the analyses at $\sqrt{s} = 900$ GeV, $\sqrt{s} = 2.36$ TeV and $\sqrt{s} = 7$ TeV. The only differences are the additional 5% uncertainty due to the efficiency correction at $\sqrt{s} = 2.36$ TeV and the 5% uncertainty at low p_T at $\sqrt{s} = 900$ GeV.

The track reconstruction efficiency as a function of η and p_T at $\sqrt{s} = 900$ GeV is shown in

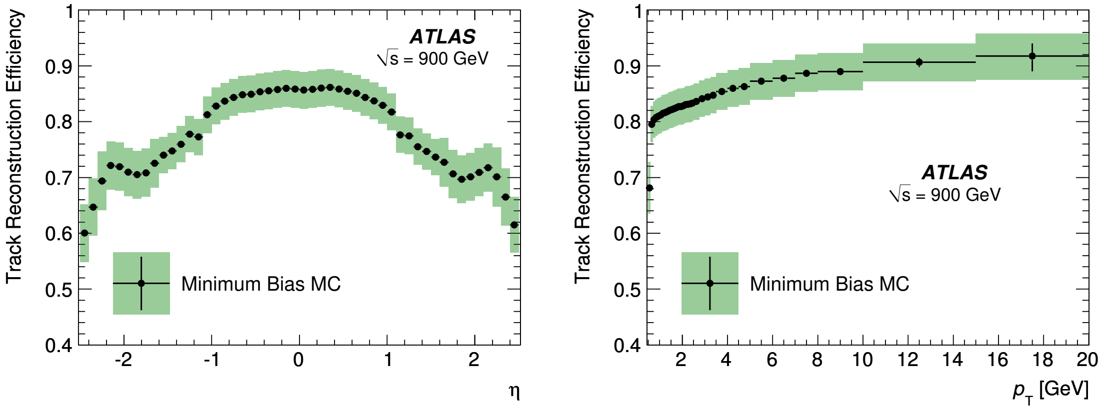

(a) Pseudorapidity

(b) Transverse Momentum

Figure 8.16: The track reconstruction efficiency and the systematic uncertainty as a function of η and p_T at $\sqrt{s} = 900$ GeV [4]

Fig. 8.16. The initial increase in efficiency between the first two p_T bins is due to the track momentum resolution. The efficiency as a function of η follows the distribution of the amount of material in the detector. The systematic uncertainties are shown as green bands and increase at higher η, because the uncertainty on the material budget is larger in the forward regions.

Chapter 9

Correction Procedure and Systematic Uncertainties

9.1 Uncorrected Distributions

The uncorrected charged particle multiplicity distributions are shown in Fig. 9.1. These are the distributions of reconstructed tracks after the application of all event and track selection criteria. No correction was applied to account for events and tracks lost due to event and track selection efficiency. The distributions are shown for data and simulation at $\sqrt{s} = 900$ GeV.

The simulation samples were produced using the Pythia MC09 tune. The contribution from the non-, single- and double-diffractive components to each distribution is shown. The distributions for each component were weighted by the cross-section predicted for that component by Pythia and the sum of the distributions was normalised to the number of tracks in data. The insets show the ratio of each distribution from simulation to data. Direct comparisons of the distributions between data and simulation cannot be made because although the track reconstruction efficiency is the same, the event selection efficiency differs.

The number and size of the bins used for each distribution were determined from the statistical uncertainty on each bin in the uncorrected distributions. This means that the bin widths are small at low n_{tr} and p_T but increase at high n_{tr} and p_T. The multiplicity as a function of the pseudorapidity has a constant bin width. Different bin widths and ranges were used at the different centre of mass energies because the amount of data analysed varies.

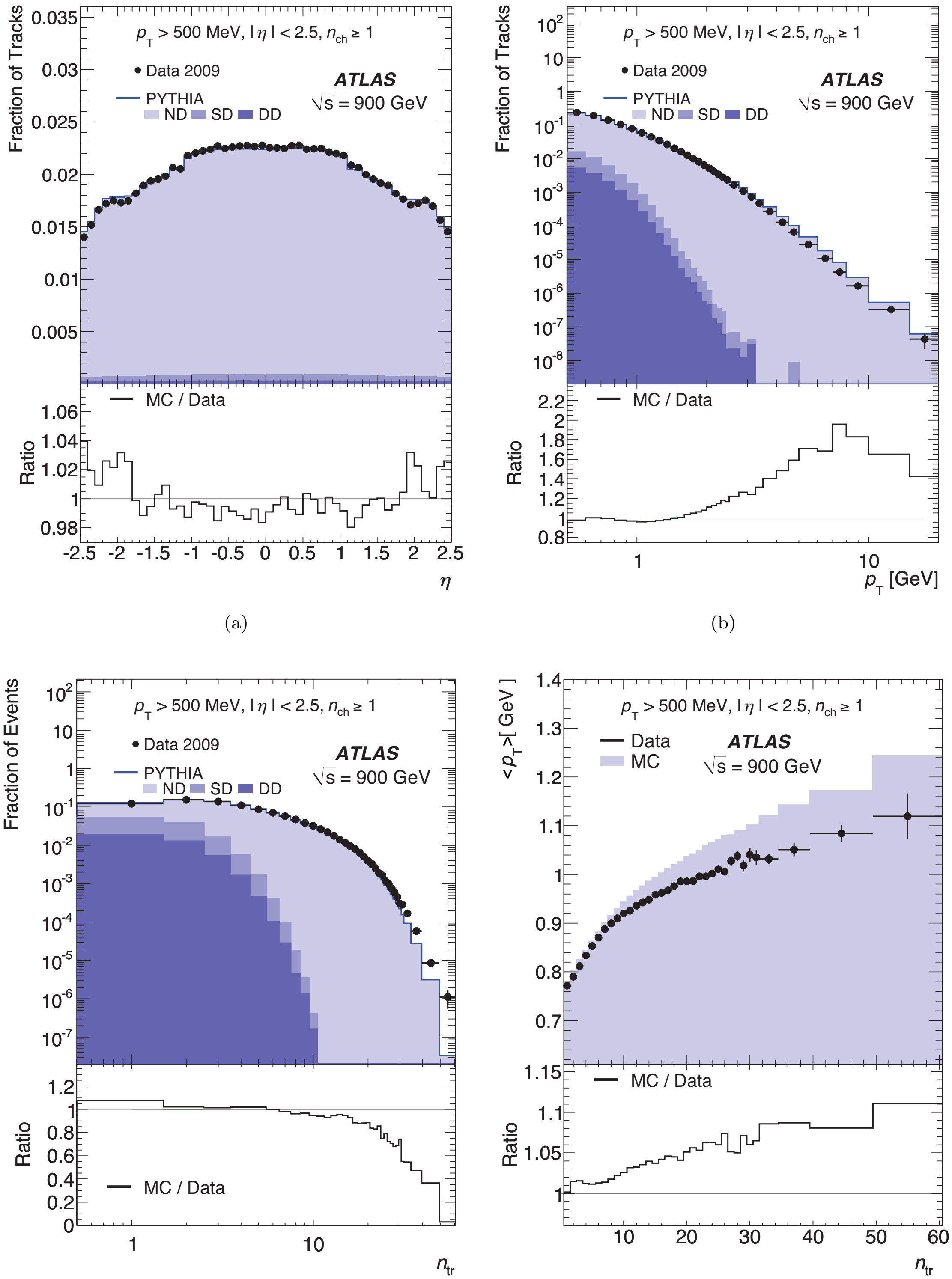

(a)

(b)

(c)

(d)

Figure 9.1: Uncorrected distributions of reconstructed tracks from data and the Pythia MC09 Monte Carlo tune at $\sqrt{s} = 900$ GeV as a function of pseudorapidity (a), transverse momentum (b), the multiplicity (c) and the average transverse momentum as a function of the number of reconstructed tracks [53]. The simulation includes the non-, single- and double-diffractive components weighted according to cross-sections predicted by Pythia. The distributions are normalised by the number of reconstructed tracks. The insets show the ratio of the simulation to data.

9.2 Correcting from Tracks to Primary Particles

In order to obtain the charged particle multiplicity distributions from the distributions as a function of the number of reconstructed tracks (Fig 9.1), corrections need to be applied to account for the event and track selection efficiencies. The corrections were made by applying weights to each event for the event selection efficiency and to each track for the track selection efficiency. The correction procedure applied at $\sqrt{s} = 900$ GeV, $\sqrt{s} = 2.36$ TeV and $\sqrt{s} = 7$ TeV was identical.

9.2.1 Event Selection Efficiency Correction

The trigger and vertex efficiency were corrected for using the following weights applied to each event:

$$w_{\mathrm{ev}}(n_{\mathrm{Sel}}^{\mathrm{BS}}) = \frac{1}{\epsilon_{\mathrm{trig}}(n_{\mathrm{Sel}}^{\mathrm{BS}})} \cdot \frac{1}{\epsilon_{\mathrm{vtx}}(n_{\mathrm{Sel}}^{\mathrm{BS}})}.$$

Here, $\epsilon_{\mathrm{trig}}(n_{\mathrm{Sel}}^{\mathrm{BS}})$ and $\epsilon_{\mathrm{vtx}}(n_{\mathrm{Sel}}^{\mathrm{BS}})$ are the trigger and vertex reconstruction efficiencies discussed in Section 7.1 and 7.2 respectively. The trigger and vertex efficiency are parametrised as a function of the number of pre-selected tracks, $n_{\mathrm{Sel}}^{\mathrm{BS}}$, to allow the efficiency to be measured in data. The correction for the trigger and vertex efficiency is non-zero only for events containing few pre-selected tracks.

9.2.2 Track Selection Efficiency Correction

The p_T and η distributions of selected tracks were corrected by using a weight applied to each track:

$$w_{\mathrm{trk}}(p_{\mathrm{T}}, \eta) = \frac{1}{\epsilon_{\mathrm{trk}}(p_{\mathrm{T}}, \eta)} \cdot (1 - f_{\mathrm{sec}}(p_{\mathrm{T}})) \cdot (1 - f_{\mathrm{ps}}(p_{\mathrm{T}}, \eta)),$$

where

- ϵ_{trk} is the track reconstruction efficiency in a specific p_T and η bin (see Section 8)
- $f_{\mathrm{sec}}(p_{\mathrm{T}})$ is the fraction of secondary particles (see Section 8.6)
- $f_{\mathrm{ps}}(p_{\mathrm{T}}, \eta)$ is fraction of tracks produced by primary particle outside the phase space.

No correction was applied for fake tracks, because the fraction of fake tracks was shown to be below 10^{-3}[37]. The fraction of secondaries was corrected as a function of p_T as shown in Fig. 8.11.

The track reconstruction efficiency was applied as a two-dimensional correction as a function of p_T and η (see Fig. 9.2). As the charged particle multiplicity decreases rapidly with p_T, there are large fluctuations in the track reconstruction efficiency at high p_T due to the limited size of the simulation sample. To minimise these fluctuations, which would have resulted in large systematic uncertainties, the correction for the track reconstruction efficiency used fewer bins in η for $p_T > 7$ GeV.

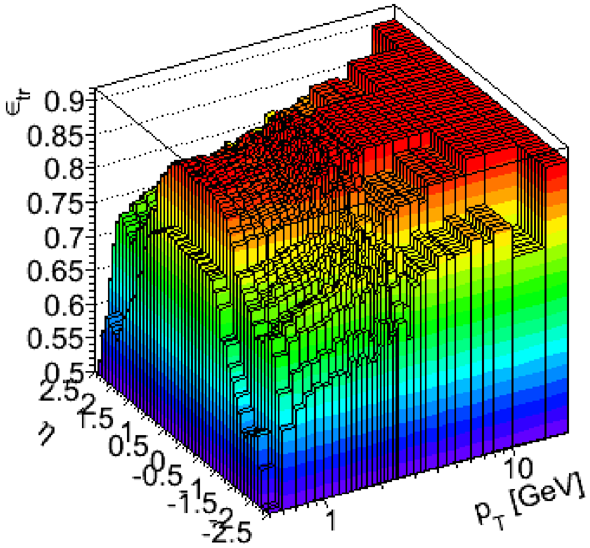

Figure 9.2: The track reconstruction efficiency as a function of p_T and η at $\sqrt{s} = 900$ GeV [53].

A certain fraction of the selected tracks were produced by particles outside the kinematic acceptance of the analysis, i.e., particles with $p_T < 500$ MeV or $|\eta| > 2.5$. The fraction of these tracks depends on the track resolution in p_T and η and they need to be removed from the final distributions. The track reconstruction efficiency, however, does not correct for these tracks because it is calculated for generated particles within the kinematic range of the analysis. Therefore an additional correction factor, the phase space correction factor or f_{ps}, was used. Fig 9.3 shows the fraction of selected tracks from particles outside the phase space. The phase space correction is only non-zero for tracks near the edge of the acceptance, i.e. tracks with $0.5 < p_T < 0.7$ GeV or $|\eta| > 2.4$.

Due to the track parameter resolution, some tracks pass the selection cuts but migrate to a different bin from the original generated particle. Bin migration occurs when the track parameter resolution is significantly larger than the bin width. The η resolution is much smaller than the bin width in η, therefore the multiplicity as a function of η is not affected by bin migration. The p_T resolution, on the other hand, is not significantly smaller than the bin width and varies with p_T. The p_T resolution was studied using $K_s^0 \to \pi^+\pi^-$ decays and found to be in agreement between data and simulation [74]. Therefore the change to the distribution due to the finite resolution was estimated using the Monte Carlo simulation samples. The p_T resolution changed the distribution by 0.3% for most of the p_T range, but to a larger degree at very low p_T (2%) or very high p_T(1% for $p_T > 7$ GeV).

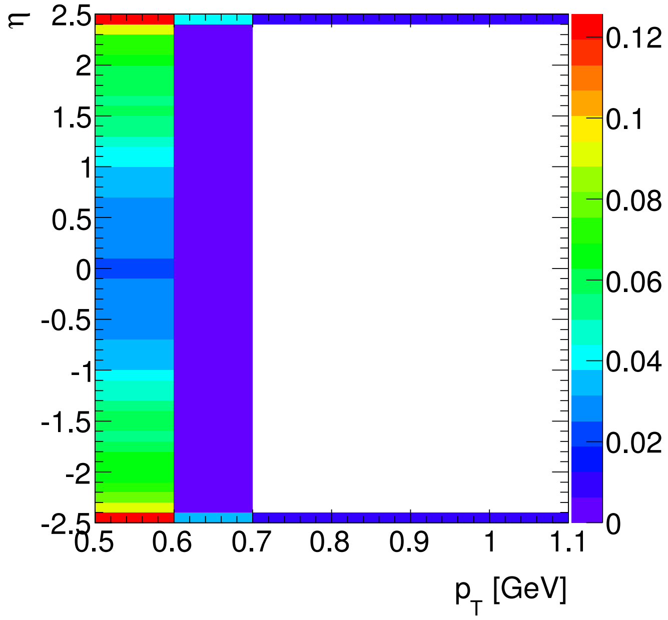

Figure 9.3: The correction for tracks produced by particles outside the kinematic acceptance of the analysis at $\sqrt{s} = 900$ GeV [53].

9.3 Unfolding the n_{ch} distribution

For the n_{ch} and $\langle p_{\mathrm{T}} \rangle$ vs n_{ch} distributions, a Bayesian unfolding technique [67] was used to correct from the number of selected tracks to the number of charged particles in an event. A two-dimensional unfolding matrix, $M_{\mathrm{ch,Sel}}$, expressing the probability that a particular selected track multiplicity n_{Sel} was due to n_{ch} particles, was populated using the Monte Carlo simulation. The matrix was then used to convert the n_{Sel} distribution to the n_{ch} distribution via matrix multiplication. The unfolding matrix was normalised such that the sum over all n_{ch} for a given n_{Sel} is unity. This normalisation ensured that the number of events was conserved[1]. Table 9.1 shows the first 100 entries of the matrix. For low multiplicity events the matrix is largely diagonal, but picks up off-diagonal terms with increasing multiplicity.

The unfolding matrix is determined by the average track reconstruction efficiency for events containing different amounts of charged particles. The track reconstruction efficiency varies with the particle transverse momentum and pseudorapidity. Therefore the contents of the unfolding matrix are sensitive to the kinematic distributions of the particles in each bin of n_{ch} in the simulation. To assess the size of the effect, the unfolding matrix was filled using both PHOJET and the MC09 tune of PYTHIA and the full correction procedure was applied to the data. The total number of events varied by 2% between the two generators, but the number of events for $n_{\mathrm{ch}} = 1$ varied by 5%.

Therefore an iterative method was developed to reduce the dependence on the simulation sample used to fill the unfolding matrix. In the first iteration of the correction procedure, the n_{ch} distribution was calculated using the matrix determined solely from the MC simulation. The n_{ch} distribution in the simulation was then reweighted by the n_{ch} distribution measured in the first iteration and the contents of the matrix were updated. The new unfolding matrix was then applied to the raw data to determine the n_{ch} distribution. The procedure was repeated until the change in the n_{ch} distribution between iterations was less than 1%. The procedure typically converged after four iterations.

A certain number of events were lost because no tracks were reconstructed. The matrix correction does not correct for these events, because the fraction of events with $n_{Sel} = 0$ was not included in the analysis[2]. The fraction of events lost depends directly on the track reconstruction efficiency.

---

[1] The total number of events is conserved by the application of the unfolding matrix, but not by the full correction procedure. This is due to the correction that is made for events in which no tracks were reconstructed. This correction depends on number of events containing few tracks.

[2] The number of events with $n_{Sel} = 0$ was not measured because the event selection efficiency of such events is

n_{ch} \ n_{Sel}	1	2	3	4	5	6	7	8	9	10
1	0.81	0.027	0	0	0	0	0	0	0	0
2	0.14	0.6	0.033	0	0	0	0	0	0	0
3	0.031	0.26	0.49	0.035	0	0	0	0	0	0
4	0.0071	0.082	0.3	0.41	0.037	0	0	0	0	0
5	0	0.022	0.12	0.32	0.35	0.038	0	0	0	0
6	0	0.0053	0.038	0.15	0.32	0.3	0.037	0	0	0
7	0	0	0.011	0.056	0.18	0.31	0.25	0.035	0	0
8	0	0	0	0.018	0.076	0.2	0.3	0.21	0.033	0
9	0	0	0	0.0053	0.028	0.095	0.21	0.28	0.18	0.031
10	0	0	0	0	0.0091	0.039	0.12	0.22	0.26	0.16

Table 9.1: The first 10 × 10 entries of $M_{ch,Sel}$ matrix used to correct distributions from N_{Sel} to N_{ch} at $\sqrt{s} = 900$ GeV. The sum over all entries along the n_{ch}-axis for a given n_{Sel} is unity [53].

Therefore, a correction factor $f_W = 1/(1 - (1 - \langle\epsilon\rangle)^{n_{\rm ch}})$ was applied to the $n_{\rm ch}$ distribution using the average track reconstruction efficiency. The correction assumes that the track reconstruction efficiency is independent of $n_{\rm ch}$. The fraction of events in each $n_{\rm ch}$ bin with no reconstructed tracks is estimated by applying the efficiency to the power of the number of charged particles in that bin. Integrated over the full kinematic acceptance in p_T and η, the average value of the track reconstruction efficiency at $\sqrt{s} = 900$ GeV is $76 \pm 5\%$.

The $\langle p_{\rm T}\rangle$ versus $n_{\rm ch}$ distribution was corrected in three steps. Firstly, each event was weighted by $w_{\rm ev}(n_{\rm Sel}^{\rm BS})$ to correct for the event selection efficiency. Secondly, a correction was applied to convert the average reconstructed track momentum to the average primary particle momentum in each bin of $n_{\rm Sel}$. This correction was determined from the simulation. Finally, the matrix $M_{\rm ch,Sel}$ was used to correct from $n_{\rm Sel}$ to $n_{\rm ch}$. In summary, the value of $\langle p_T\rangle$ in each bin is given by:

$$\langle p_T\rangle_i = \frac{\Sigma_j M_i^j \langle p_T\rangle_j n_{Sel}^j}{\Sigma_j M_i^j n_{Sel}^j} \tag{9.1}$$

where the index i labels the number of charged particles and the index j labels the number of reconstructed tracks. Equation 9.1 can be viewed as a generalisation of the weighted mean of the average transverse momentum.

For the analysis at $\sqrt{s} = 2.36$ TeV, the lack of an appropriate simulation sample describing the efficiency with the SCT in standby meant that the $M_{\rm ch,Sel}$ could not be estimated accurately

---

extremely low, which would mean that these events would have required a large correction. In addition, such events would be particularly sensitive to non-collision backgrounds from the beam.

from the simulation. The matrix was initially populated using the standard simulation sample and then corrected by the average of the data-driven efficiency correction discussed in Section 8.5. To apply the correction, a fraction of the selected tracks in each event was randomly discarded. The fraction of tracks discarded was determined by the amount that the track reconstruction efficiency decreased after the correction. This improved the description provided by the matrix, but it does not account for the interplay of the highly η-dependent SCT hit efficiency with the variation of the η distribution as a function of n_{ch}. Therefore, the matrix was used to unfold the n_{Sel} distribution to obtain the number of events, but not to measure the n_{ch} or the $\langle p_{\mathrm{T}} \rangle$ vs. n_{ch} distribution. An additional cross-check was made to estimate the systematic uncertainty on the number of events due to this limitation, using the n_{ch} distribution measured with a different technique [120]. The systematic uncertainty on the number of events was found to be 1% using this technique.

9.4 Validation of the Correction Procedure

The correction procedure was validated using the Monte Carlo simulation by comparing the corrected particle distributions to the original primary particle distributions. The corrected distributions were obtained by applying the full correction procedure to the reconstructed track distributions from simulation.

Figure 9.4 shows both the original primary particle multiplicity distributions and the corrected charged particle multiplicity distributions. For the multiplicity as a function of the pseudorapidity, the two are consistent to within 1%. The differences for particles with high p_T are because the distribution was not corrected to account for bin migration due to the momentum resolution. However, this effect is included as a systematic uncertainty. For the n_{ch} distribution the 2% discrepancy in the first bin is because the vertex reconstruction efficiency was measured in data. The efficiency is slightly lower in simulation than in data. All observed differences were added as systematic uncertainties, but their contribution to the total uncertainty is small.

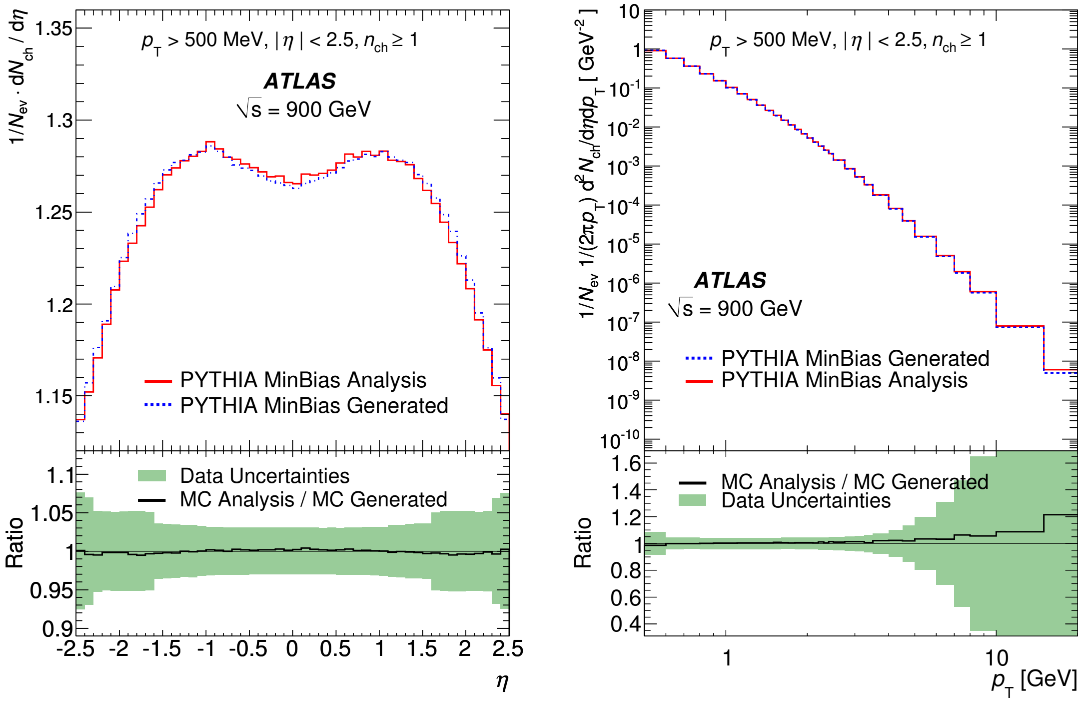

(a) Pseudorapidity (b) Transverse Momentum

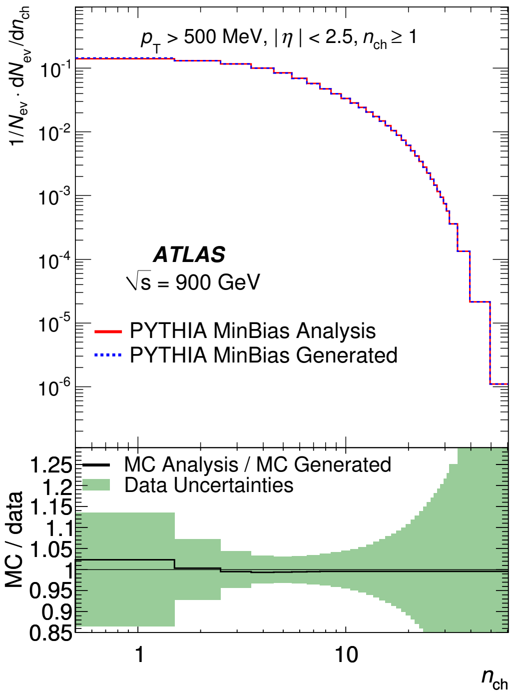

(c) Multiplicity

Figure 9.4: The corrected particle distributions (red) to the original primary particle distributions (blue) in simulation at $\sqrt{s} = 900$ GeV [53]. The corrected particle distributions were obtained using the identical correction procedure and correction factors as those applied to the data. The insets show the ratio of the corrected to input distributions. The systematic uncertainties for the data are shown as a filled green band on the inset.

9.5 Summary of the Systematic Uncertainties on the Multiplicity Distributions

The individual components of the systematic uncertainty have been discussed. The uncertainties on the trigger and vertex reconstruction efficiency discussed in Sections 7.1 and 7.2 are negligible. Uncertainties due to the correction procedure were discussed in Sections 9.2 and 9.3. However, the largest systematic uncertainty is due to the track reconstruction efficiency as shown in Fig. 8.16, which was discussed in Section 8. The systematic uncertainty is significantly larger at forward pseudorapidity, low transverse momentum, or for events containing a single charged particle.

The systematic uncertainties are summarised in Table 9.2, which shows the uncertainties on the charged particle density at central pseudorapidity. The systematic uncertainties are largely identical for the analyses at the three centre of mass energies. However, the systematic uncertainty on the track reconstruction efficiency at $\sqrt{s} = 2.36$ TeV is significantly larger. This is due to uncertainties of the correction used to estimate the change to the track reconstruction efficiency because the SCT was in standby.

The systematic uncertainties on the final charged particle distributions due to the uncertainties on the individual correction factors were determined by varying each factor by $\pm 1\sigma$ of the uncertainty and propagating them through the correction procedure to obtain the final distributions. This does not fully account for the η and p_T dependence of the track reconstruction efficiency. The different sources of systematic uncertainty were assumed to be uncorrelated, so the total uncertainty is determined by adding them in quadrature. The one exception is that the uncertainty on the number of events due to the track reconstruction efficiency is fully correlated with the uncertainty on the track reconstruction efficiency itself. Therefore in the charged particle multiplicity as a function of η, the uncertainty on the number of events cancels part of the uncertainty on the track reconstruction efficiency.

Table 9.2: Summary of systematic uncertainties on the number of events, N_{ev}, and on the charged-particle density $(1/N_{\mathrm{ev}}) \cdot (\mathrm{d}N_{\mathrm{ch}}/\mathrm{d}\eta)$ at $\eta = 0$ at 900 GeV, 2.36 TeV and 7 TeV. The uncertainty on N_{ev} is anticorrelated with $\mathrm{d}N_{\mathrm{ch}}/\mathrm{d}\eta$. All other sources are assumed to be uncorrelated.

Systematic uncertainty on the number of events, $\boldsymbol{N_{\mathrm{ev}}}$			
	900 GeV	2.36 TeV	7 TeV
Trigger efficiency	$< 0.1\%$	$< 0.1\%$	0.2%
Vertex-reconstruction efficiency	$< 0.1\%$	$< 0.1\%$	$< 0.1\%$
Track-reconstruction efficiency	1.1%	1.8%	0.8%
Different MC tunes	0.4%	0.4%	0.4%
Total uncertainty on N_{ev}	1.2%	2.6%	0.9%

Systematic uncertainty on $\boldsymbol{(1/N_{\mathrm{ev}}) \cdot (\mathrm{d}N_{\mathrm{ch}}/\mathrm{d}\eta)}$ at $\boldsymbol{\eta = 0}$			
	900 GeV	2.36 TeV	7 TeV
Track-reconstruction efficiency	4.0%	6.0 %	3.8 %
Trigger and vertex efficiency	$<$ 0.1%	$<$ 0.1%	$<$ 0.1%
Secondary fraction	0.1%	0.1%	0.1%
Total uncertainty on N_{ev}	-1.2%	-2.6%	-0.9%
Total uncertainty on $(1/N_{\mathrm{ev}}) \cdot (\mathrm{d}N_{\mathrm{ch}}/\mathrm{d}\eta)$ at $\eta = 0$	2.7%	4.5%	3.0%

Chapter 10

Results

The distributions of primary charged particles for events with $n_{\mathrm{ch}} \geq 1$ in the kinematic range $p_T > 500$ MeV and $|\eta| < 2.5$ are shown in Fig. 10.1 at $\sqrt{s} = 900$ GeV, Fig. 10.3 at $\sqrt{s} = 2.36$ TeV and Fig. 10.2 at $\sqrt{s} = 7$ TeV. At each centre of mass energy, the results are compared to the predictions from a set of Monte Carlo models discussed in Section 2.5. In addition to the models produced prior to LHC results, the data are compared to the results from the ATLAS Minimum Bias Tune (AMBT) 1 [126].

The data are presented as inclusive distributions. In particular, this means that no correction was made to remove the single diffractive component, which facilitates comparisons to the predictions from a wide range of models and can provide better constraints on models of diffraction.

10.1 Charged Particle Multiplicities at $\sqrt{s} = 900$ GeV

Figure 10.1(a) shows the charged particle multiplicity as a function of the pseudorapidity at $\sqrt{s} = 900$ GeV. It is approximately flat for $|\eta| < 1.5$, but decreases at forward pseudorapidity. The average value is $1.335 \pm 0.003(\text{stat.}) \pm 0.036(\text{syst.})$ charged particles per event and unit of pseudorapidity for $|\eta| < 0.2$. All the Monte Carlo tunes predict a charged particle multiplicity $5 - 10\%$ lower than the measured multiplicity. However, the shape of the pseudorapidity distribution is well described by all models except Pythia DW, which predicts a more pronounced dip in the multiplicity at central pseudorapidity and the Perugia0 model, which predicts a more rapid decrease in the multiplicity at forward η .

The charged particle multiplicity as a function of p_T is shown in Fig. 10.1(b). Significant discrepancies between the measured and predicted multiplicity are observed for $p_T > 0.7$ GeV. The discrepancies increase with p_T. The best agreement with the data is obtained by AMBT1, Perugia0 and PHOJET, which describe the p_T spectrum to within 20%. The ATLAS MC09 tune predicts too many particles at high p_T, while DW predicts too few.

Figure 10.1(c) shows the charged particle multiplicity distribution. The PYTHIA-based models predict more events with $n_{\mathrm{ch}} = 1$ than in data, but fewer events for $n_{\mathrm{ch}} \gtrsim 10$. This results in an average number of charged particle lower than in data as noted in Figs. 10.1(a) and 10.1(b). PHOJET and AMBT1 describe the n_{ch} spectrum to within 10%. Most models do not predict sufficient high multiplicity events. The discrepancy for events with $n_{\mathrm{ch}} \gtrsim 40$ is almost a factor of two, but the data are limited by the systematic uncertainties because the uncertainty on the efficiency to reconstruct each track is additive.

The average p_T as a function of n_{ch} is shown in Fig. 10.1(d). The average transverse momentum increases with the number of charged particles. The slope of the distribution changes around $n_{\mathrm{ch}} = 10$ as previously noted by CDF [8]. The Perugia0 and AMBT1 models describe the data well, but the other models have discrepancies at the 10% level. The other PYTHIA-based models predict too large an average transverse momentum in high multiplicity events, while PHOJET predicts too small an average p_T. The average p_T as a function of n_{ch} is particularly sensitive to the values of the colour reconnection parameters in the models. Therefore the ATLAS MC09c tune, which was based on the ATLAS MC09 tune, but with colour reconnection parameters retuned using the CDF tune of $\langle p_{\mathrm{T}} \rangle$ vs n_{ch} provides a significantly better description of the data.

10.2 Charged Particle Multiplicities at $\sqrt{s} = 7$ TeV

The charged particle multiplicity as a function of the pseudorapidity at $\sqrt{s} = 7$ TeV is shown in Fig. 10.2(a). The distribution has a slightly more pronounced dip at central pseudorapidity than at $\sqrt{s} = 900$ GeV, but then is approximately constant for $|\eta| < 1.5$. The average value is 2.427 ± 0.004(stat.) ± 0.073(syst.) charged particles per event and unit of pseudorapidity for $|\eta| < 0.2$. The multiplicity is $\sim 5\%$ higher than the prediction from the ATLAS MC09 tune of PYTHIA. The DW, Perugia0 and PHOJET models predict a multiplicity that is 20% lower than the measured value, a larger discrepancy than at $\sqrt{s} = 900$ GeV.

The multiplicity as a function of the transverse momentum is shown in Fig. 10.2(b). At $\sqrt{s} =$

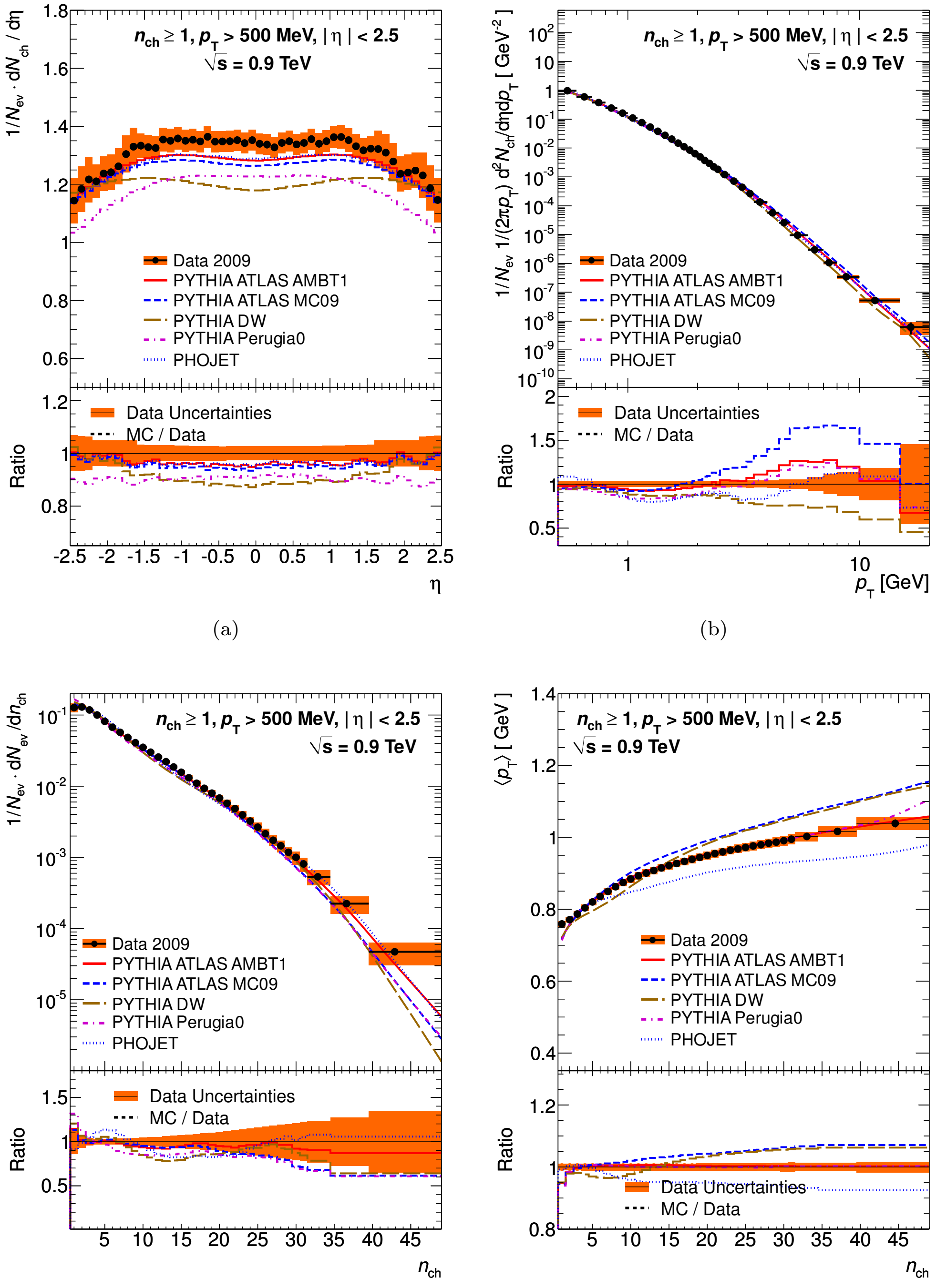

(a)

(b)

(c)

(d)

Figure 10.1: Charged particle multiplicities for events with $n_{\text{ch}} \geq 1$ within the kinematic range $p_T > 500$ MeV and $|\eta| < 2.5$ at $\sqrt{s} = 900$ GeV. The panels show the charged particle multiplicity as a function of the pseudorapidity (a) the charged particle multiplicity as a function of the transverse momentum (b), the charged particle multiplicity (c), and the average transverse momentum as a function of the number of charged particles in the event (d) [4]. The markers represent the data and the curves predictions from different Monte Carlo models. The vertical bars represent the statistical uncertainties, while the green shaded bands show the statistical and systematic uncertainties added in quadrature. The values of the ratio histograms used the bin centroids.

7 TeV the larger range means that the multiplicity varies by ten orders of magnitude. None of the models describe the shape of the p_T spectrum. They predict a lower multiplicity at low p_T and a higher multiplicity at high p_T than measured in data. The best agreement at low p_T is for the ATLAS MC09 and AMBT1 tunes, while at mid-p_T PHOJET provides a slightly better description of the data.

None of the models correctly describes the multiplicity distribution in Fig. 10.2(c). They predict more events at low n_{ch} and fewer events at high n_{ch}. The slope of the average p_T as a function of n_{ch} in Fig. 10.2(d) changes around $n_{\mathrm{ch}} = 10$ as at $\sqrt{s} = 900$ GeV. All the models favour a higher average p_T, with the most accurate prediction being provided by the Perugia0 and AMBT1 tunes.

At $\sqrt{s} = 7$ TeV the charged particle multiplicity is higher than at $\sqrt{s} = 900$ GeV as expected. However, most models did not predict a sufficient increase in the multiplicity when the centre of mass energy increased from $\sqrt{s} = 900$ GeV to $\sqrt{s} = 7$ TeV. Therefore larger discrepancies between data and simulation are observed at $\sqrt{s} = 7$ TeV in all distributions. In particular, this means that the parameters controlling the extrapolation in the multiplicity with the centre of mass energy, needed retuning.

Because of these large discrepancies, the ATLAS collaboration has produced the AMBT1 tune using the LHC data at $\sqrt{s} = 900$ GeV and $\sqrt{s} = 7$ TeV. To limit the contribution from the large uncertainties on the modelling of diffractive processes in PYTHIA, the tune was based on the distributions with $n_{\mathrm{ch}} > 6$, which eliminates the contribution from diffractive events [126]. Results from ATLAS underlying event measurements at $\sqrt{s} = 900$ GeV and $\sqrt{s} = 7$ TeV [129] were also used. AMBT1 was based on the ATLAS MC09c tune, but five parameters describing the colour reconnection and multiple parton interactions were varied. The parameters describing the distribution of hadronic matter and colour reconnection were adjusted to improve the description of the shape of the n_{ch} and p_T distributions. The parameters describing the cut-off for multiple parton interactions and its extrapolation with energy, on the other hand, did not change. The resulting tune describes the minimum bias data at $\sqrt{s} = 900$ GeV and $\sqrt{s} = 7$ TeV well with the high p_T region described to an accuracy of 10%.

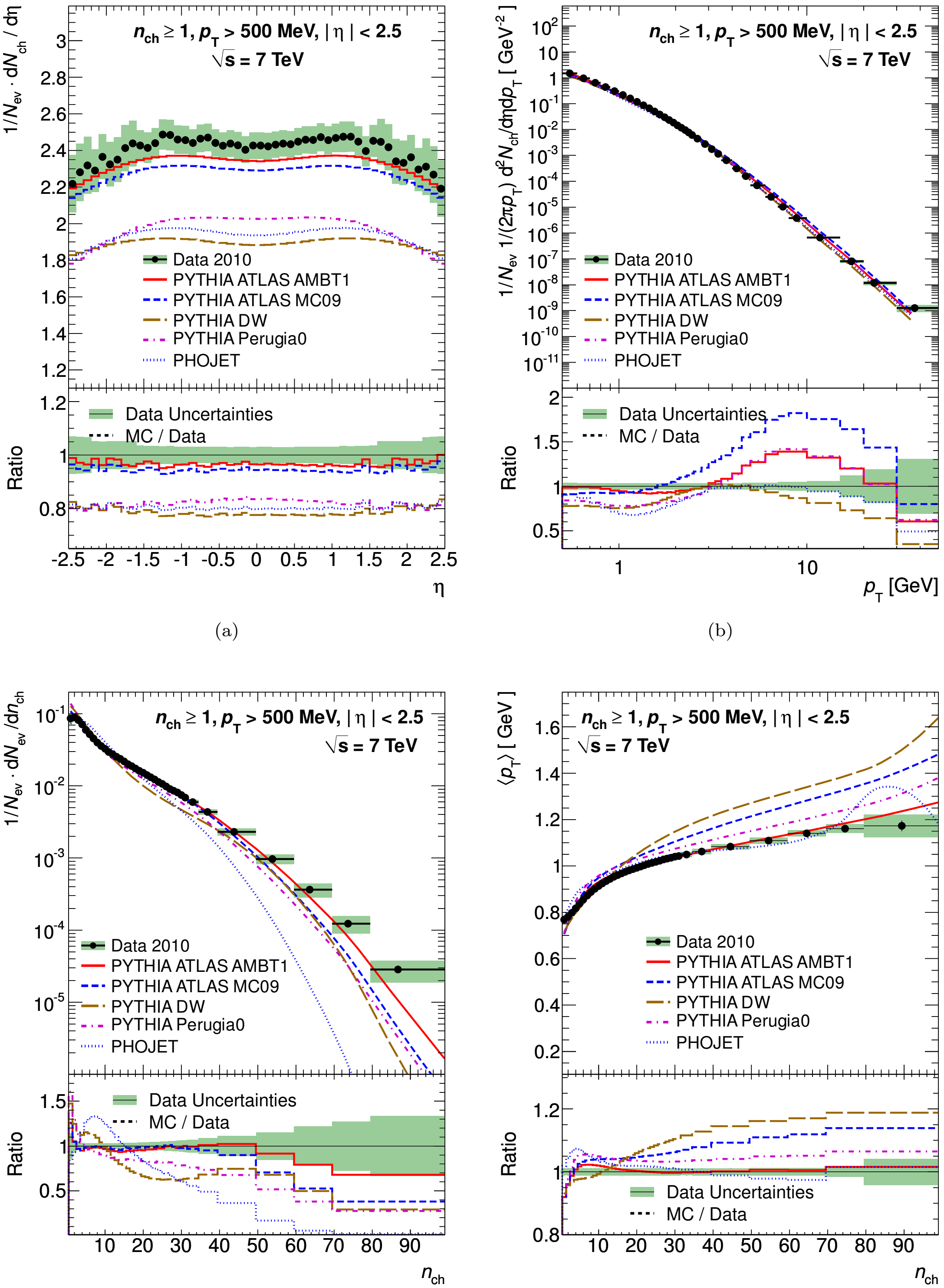

(a)

(b)

(c)

(d)

Figure 10.2: Charged particle multiplicities for events with $n_{\text{ch}} \geq 1$ within the kinematic range $p_T > 500$ MeV and $|\eta| < 2.5$ at $\sqrt{s} = 7$ TeV. The panels shows the charged particle multiplicity as a function of the pseudorapidity (a) and of the transverse momentum (b), the charged particle multiplicity (c), and the average transverse momentum as a function of the number of charged particles in the event (d). The markers represent the data and the curves predictions from different Monte Carlo models. The vertical bars represent the statistical uncertainties, while the green shaded ares show the statistical and systematic uncertainties added in quadrature. The values of the ratio histograms used the bin centroids [127].

10.3 Charged Particle Multiplicities at $\sqrt{s} = 2.36$ TeV

The charged particle multiplicity as a function of pseudorapidity at $\sqrt{s} = 2.36$ TeV is shown in Fig. 10.3(a). The best description is provided by the AMBT1 tune, which describes the data to within 5%. The other tunes shown predict charged particle multiplicity 10-20% lower than measured. The average value is $1.707 \pm 0.028(\text{stat.}) \pm 0.076(\text{syst.})$ charged particles per event and unit of pseudorapidity for $|\eta| < 0.5$. The average multiplicity was calculated using a larger range in η than at the other centre of mass energies to minimise the statistical uncertainty.

Figure 10.3(b) shows the charged particle multiplicity as a function of the transverse momentum. It is measured in a reduced range, $0.5 < p_T < 10$ GeV, due to the limited size of the dataset. All the Monte Carlo models are consistent with the data, except possibly in the highest transverse momentum bin. The n_{ch} and $\langle p_{\text{T}} \rangle$ vs n_{ch} distributions were not measured at $\sqrt{s} = 2.36$ TeV due to difficulties in obtaining an accurate estimate of the unfolding matrix as discussed in Section 9.3. The n_{ch} distribution at $\sqrt{s} = 2.36$ TeV was measured using a different method discussed in [120].

10.4 Other Measurements at $\sqrt{s} = 900$ GeV

Although charged particle multiplicity distributions are extremely sensitive to the details of the experimental procedure, a comparison of the p_T spectrum measured by ATLAS was made to measurements published by other experiments at the same centre of mass energy. Figure 10.4 compares the multiplicity as a function of the transverse momentum measured by ATLAS at $\sqrt{s} = 900$ GeV to the same distribution measured by CMS [96] and UA1 [20]. The multiplicity measured by CMS is systematically lower than that measured by ATLAS, which is expected due to the definition of NSD events used by CMS. The removal of the single diffractive component reduces the multiplicity at low transverse momentum. In addition, the multiplicity is reduced because events with $n_{\text{ch}} = 0$ were included in the number of events used in the normalisation by CMS. The UA1 results have a multiplicity which is 20% higher than the ATLAS. The double-arm scintillator trigger used by UA1 rejects events with low charged particle multiplicity, which would increase the average multiplicity, however the discrepancy has not been fully understood.

To make a direct comparison to the results from CMS, a Monte Carlo-based correction was used to remove the single diffractive component. The Pythia DW tune was used to make the

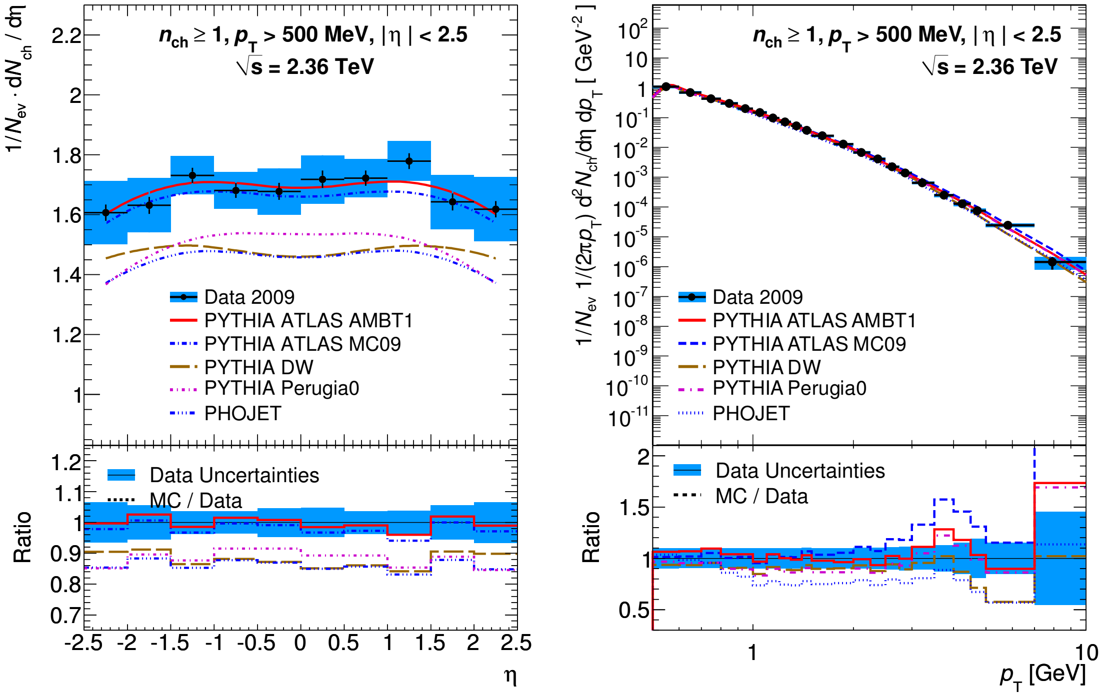

(a)

(b)

Figure 10.3: Charged particle multiplicities for events with $n_{\rm ch} \geq 1$ within the kinematic range $p_T > 500$ MeV and $|\eta| < 2.5$ at $\sqrt{s} = 2.36$ TeV. The panels shows the charged particle multiplicity as a function of the pseudorapidity (a) and of the transverse momentum (b). The markers represent the data and the curves predictions from different Monte Carlo models. The vertical bars represent the statistical uncertainties, while the green shaded ares show the statistical and systematic uncertainties added in quadrature. The values of the ratio histograms used the bin centroids.

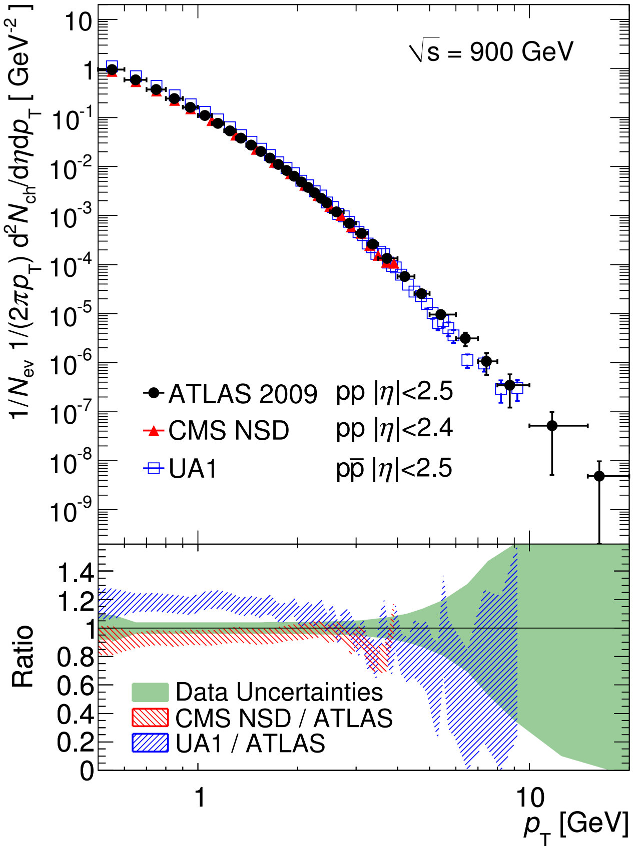

Figure 10.4: The multiplicity as a function of the transverse momentum. The ATLAS pp data (black circles) are compared to the UA1 $p\bar{p}$ data (blue open squares) and CMS NSD pp data (red triangles) [4]. All three measurements were made using data at the same centre of mass energy.

correction, because it is most similar to the tune used by CMS. After the correction, the average charged particle density for $|\eta| < 2.4$ was found to be 1.240 ± 0.040 (syst), which is consistent with the CMS measurement of 1.202 ± 0.043 (syst.).

10.5 Multiplicity vs Centre of Mass Energy

The charged particle multiplicity distributions at the three centre of mass energies are compared in Fig. 10.5. The multiplicity increases, the η distribution falls off more rapidly and the p_T spectrum hardens with increasing centre of mass energy. At higher centre of mass energy the average multiplicity increases. Therefore the fraction of events at low n_{ch} at higher energies decreases, while the fraction of events at high n_{ch} increases. The fraction of events with $n_{\text{ch}} = 10$ is approximately independent of the centre-of-mass energy for $p_T > 500$ MeV.

Finally, the dependence of the charged particle multiplicity at central pseudorapidity on the centre-of-mass energy is compared to the predictions from different models in Fig. 10.6. A fit of the form $a + b \ln s$, motivated by Feynman scaling, to the ATLAS measurements in shown. Although the fit successfully describes the three ATLAS measurements, it requires a significantly lower multiplicity at lower centre of mass energies than those shown in Section 2.4.3. This shows that Feynman scaling cannot be used to describe the dependence of the multiplicity on the centre of mass energy from all measurements simultaneously.

The three ATLAS PYTHIA tunes describe the increase in multiplicity with centre of mass energy well. The most accurate description is provided by the AMBT1 tune as expected because it was produced from these measurements. The Perugia0 and DW tunes as well as PHOJET predict a slower increase in the multiplicity with the centre of mass energy. None of the models predict a multiplicity as high as measured in data. PHOJET correctly predicts the multiplicity at $\sqrt{s} = 900$ GeV, but predicts a significantly lower multiplicity than is measured at $\sqrt{s} = 7$ TeV.

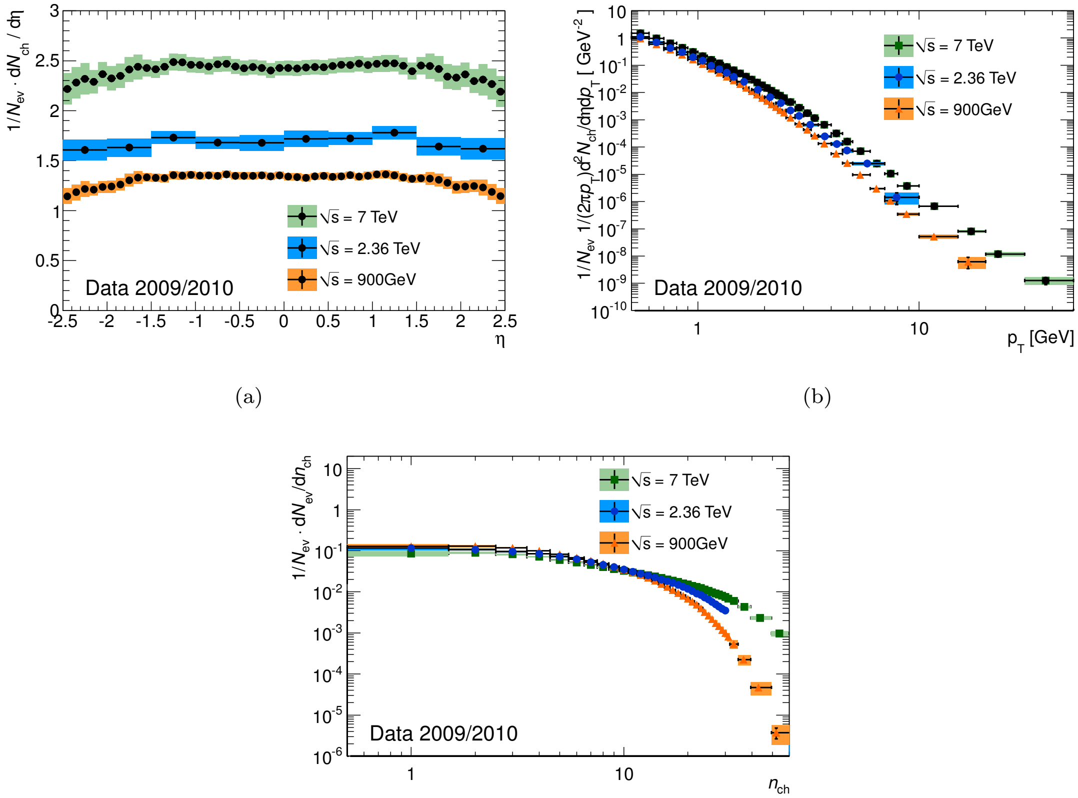

(a) (b)

(c)

Figure 10.5: The charged particle pseudorapidity (a), transverse momentum density (b) and the charged particle multiplicity (c) for each centre of mass energies. The coloured bands denote the quadratic sum of the statistical and systematic uncertainty. The charged particle multiplicity at $\sqrt{s} = 2.36$ TeV is measured using the pixel track method [120]

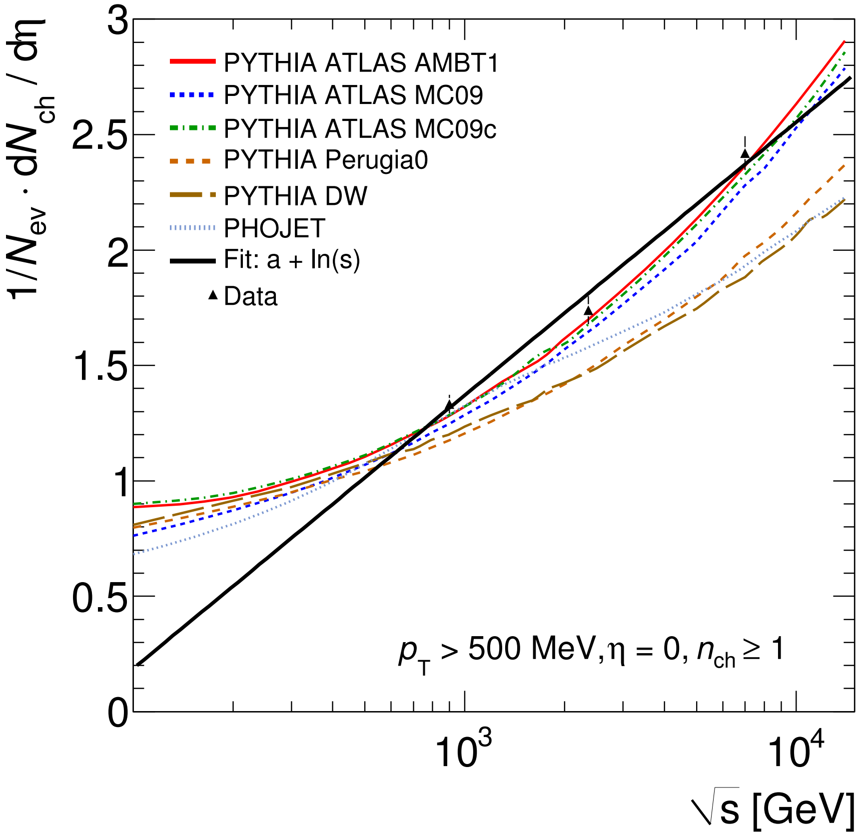

(a)

Figure 10.6: The average charged particle multiplicity per unit of rapidity for $\eta = 0$ as a function of the centre of mass energy. Results are shown both for $n_{\mathrm{ch}} \geq 1$ and $p_T \geq 500$ MeV as discussed here and for $n_{\mathrm{ch}} \geq 2$ and $p_T \geq 100$ MeV from [127]. The markers represent the data and the curves prediction from different Monte Carlo models.

Chapter 11

Conclusion

Charged particle multiplicity distributions measured by the ATLAS experiment at the LHC have been presented. The charged particle multiplicity was measured at the three centre of mass energies at which collisions were delivered by the LHC: $\sqrt{s} = 900$ GeV, $\sqrt{s} = 2.36$ TeV and $\sqrt{s} = 7$ TeV. Over seven hundred thousand proton-proton interactions were used to study the properties of events containing at least one primary charged particle with $|\eta| < 2.5$ and $p_T > 500$ MeV. Tracks were reconstructed using information from all three sub-detectors of the ATLAS Inner Detector: the silicon pixel detector, the silicon strip detector (SCT) and the Transition Radiation Tracker (TRT).

The data were corrected to obtain inclusive inelastic distributions to facilitate comparisons to a wide range of models of soft hadronic interactions. Four different distributions were measured: the charged particle multiplicity, the multiplicity as a function of pseudorapidity, the multiplicity as a function of the transverse momentum and the average transverse momentum as a function of the multiplicity.

The event selection efficiency was measured in data. The track reconstruction efficiency was estimated using the simulation. Detailed studies were made to understand the performance of the track reconstruction software in data and simulations. The dominant systematic uncertainty on the charged particle multiplicity distributions is the uncertainty on the track reconstruction efficiency due to the amount of material in the Inner Detector. A number of techniques were developed and used to estimate that the uncertainty on the material budget is less than 10%, resulting in an uncertainty of 3% on the track reconstruction efficiency.

The data at $\sqrt{s} = 2.36$ TeV was taken with the silicon tracker partially depleted with significantly reduced efficiency, which was not modelled by the simulation. Therefore a data-driven correction was applied to the track reconstruction efficiency, which resulted in a larger systematic uncertainty on the track reconstruction efficiency.

The charged particle multiplicity per event and unit of pseudorapidity at $\eta = 0$ was measured to be:

- $1.335 \pm 0.003(\text{stat.}) \pm 0.036(\text{syst.})$ at $\sqrt{s} = 900$ GeV,
- $1.707 \pm 0.028(\text{stat.}) \pm 0.076(\text{syst.})$ at $\sqrt{s} = 2.36$ TeV, and
- $2.427 \pm 0.004(\text{stat.}) \pm 0.073(\text{syst.})$ at $\sqrt{s} = 7$ TeV.

At each centre of mass energy, the charged particle multiplicity was measured to be higher than the predictions from several Monte Carlo models, which had been tuned to charged particles measurements made prior to the LHC. In particular, most models underestimated the increase in multiplicity with the centre of mass energy such that the discrepancies increased with energy. An updated tune based on these measurements has been produced by the ATLAS experiment. This new tune describes the charged particle multiplicity at $\sqrt{s} = 900$ GeV, $\sqrt{s} = 2.36$ TeV and $\sqrt{s} = 7$ TeV to better than 5%.

Bibliography

[1] G. Aad et al. Cosmic-Ray Detection Efficiencies for the ATLAS Pixel Detector. ATL-COM-INDET-2010-051.

[2] G. Aad et al. The ATLAS Experiment at the CERN Large Hadron Collider. *JINST*, 3:S08003, 2008.

[3] G. Aad et al. The ATLAS Pixel Detector Electronics and Sensors. *JINST*, 3:P07007, 2008.

[4] G. Aad et al. Charged-particle Multiplicities in pp Interactions at $\sqrt{s} = 900$ GeV Measured with the ATLAS Detector at the LHC. *Phys. Lett.*, B688:21–42, 2010.

[5] G Aad et al. Drift Time Measurement in the ATLAS Liquid Argon Electromagnetic Calorimeter using Cosmic Muons. 2010. accepted by EPJC.

[6] G Aad et al. Performance of the ATLAS Detector using First Collision Data. *JHEP*, 1009:056, 2010.

[7] G. Aad et al. Track Reconstruction Efficiency in $\sqrt{s}$=7 TeV Data for Tracks with $p_T >$ 100 MeV. Technical Report ATL-COM-PHYS-2010-363, CERN, Geneva, June 2010.

[8] T. Aaltonen et al. Measurement of Particle Production and Inclusive Differential Cross Sections in p$\bar{\text{p}}$ Collisions at $\sqrt{s} = 1.96$ TeV. *Phys. Rev.*, D79:112005, 2009.

[9] K. Aamodt et al. The ALICE experiment at the CERN LHC. *JINST*, 3:S08002, 2008.

[10] F. Abe et al. Transverse Momentum Distributions of Charged Particles Produced in $\bar{\text{p}}$p Interactions at $\sqrt{s} = 630$ GeV and 1800 GeV. *Phys. Rev. Lett.*, 61:1819, 1988.

[11] F. Abe et al. Pseudorapidity Distributions of Charged Particles Produced in $\bar{\text{p}}$p Interactions at $\sqrt{s} = 630$ GeV and 1800 GeV. *Phys. Rev.*, D41:2330, 1990.

[12] V. A. Abramovsky, V. N. Gribov, and O. V. Kancheli. Character of Inclusive Spectra and Fluctuations produced in Inelastic Processes by Multi-Pomeron Exchange. *Yad. Fiz.*, 18:595–616, 1973.

[13] D. Acosta et al. Soft and Hard Interactions in $p\bar{p}$ Collisions at $\sqrt{s} = 1800$-GeV and 630-GeV. *Phys. Rev.*, D65:072005, 2002.

[14] D. Acosta et al. The underlying event in hard interactions at the Tevatron $\bar{p}p$ collider. *Phys. Rev.*, D70:072002, 2004.

[15] R. Adolphi et al. The CMS experiment at the CERN LHC. *JINST*, 3:S08004, 2008.

[16] A. Affolder et al. Charged Jet Evolution and the Underlying Event in $p\bar{p}$ Collisions at 1.8 TeV. *Phys. Rev.*, D65:092002, 2002.

[17] S. Agostinelli et al. GEANT4: A Simulation toolkit. *Nucl. Instr. Meth.*, A:506, 2003.

[18] P. F. Akesson et al. ATLAS Tracking Event Data Model. Technical Report ATL-SOFT-PUB-2006-004. ATL-COM-SOFT-2006-005. CERN-ATL-COM-SOFT-2006-005, CERN, Geneva, July 2006.

[19] M. S. Alam et al. The ATLAS Silicon Pixel Sensors. *Nucl. Instr. Meth.*, A456(3):217 – 232, 2001.

[20] C. Albajar et al. A Study of the General Characteristics of $p\bar{p}$ Collisions at $\sqrt{s} = 0.2$ TeV to 0.9 TeV. *Nucl. Phys.*, B335:261, 1990.

[21] M. Albrow et al. Tevatron-for-LHC Report of the QCD Working Group. 2006.

[22] T. Alexopoulos et al. The Role of Double Parton Collisions in Soft Hadron Interactions. *Phys. Lett.*, B435:453–457, 1998.

[23] S. Allwood-Spiers et al. Vertex Reconstruction for Analysis of Charged Particle Multiplicities in pp Interactions at $\sqrt{s} = 900$ GeV. ATL-COM-INDET-2010-009.

[24] G. J. Alner et al. Scaling Violation Favoring High Multiplicity Events at 540 GeV CMS Energy. *Phys. Lett.*, B138:304, 1984.

[25] G. J. Alner et al. An Investigation of Multiplicity Distributions in Different Pseudorapidity Intervals in anti-p p Reactions at a CMS Energy of 540 GeV. *Phys. Lett.*, B160:193, 1985.

[26] G. J. Alner et al. Scaling of Pseudorapidity Distributions at C.M. Energies Up to 0.9-TeV. *Z. Phys.*, C33:1–6, 1986.

[27] G. J. Alner et al. Scaling Violations in Multiplicity Distributions at 200 GeV and 900 GeV. *Phys. Lett.*, B167:476–480, 1986.

[28] G. J. Alner et al. UA5: A General Study of Proton-Antiproton Physics at $\sqrt{s} = 546$ GeV. *Phys. Rept.*, 154:247–383, 1987.

[29] K. Alpgard et al. Comparison of $p\bar{p}$ and pp Interactions at $\sqrt{s} = 53$ GeV. *Phys. Lett.*, B112:183, 1982.

[30] A. Augusto Alves et al. The LHCb Detector at the LHC. *JINST*, 3:S08005, 2008.

[31] Claude Amsler et al. Review of Particle Physics. *Phys. Lett.*, B667:1, 2008.

[32] A. Andreazza et al. Study of the Energy Loss in the ATLAS Pixel Detector with Cosmics Data. ATL-INDET-INT-2010-007.

[33] R. E. Ansorge et al. Diffraction Dissociation at the CERN pulsed $p\bar{p}$ Collider at C.M. Energies of 900 and 200 GeV. *Z. Phys.*, C33:175, 1986.

[34] R. E. Ansorge et al. Charged Particle Correlations in $\mathrm{p\bar{p}}$ Collisions at C.M. Energies of 200, 546, and 900 GeV. *Z. Phys.*, C37:191–213, 1988.

[35] R. E. Ansorge et al. Charged Particle Multiplicity Distributions at 200 and 900 GeV C.M. Energy. *Z. Phys.*, C43:357, 1989.

[36] S. Aoun et al. Properties of the Pixel Cluster Charge in Cosmic Ray Data and Simulation. ATL-INDET-INT-2010-004.

[37] J. Arguin et al. Track Reconstruction Efficiency in 900 GeV Data. ATL-COM-INDET-2010-010.

[38] G. Arnison et al. Charged Particle Multiplicity Distributions in Proton Anti-Proton Collisions at 540 GeV Center Of Mass Energy. *Phys. Lett.*, B123:108, 1983.

[39] P. Aurenche and Fritz W. Bopp. Rapidity Spectra in Proton Proton and Proton-AntiProton Scattering up to 540 GeV in a Dual Parton Model. *Phys. Lett.*, B114:363, 1982.

[40] P. Aurenche et al. Extrapolation of Multistring Production Mechanism to Super Collider Energies. SI-84-6.

[41] J. Bartels, T. Gehrmann, and M. G. Ryskin. Spin dependence of Deep Inelastic Diffraction: An Outline. Prepared for 2nd Topical Workshop on Deep Inelastic Scattering off Polarized Targets: Theory Meets Experiment (SPIN 97), Zeuthen, Germany, 1-5 Sep 1997.

[42] P Behera et al. Charged Particle Multiplicities in pp Interactions at $\sqrt{s} = 7$ TeV.

[43] P. Behera et al. Measurement of the Lorentz Angle and Depletion Depth in the ATLAS Pixel Detector with Cosmic Rays Data. ATL-COM-INDET-2010-041.

[44] P. Behera et al. Threshold Tuning of the ATLAS Pixel Detector. ATL-COM-INDET-2010-044.

[45] W. H. Bell et al. MBTS Trigger Efficiency for the Minimum Bias Analysis using Inner Detector Tracks from pp Interactions at $\sqrt{s} = 900$ GeV. ATL-COM-DAQ-2010-003.

[46] William Bell. Private Communication.

[47] Siegfried Bethke. The 2009 World Average of $\alpha_s(M_Z)$. *Eur. Phys. J.*, C64:689–703, 2009.

[48] Hans Bichsel. Straggling in thin silicon detectors. *Rev. Mod. Phys.*, 60(3):663–699, July 1988.

[49] J. Biesiada et al. Study of the Material Budget in the ATLAS Inner Detector with K^0_{s} in 900 GeV Collision Data. ATL-COM-INDET-2010-022.

[50] J. Biesiada et al. The Implementation and Performance of the ROD DSP Software in the ATLAS Pixel Detector. ATL-INDET-INT-2010-006.

[51] Pierre Billoir and S. Qian. Fast Vertex Fitting with a Local Parametrization of Tracks. *Nucl. Instr. Meth.*, A311:139–150, 1992.

[52] J. P. Blewett. 200 GeV Intersecting Storage Accelerators. Paper published in the Proceedings of The 8th International Conference on High-Energy Accelerators, 20-24 Sep 1971, Geneva, Switzerland.

[53] G. I. Brandt et al. Correction of Track to Charged Particle Distributions in pp Interactions at $\sqrt{s} = 900$ GeV. ATL-COM-PHYS-2010-038.

[54] W. Braunschweig et al. Charged multiplicity distributions and correlations in e^+e^- annihilation at petra energies. *Zeitschrift für Physik C Particles and Fields*, 45:193–208, 1989.

[55] A. Breakstone et al. Charged Multiplicity Distribution in pp Interactions at ISR Energies. *Phys. Rev.*, D30:528, 1984.

[56] A. Buckley et al. Systematic Event Generator Tuning for the LHC. *Eur. Phys. J.*, C65:331–357, 2010.

[57] A. Capella. Dual Parton Model. *Surveys in High Energy Physics*, 16(3-4):175 – 186, 2001.

[58] A. Capella et al. Dual parton model. *Physics Reports*, 236(4-5):225 – 329, 1994.

[59] A. Capella and J. Tran Thanh Van. Hadron-Nucleus Interactions and the Leading Particle Effect in a Dual-Parton Model. *Zeitschrift für Physik C Particles and Fields*, 10(3):249 –262.

[60] CERN. Summary of the Analysis of the 19 September 2008 Incident at the LHC. Technical report, CERN, Geneva, Oct 2008.

[61] V. M. Chudakov and V. V. Lugovoi. Dual Parton Model of Inelastic pp Interactions and Cascade Breaking of String. *Z. Phys.*, C59:511–523, 1993.

[62] G. Cohen-Tannoudji et al. Partons at Low p_T. *Phys. Rev.*, D21:2699, 1980.

[63] John C. Collins and Davison E. Soper. Back-To-Back Jets in QCD. *Nucl. Phys.*, B193:381, 1981.

[64] John C. Collins and Davison E. Soper. Parton Distribution and Decay Functions. *Nucl. Phys.*, B194:445, 1982.

[65] T. Cornelissen et al. Concepts, Design and Implementation of the ATLAS New Tracking (NEWT). (ATL-SOFT-PUB-2007-007. ATL-COM-SOFT-2007-002), Mar 2007.

[66] T. Cornelissen and W. Liebig. ATLAS Inner Detector Results from the 2004 Combined Test Beam Data. *Nuclear Physics B Proceedings Supplements*, 172, 2007.

[67] G. D'Agostini. A Multidimensional Unfolding Method based on Bayes' Theorem. *Nucl. Instr. Meth.*, A362:487–498, 1995.

[68] L. dell'Asta et al. Measuring the Charge Scale of the Pixel Detector with Cosmic Ray Data. ATL-INDET-INT-2010-0003.

[69] Daniel Dobos. *Commissioning Perspectives for the ATLAS Pixel Detector.* PhD thesis, Universität Dortmund, 2007.

[70] A. Donnachie and P. V. Landshoff. Total Cross-Sections. *Phys. Lett.*, B296:227–232, 1992.

[71] J. Dopke et al. Commissioning of the ATLAS Pixel Optical Readout Link. ATL-COM-INDET-2010-047.

[72] S. D. Drell and Tung-Mow Yan. Partons and Their Applications at High Energies. *Ann. Phys.*, 66:578, 1971.

[73] J. Große Knetter. *Vertex Measurement at a Hadron Collider - The ATLAS Pixel Detector.* Habilititation Thesis, Universität Bonn, 2008.

[74] T. Eifert and M. Schott. Estimating Track Momentum Resolution in Minimum Bias Events using Simulation and K_s^0 in 900 GeV Collision Data. ATL-COM-INDET-2010-016.

[75] K. Ellis et al. QCD and collider physics. *Camb. Monogr. Part. Phys. Nucl. Phys. Cosmol.*, 8:1–435, 1996.

[76] R. Engel. Photoproduction Within the Two Component Dual Parton Model. 1. Amplitudes and Cross-Sections. *Z. Phys.*, C66:203–214, 1995.

[77] R. Engel and J. Ranft. Hadronic Photon-Photon Interactions at High-Energies. *Phys. Rev.*, D54:4244–4262, 1996.

[78] F. Englert and R. Brout. Broken Symmetry and the Mass of Gauge Vector Mesons. *Phys. Rev. Lett.*, 13:321–322, 1964.

[79] L. Evans and P. Bryant. LHC Machine. *JINST*, 3(08):S08001, 2008.

[80] R. P. Feynman. Very High-Energy Collisions of Hadrons. *Phys. Rev. Lett.*, 23(24):1415–1417, Dec 1969.

[81] K. Fialkowski and A. Kotanski. Hadron Multiplicity Distributions in a Dual Model. *Phys. Lett.*, B107:132, 1981.

[82] R. Fruehwirth et al. Convoluted Landau and Gaussian Fitting Function. http://root.cern.ch/root/html/tutorials/fit/langaus.C.html.

[83] N. Garelli et al. The Tuning and Calibration of the Charge Measurement of the Pixel Detector. ATL-COM-INDET-2010-017.

[84] H.M. Gray. Pixel Cluster and Track Statistics from the 2008 Cosmic Data-taking. ATL-INDET-INT-2009-007.

[85] H.M. Gray and M. Hoeferkamp. The Thickness of the ATLAS Pixel Detector Sensors. ATL-INDET-INT-2009-008.

[86] V. N. Gribov. A Reggeon Diagram Technique. *Sov. Phys. JETP*, 26:414–422, 1968.

[87] D. J. Gross and Frank Wilczek. Asymptotically Free Gauge Theories. 1. *Phys. Rev.*, D8:3633–3652, 1973.

[88] J.F. Grosse-Oetringhaus and K. Reygers. Charged-Particle Multiplicity in Proton-Proton Collisions. 2009.

[89] F. Guescini, A. Lister, and S. Nektarijevic. Beam Background Studies for the Minimum Bias Measurements from pp Interactions at $\sqrt{s} = 900$ GeV. ATL-COM-PHYS-2010-037.

[90] G. S. Guralnik, C. R. Hagen, and T. W. B. Kibble. Global Conservation Laws and Massless Particles. *Phys. Rev. Lett.*, 13:585–587, 1964.

[91] R. Harr et al. Pseudorapidity Distribution of Charged Particles in $\bar{p}p$ Collisions at $\sqrt{s} =$ 630-GeV. *Phys. Lett.*, B401:176–180, 1997.

[92] P. W. Higgs. Broken Symmetries, Massless Particles and Gauge Fields. *Phys. Lett.*, 12:132–133, 1964.

[93] ICRU. Average Energy Required to Produce an Ion Pair (International Commission on Radiation Units and Measurements, Bethesda, MD). Technical Report 31, 1979.

[94] A. B. Kaidalov. The Quark-Gluon Structure of the Pomeron and the Rise of Inclusive Spectra at High-Energies. *Phys. Lett.*, B116:459, 1982.

[95] A. B. Kaidalov and K. A. Ter-Martirosian. Pomeron as Quark-Gluon Strings and Multiple Hadron Production at SPS Collider Energies. *Phys. Lett.*, B117:247–251, 1982.

[96] V. Khachatryan et al. Transverse Momentum and Pseudorapidity Distributions of Charged Hadrons in pp Collisions at $\sqrt{s} = 0.9$ and 2.36 TeV. *JHEP*, 02:041, 2010.

[97] T. Kuhl and T. T. Voss. Determination of Secondary Tracks in the Minimum Bias Analysis. ATL-COM-INDET-2010-011.

[98] Regina Kwee. Private Communication.

[99] LHC Study Group. The Large Hadron Collider: Conceptual design. 1995. CERN-AC-95-05-LHC.

[100] Clark S. Lindsey et al. Results from E735 at the Tevatron $p\bar{p}$ Collider with $\sqrt{s} = 1.8$ TeV. *Nucl. Phys.*, A544:343–356, 1992.

[101] C. Ohm and T. Pauly. The ATLAS Beam Pick-up Based Timing System. Technical Report ATL-DAQ-PROC-2009-005, ATL-COM-DAQ-2009-022, CERN, Geneva, Apr 2009.

[102] R.H. Pehl et al. Accurate Determination of the Ionization Energy in Semiconductor Devices. *Nucl. Instr. Meth.*, 59, 1968.

[103] G. Piacquadio, K. Prokofiev, and A. Wildauer. Primary Vertex Reconstruction in the ATLAS Experiment at LHC. *Journal of Physics: Conference Series*, 119(3):032033, 2008.

[104] H. D. Politzer. Asymptotic Freedom: An Approach to Strong Interactions. *Phys. Rept.*, 14:129–180, 1974.

[105] I. Ia. Pomeranchuk. Stability of a Fermi Liquid. *Sov. Phys. JETP*, 35, 1958.

[106] R. Frühwirth. Application of Kalman Filtering to Track and Vertex Fitting. *Nucl. Instr. Meth.*, A262, 1987.

[107] R.D. Ryan. Precision Measurements of the Ionization Energy and Its Temperature Variation in High Purity Silicon Radiation Detectors. *IEEE Trans. Nucl. Sci.*

[108] A.K. Salzburger. *Track Simulation and Reconstruction in the ATLAS Experiment.* PhD thesis, Innsbruck University, 2008.

[109] F. Scholze. Determination of the Electron-hole Pair Creation Energy for Semiconductors from the Spectral Responsivity of Photodiodes. *Nucl. Instr. Meth.*, A439(2-3):208 – 215, 2000.

[110] T. Sjostrand et al. PYTHIA 6.4 Physics and Manual. *JHEP*, 05:026, 2006.

[111] T. Sjostrand et al. A Brief Introduction to PYTHIA 8.1. *Comput. Phys. Commun.*, 178:852–867, 2008.

[112] T. Sjostrand and P. Z. Skands. Transverse-Momentum-Ordered Showers and Interleaved Multiple Interactions. *Eur. Phys. J.*, C39:129–154, 2005.

[113] T. Sjostrand and P.Z. Skands. Multiple interactions and the structure of beam remnants. *JHEP*, 03:053, 2004.

[114] T. Sjostrand and M. van Zijl. A Multiple Interaction Model for the Event Structure in Hadron Collisions. *Phys. Rev.*, D36:2019, 1987.

[115] P. Z. Skands. The Perugia Tunes. 2009. arXiv:0905.3418.

[116] S Strandberg. Results from the Commissioning of the ATLAS Pixel Detector. *JINST*, 4(ATL-INDET-PROC-2008-008. ATL-COM-INDET-2008-027):P03020. 8 p, Dec 2008.

[117] The ATLAS Collaboration. ATLAS Inner Detector: Technical Design Report. Vol. 1. CERN-LHCC-97-16.

[118] The ATLAS Collaboration. ATLAS Inner Detector: Technical Design Report. Vol. 2. CERN-LHCC-97-17.

[119] The ATLAS Collaboration. ATLAS Monte Carlo Tunes for MC09. ATL-PHYS-PUB-2010-002.

[120] The ATLAS Collaboration. Charged Particle Multiplicities in pp Interactions at $\sqrt{s} = 2.36$ TeV Measured with the ATLAS Detector at the LHC. ATL-COM-PHYS-2010-390,ATLAS-CONF-2010-047.

[121] The ATLAS Collaboration. Charged Particle Multiplicities in pp Interactions at $\sqrt{s} = 7$ TeV Measured with the ATLAS Detector at the LHC. ATL-COM-PHYS-2010-188,ATLAS-CONF-2010-024.

[122] The ATLAS Collaboration. Luminosity and Run Statistics Plots for 2010 Beam Data. `https://twiki.cern.ch/twiki/bin/view/Atlas/RunStatsPublicResults2010`.

[123] The ATLAS Collaboration. Performance of the ATLAS Silicon Pattern Recognition Algorithm in Data and Simulation at $\sqrt{s} = 7$ TeV. ATLAS-CONF-2010-072.

[124] The ATLAS Collaboration. Performance of the Minimum Bias Trigger in pp Collisions at $\sqrt{s} = 7$ TeV. ATL-COM-DAQ-2010-083.

[125] The ATLAS Collaboration. Tracking Results and Comparison to Monte Carlo Simulation at $\sqrt{s} = 900$ GeV. ATLAS-CONF-2010-011, ATL-COM-PHYS-2010-092.

[126] The ATLAS Collaboration. Charged Particle Multiplicities in pp Interactions at $\sqrt{s} = 0.9$ and 7 TeV in a Diffractive Limited Phase-Space measured with the ATLAS Detector at the LHC and a new PYTHIA6 tune. Technical Report ATLAS-CONF-2010-031, CERN, Geneva, July 2010.

[127] The ATLAS Collaboration. Charged Particle Multiplicities in pp Interactions for Track $p_T >$ 100 MeV at $\sqrt{s} = 0.9$ and 7 TeV Measured with the ATLAS Detector at the LHC. Technical Report ATLAS-CONF-2010-046, CERN, Geneva, July 2010.

[128] The ATLAS Collaboration. The ATLAS Inner Detector Commissioning and Calibration. *EPJC*, 2010.

[129] The ATLAS Collaboration. Track-based Underlying Event Measurements in pp Collisions at $\sqrt{s} = 900$ GeV and 7 TeV with the ATLAS Detector at the LHC. Technical Report ATLAS-CONF-2010-029, CERN, Geneva, July 2010.

[130] W. Thome et al. Charged Particle Multiplicity Distributions in pp Collisions at ISR Energies. *Nucl. Phys.*, B129:365, 1977.

[131] S Van der Meer. Calibration of the Effective Beam Height in the ISR. Technical Report CERN-ISR-PO-68-31. ISR-PO-68-31, CERN, Geneva, 1968.

[132] G. Veneziano. Regge Intercepts and Unitarity in Planar Dual Models. *Nucl. Phys.*, B74:365, 1974.

[133] W. Waltenberger et al. Adaptive Vertex Fitting. *Journal of Physics G: Nuclear and Particle Physics*, 34(12):N343, 2007.

[134] B. M. Waugh et al. HZTool and Rivet: Toolkit and Framework for the Comparison of Simulated Final States and Data at Colliders. 2006. arXiv:hep-ph/0605034.

[135] D. Wicke. New Algorithm For Solving Tracking Ambiguities. *DELPHI*, 236:98–163, 1998.

[136] D. Wicke and P. Z. Skands. Non-Perturbative QCD Effects and the Top Mass at the Tevatron. *Nuovo Cim.*, 123B:S1, 2008.

Appendix A

Definitions

A.1 Coordinate System

The ATLAS coordinate system is right handed with the origin at the nominal interaction point. The z-axis lies along the direction of the beam with positive z defined to be the A-side (Geneva side) of the detector. The positive x-axis points towards the centre of the LHC and the positive y-axis points upwards. The azimuthal angle, ϕ, is measured clockwise around the positive beam access, and the polar angle, θ along the beam access. The pseudorapidity, related to the polar angle, is defined as $\eta = -\ln\tan\theta/2$. The transverse momentum, p_T, energy, E_T, and missing transverse energy, $\not{E}_T$ are defined in the x-y plane. The distance ΔR in the angle space containing the pseudorapidity is defined to be $\Delta R = \sqrt{\Delta\eta^2 + \Delta\phi^2}$.

Appendix B

Technical Aspects of Track Reconstruction

This section covers certain more technical aspects of track reconstruction. It discusses the estimation of track seed parameters and the impact of the correction for the beam spot.

B.1 Estimation of Seed Parameters

A track seed is simply a collection of space points and does not provide a parameterisation of track parameters with respect to the origin. A crude estimate of the perigee parameters, however, can be made by assuming a perfect helical track model in a constant magnetic field. The track projected into the transverse plane follows a circular trajectory, which is uniquely described by three parameters: the transverse momentum, p_T, the transverse impact parameter, d_0, and the azimuthal angle, ϕ_0. Figure B.1 illustrates the circle that can be obtained from three space points.

The transverse momentum was obtained from the radius, ρ, of the circle using the following equation, which assumes that the magnetic field, B, is homogeneous and parallel to the z-axis:

$$\rho[\mathrm{mm}] = \frac{p_T[\mathrm{GeV}]}{3 \cdot 10^{-4} \times q[\mathrm{e}] \times B[\mathrm{T}]} \tag{B.1}$$

The nominal value of the magnetic field in the ATLAS solenoid, 2 T, and the charge of the particle, $q[\mathrm{e}]$ was used.

The distance of closest approach of the track to the origin, d_0, is calculated at the point where the circle intersects a line between the origin and the circle centre:

$$d_0 = \sqrt{c_X^2 + c_Y^2} - \rho \qquad \text{(B.2)}$$

where c_X and c_Y are the coordinates of the circle centre with respect to the origin.

The azimuthal angle of the track at the point of closest approach is ambiguous as illustrated in Fig. B.2. This ambiguity can be resolved by constructing a vector between the positions of the first and second space points and projecting it onto the two possible momentum directions. The azimuthal angle is given by the solution parallel to the vector.

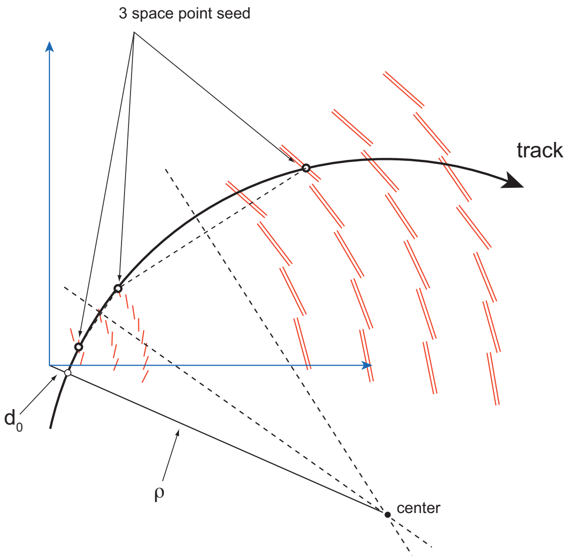

Figure B.1: A sketch of the technique used to estimate the track parameters of the seeds. From [123].

The longitudinal parameters are determined by assuming that the track propagates without bending in the rz-plane. The pseudorapidity, η, of the seed is estimated from the average η position of the three space points. The longitudinal impact parameter, z_0, is estimated from the intersection of a straight line, with the same average η value, with the nominal interaction point.

B.2 Beam Spot Correction

Track parameter distributions, particularly as a function of the pseudorapidity, depend on where the charged particle originated from. For example, two tracks at the same pseudorapidity, which

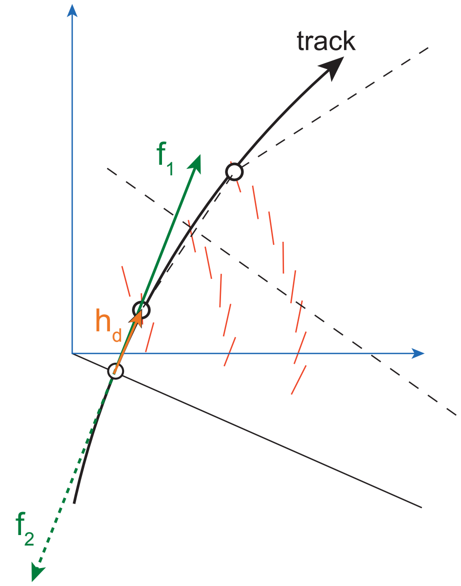

Figure B.2: The resolution of the ambiguity between two possible solutions for the azimuthal direction of the track. The vector between the position of the first and second space point is labelled by h_d. The two possible momentum directions are indicated by f_1 and f_2. The azimuthal angle is calculated using the momentum vector parallel to h_d, i.e. f_1. From [123]

were produced at different z positions, can pass through a different number of layers of silicon, which would result in a different number of hits for each track. Collisions between pairs of protons occur at any position within the luminous region described by the beam spot. The longitudinal dimension of the beam spot in the simulation samples was a factor of two larger than in the data. This is reflected in the width of the longitudinal impact parameter distribution in Fig. B.3, where the dashed histogram from simulation is twice as broad as the data shown by the markers. To correct for this discrepancy, a weight was applied to each event in simulation. The weights are calculated from the ratio of reconstructed z-vertex distribution in data to simulation. The filled yellow histogram in Fig. B.3 demonstrates that after these weights have been applied, the z_0 distribution in the simulation describes the data. These weights are applied to obtain all subsequent track parameter distributions in this section.

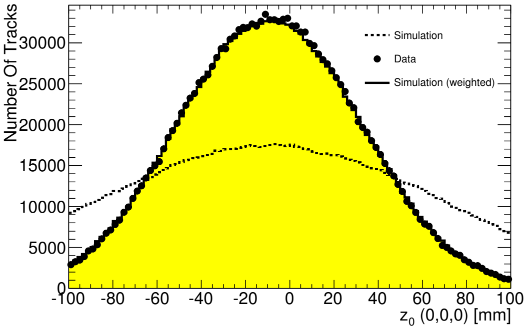

Figure B.3: The distribution of z_0 with respect to the nominal interaction point in data and simulation. The dashed histogram shows the z_0 distribution in the default simulation, while the yellow filled solid histogram shows the z_0 after the simulation has been reweighted to the beam spot in the data.

B.3 Correction for the Number of Inactive Silicon Modules

The number of inactive pixel modules varied between the different datasets in the data taken at $\sqrt{s} = 900$ GeV by ATLAS due to transient problems with the data acquisition system. In total there were between 51 and 75 disabled modules in each run. Although this is only a small fraction of the total number of modules in the pixel detector (4% in the worst case) it can have a large local impact on track reconstruction efficiency, track properties and track parameter resolution.

The most sensitive variables are the average number of pixel hits per track and the tails of the impact parameter distribution. The location of the inactive modules is also important as modules closest to the interaction point have the largest impact on the track parameter resolution. The transverse impact parameter resolution, for example, depends largely on the extrapolation distance from the innermost measurement point to the position at which is it evaluated. Therefore, if the B-layer module that the track passes through is disabled, the impact parameter resolution is significantly degraded.

Figure B.4 compares the number of reconstructed tracks as a function of η and ϕ in simulation samples reconstructed with either 51 or 69 pixel modules disabled. The large local changes in the number of tracks occur where additional B-layer modules were disabled.

For correct for this, the simulation was reprocessed with 75 modules disabled. In addition, the data at $\sqrt{s} = 900$ GeV was reprocessed in the same way such that additional modules were disabled

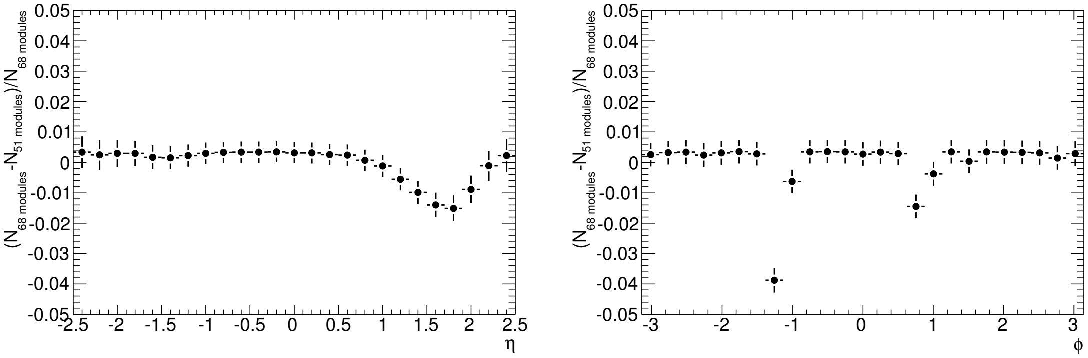

Figure B.4: The fractional change to the number of reconstructed tracks as a function of η (left) and ϕ (right) in a simulation sample with either 51 or 69 modules disabled.

in those parts of the dataset which had fewer disabled modules. This significantly improved the level of agreement between data and simulation.

Appendix C

Datasets

The runs used for the measurement of the charged particle multiplicities at each centre of mass energy are shown in Table C.1. The range of luminosity blocks shown are those which met the data quality criteria. The number of events and tracks used in the analysis from each run are shown. The dataset for the analysis at $\sqrt{s} = 900$ GeV included almost 2 million tracks, while the dataset used at $\sqrt{s} = 7$ TeV, despite consisting of a single run, included almost 4 million tracks. The dataset for the analysis at $\sqrt{s} = 2.36$ TeV was far smaller and only included approximately 40,000 tracks.

Run Number	LumiBlock Range	Number of Events	Number of Selected Tracks
141749	22-100	7082	40714
141811	126-165	11271	63757
142149	65-87	778	4575
142154	22-35	1668	9439
142165	134-257	47904	274728
142166	38-96	30848	176921
142174	8-47	10354	59029
142189	140-147	324	1921
142191	7-36, 141-233	52474	297282
142193	33-153	81505	466429
142195	11-54	41626	238374
142383	260-282	40367	230453
Total at $\sqrt{s} = 900$ GeV	-	326201	1863622
142308	340-368	3153	20717
142402	169-187	2776	18266
Total at $\sqrt{s} = 2.36$ TeV	-	5929	38983
152166	206-300	369673	3769168
Total at $\sqrt{s} = 7$ TeV		369673	3769168

Table C.1: The runs used to study the charged particle multiplicity. The inclusive range of luminosity blocks used is shown, as well as the number of events and tracks used in the analysis.